The formation of CaO-SrO solid solutions and investigations of their surface properties.

de Agudelo, M. M. Ramirez

Award date:
1980

Awarding institution:
University of Bath

THE FORMATION OF CaO - SrO SOLID SOLUTIONS

AND

INVESTIGATIONS OF THEIR SURFACE PROPERTIES

Submitted by M.M. Ramirez de Agudelo

for the degree of Ph.D. of the

University of Bath

1980

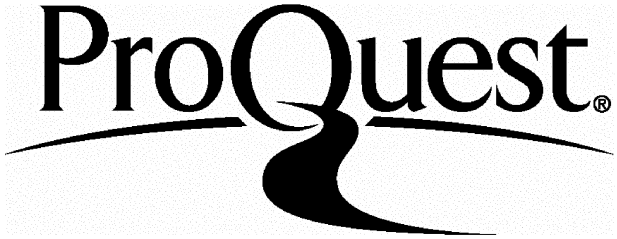

A mis padres,

a Panin y

especialmente a Alejandro

ACKNOWLEDGEMENTS

I am greatly indebted to Professor F.S. Stone for his continued interest, encouragement and discussion throughout the supervision of this research, and his advice has been invaluable during the compilation of the thesis.

I would also like to thank the following persons :

Mr. J. Grosicki for many helpful exchanges of ideas and for his assistance and friendship.

Mr. E. Minshall for his valuable advice on numerous experimental matters and personal contacts.

Dr. S. Lopez for his enthusiasm, inspiration and company while working late hours in the laboratory.

Mr. M. Lock for his skillful and prompt expertise in all the glassblowing involved.

Mr. J. Stainer for his endeavours on my behalf in the Physical Chemistry Stores.

Mrs. E. Giles for her care in typing this thesis.

Professor P. Andreu who first aroused my interest in Surface Chemistry and Catalysis.

The 'Fondo Destinado a la Investigacion en Materia de Hidrocarburos y Formacion de Personal Tecnico (FONINVES)' of Venezuela for financial support.

Other members of the School of Chemistry, especially of laboratories 4W-05 and 4W-1.20 for providing a convivial working atmosphere.

Finally, profound and most special thanks to my husband, Mr. Miguel Agudelo for his moral support during the course of this project and for all his unfailing help with the preparation and realization of this thesis.

MEMORANDUM

The work described in this thesis was conducted in the School of Chemistry of the University of Bath during the period October 1976 to September 1980 and has not been submitted for any other degree. All the work described is the original work of the author except where specially acknowledged.

SUMMARY

The present work is concerned with the preparation, the phase characterization, the surface characterization and the catalytic properties of CaO-SrO solid solutions.

Double carbonates of calcium and strontium were prepared and examined by X-ray diffraction analysis. A miscibility gap was found in the range 20-45% Sr content.

CaO-SrO solid solutions have been prepared by thermal decomposition of the double carbonates at 1450 K. The lattice parameter variation with Sr content has been evaluated and complete miscibility has been proved to exist in the full range of composition.

UV-Vis diffuse reflectance spectroscopy has been used to study the adsorption of CO and butene on the solid solutions. CO produced dimeric and polymeric anion species. Butene produced carbanionic species and there was evidence of polymerization. Butene does not interact chemically with the pre-formed CO anionic species nor is there interaction of CO with chemisorbed butene. Both CO and butene polymeric species remained on the surface even after prolonged outgassing.

Nitrobenzene and oxygen adsorption on CaO-SrO produced anion radical species which were studied by ESR spectroscopy. The surface concentration of the nitrobenzene anion radical, as determined from the integrated ESR spectrum, has been used as a measure of the electron-donor character of the solids. Isomerization of trans-but-2-ene was chosen as a model reaction for the comparison of the catalytic activity through the solid solution series. The mild conditions under which the reaction can be

carried out indicated high basicity and electron-donor character for these solids. The change in these properties with composition has been interpreted in terms of structural, ionic and electronic factors. The structural factor consists of the change in lattice dimensions, in cation size and in surface area. The ionic and electronic factors consist of the ionicity of the metal-oxygen bond, the cation polarizing effect and the influence of the cation field.

OS.60 which is the solid solution with 60% Sr content has shown the greatest basicity and the highest catalytic activity for the isomerization of trans-but-2-ene.

CONTENTS

CHAPTER I

INTRODUCTION

CHAPTER II

EXPERIMENTAL TECHNIQUES

CHAPTER III

METHODS AND RESULTS

CHAPTER I

1. INTRODUCTION

1.1 Calcium, Strontium and their Oxides and Carbonates

1.1.1 The Elements

The chemical behaviour of calcium and strontium and of the alkaline earth elements in general, depends upon the ease with which each atom can lose two electrons to form a divalent cation and upon the possible geometrical arrangements of these cations with ions of other elements to form compounds. Calcium and strontium are extremely reactive and Table 1.1.1 summarizes some of their chemical properties.

Table 1.1.1. Properties of Calcium and Strontium

	Ca	Sr	Remarks	Ref.
Electro-negativity	1.00	0.95	Pauling Scale	(1)
Ionization Potential/eV.	6.113	5.695	$M \longrightarrow M^+ + e^-$	(2)
	11.871	11.030	$M^+ \longrightarrow M^{2+} + e^-$	
	50.908	43.6	$M^{2+} \longrightarrow M^{3+} + e^-$	
Ionic Radius of M^{2+}/Å	1.00	1.16	Coordination N.6	(3)
	1.18	1.29	Coordination N.9	

1.1.2 Calcium Oxide and Strontium Oxide

Calcium and strontium oxides possess the rock salt structure as would be expected for an ion radius ratio of 0.648 and 0.759 respectively. In the unit cell, each ion is surrounded by six ions of the opposite sign in an octahedral arrangement.

The formal description is as follows :-

System : Cubic face-centred

Space Group : F_{M3M}; O_H^5

a_o (CaO) : 4.8105 Å (4a)

a_o (SrO) : 5.160 Å (4b)

Distance M - O (5) : CaO : 2.041 Å

SrO : 2.573 Å

Table 1.1.2 lists some physical properties of the oxides. Besides these properties, it is appropriate to comment on the defect structure.

Table 1.1.2. Physical Properties of CaO and SrO

	CaO	SrO	Ref.
Melting Point/K	2853	2703	(6c)
Boiling Point/K	3123	3273	(6c)
Refractive Index	1.838	1.810	(6c)
Density/g cm^{-3}	3.25-3.38	4.7	(6c)
Magnetic susceptibility (10^{-6}cgs)	15.0	-35.0	(6c)
S^o/J K^{-1} mol^{-1}	39.71	54.34	(6c)
H_f/kJ mol^{-1}	-318.02	-295.81	(6c)
H_{fus}/kJ mol^{-1}	50.70	69.97	(6c)
H_{sub}/kJ mol^{-1}	615.93	674.79	(6a)
Lattice energy/kJ mol^{-1}	816	769	(6b)
Charge on metal ion	0.57	0.59	(1)
Bond strength/kJ mol^{-1}	368.72	402.24	(1)

Surplice (7), using ionic conductivity measurements in the range 300 - 1400°C, observed high temperature activation energies (3.5 eV for CaO and 2.0 eV for SrO) which, as with Mgo (8) suggest the presence of thermally created Schottky defects. Copeland and Swalin (9) found that for SrO Frenkel disorder in the anion sub-lattice (interstital O^-) predominates in the temperature range 600 - 1400°C. Schottky defect formation in SrO has the very high formation energy of 3.7eV (10). A wide variety of defects can be created by irradiation or neutron bombardment(11).

Optical reflectivity measurements in single crystals have revealed the excitation structure in CaO (12a) and SrO (12b, 12c) which is summarized in Table 1.1.3.

Table 1.1.3. Exciton Energies for CaO and SrO

	Band gap/eV	Exciton energies/eV			
		1st	2nd	3rd	4th
CaO	7.7	7.034	7.012	6.973	6.939
SrO	6.7	6.126	6.082	5.784	5.711

In studies of polycrystalline alkaline earth oxides, decomposition of magnesium hydroxide has been widely used for the preparation of MgO but in the case of CaO and SrO the partial solubility of the hydroxides (2 g dm^{-3} for $Ca(OH)_2$ and 4 g dm^{-3} for $Sr(OH)_2$ at 293 K) hinder their precipitation from aqueous solutions and furthermore strontium hydroxide sublimes. However, CaO and SrO can be readily obtained by the decomposition of their carbonates. Calcination in vacuum produces specimens of higher surface area than those obtained by calcination in air. Sintering is greater for CaO than for SrO; surface areas ranging from 10 m^2g^{-1} to 100 m^2g^{-1} are typical for CaO and 2 m^2g^{-1} to 6 m^2g^{-1} for SrO.

The oxides are very thermally stable, but extremely reactive. They react rapidly with water and CO_2 to form the hydroxides and carbonates. As for their electron donor character, a most important property in the context of the present work, they have been classified as solid bases (13). They have been widely studied in this respect, and most of their bulk and surface properties have been characterized. In view of the importance of surface properties in the work to be described later, these aspects will now be reviewed.

Surface states have been studied by reflectance spectroscopy. The first report on the alkaline earth oxides was that of Nelson and Hale (19), who carried out a diffuse reflectance investigation of MgO, CaO and SrO powders. In addition to absorption bands they observed fluorescence (which could be quenched by O_2, H_2O, and CO_2) and they postulated the presence of surface states which created an effective surface band gap at lower energies (summarized for CaO and SrO in Table 1.1.4) than the band gaps typical of the bulk (Table 1.1.3). Zecchina, Lofthouse and Stone (15) conducted a more detailed study of the energies of surface states on MgO and CaO, and Zecchina and Stone (16) extended it to SrO and BaO. Their values for CaO and SrO are summarized in Table 1.1.4 and show good agreement with those of Nelson and Hale (14). They presented a more detailed interpretation of the spectra (Fig. 1.1.1) and ascribed the bands as due to excitons bound to surface states arising from different coordinative unsaturation.

Table 1.1.4. Absorption maxima/eV

	1st		2nd		3rd
	(14)	(15) (16)	(17)	(15) (16)	(15)
CaO	5.3	5.5	4.4	4.4	3.8
SrO	4.9	4.9	3.9	3.9	

The photoluminescence spectra have been studied by Coluccia, Deane and Tench (17). The luminescence observed was thought to be associated with coordinative unsaturation of surface cations, and could be quenched by O_2 and H_2.

Spectroscopic studies of adsorbed species on polycrystalline CaO and SrO have been carried out by several different techniques.

Early reflectance work on the adsorption of nitrocompounds was reported by Frei, Zeitlin **et al.**(18,19), and revealed that the reflectance spectra of the adsorbed species presented regular bathochromic shifts. These were interpreted in terms of electronic polarization theory. The authors regarded a cation polarization effect on the adsorbed anion formed on the surface as responsible for the observed shift, and this effect was smaller for strontium than for calcium.

Zecchina, Lofthouse and Stone (15,16) used reflectance spectroscopy to study the adsorption of N_2O, H_2O and CO_2 on the alkaline earth oxides. Physically adsorbed molecules of N_2O were considered responsible for the reversible change in the spectra observed with this gas, which involved only excitons bound to surface ions. CO_2 and H_2O, on the other hand, interacted extensively with the surface to change the electronic structure of both the excited and ground states. The exciton bands due to surface states were destroyed as a result of strong chemisorption, and formation of carbonates and hydroxides was observed.

The effect of CO adsorption on the reflectance spectra of CaO and SrO (Fig. 1.1.2) was reported by Zecchina and Stone (20). Changes in the spectra were interpreted as an electron donor process in which CO accepts electrons from surface oxide ions and forms anionic clusters in the adsorbed state.

The reflectance spectra of olefins and aromatic hydrocarbons on

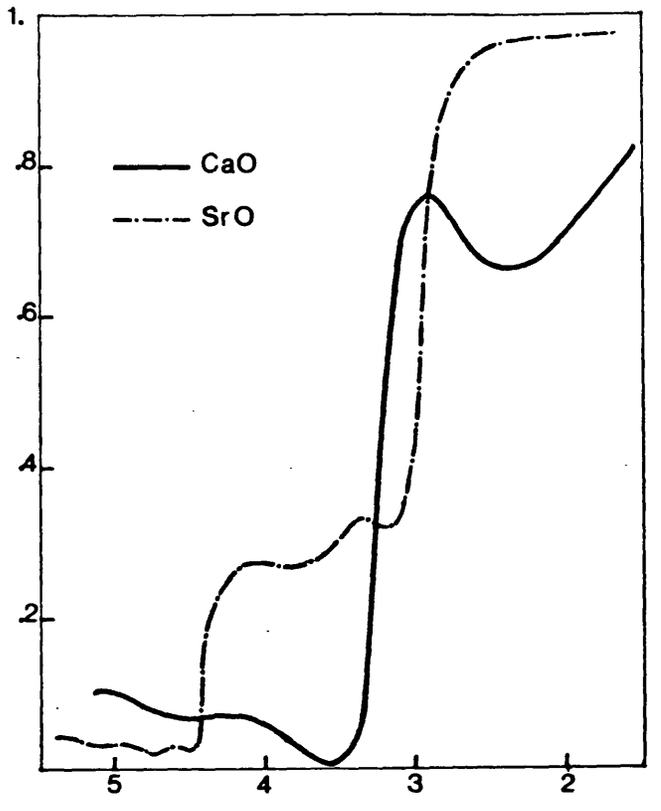

Figure 1.1.1

Reflectance Spectra
of CaO and SrO

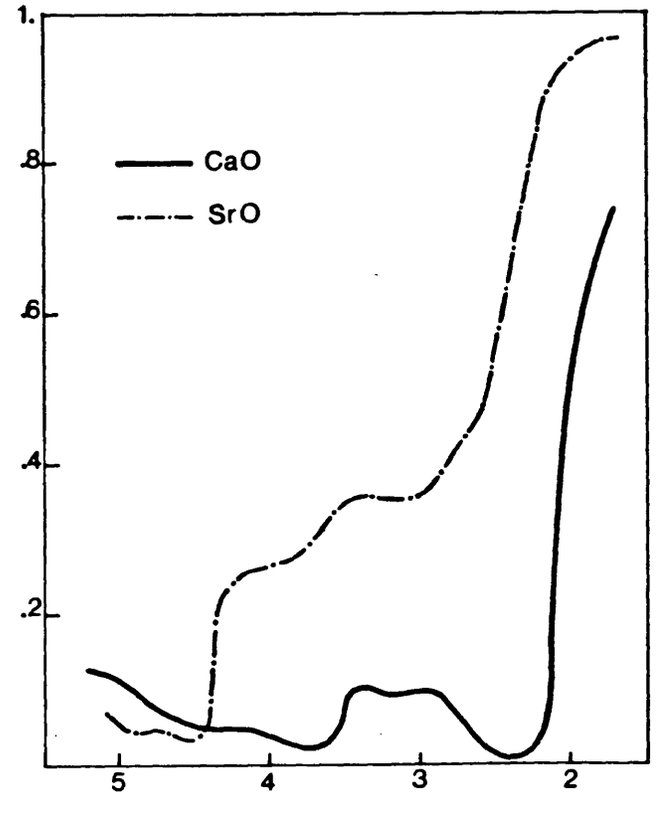

Figure 1.1.2

CO Chemisorbed Spectra

SrO (21) suggest that the oxide has the ability to donate electrons to the adsorbates, forming anionic species of considerable stability.

Tench et al. (22) studied the adsorption of pyridine and its reaction with O_2 on CaO and SrO by means of ESR, reflectance and photoluminescence spectroscopy. Adsorption led to the formation of 4.4'-dipyridyl anions which reacted with O_2 to form the 4,4'-dipyridine molecule and O_2^- through an electron transfer process. Adsorption of 2,2'-dipyridine on CaO gave three different types of surface species, namely physisorbed neutral molecules, chemisorbed neutral molecules and chemisorbed monoanions, as has been shown by Coluccia et al. (23).

The anion radicals, of nitrobenzene (Fig. 1.1.3) and m-dinitrobenzene formed by adsorption on CaO have been observed by ESR by Tanabe et al. (24). The change in anion radical concentration on heat treatment was different from the change in basicity measured by titration using bromothymol blue as indicator (pK_a = 7.1) and also the amount of the radicals was much smaller than that of basic sites (Fig. 1.1.4). However, they found a good correlation between the change in anion radical concentration and the change in the catalytic activity for the polymerization of styrene, i.e. the reducing property, suggesting that two different kinds of sites exist separately on the surface of CaO. Nitrobenzene anions formed on SrO were found to be extremely stable, even towards oxygen (21).

Tanabe et al. (25) studied the adsorption of NO to produce NO_2^{2-} by means of ESR and found that the spin concentration correlated with the activity for cis-trans 2-butene interconversion.

The formation and stability of oxygen radicals on CaO was studied by Cordischi, Indovina and Occhiuzzi (26). They confirmed the formation of O_2^- and O_3^- radicals, O_3^- being selectively destroyed by heat treatment. Preadsorption of H_2 inhibited the

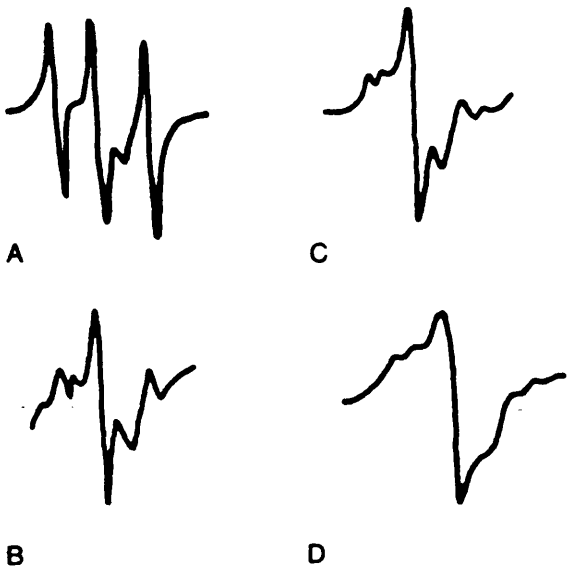

Figure 1.1.3

ESR Signal of Nitrobenzene on CaO

A - immediately after adsorption B - 10 minutes after

C - 30 minutes D - one day

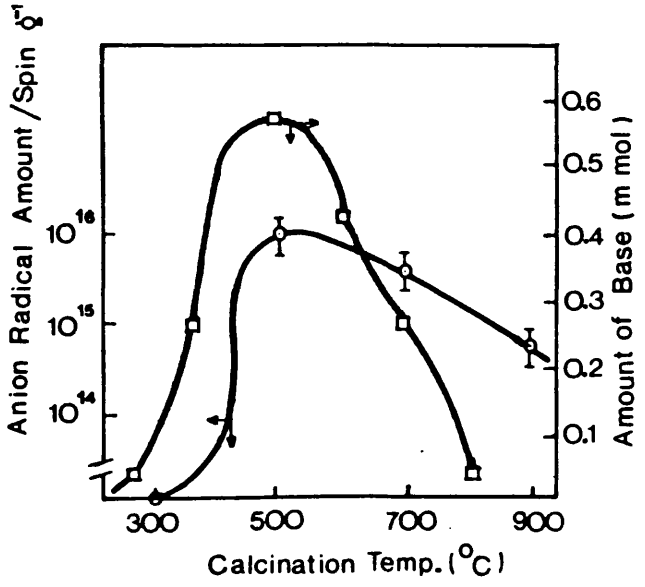

Figure 1.1.4

Basic Properties of CaO

formation of O_3^- but stabilized O_2^-. Stabilization of O_2^- by preadsorption of pyridine on SrO was suggested by experiments made by Che, Coluccia and Zecchina (27).

SO_2^- radicals were formed on CaO when SO_2 was adsorbed and its reaction with O_2 formed SO_4^- radicals at 77 K and SO_3^- at room temperature (28).

A study of the base strength distribution of alkaline earth oxides was carried out by Kikuchi et al. (28). By titration with benzoic acid, using a series of H_- indicators, they showed that the base strength of alkaline earth oxides decreases in the order SrO (H_- = 26.5) $\simeq$ CaO (H_- = 26.5) > MgO (H_- = 18.4 to 26.5) (Fig. 1.1.5). The distribution of base strength was explained in terms of the extent of polarization of the various surface oxygen anions which are located in a surface possessing many kinds of defects with an irregular cation environment.

It is significant that CaO prepared by heating the hydroxide at 1173 K does not show any basicity at all, even at the weakest basic strength of H_o = + 7.1 (24), whereas a sample prepared from the carbonate shows fairly strong basicity (29). Also for SrO the same effect can be observed (13, p. 52) from a comparison of Figures 1.1.5 and 1.1.6.

The nature and structure of basic sites on the alkaline earth metal oxides has not by any means been exhaustively studied. Tanabe et al. (24) proposed two types of basic sites on the surface of CaO prepared from $Ca(OH)_2$ calcined at 1173 K, namely those which are strongly basic O^{2-} sites per se and strongly basic O^{2-} adjacent to surface OH groups; the reducing site was tentatively ascribed as a terminal dislocation or a point defect appearing on the surface by dehydration of the hydroxide.

The catalytic activity of CaO and SrO has usually been

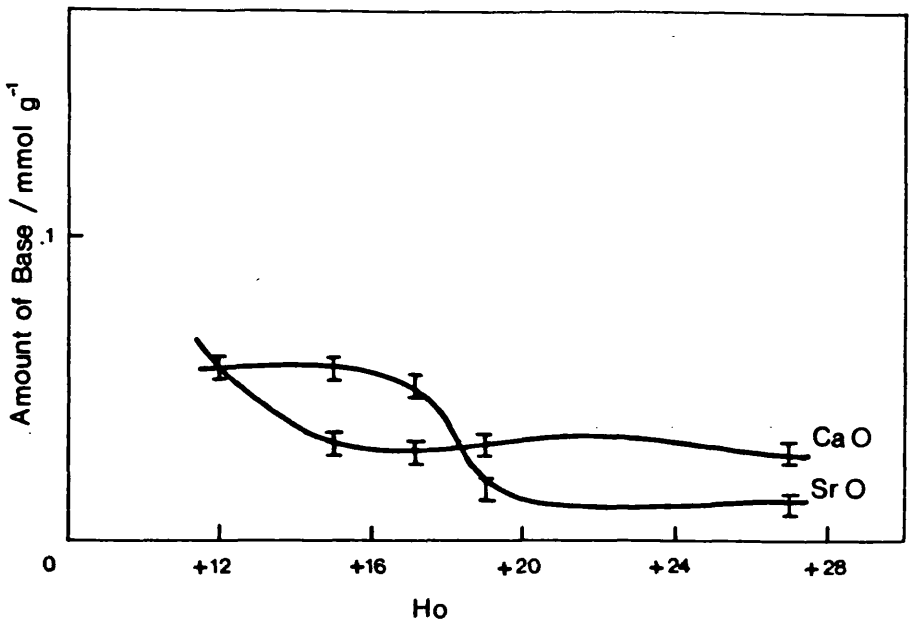

Figure 1.1.5

Amount and strength of Base for CaO and SrO

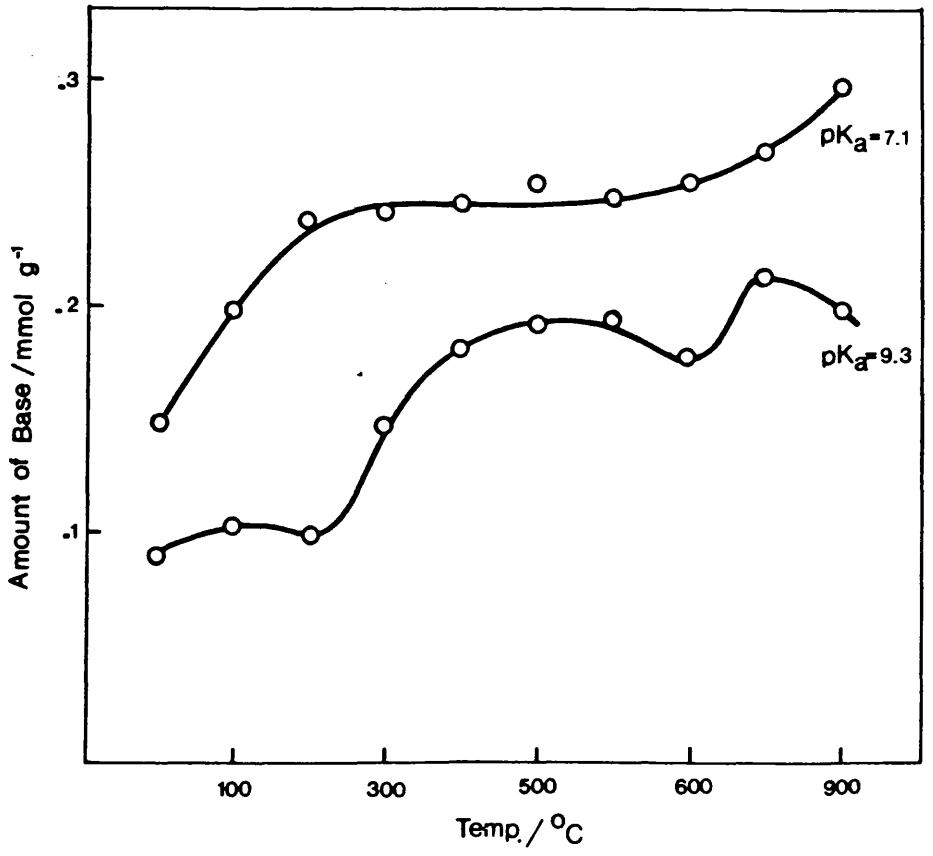

Figure 1.1.6

Basicity of SrO vs. Heat treatment

attributed to their basic character and in most of the reactions studied the poisoning effect of acids has confirmed this idea. Some of the reactions in which they have been used as catalysts are hydrogen chloride elimination from 1,1,2-trichloroethane (29,30), polymerization of styrene (24), hydrogenation of olefins (31a), hydrogen transfer between ketones and alcohols (31b), 2-propanol decomposition (31c), esterification of benzaldehyde (31d), decomposition of diacetone alcohol (31e), elimination reactions of dihalobutanes (31f), decomposition of NO (31g), dehydrogenation of C_6H_{12}, and isopropylalcohol, decomposition of N_2H_4 (31h) and isomerization of olefins (32). Since the isomerization of butene is part of the scope of the present work, it will be considered in more detail later.

1.1.3 The Carbonates

Three forms of calcium carbonate are well recognized, namely calcite, aragonite and vaterite. Strontium carbonate crystallizes in the strontianite structure, which is an aragonite-type structure, but there is also a rhombohedral structure (calcite-type) stable above 1200 K (33).

The calcite structure (Fig. 1.1.7) (34) can be described as a NaCl-like arrangement of Ca^{2+} and CO_3^{2-} ions, distorted by the spatial requirements of its disc-shaped anions. The symmetry is rhombohedral, the Ca^{2+} ions occupying the corners and the centres of the faces of the cell while the CO_3^{2-} ions lie at the centre of the cell and at the mid-points of its edges. The planes of CO_3^{2-} groups are all perpendicular to the vertical c axis of the cell (35). The formal description of the structure is as follows (36) :

Lattice : Rhombohedrally-centered hexagonal

$$a_o = 4.989 \text{ Å}$$

$$c_o = 17.062 \text{ Å}$$

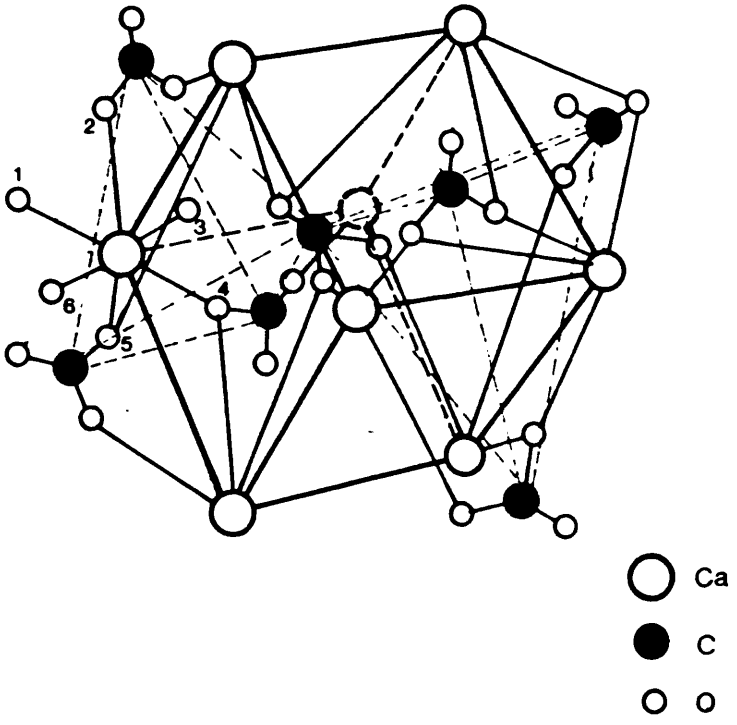

Figure 1.1.7

Calcite structure

$\alpha = 46^{o}05'$

Number of formula units per unit cell : 6

Space group : $R\bar{3}c$ ($n^{o}167$); D^{6}_{3D}

The structure of aragonite (37), shown in Figure 1.1.8, is related to that of nickel arsenide in the same way as the calcite structure is related to that of sodium chloride. It may be regarded as a distorted NiAs structure with arsenic replaced by calcium and nickel by carbonate groups. All the CO_3^{2-} groups are parallel and each calcium ion is surrounded by nine oxygen neighbours each of which in turn is bonded to three calcium ions. The formal description is as follows (37, 38) :

Lattice : Orthorhombic

Number of formula units per unit cell : 4

Space group : Pmcn ($n^{o}62$); D^{16}_{2H}

Table 1.1.5. lists the values of the lattice constants for the aragonite-type structure of $CaCO_3$ and $SrCO_3$.

Table 1.1.5. Lattice Constants of $CaCO_3$ and $SrCO_3$

	$CaCO_3$	$SrCO_3$
a_o/Å	5.740	5.197
b_o/Å	4.961	8.414
c_o/Å	7.967	6.029

The unstable μ-form of calcium carbonate has been suggested to crystallize in the vaterite structure (34). It is like aragonite, orthorhombic and pseudohexagonal, but it has a different tetramolecular cell. The formal description is as follows (39) :

Lattice : Orthorhombic

$a_o = 4.13$ Å

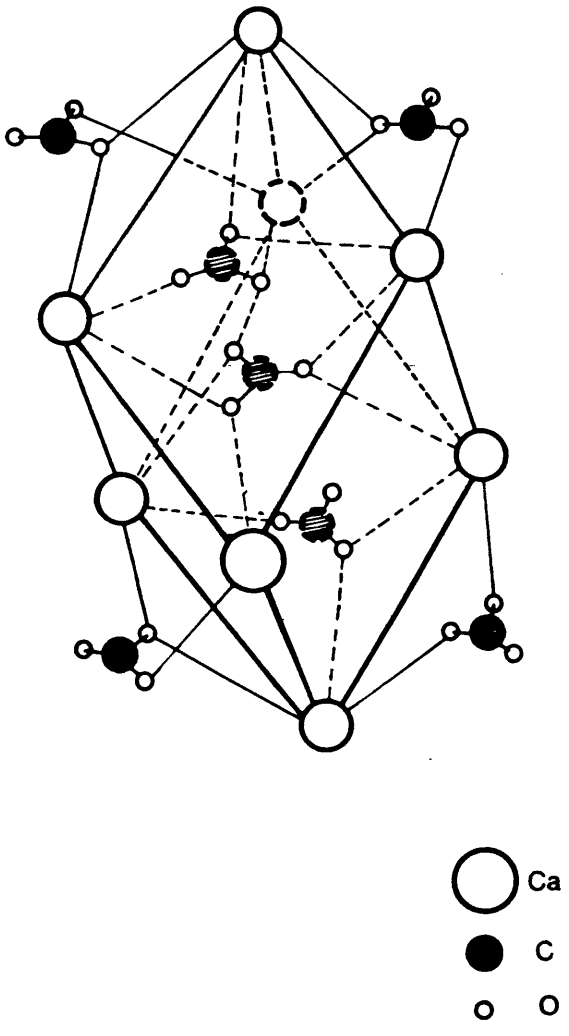

Figure 1.1.8

Aragonite structure

$$b_o = (\sqrt{3}\, a_o) = 7.15\ \text{Å}$$

$$c_o = 8.48\ \text{Å}$$

Space group : $P6_3/nmc$ ($n^o 194$); V_b^{16}

Calcium carbonate occurs abundantly as limestone, which is mainly composed of calcite but which also contains magnesium carbonate, silica and oxides of iron and aluminium. Marble is fairly pure calcite formed in nature by recrystallization under pressure. Coral, pearls and some shells consist of aragonite and this form of $CaCO_3$ is also deposited from warm carbonated water around hot springs. Vaterite occurs in shells of birds' eggs and gastropods and occasionally in rocks. Strontianite is a low-temperature hydrothermal mineral found chiefly as veins in igneous rocks (40).

Thermodynamic data indicate that the predominance of one form of $CaCO_3$ over another at ordinary temperatures is determined by kinetics rather than thermodynamics (41). Table 1.1.6. summarizes the standard enthalpy of formation (ΔH_f^o), entropy (S^o), free energy (ΔG_f^o) and solubility product (K_{sp}) for $CaCO_3$ and $SrCO_3$ at 298 K (42). The calcite-aragonite polymorphism is brought about by the fact that the radius of the calcium ion is very close to the limiting value for the transition from the rhombohedral carbonate structure to that of the orthorhombic carbonates. The temperature at which aragonite changes spontaneously into calcite at atmospheric pressure is about 680 - 730 K (43).

Table 1.1.6. Thermodynamic Properties of $CaCO_3$ and $SrCO_3$ at 298 K

	ΔH_f^o/kJ mol^{-1}	S^o/J deg^{-1}	ΔG_f^o/kJ mol^{-1}	$K_{sp} \times 10^9$
$CaCO_3$ Calcite	-1205.72	92.8	-1127.68	4.7
Aragonite	-1205.89	88.6	-1126.64	6.9
$SrCO_3$	-1217.22	97.0	-1136.5	1.6

The carbonates can be readily synthesized by mixing carbonate solutions with solutions containing the cations. For calcium carbonate the temperature of precipitation and ageing will determine the precipitated structure. Wray and Daniels (44) have studied this effect and found that while increasing the temperature favoured the aragonite structure, ageing favoured the calcite structure. Vaterite is precipitated when mixing is fast and under stirred conditions, and also at low temperatures (273 - 283 K).

The application of heat to carbonates causes dissociation to the oxide. In the equilibrium $MCO_3 \rightleftarrows MO + CO_2$ the temperature at which carbonates exhibit a dissociation pressure of CO_2 of 1 atmosphere is approximately 1180 K for $CaCO_3$ (45) and 1460 K for $SrCO_3$ (46). Differential thermal analysis of calcite shows an endothermic reaction (decomposition) starting at about 898^{o}K, peaking at 1113 K and ending at 1163 K. For aragonite the reaction starts at 873 K, peaks at 1133 K and ends at 1193 K. For strontianite a series of relatively small endothermic reactions start at about 1073 K and continue past 1273 K (47).

1.2 Solid Solutions

1.2.1 General

Solid solutions are single phase materials with chemical compositions which do not obey the law of simple multiple proportions, i.e. formulae subscripts are not simple integers.

Three important types of solid solutions can be distinguished :

1. Substitutional Solid Solutions. These are formed by diadochic atoms or ions (elements that can occupy the same site in a crystal structure). A random arrangement of atoms is invariably found if the molten mixture has been cooled quickly, but in some cases rearrangement to form a more regular structure takes place if the melt is cooled slowly or if the quenched material is annealed.

For the substitution of a foreign atom in a host structure it is necessary that the chemical properties of the foreign and host atoms should be similar. A necessary condition for the formation of a continuous series of solid solutions of components A and B is that they have the same crystal structure. There are many complicating factors, so that in general no deductions can be made a priori. However, one may broadly state that complete miscibility of structurally similar atoms or ions is possible only if their sizes do not differ by more than about 15% (48), and secondly bonds in the two crystals must be of similar type.

The thermodynamic condition for the formation of an ideal solid solution is that the mutual energy of an AB pair should be equal to the arithmetic mean of the mutual energies of AA and BB pairs; in other words, the exchange of molecules in the lattice of the mixed crystal leaves the energy unchanged (49).

The melting point and the cell dimensions of such a solid solution vary regularly with composition. Early X-ray studies

indicated that the parameters of the unit cell varied linearly with concentration (Vegard's law (50)). Later measurements showed that in most cases the linear dependence was only a first approximation. For instance, metallic solid solutions with f.c.c. structures showed a square dependence on concentration :

$$a(C) = a_1 + C\Delta_1 a + C^2\Delta_2 a + \ldots\ldots \qquad 1.2.1$$

Zen (51) has reviewed the validity of Vegard's law and found that only solid solutions in which the end members do not have very different molar volumes will exhibit a linear behaviour, i.e.

$$[(V_1/V_0)-1] << 1 \qquad 1.2.2$$

where V_1 and V_0 are the volume of the unit cell of the end members.

Frevel (52) has reported a method for the quantitative identification of substitutional solid solutions based on the empirical equation :

$$|a_x - a_o| = C^{\alpha} |a_1 - a_o|^{\beta} \qquad 1.2.3$$

where a signifies the lattice parameters of the end member (o and 1) and of the solid solution (x) and C is a constant; α and β are determined experimentally or empirically by using published data. Of the five types of curve which have been identified so far (see diagram below), this equation applies to types 1, 2 and 3.

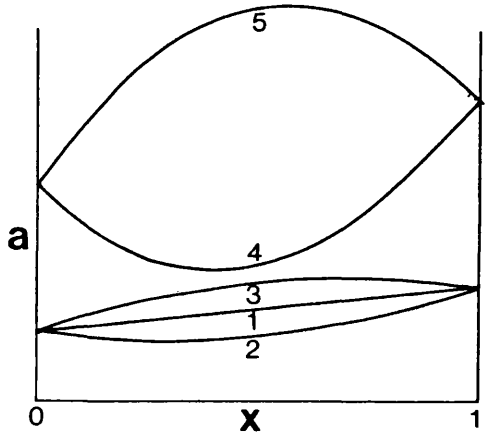

2. Interstitial Solid Solutions Between the ions or atoms packed in a crystal structure, interstices exist within which suitable small ions or atoms may lodge. Therefore, elements such as H, B, C, N, and O are the most likely to be found in this type of solution.

3. Omission Solid Solutions These are crystals in which a particular type of site is incompletely filled, forming defect structures. They are sometimes called defect solid solution series.

1.2.2 Calcium Carbonate - Strontium Carbonate Solid Solutions

The coprecipitation of mixed carbonates can be carried out in the same way as that of precipitation of the pure compounds. The main importance of these solid solutions is in their use as starting materials for the preparation of CaO-SrO solid solutions. Accordingly, research has been directed towards their preparation, crystallography and thermal behaviour.

Huber and Wagener (53), in their investigation on the use of calcium oxide - strontium oxide solid solutions as emitters, employed calcium carbonate - strontium carbonate solid solutions as starting materials. The strontium-rich mixtures exhibited the strontianite structure and the calcium-rich ones showed the calcite structure.

The first crystallographic study of the mixed carbonates was conducted by Guichard and Wyart (54) on the solid solution $(Ca_{0.5}Sr_{0.5})CO_3$ obtained by coprecipitation from a chloride solution using $(NH_4)_2CO_3$. The lattice parameters of the produced strontianite structure were :

$$a_0 = 5.05\ \text{Å}, \quad b_0 = 8.28\ \text{Å}, \quad c_0 = 5.83\ \text{Å}$$

A wider concentration range was later studied by Terada (55) but he was only concerned with the type of structure present and did not make a quantitative measurement of the parameters. He

observed two phases (calcite and aragonite) to be always present below 40 mol percents of $SrCO_3$. Ostapchenko (56) has studied the binary and ternary carbonates of alkaline earth metals. For the carbonates of calcium and strontium coprecipitated by soda at 90°C he observed a region of two-phase solid solutions in the 20-45% $SrCO_3$ content interval, but a single phase of strontianite type above 45% and of calcite type below 20%.

Holland et al. (57, 58, 59), in their investigation of the distribution coefficient in the context of the geochemistry of carbonates, have studied the effect of precipitation temperature and the source of carbonate ions on the coprecipitated mixed carbonates. In the first report (57) they covered the temperatures 303 K and 368 K and the precipitation was carried out by using either the hydrolysis of trichloroacetate (368 K) or by passing CO_2 into an ammoniacal solution of chlorides. Sr^{2+} ions are much more readily precipitated as the aragonite structure than as the calcite structure under these conditions. They also found that when precipitation is carried out at 373 K by carbonate ions generated from trichloroacetate ions, aragonite and strontianite were the predominant structures but calcite was present as well. Ammonia suppressed the calcite nucleation. The calcite/aragonite ratio was observed to depend on the degree of supersaturation maintained during the precipitation (rate of precipitation). The dependence of the lattice parameters on concentration showed a negative deviation from Vegard's law, suggesting a small heat of mixing for the system. Calcite (59) was mainly precipitated by slow introduction of CO_2 into $CaCl_2$-$SrCl_2$-NH_4OH solutions at 373 K but in this case also aragonite was present.

The thermal analysis of the double carbonates has been considered by various authors. Like the pure carbonates, the

coprecipitated mixed carbonates decompose on heating to yield mixed oxides and hence the importance of their thermal behaviour. Evstigneeva, Iofis and Bundel (60) measured the equilibrium pressure of CO_2 in the range 923-1123 K. Their results indicated the disappearance of the miscibility gap with increasing temperature and hence the occurrence of unlimited miscibility. Hall and Sharp (61) have reported the thermal analysis of some double carbonates without specifying the studied concentration range, and their observations can be summarized as follows : (i) small exotherm at 772 K, (ii) large endotherm with peak at 1003 K, (iii) weight loss at 823-1023 K and (iv) endotherm at 920 K.

Kinetic studies have been performed by Zemtsova, Prodan and Pavlyuchenko (62) on samples with 95, 50 and 40% $SrCO_3$ content. The decomposition of single phase specimens (95 and 50%) with the aragonite structure occurs in vacuo in a single stage process and it is accompanied by the enrichment of the solid solution in $SrCO_3$. Meanwhile the decomposition of the two-phase specimen (40%) involved a two-stage process, the first one being the preferential consumption of the calcite-type phase and the second stage involved the preferential consumption of the aragonite-type phase and a change in the composition of the solid solution in the direction of pure $SrCO_3$.

1.2.3 Calcium Oxide - Strontium Oxide Solid Solutions

Although both of the pure oxides, CaO and SrO, have been proved to be highly reactive basic catalysts, very little research has been directed toward their solid solutions and certainly no work has yet been published on their catalytic activity.

As mentioned in the previous section a suitable method of preparation is by controlled decomposition of the coprecipitated

carbonates in vacuo. Kinetic studies have shown that the slow decomposition of the carbonate solid solutions favours the homogenization of the forming oxide (60). Ostapchenko (56) found a breakdown of the linearity of the lattice parameter with composition at about 40% SrO content when the solid solutions were formed at 1023 K. Huber and Wagener (53) prepared the solid solutions by annealing the carbonates for 2 hours at 1300 K and 1500 K. The X-ray determined lattice parameters of the samples prepared at 1300 K were 0.3% higher than the values observed for samples prepared at 1500 K. Furthermore, the surface lattice parameter determined by electron diffraction was shown to be equal to that of CaO after 2½ hours heating at 1450 K. It was concluded that a preferred vaporization of SrO occurs from the oxide layer during the preparation at such a high temperature.

Heinz and Muenchberg (63) have shown the CaO-SrO system exhibits complete miscibility over the entire range of composition when the solid solutions are formed at 1873 K and moreover no segregation occurred on cooling to room temperature. Their lattice parameter data showed a slight negative deviation from Vegard's law (Fig. 1.2.1.). However, this may be due to an error in the determination of the composition. Since preferential vaporization of SrO occurs at high temperature, the measured lattice paramater for a solid held at elevated temperature will correspond to a solid solution with lower Sr content than that assumed from the Sr content of the original carbonates, or in other words it is, as observed, smaller than the expected value.

It has been found experimentally that the work function of the solid solution is considerably less than that of the pure oxides (64). In order to compute the variation with composition, Logatchov and Moijes (65) have used a model based on the relaxation

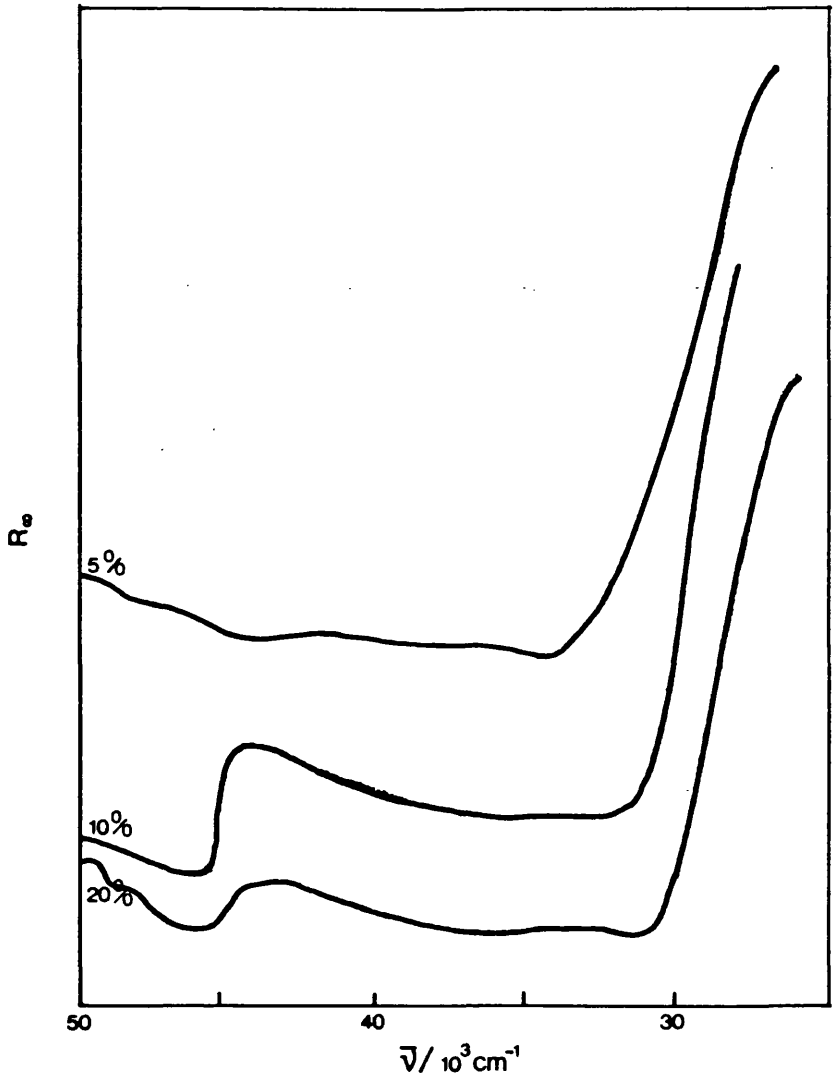

Figure 1.2.2

Reflectance Spectra of $(Ca_{1-x}\ Sr_x)O$

for x = 0.05, 0.1 and 0.2

of the surface due to the enrichment of the surface by Sr^{2+} ions regardless of the results of Huber and Wagener. The lower work function of these solids is reflected in their low surface exciton energies as measured by Trevethan (21) using reflectance spectroscopy (Fig. 1.2.2). He studied the solutions with 5, 10 and 20% SrO content. Adsorption of CO led to the formation of stable anionic CO clusters as already observed for the pure oxides (20). The spectral changes due to N_2O adsorption were tentatively ascribed to anionic species like NO_2^-, O_3^- and O_2^-.

1.3 Base Catalysis

1.3.1 Fundamentals

Base catalysis should be understood as the catalytic action of solid bases (5, 13). The comparatively little work that has, as yet, been performed on solid bases will undoubtedly be augmented as more examples of their applications as effective catalysts are discovered, as has happened already with acid catalysts.

Two traditional definitions have been given of bases, and these are adequate for an understanding of the acid-base phenomena shown by various solids and convenient for the clear description of solid bases :

1. Following the Bronsted definition, a basic centre on a surface is a centre posessing proton acceptor properties;
2. From the Lewis point of view, a basic centre is a site capable of donating an electron pair.

Table 1.3.1 lists most of the solid bases in common use. Special mention should be made of the alkaline earth metal oxides, whose basic properties and catalytic action are the subject of the research to be described later and from which CaO and SrO have already been discussed in Section 1.1.2. The fact that alumina

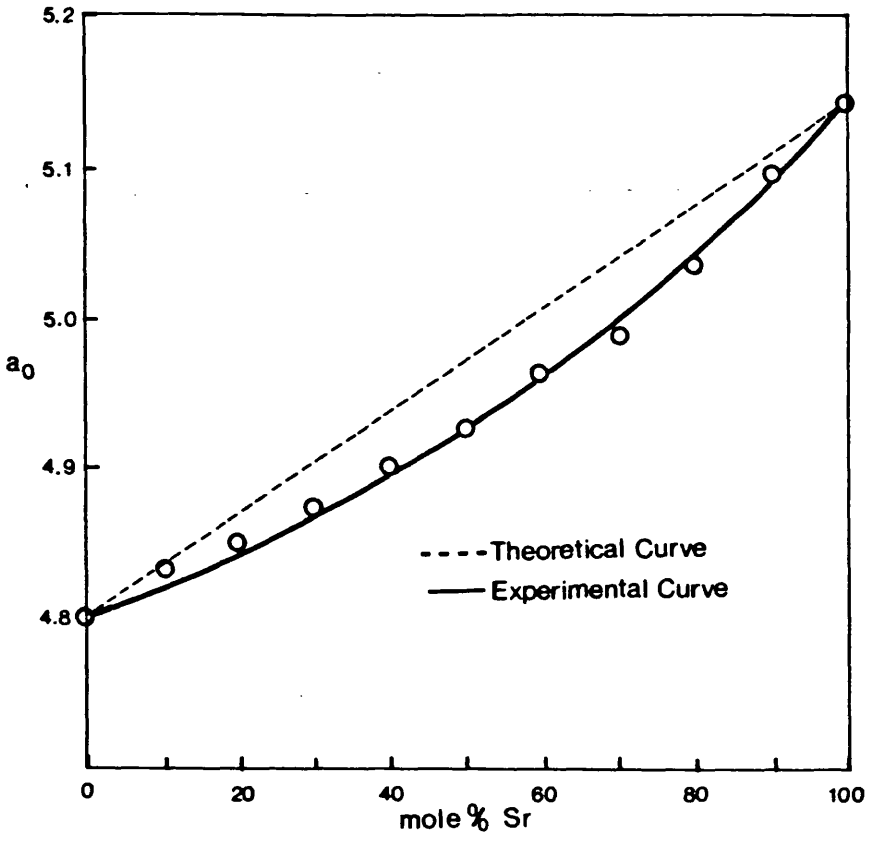

Figure 1.2.1

Lattice Parameter vs Composition of

CaO - SrO Solid Solutions

Table 1.3.1. Solid Bases

Type	Examples
Supported Bases	NaOH or KOH supported on SiO_2 or Al_2O_3 Alkali metal or alkaline earth metals dispersed on SiO_2, Al_2O_3, Carbon, K_2CO_3, or in oil Li_2CO_3 on SiO_2
Inorganic Solids	BeO, MgO, CaO, SrO, BaO, $CaCO_3$, $SrCO_3$, $BaCO_3$, SiO_2, Al_2O_3, ZnO, Na_2CO_3, K_2CO_3, $KHCO_3$, $(NH_4)_2CO_3$, $KNaCO_3$
Mixtures of Oxides	SiO_2 - MgO, SiO_2 - CaO, SiO_2 - SrO, SiO_2 - BaO
Charcoal	Heat-treated at 1200 K or activated with N_2O or NH_3

and ZnO show both acidic and basic properties is of special significance for acid-base bifunctional catalysis.

A complete description of basic properties on solid surfaces requires the determination of base strength and of the amount and nature of the base centres. The base strength of a solid base is 'the degree of ability' of the surface to convert an adsorbed electrically neutral acid to its conjugated base. If the reaction proceeds by means of proton transfer the Hammett function (H_0) is used for measuring the base strength (eq. 1.3.1), i.e. :

$$AH + B \rightleftharpoons A^- + BH^+$$

$$H_0 = pK_a + \log \frac{(A^-)}{(AH)} \qquad 1.3.1$$

Basicity is usually expressed as the number of basic sites per unit weight or per unit surface area. It is thought to be localized on specific basic sites; a proper description of these sites

requires information about both their quality and quantity, but unfortunately the two are not always independent. There is agreement that the strength of sites is heterogeneous, but their quality, whether they are Bronsted or Lewis, is often disputed.

There exist three principal methods to determine the basicity of a surface :

1. Ion Exchange Adsorption This consists of the titration of an aqueous suspension of the catalyst by an acid. In other words the base amount can be determined from the exchanges taking place between hydroxide ions, for instance, and anions at the surface. One can also use this method to estimate the strength of the basic sites by changing the pH of the ion exchange solution. A disadvantage is that there is the possibility of modifying the catalyst surface as a result of its interaction with the aqueous medium.

2. Adsorption of Acids One may estimate the number of basic sites on the surface from the corresponding amount of adsorbed acid. The strength depends on the stability of the bonds with the surface. Temperature-programmed desorption (TPD) is one of the methods by which this can be done, the strongest bond being the one that needs the highest temperature to break it. Acids can be adsorbed from an aqueous medium, and acids such as benzoic, acetic and hydrochloric have been used to determine the amount of basic sites on sugar charcoal (66). Also some attention has been given to the Lewis acid, BF_3 (67). The conventional method to follow the adsorption has been the change of pH of the aqueous solution. Acids can also be adsorbed from the gas phase. The use of spectroscopic techniques has permitted not only the determination of the amount adsorbed but also the elucidation of the adsorbed species and the type of bonding with the surfaces. The

absorption maxima of UV-Vis and IR spectra can provide a qualitative (sometimes quantitative) interpretation of the basic strength in its widest sense. Molecules like 1,3,5-trinitrobenzene (68), o-nitrophenol (18, 19, 69) the three mononitrophenols (70), p-nitrophenol, phenolphthalein and thymolphthalein (71) have been used.

Anion radicals formed on the surface of solid bases can be investigated by EPR. The value of the integrated area of the signal is directly proportional to the amount of the radical and also the g-tensor is conclusive in their identification. More details on the use of EPR as a quantitative technique will be given in the next chapter.

3. Titration In this third method we can distinguish several variants. Firstly, using indicators, the amount of basic sites can be measured by titrating a suspension in benzene of a solid on which an indicator has been adsorbed in its conjugated basic form, with benzoic acid dissolved in benzene. The amount of benzoic acid titres are a measure of the amount of basic sites (in mmole g^{-1} or mmole m^{-2}) having a base strength corresponding to the pK_a of the indicator used. Table 1.3.2 collects the indicators used for measuring basic properties. Back titration has also been used for measuring basicity (72) but this only allows one to estimate the base strength qualitatively, deriving it from the strength of the acid used.

Traditional methods to follow titrations have often been used (73) but recently spectroscopic techniques have been introduced to help in the observation of either the colour changes due to the indicator or a different evaluation of the end point. As an ingenious example can be mentioned the method introduced by Malinowski, Hombek and

Table 1.3.2. Indicators

Indicators	Colour		pK_a
	Acid form	Basic form	
Bromothymol Blue	Yellow	Green	7.2
2,4,6-Trinitroaniline	Yellow	Reddish-orange	12.2
2,4-Dinitroaniline	Yellow	Violet	15.0
4-Cl-2-Nitroaniline	Yellow	Orange	17.2
4-Nitroaniline	Yellow	Orange	18.4
4-Chloroaniline	Colourless	Pink	26.5

Kijenski (74) to determine the hydroxyl groups and water adsorbed by titration with alkali metal naphthenide solution ($pK_a \simeq 33$) and observing the end point by either ESR or visually.

A second variant is calorimetric titration, which consists of observing the rise in temperature due to the heat of reaction between solid acids and bases in benzene (75).

Finally, a third way of interpreting the basicity of simple oxides is on the basis of a qualitative comparison between the tendency of oxygen acids to add a proton and the ease of separation of an ion of oxygen. Thus, a substance is called a base if, as a result of the separation from it of an oxygen ion, an acid is formed :

$$\text{base} \longrightarrow \text{acid} + O^{2-}$$

$$\text{e.g.} \quad CaO \longrightarrow Ca^{2+} + O^{2-}$$

Proceeding with this definition, the larger the basicity the smaller the energy of the bond of the element to oxygen; hence on increasing the charge of a transition metal ion, for example, the basicity of the corresponding oxide falls. In the periodic table of elements an increase of atomic number of a metal in a particular

group increases basic properties. From right to left in a specific period, basic properties grow. Basic oxides are mainly bonded ionically, and so increasing the covalency of the bond decreases the basicity.

For oxides of non-transition metals, it is logical to apply the Lewis definition for the coordination properties of the surface atoms. Qualitative speculations about their donor capacity can be drawn from the charge/radius ratio. As a rule the donor-acceptor bond is weakly covalent but strongly electrostatic.

After this description of the general background necessary for understanding base catalysis, the next section will deal with some examples of base-catalyzed reactions.

1.3.2 Base-catalyzed Reactions

Acid-catalyzed reactions are very common, with many industrial examples, and they have been widely investigated. In contrast, and in spite of their high stereospecificity, good yields and mild conditions of operation, base-catalyzed reactions (76, 77, 78) have not received their due attention, neither from research scientists nor from industrialists.

Considering that base-catalyzed reactions mainly involve either the removal of a proton or the formation of an anion it is important to consider the acidity of the reactant and also the stability of the possible anions which may be formed.

The stabilization of a carbanion, as an example, can be assisted by the presence of a highly electronegative group adjacent to the charged atom or by the sharing of the negative charge through a conjugated system. Groups such as : $-NH_3$, $-NR_3$, $-NO_2$, -CN, -COOH, -COOR, -CHO, -F, -Cl, Br, -OH, in the β position can help not only in the stabilization of the anion but also in its formation.

Thermodynamic and kinetic acidity must necessarily be distinguished In considering an acid and its conjugated base, the thermodynamic acidity is the position of the equilibrium, whilst the kinetic acidity is a measure of the time which it is achieved. The reaction rate and possible products will depend not only on the catalyst (basicity, base strength, etc.) but also on the reactant acidity and possible intermediates.

Some individual base-catalyzed reactions will be briefly considered in the next paragraphs, with particular emphasis on those where CaO and SrO have been investigated.

1. Isomerization Isomerization reactions can be grouped according to the type of reactant which undergoes reaction.

(A) Monoolefins :

(a) Acyclic alkenes. In this group only double-bond shift and cis -trans isomerization take place, the most stabilized intermediate being that which yields the cis isomer :

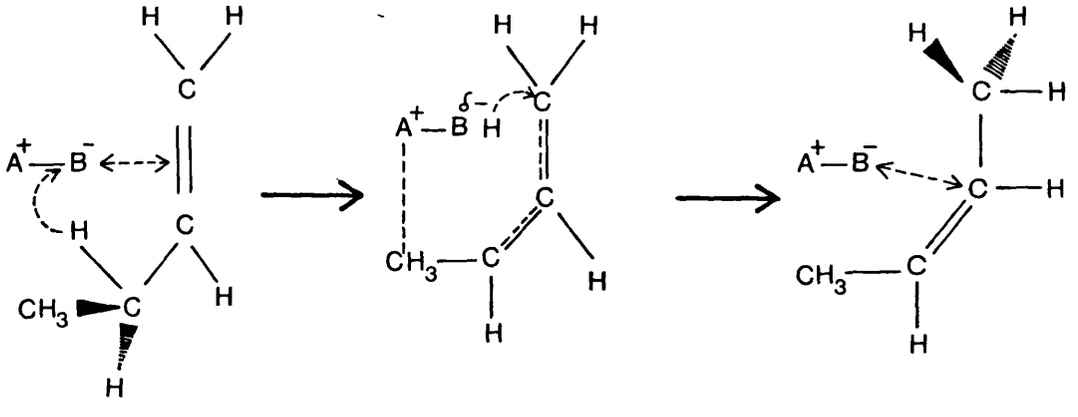

The activity of CaO as an isomerization catalyst has been determined using a number of pentenes and hexenes (79), and a high stereospecificity yielding the cis isomer was observed.

(b) Cyclic alkenes. Besides the double bond shift, hydrogen transfer reactions are side reactions for this group. Possible products can be predicted from conformational analysis. Activity of CaO for the isomerization of 3-carene was studied by Tanabe et al. (80). The main product was 2-carene and no hydrogen migration was observed; no formation of 4-carene was in agreement with the mechanism expected from conformational analysis.

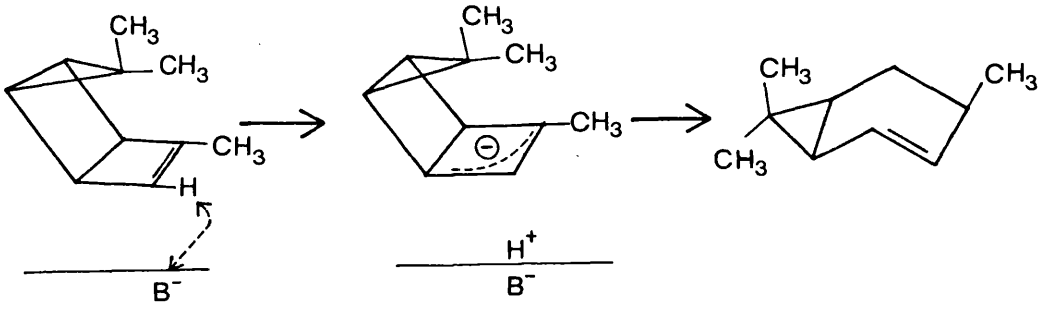

(B) Dienes and Polyenes :

The interest in dienes and polyenes originates from the discovery that hydrogen transfer reactions yielding aromatic compounds occur in competition with the isomerization reactions. In all cases a high degree of stereospecificity is noted with the initial formation of a large amount of cis product during each step of the isomerization, the final products being conjugated dienes.

The ease with which aromatization occurs was demonstrated when 5,5-dimethyl-3-methylenecyclohexene yielded m-xylene and methane over a sodium-organosodium catalyst (81).

2. Carbon-carbon Additions

(A) Oligomerization of Olefins :

Simple olefins which can form allylic carbanions can undergo

oligomerization in the presence of bases. The most widely used catalyst has been sodium. In some cases a promoter is indispensable in the initiation step to produce an organosodium compound which leads to the formation of the carbanion.

The following example illustrates the steps involved in the catalytic chain reaction (82) :

$$\text{Promoter} + Na \longrightarrow B^-Na^+$$

$$C_6H_5CH_3 + B^-Na^+ \longrightarrow C_6H_5CH_2^-Na^+ + BH \qquad \text{Initiation}$$

$$C_6H_5CH_2^-Na^+ + CH_2{=}CH_2 \longrightarrow C_6H_5(CH_2)_2CH_2^-Na^+ \qquad \text{Addition}$$

$$C_6H_5(CH_2)_2CH_2^-Na^+ + C_6H_5CH_3 \longrightarrow C_6H_5(CH_2)_2CH_3 + C_6H_5CH_2^-Na^+ \qquad \text{Propagation}$$

Dimerization of propene over supported potassium or sodium on graphite or potassium carbonate (83) and the codimerization of ethylene with propene on alkalimetal catalysts (84) to yield n-pentenes constitute a couple of examples of this sort of reaction.

(B) Reactions of Alkylaromatics with Olefins

Alkylaromatics suitable for this reaction are those which contain a benzylic hydrogen, and olefins such as ethylene, propene, conjugated alkadienes and styrene and its derivatives. We can distinguish different groups of reactions, e.g., ethylation of alkylbenzenes and alkyl-naphthalenes, and the propylation, alkenylation and aralkylation of alkylbenzenes. The most remarkable feature of this reaction on base catalysts is the selective growing of the alkyl side chain of the alkyl-aromatic (85).

$$\underset{(X)}{C_6H_5CH_3} + B^-Na^+ \longrightarrow \underset{(Y)}{C_6H_5CH_2^-Na^+} + BH$$

$$Y + \underset{\pi}{CH_2{=}CH}\text{-}CH{=}CH_2 \longrightarrow \underset{(Z)}{(C_6H_5CH_2CH_2CH{=}{=}CH{=}{=}CH_2)^-Na^+}$$

$$Z + X \longrightarrow C_6H_5CH_2CH_2CH{=}CHCH_3 + Y$$

(C) Reaction of Alkylpyridines with Olefins

These reactions are a good example of a case where the acidity of the reactant plays a decisive role. The picolyl hydrogens of 2- and 4-alkylpyridines are more acidic than the corresponding benzylic hydrogens; for this reason these reactions occur under mild conditions and even below room temperature as is the case when conjugated dienes, styrene or vinylpyridines are used.

Finally, let us summarize the carbon-carbon addition reactions by remarking that besides the high stereospecificity of these reactions it is also rather important that in contrast with the acid-catalyzed carbon-carbon additions which result exclusively in addition of the alkyl group to the aromatic ring, in base-catalyzed reactions the alkylation occurs in the side chain. Thus these reactions are unique in that they allow one to enlarge the alkyl group of an alkylaromatic.

3. Hydrogenation Different catalysts show different degrees of hydrogenation but still total hydrogenation is possible with a quite high yield even for aromatic reactants. The hydrogenation of benzene (86) has been the subject of attention; spectroscopic studies (IR, UV-Vis and EPR) have been made in the system K/Al_2O_3 and it is concluded that the surface species are aromatic radical anions.

4. Dehydrogenation, Aromatization and Hydrogen Transfer

These reactions may take place simultaneously with other reactions already mentioned. The first reported example of a base-catalyzed dehydrogenation was the aromatization of d-limonene using a sodium-benzylsodium catalyst (87). CaO and MgO were shown to be almost inactive for this reaction (88).

5. Alcohol Reactions Depending on the experimental conditions, dehydration of a simple alcohol produces an olefin which may undergo

any of the reactions already described.

The decomposition of diacetone alcohol on alkaline earth metal oxides (89) produced acetone as a unique product and revealed that the number of active sites (basic) followed the order MgO>CaO>SrO>BaO but the order of base strength was MgO<CaO<SrO<BaO.

1.4 Isomerization of Butene

1.4.1 General

Butene exists in four isomeric forms, namely 1-butene, cis-2-butene, trans-2-butene and iso-butene. Double bond isomerization interconnects the first three isomers but the fourth can only be obtained through a skeletal isomerization process.

Thermodynamics predict three interacting equilibria among but-1-ene, cisbut-2-ene and transbut-2-ene, the last one being the most stable isomer. Figure 1.4.1 shows their thermodynamic relationships.

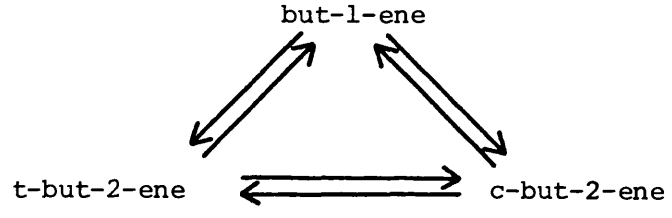

at room temperature (90) : $\Delta G^{o}_{ct} = -3.22$ kJ mol^{-1}

$\Delta G^{o}_{lt} = -8.40$ kJ mol^{-1}

$\Delta G^{o}_{lc} = -5.18$ kJ mol^{-1}

Figure 1.4.1

Furthermore, this relationship holds at any temperature, since :

$$\Delta G^{o}_{ct}/\text{kJ mol}^{-1} = -3.97 + 2.51 \times 10^{-3}\ T \qquad 1.4.1$$

$$\Delta G^{o}_{lt}/\text{kJ mol}^{-1} = -11.374 + 10.0 \times 10^{-3}\ T \qquad 1.4.2$$

$$\Delta G^{o}_{1c}/kJ\ mol^{-1} = -7.403 + 7.5 \times 10^{-3}\ T \qquad 1.4.3$$

Equations 1.4.1, 1.4.2 and 1.4.3 (90) allow one to calculate the equilibrium constants and the equilibrium compositions at any temperature by using equations 1.4.4, 1.4.5, 1.4.6 and 1.4.7 :

$$K_{ij} = \exp(-\Delta G^{o}_{ij}/RT) \qquad 1.4.4$$

$$X_{te} = \frac{1}{1 + K_{t1} + K_{tc}} \qquad 1.4.5$$

$$X_{ce} = 1 - X_{te}(1 + K_{t1}) \qquad 1.4.6$$

$$X_{1e} = 1 - X_{te} - X_{ce} \qquad 1.4.7$$

There has been a vast amount of research on the isomerization of butene in the last 30 years. Towards the end of the nineteen-sixties much emphasis was placed on the molecular mechanism of acid catalysts in seeking for the possible intermediate and transition states, but a complete kinetic-molecular mechanism is still not yet established. Moreover, a point worthy of note is that all workers on butene isomerization have assumed that the surface reaction is the rate controlling step. It may be argued that if product desorption were slow compared with the surface reaction, the butenes could attain thermodynamic equilibrium and desorb accordingly. Although the equilibrium ratios on the surface need not be identical with those in the gas, it seems unlikely that cis-butene would desorb selectively over trans-butene, as would be required to explain the high stereoselectivity observed.

1.4.2 Mathematical Approach to the Kinetics

There have been two suggestions as to how to approach the mathematical solution of the triangular system indicated in Figure 1.4.1.

1. Haag and Pines Approach It is assumed that there are three first order reversible reactions (91) :

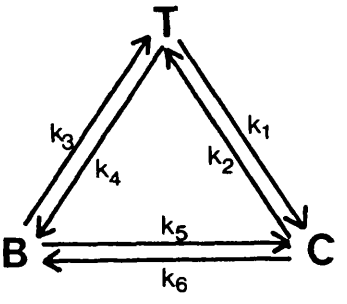

Figure 1.4.2

The innovation of this approach consists in reducing the mathematics until second order derivative equations are obtained. Since there is a slight discrepancy with the signs in Haag and Pines' integrated solution (x as a function of t, p. 389 in Ref. 91), a detailed solution is included in Appendix 1.1.

The solutions in terms of the molar fractions of B (X_b) and C (X_c) are given in equations 1.4.8 and 1.4.9 respectively.

$$X_b = \frac{1}{q}\left[(k_3+\frac{P_1}{n}r_2)\exp(r_1t)-(k_3+\frac{P_1}{n}r_1)\exp(r_2t)\right] + \frac{P_1}{n} \qquad 1.4.8$$

$$X_c = \frac{1}{q}\left[(k_1+\frac{P_2}{n}r_2)\exp(r_1t)-(k_1+\frac{P_2}{n}r_1)\exp(r_2t)\right] + \frac{P_2}{n} \qquad 1.4.9$$

where,

$$m = k_1 + k_2 + k_3 + k_4 + k_5 + k_6 \qquad 1.4.10$$

$$n = k_1k_4 + k_1k_5 + k_1k_6 + k_2k_3 + k_2k_4 + k_3k_5 + k_3k_6 + k_4k_6 \qquad 1.4.11$$

$$P_1 = k_1k_4 + k_1k_5 + k_3k_5 \qquad 1.4.12$$

$$P_2 = k_1k_6 + k_2k_3 + k_3k_6 \qquad 1.4.13$$

$$q = (m^2 - 4n)^{-\frac{1}{2}} \qquad 1.4.14$$

$$r_1 = (-m + q)/2 \qquad 1.4.15$$

$$r_2 = (-m - q)/2 \qquad 1.4.16$$

From observation of equation 1.4.8 and 1.4.9 it can be deduced that it is not easy to evaluate the rate constants from ordinary kinetic data of concentration vs. time. Moreover, the thermodynamic requirements (given by the equilibrium constants) and the principle of microscopic reversibility (equation 1.4.17 and 1.4.18) put the problem into mathematical constraints.

$$K_{tc} = \frac{k_1}{k_2} \qquad K_{t1} = \frac{k_3}{k_4} \qquad K_{1c} = \frac{k_5}{k_6} \qquad 1.4.17$$

$$k_1 k_4 k_6 = k_2 k_3 k_5 \qquad 1.4.18$$

In other words, we are dealing with a mathematical multiparameter (rate constants) problem which has fixed bounds (rate constants $\neq 0$, $X_b \neq 0$, $X_c \neq 0$ and $t \neq 0$) and fixed constraints (equation 1.4.17 and 1.4.18) and this can only be solved by optimization methods which in turn require a minimization process that can only be achieved by computing.

2. Wei and Prater Approach This second approach (92) is based on the analysis of the structure of the kinetic system. It is a general approach to solve monomolecular systems. A reaction system of n molecular species is called monomolecular if the coupling between each pair of species is by first order reactions only.

The method requires a special experimental set-up and uses matrix mathematics. The mathematic details of the specific case in which n = 3 have been considered in Appendix 1.2, there are not final equations but instead there is a method of achieving the solution of the kinetic problem, i.e. the rate constants determination.

The experimental requirements for this approach are to study the path to equilibrium of different initial compositions which are determined from the previous experiment.

3. Hightower and Hall Suggestions Finally, the most widely used treatment of data, is that suggested by Hightower and Hall (93) in 1967,

but this has nothing like the mathematical depth of the previous two approaches just described. It considers the disappearance of reactant as a first order reversible reaction exemplified as equation 1.4.19

$$\text{Ln}\ (X_e - X) = kt + \text{Ln}X_e \qquad 1.4.19$$

Literally their explanation for using this equation is : "this equation holds rigorously for a reversible reaction where one reactant becomes a single product, the reactions being first order in both directions. Although not an exact solution for a three component system, it is a linear equation (the exact solution for first order reactions among three species cannot be conveniently linearized) and is therefore useful for plotting kinetic data."

Unfortunately this equation is not even correct for a first order reversible reaction in which a single reactant becomes a single product, since the right equation is :

$$\text{Ln}\ \frac{X_e - X}{X_e - 1} = \frac{k}{X_e - 1}\ t \qquad 1.4.20$$

However, this 'wrongly' postulated equation has become the most popular one, and parameters evaluated from it (rate constants, Arrhenius parameters, etc.) have been interpreted as an average of the real ones.

1.4.3 Mechanisms

Different mechanisms take place depending on the nature of the catalyst, here the mechanisms on acid and base catalyst will be reviewed.

1. Mechanisms on acid catalysts Hydrocarbon reactions on acid catalysts proceed via carbonium ion mechanisms. The first postulated mechanism (94) is the so-called 'hydrogen switch' mechanism, which

demands that the catalyst furnish a hydrogen and accept a hydrogen at a distance of approximately 3.5 Å. Thus, this concerted mechanism assumes that a hydrogen from the catalyst approaches the carbon atom 1 while another site can take the hydrogen from the carbon atom 3 (Fig. 1.4.3).

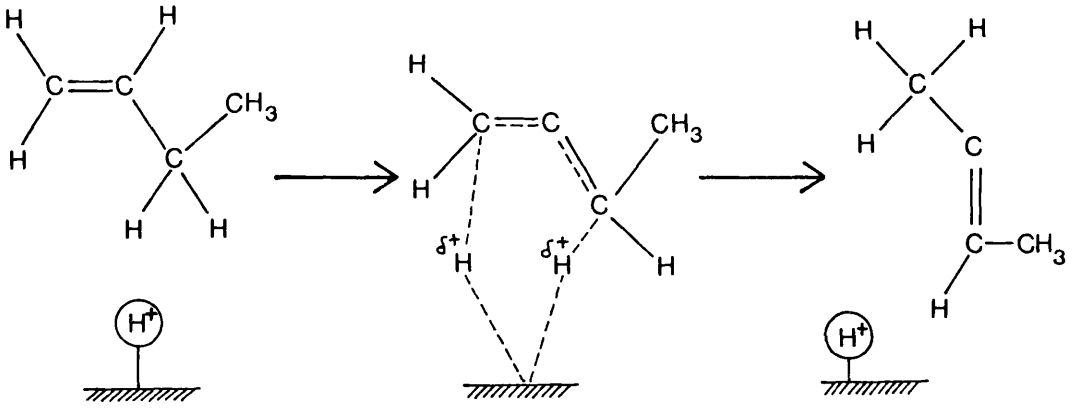

Although some authors favour this mechanism (e.g. Brouwer (95)), it cannot explain skeletal isomerization nor direct cis-trans interconversion.

A modification of this mechanism was suggested by Medema and Houtman (96) to relieve the geometrical requirement imposed by the necessity of participation of two sites acting simultaneously. When starting with 1-butene or cis-butene a hydrogen switch mechanism can occur involving only one oxygen atom from the surface.

In order to account for these anomalies and to explain their own kinetic results (in fact, similar rates for double bond shift and cis-trans intervonversion), Pines and Haag (97) suggested a conventional carbonium ion mechanism with a common intermediate, the secondary butyl carbonium ion (Fig. 1.4.4).

A detailed explanation of this mechanism was later given by Hightower and Hall (98). Figure 1.4.5 resembles the surface complex intermediate. The hybridization of C_2 is sp^2 so that the C_1,

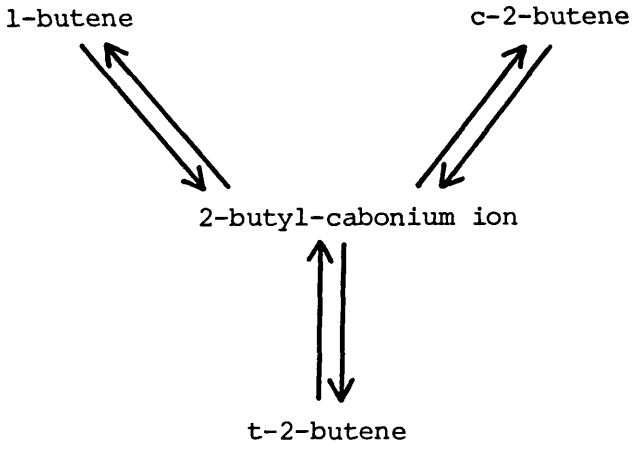

Figure 1.4.4

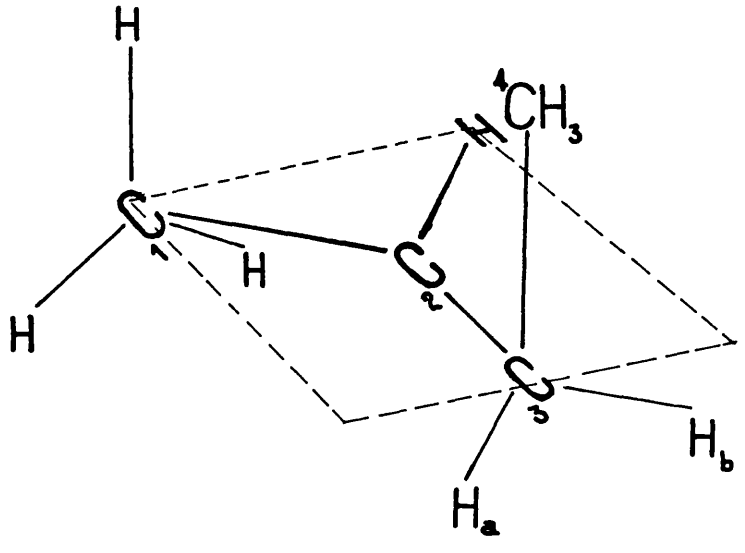

Figure 1.4.5.

C_2-H and the C_3 atoms all line in a plane parallel to the surface, leaving H_a and H_b directed toward the surface and the C_4H_3 extending

away from the surface. Owing to the steric hindrance of the CH_3-group with the surface, rotation about the C_2-C bond will be greatly inhibited. However, rotation through the C_1-C_2 bond may occur.

Statistics modified by an energetic argument may be applied to this complex to predict the observed selectivities. Although H_a and H_b are energetically similar, they are geometrically different, since loss of H_a will result in cisbut-2-ene formation but loss of H_b will yield the trans isomer. Therefore, selectivity of cis/trans formation from 1-butene should be 1 and should not be a function of the temperature. In a similar way the ratio 1-butene/trans-butene formed from the cis isomer should be 3 to 1 since loss of any hydrogen on C_1 will produce 1-butene but only loss of H_b will result in trans formation. However, the C_1-H bond is primary and stronger than the secondary C_3-H bond. If the 800 cal/mole difference in activation energy is used in the Boltzmann equation to calculate the relative probability of barrier crossing in the two directions, this reduces the odds by 1 to 4 at room temperature. A combination of the two arguments predicts 1-butene/transbut-2-ene to be 0.75.

However, once again, this mechanism as it stands is incomplete. An equal or faster rate of formation of trans as compared to cis from 1-butene would be expected on the basis of statistical, steric and energetic considerations whereas the opposite is found to be the case.

Some kinetic-mechanistic sketches have been proposed to explain certain ratios of selectivities, such as that of Lucchesi et al. (99), which predicted no direct 1-butene to trans-butene interconversion :

1-butene $\rightleftharpoons$ c-2-butene $\rightleftharpoons$ t-2-butene

and that of Leftin and Hermana (100) which implies that trans must be

formed from cis through 1-butene as intermediate

c-2-butene $\rightleftharpoons$ 1-butene $\rightleftharpoons$ t-2-butene.

These sketches have been ruled out when the evaluation of the six relative constants demonstrated that all were significant (101, 102, 103).

2. Mechanism on Basic Catalysts Research on basic catalysts has not progressed as far and in as detailed a way as it has done on acid catalysts. However, a few aspects have been clarified and some experimental facts have been explained in terms of mechanistic considerations.

The mechanism on basic catalysts has an opposite picture to that which we have seen on acid catalysts. In this case the reaction proceeds via a carbanion mechanism. Carbanions are quite restricted as regards rotation. Furthermore, carbanions from the trans and cis molecules are rather different. Cis can only produce the anti form (Fig. 1.4.6 a) and trans only the syn form (Fig. 1.4.6 b), but 1-butene can produce both of them.

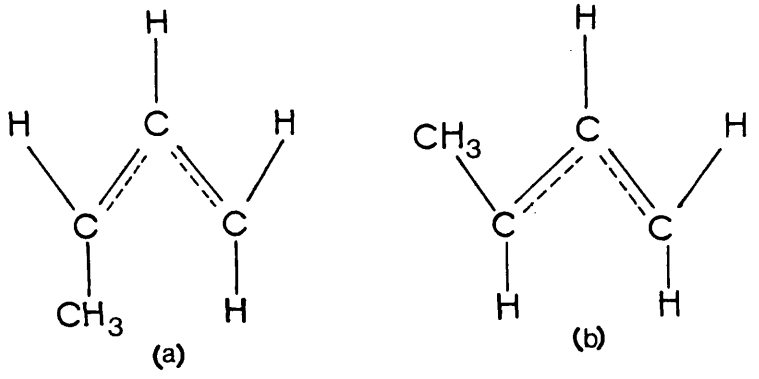

Figure 1.4.6

Postulation of a π-allyl carbanion seems to preculde the direct interconversion cis-trans but observation that π-allyl carbanions are

dynamic (104) and can undergo rapid σ to π-allyl interconversion suggests the possibility of a mechanism of cis-trans interconversion which does not involve 1-butene as intermediate.

Thus, it might be supposed that on basic catalysts a unique intermediate cannot be postulated. The following scheme (105), so far the most accepted, implies the direct interconversion of the syn and anti forms, probably through a σ-allyl intermediate.

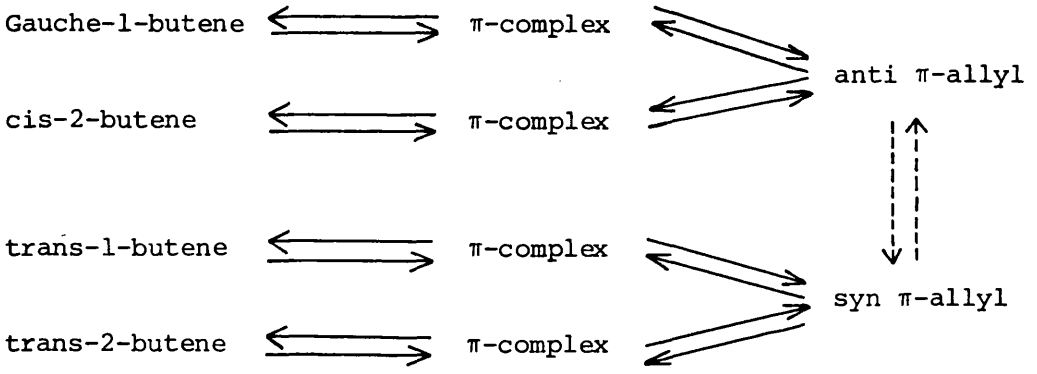

Baird and Lunsford (106) explained the favoured formation of cis over trans when 1-butene is isomerized on MgO by a preferential formation of the anti-π-allyl carbanion held in this position by the electrostatic interactions between the terminal carbon atoms and two Mg cations.

A theoretical study of the nature of the chemical activation of the 1-butene molecule due to dissociative adsorption on basic catalysts (107) has been analyzed by Chuvylkin et al. within the scope of an approximate SFC MO method. Five species were postulated as taking part in the reaction. Besides the syn and anti forms, three more species were proposed as possible intermediates. These are pictured in Figure 1.4.7.

The calculations reveal the following stability order S>A>D>C>T. As expected, the syn and anti forms are highly stabilized by the electrical field on the surface. The T and C forms may present either true transition states or states rather like intermediates

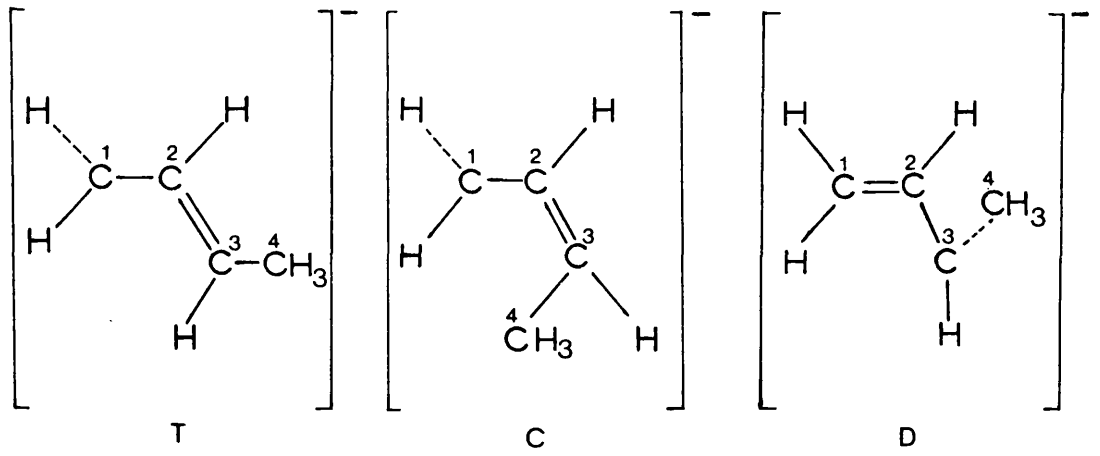

Figure 1.4.7

participating in conclusive stages but due to the greatly polarized charge distribution they can be only formed on very strong basic catalysts. Since the hydrogens on the C_4 atom of structure D are highly activated, this species can be important when dehydrogenation reactions take place.

1.4.4 The Nature of the Active Sites

The role of the catalyst in the catalytic process has been a matter of continuous research. The nature of the active site plays a most important part when designing new catalysts, or even when trying to improve old ones. However, this endeavour has not achieved its aims as yet and most of the catalysts (mainly the industrial ones) remain unknown from this point of view.

On acid catalysts, as the mechanism implies, the active sites were supposed to be of Bronsted type. The existence of a polymerization reaction parallel to that of isomerization and the formation of a polymeric complex on the surface led some

workers to investigate its effects on the isomerization reaction. Thus, it has been found (108) that the polymer formed during the reaction is also active for inducing isomerization.

The role of the d electrons of the first transition series has been investigated for the isomerization of cis-butene (109) and 1-butene (110). A twin peak pattern of activity which can be expected from crystal field theory was observed.

On CaO (111) and SrO (112) two kinds of sites have been reported. Site I is a basic O^{2-} adjacent to completely coordinated metal ions and Site II is a basic O^{2-} adjacent to an incompletely coordinated metal or oxygen deficient site. Therefore, Site II is a stronger basic site than Site I (the incompletely coordinated metal ion increases the electron density of the adjacent O^{2-}). A third type of site on CaO with unusually strong basic character has been suggested to be an O^{2-} ion adjacent to a cation vacancy (25). It has also been suggested that isomerization of 1-butene to trans-butene takes place on acidic sites formed from decarboxylation of the catalyst (SrO (112), CaO and MgO (113)).

1.5 The Aims of the Present Work

The alkaline earth oxides have been the subject of investigation in a very wide field, but much work remains to be done on the characterization of their surface properties, especially as regards their donor character.

CaO and SrO have been found to be strong solid bases with very high catalytic activity. The overall theme of the present work is to study the mixed system, since the small difference in the cationic sizes of Ca^{2+} and Sr^{2+} implies a possible complete miscibility of the two oxides. Our main objectives can be formulated as :

- the attainment of solid solution in the CaO-SrO system at the lowest practicable temperature.

- Phase identification and characterization by means of X-ray diffraction analysis.

- Surface characterization of CaO-SrO solid solutions by means of specific surface area measurements, diffuse reflectance spectroscopy and electron spin resonance spectroscopy.

- Catalytic activity as a function of Ca and Sr content. A suitable catalytic reaction has to be chosen which provides adequate means for comparison of the catalytic activity through the full range of composition.

- Finally, the search for possible correlations between the method of preparation, their surface properties and their catalytic activity pattern.

CHAPTER II

2. EXPERIMENTAL TECHNIQUES

2.1 Introduction

The objective of this chapter is to give the general theoretical background to the experimental techniques used in this work. Emphasis will be laid on the development of equations and concepts which will also be useful for calculations and discussion of results reported later.

2.2. X-Ray Diffraction Analysis

X-ray diffraction analysis is a well-established technique for the investigation of crystalline solids (114 - 117). Crystals can be grouped into six systems having certain minimum symmetry requirements which can be expressed in terms of the unit cell parameters and the axial angles. Table 2.2.1 lists the three systems in which $CaCO_3$, $SrCO_3$, CaO and SrO are classified. The geometric conditions for which a diffracted X-ray beam is produced can be expressed in terms of the Bragg equation :

$$n\lambda = 2d \sin \theta \qquad 2.2.1$$

where λ is the wavelength, d is the interplanar spacing and 2θ is the angle of deviation of the diffracted beam. The d spacing can be related to the lattice parameter of the crystal unit cell by means of the Miller indices, and the equations for the systems cited in Table 2.2.1 are listed in Table 2.2.2.

2.2.1 Method of X-Ray Powder Photography

The powder method (115, 116) enables crystal phases to be identified and investigated. For the production of a powder diagram, the sample is placed between the path of the x-ray beam and the photographic film. Some of the crystals composing the

Table 2.2.1 Crystal Systems

System	Lattice Constants	Examples
Orthorhombic	$a \neq b \neq c$	Aragonite
	$\alpha = \beta = \gamma = 90^{o}$	Strontianite
Hexagonal	$a = b \neq c$	Vaterite
(Rhombohedral)	$\alpha = \beta = \gamma \neq 90^{o} < 120^{o}$	Calcite
Cubic	$a = b = c$	CaO
	$\alpha = \beta = \gamma = 90^{o}$	SrO

Table 2.2.2 d-Spacings

System	d_{hkl}	
Orthorhombic	$\left[\frac{h^2}{a^2} + \frac{k^2}{b^2} + \frac{l^2}{c^2}\right]^{-\frac{1}{2}}$	2.2.2
Hexagonal (Rhombohedral)	$a \frac{(h^2+k^2+b^2)\sin^2\alpha + 2(hk+hl+kl)(\cos^2\alpha-\cos\alpha)}{1 + \cos^3\alpha - 3\cos^2\alpha}$	2.2.3
Cubic	$a(h^2 + k^2 + l^2)^{-\frac{1}{2}}$	2.2.4

sample may be orientated to have a set of planes hkl making the appropriated glacing angle with the x-ray beam to satisfy the Bragg equation. The reflections occur in a direction making an angle 2θ with the direction of the beam. The locus of directions making an angle 2θ with a given direction is a cone of half opening angle and the rays in the cone cut the film in a continuous circle. From a measurement of the radius of the circle and the known crystal to film distance the cone angle and d are determined.

Three variations of placing the free ends of the film are common in practice. In the van Arkel arrangement the rays enter through a hole punched in the middle of the film and leave between the free ends. In the Bradley and Jay arrangement the rays enter through the free ends of the film and leave through a punched hole. In the third arrangement suggested by Straumanis and Ievins the x-ray beam both enters and leaves through punched holes. Unless the camera circumference is too great to be encircled conveniently by a single strip of film, the Straumanis-Ievins arrangement is the most convenient, since it avoids the necessity of any measurements in the camera. From the position corresponding to $\theta = 0$ which is given by the average of the positions halfway between the low angle lines and from the position corresponding to $\theta = \frac{1}{2}\pi$ which is obtained similarly from the high angle lines, the separation corresponding to $2\theta = 180^{o}$ is obtained. Thus, if R is that distance, π/R is an interpolating factor in radians per unit length of the film.

Hence

for the exit side : $$\theta = \frac{\pi L}{4R} \qquad 2.2.5$$

and for the entry lines $$\theta = \frac{1}{2}\pi - \frac{\pi H}{4R} \qquad 2.2.6$$

where L is the distance between two low angle lines and H is the distance between two high angle lines.

The most satisfactory camera for powder photography is one providing high quality diffraction patterns with short exposures. The aim should be (i) maximum line intensity, (ii) optimum resolution of lines, (iii) minimum background, (iv) completeness of pattern and (v) good line profile and quality. Two types of camera have been used in the present research, namely the Debye-Scherrer camera and the Guinier camera.

In the typical Buerger design of Debye-Scherrer camera, the film is held tightly against the inner cylindrical surface of the camera and protected from light during exposure by a well-fitted cover. It is important that this metal surface be precisely cylindrical in shape and even more important that the axis of the sample-supporting spindle be accurately centred in this cylinder. The incident beam is passed through a filter to eliminate the Kβ radiation after which the Kα beam is collimated through the entry pinhole. The resulting narrow pencil of rays bathes the cylindrical sample and sections of the various diffraction cones are intercepted by the cylindrically disposed film. The powder specimen is rotated, in order to increase the number of particles contributing to each reflection. The main advantages of this method are the small amount of sample required (~0.1 mg), the practically complete coverage of all the reflections produced by the specimen, the relative simplicity and the accuracy with which the lattice constants can be determined. There are two sizes for commercial cameras. The apparently strange camera diameters of 57.3 mm and 114.7 mm have the effect of making 1 mm of the film equal to 2° and 1° 2θ respectively.

By making use of so-called focusing geometry cameras can be constructed that give much greater resolution than Debye-Scherrer cameras of the same radius. The Guinier-type cameras are of this kind, and they possess the additional advantage of precluding

absorption errors. Guinier cameras use a focusing monochromator of the Johansson type which is a quartz lamina of dimension 35 mm x 15 mm x 0.3 mm. To obtain the best focusing conditions the specimen should lie on the same circunference as that of the film. The Guinier-de Wolff design has become the most widely used camera of this kind, with a diameter of 114.6 mm and with the advantage of allowing the exposure of four samples simultaneously. Unfortunately it is not easy to evaluate the effective radius of this camera, mainly because the specimen and the film may not lie exactly on the same cylindrical surface. The specimen may not be a plane of uniform thickness. However, one way of calibration which eliminates the systematic errors is to calibrate the film itself with a substance of known parameters. Another but less accurate method is to use the θ values of a standard substance from its known parameters and combine them with the distance D to the focal line to calculate the camera constant

$$K = \frac{\Sigma\theta D}{\Sigma D^2} \qquad 2.2.7$$

A good approximation is :

$$\theta = \frac{L}{4R} \qquad 2.2.8$$

where R can be checked or calculated from standard substances.

2.2.2 Powder Diffractometry

A powder diffractometer disperses x-rays of a single wavelength by diffracting them from planes of different spacings and uses a local intensity-measuring receiver rather than a photographic film. To maintain the distance from goniometer to sample constant, the sample surface is made flat and is caused to rotate with one half the angluar velocity with which the goniometer revolves (2θ:θ motion).

Thus the sample surface always remains tangent to the focusing circle. The method suffers from errors due to the use of a flat rather than a curved sample, the 'transparency' of the sample (low absorption coefficient) and the fact of being a three-dimensional system and not an idealized two-dimensional one.

The basic equation of this method describes the radius of the circle defined by the base of the diffracted cone and the receiving slits :

$$b = R \sin 2\theta \qquad 2.2.9$$

where R is the radius of the goniometer circle. One of the main features of a powder diffractometer is the requirement of alignment and angular calibration which is essential to the attainment of optimum resolution, maximum intensity and correct angular readings. Several operations comprise the overall alignment process, such as goniometer-sample alignment, goniometer-x-ray tube alignment, calibration of the $0^{o}2\theta$ position and calibration of the angular registration between 0^{o} and 180^{o} 2θ.

The geometrical properties of the diffractometer introduce aberrations into the pure diffraction profile which cause it to be (1) somewhat asymetrical, (2) broadened and (3) displaced from its theoretical angle 2θ on the goniometer scale. The breadth and shape of the diffraction line are important in the measurement of crystallite size and lattice distortion while the displacement of the line is significant in the determination of interplanar spacing and lattice constants.

2.2.3 Precision Determination of Lattice Constants

High accuracy in lattice parameter determination involves two separable problems, namely wavelength accuracy and accuracy of the

Bragg angle measurement. Wavelengths are now known to very high precision. Table 2.2.3 lists some wavelengths determined with an accuracy of about ±0.000005 Å (118).

Table 2.2.3 X-Ray Wavelength

	$K\alpha_1$ (Å)	$K\alpha_2$ (Å)	$K\alpha$ (Å)	$K\beta$ (Å)
Mo	0.79930	0.71359	0.71073	0.63292
Cu	1.54056	1.54439	1.54184	1.39222
Ni	1.65791	1.66175	1.65919	1.50014
Co	1.78897	1.79285	1.79026	1.62079
Fe	1.93604	1.93998	1.93735	1.75661

Indexing is a necessary preliminary to the calculation of unit cell dimensions from the observed position of the lines. The values computed by the direct use of the mathematical equations (Table 2.2.2) are found to vary from one reflection to another, the variations being due to random errors (which decrease in magnitude as θ increases) and systematic errors (which also tend to a minimum as θ approaches 90^{o}).

The increase in precision of interplanar spacing measurement with increasing θ is readily demonstrated by differentiating the Bragg equation with respect to θ

$$\frac{\Delta d}{d} = - \cot \theta \, \Delta\theta \qquad 2.2.10$$

Table 2.2.4 summarizes the various sources of systematic errors and their mathematical expressions obtained from the Bradley and Jay treatment (119) which refer to the Debye-Scherrer method.

Two principal approaches can be made to the problem of correcting the various errors that affect the determination of lattice constants

Table 2.2.4 Systematic Errors in θ Determination

	Error	Δθ	Equation	Remarks
1.	Radius error and film shrinkage	$\theta\left[\frac{\Delta S}{S} + \frac{\Delta R}{R}\right]$	2.2.11	ΔS = Shrinkage error ΔR = Radius error
2.	Specimen eccentricity	$-\frac{U}{R}\cos\sigma\sin\theta\cos\theta$	2.2.12	U = Magnitude of eccentricity σ = Angle between the rotation axis of the specimen
3.	Sample absorption and radial divergence of beam	$\frac{r}{2R}\left[1 + \frac{R}{\Delta X}\right]\sin\theta\cos\theta$	2.2.13	r = Specimen radius ΔX = Distance point beam source and specimen centre
4.	Axial divergence of beam	$-\frac{1+X}{96}\left(\frac{h}{R}\right)^2\cot 2\theta$	2.2.14	h = Axial divergence $0<X<1$ depends on the uniformity of the beam

by the Debye-Scherrer technique. These are refinements in experimental technique and mathematical procedures for minimizing the errors.

According to Straumanis (120) certain of the errors listed in Table 2.2.4 can be eliminated. Error 1 is eliminated by placing the film in the asymmetric or Straumanis position, Error 2 is reduced to vanishing point by highly precise centering of the sample spindle in the camera, and Error 3 is eliminated by using lines in the back reflection region, decreasing the sample diameter and making the sample more transparent for x-rays.

For cameras of 114.6 mm in diameter line positions should be measured with a precision of 0.01 or 0.02 mm. Extrapolation methods are used for minimizing the errors through mathematical procedures. For the cubic system the method consists of extrapolating the a values, usually above 80^{o}, against a function of θ. Two functions have been suggested and widely applied, namely

Bradley and Jay $$f(\theta) = \cos^2\theta \qquad 2.2.15$$

Nelson and Riley (121) $$f(\theta) = \frac{\cos^2\theta}{\sin\theta} + \frac{\cos^2\theta}{\theta} \qquad 2.2.16$$

2.3 Electronic Spectroscopy

2.3.1 Fundamentals

In a solid one has to deal with a large number of interacting particles and consequently the problem of calculating the wave functions and energy level is extremely complicated. The usual approximation is to consider the problem as involving the behaviour of electrons in a potential which has the periodicity of the crystal lattice. If we consider the motion of an electron in such a periodic potential, we arrive at the following results (122) : (i) there exist allowed energy bands separated by forbidden regions, and

(ii) the energy of the electron as a function of the wave vector (k) is periodic in k. According to the band theory, a solid for which a certain number of bands are completely filled and the others are completely empty is an insulator, whilst a solid containing an incompletely filled energy band has metallic character (conducting properties).

If an insulator is irradiated with light of suitable wavelength, absorption may occur and an electron in the full band may be given sufficient energy to be raised into the next band where there is an abundance of empty states. The excited electron can therefore move freely through the crystal in this band, which is accordingly called the conduction band. Measurement of the wavelength for which this absorption first occurs enables one to determine the energy of the band gap. Von Hippel (123) has attempted to calculate the energy involved assuming that in the excitation process an electron from the anion is transferred to the neighbour cation; his equation was later corrected for polarization effects by Klemm (124) and for overlapping of wave function from the ions by De Boer (125). The final expression was :

$$h\nu = \frac{(2\alpha - 1)}{r}e^2 + E - I - \frac{2.027}{r^4}(\alpha_1 + \alpha_2) - \Omega_+ - \Omega_- \qquad 2.3.1$$

where α is the Madelung potential, r is the smallest anion-cation distance, E is the electron affinity for the anion in the atomic state, I is the ionization energy of the cation in the atomic state, α_1 and α_2 the ion polarizabilities and Ω_+ and Ω_- the overlapping of wave functions due to the interaction of an ion with its neighbours.

However, it can also happen that the electron is excited insufficiently to be free in the conduction band. If the positive

hole (created in the valence band by the removal of the electron) and the excited electron move together through the lattice as a single entity it gives rise to what has been called by Frenkel (126) an exciton. The Frenkel exciton is best envisaged as a "tight-binding" exciton, corresponding to an electronic excitation within an isolated atom. In contrast with the Frenkel model, the Wannier exciton (127) describes a situation where the Coulombic interaction between electron and hole is reduced due to the dielectric medium of the lattice atoms.

At the surface the Madelung potential is less than in the bulk, and as a result so-called intrinsic surface states arise. In the classical limit one state will lie in the upper half of the forbidden gap and will function as a trap for electrons (acceptor-like) and the other state will lie in the lower half of the energy gap and will trap holes (donor-like). Similarly, the surface Madelung potential will cause the surface excitons to have lower energy and so become further bound at the surface imperfections such as steps, edges and corners.

2.3.2 Diffuse Reflectance Spectroscopy

When light passes through a dielectric it can be reflected and refracted at the surface and absorbed and scattered within the material itself.

In a crystal whose dimensions are large compared with the wavelength, but small compared to the cross section of the beam, it is possible to distinguish between rays striking the crystal and those passing by it. At the phase boundary the beam is partially reflected and partly refracted, but through the crystal diffraction takes place. For polycrystalline materials, because the crystal faces can be oriented in all possible directions, the

incident radiation is now reflected into the hemisphere from which the incident radiation originates. Ideal 'diffuse reflection' is thereby defined by the condition that the angular distribution of the reflected radiation is independent of the angle of incidence. However, if the dimension of the particles are comparable with, or smaller than, the wavelength it is not possible to separate the contribution to the intensity due to reflection, refraction and diffraction and the phenomenon is now described as scattering. Scattering depends upon the size, state and polarizability of the particle and on the direction of observation.

A rigorous theory exists only for single scattering (scattering from a single particle). Rayleigh theory (128) considers the scattered radiation as due only to an oscillating dipole formed with each molecule. Mie theory (129) permits the evaluation of the angular distribution of intensity and of the polarization of the scattered radiation for spherical particles of any given size. Phenomenological theories are much more simple and can be easily verified experimentally, but they are of limited applicability being restricted practically to scattering of diffuse light (i.e. light having equal intensity in all directions); the most general of these is that developed by Kubelka (130). The model used is a plane parallel layer of thickness d capable of both scattering and absorbing radiation. The theory is based on the following assumptions : (i) the Lambert cosine law (131) is valid, involving isotropic distribution of scattering, and thus any regular reflection is ignored, (ii) the particles in the layer are regarded as being randomly distributed and very much smaller than the thickness of the layer itself, and (iii) the layer is subject only to diffuse radiation.

The final expression, well known as the Kubelka-Munk function, is :

$$\frac{k}{\sigma} = \frac{(1 - R_\infty)^2}{2R_\infty} = F(R_\infty) \qquad 2.3.2$$

where k is an absorption coefficient, σ is a scattering coefficient and R_∞ is the reflectance of an infinitely thick sample. The expression holds for diffuse (or 60^o parallel) illumination and diffuse scattering.

Kortum et al. (133) have shown that deviations from the Kubelka-Munk equation are mainly due to regular mirror reflections which can be avoided by either diminishing the particle size of the absorbent or diluting the absorbent with a dispersed white standard of defined properties. The first method contributes to a better resolution of the spectrum and an overall increase of reflectance since a decrease of particle size increases the scattering coefficient. The scattering coefficient is an empirical constant, and its dependence on the wavelength and geometry of the particles is not given a priori. Kortum (134) has found that the scattering coefficient depends linearly on the inverse of the square root of the mean particle size and it is independent of wavelength for particles larger than 2μ; for smaller particles the scattering coefficient increases monotonically with increasing wavenumber. Hence the spectrum will be correct only if the scattering coefficient is independent of the wavelength and this is so for particles with a mean particle size larger than 2μ. For smaller particles, the bands are increasingly flattened toward the ultraviolet which means that the relative intensities of the individual bands are not true. In the case of finer grains, besides the band

flattening there is an increasing red-shift of the maxima of the bands. When the grain is very fine additional precautions of having a sufficiently thick layer to fulfil the requirements of infinite layer thickness must be taken into account.

Detailed information not only on the theoretical bases of reflectance spectroscopy but also on its applications can be found in the textbooks by Kortum (135) and Wendlant and Hecht (136).

Although reflectance spectroscopy is one of the most powerful experimental techniques for the study of the electronic structure of dispersed systems and their external and internal surfaces, including adsorbed layers, at the present time it is receiving little attention for the investigation of solid catalysts and their surfaces. Reviews dealing with research on solids, their surfaces and adsorbed molecules have been published by Terenin (137) and Klier (138).

2.4 Electron Spin Resonance

2.4.1 Introduction

Electron spin resonance (ESR) is a powerful technique for the study of paramagnetic species. The basic principles will be considered in Sections 2.4.2 and 2.4.3, and further details can be found in specialized texts (139 - 143).

Solid surfaces and adsorbed species have been extensively studied by ESR spectroscopy, and the application of this technique to surface chemistry and catalysis has been reviewed several times (144 - 150).

The quantitative use of ESR for the determination of the

concentration of paramagnetic species will be considered in Section 2.4.4.

2.4.2 General Principles

Any charged particle in movement has an associated magnetic moment. Thus an electron in an isolated atom has one magnetic moment associated with its spin and another with its orbital movement.

The electron spin magnetic moment $\underline{\mu}_e$ is proportional to the spin angular momentum $\underline{P}$ and the proportionality constant is called the magnetogyric ratio γ , so

$$\underline{\mu}_e = \gamma \underline{P} \qquad 2.4.1$$

According to quantum mechanics, the component of $\underline{P}$ (hence of μ) along a given direction can have only two values, say P_z

$$P_z = M_s \frac{h}{2\pi} = M_s \hbar \qquad 2.4.2$$

where h is Planck's constant and $M_s = \pm \frac{1}{2}$ is the spin quantum number.

The classical treatment of the rotational motion of a charge about a fixed centre produces

$$\gamma = -\frac{e}{2mc} \qquad 2.4.3$$

and hence,

$$\mu_z = -\frac{eh}{4\pi mc} M_S \qquad 2.4.4$$

However, spin angular momentum is a purely quantum mechanical effect which cannot be accurately described by classical analogues, so equation 2.4.4 must be rewritten as :

$$\mu_z = -g\frac{eh}{4\pi mc} M_S \qquad 2.4.5$$

where g = 2.00232 (for free electrons) is a dimensionless number and $\beta = \frac{eh}{4\pi mc}$ is the Bohr magneton, a constant having the value 9.2732 x 10^{-28} J gauss^{-1}.

In the presence of a magnetic field H, the degeneracy of the spin states is split (Zeeman effect) and thus their energies are given by

$$E = M_s g_e \beta H \qquad 2.4.6$$

or $$E_1 = -\tfrac{1}{2} g \beta H \qquad 2.4.7$$

and $$E_2 = +\tfrac{1}{2} g \beta H \qquad 2.4.8$$

and the energy difference

$$\Delta E = g \beta H \qquad 2,4,9$$

Hence in the presence of a magnetic field transitions between the Zeeman levels will be induced by electromagnetic radiation of a frequency ν given by the resonance condition, which is

$$h\nu = g \beta H \qquad 2.4.10$$

A similar equation can be derived for the electron orbital magnetic moment. Since for the orbital magnetization $g_o = 1$, the expression is

$$\mu_o = (\ell(\ell+1))^{\frac{1}{2}} \beta \qquad 2.4.11$$

where ℓ is the orbital quantum number.

If the atom contains more than one electron, the orbital and spin quantum numbers are added vectorially to form the total quantum numbers L and S and the total angular momentum quantum

number J (Russell-Saunders coupling) :

$$\underline{L} = \sum_i \underline{\ell}i; \quad \underline{S} = \sum_i \underline{s}i; \quad \underline{J} = \sum_i \underline{j}i \qquad 2.4.12$$

The gyromagnetic ratio is then defined as

$$g = 1 + \frac{\underline{J}(\underline{J}+1) + \underline{S}(\underline{S}+1) + \underline{L}(\underline{L}+1)}{2\underline{J}(\underline{J}+1)} \qquad 2.4.13$$

and

$$\underline{\mu}_J = g(J(J+1))^{\frac{1}{2}}\beta \qquad 2.4.14$$

In the presence of a magnetic field a level with a particular value of J is split into 2J + 1 components (Zeeman splitting) with an energy of

$$E_{M_j} = M_j g\beta H \qquad 2.4.15$$

Transitions between the Zeeman levels may occur in accordance with the selection rule

$$\Delta M_j = 1 \qquad 2.4.16$$

Typical ESR spectrometers work at a frequency of about 9500 MHz (in the microwave region) in the so-called X-band, but frequencies of 34000 MHz (Q-band) and 23000 MHz (K-band) are also occasionally operated.

2.4.3 Characteristics of an ESR Spectrum

In order to record an ESR spectrum the sample is bathed in microwave radiation of a constant frequency ν, and meanwhile the external magnetic field is increased at a uniform rate. At the point where the appropriate energy level splitting is just

equal to hν the microwave radiation is absorbed for the sample. The absorption of energy is detected and usually the first derivative of this quantity is plotted as a function of the magnetic field.

The shapes of the absorption lines are usually described by comparison with lorentzian and gaussian line shapes, whose analytical expressions are as follows :

$$\text{Lorentzian :} \quad y = \frac{a}{1+bx^2} \qquad 2.4.17$$

$$\text{Gaussian :} \quad y = a \exp(-bx^2) \qquad 2.4.18$$

The complete analysis of the line involves its position (g-tensor), its structure (linewidth, ΔH; fine structure and hyperfine structure) and its intensity.

The g-factor is a universal constant characteristic of the electron and given by the resonance condition (equation 2.4.10). However, the application of a magnetic field generates an internal magnetic field in the sample which will add to or subtract from the external field. Therefore the g-factor can be considered as a quantity characteristic of the molecule in which the unpaired electrons are located. For some molecules the magnitude of the induced field depends on the orientation of the molecule with respect to the external magnetic field, and the g-factor will consequently be anisotropic. The anisotropy of the g-factor is usually summarized in the form of a second-rank tensor which can be written as :

$$g = \begin{pmatrix} g_{xx} & g_{xy} & g_{xz} \\ g_{yx} & g_{yy} & g_{yz} \\ g_{zx} & g_{zy} & g_{zz} \end{pmatrix} \qquad 2.4.19$$

However, due to symmetry properties of the g-tensor (i.e. $g_{xy} = g_{yx}$) it only contains three components :

$$g^{d} = \begin{pmatrix} g_{xx} & 0 & 0 \\ 0 & g_{yy} & 0 \\ 0 & 0 & g_{zz} \end{pmatrix} \qquad 2.4.20$$

If the molecule contains a single threefold or higher axis of symmetry, then $g_{xx} = g_{yy} \neq g_{zz}$. In such cases it is common to designate the g-factors as $g_{\parallel}$ (g_{zz}) and $g_{\perp}$ ($g_{xx} = g_{yy}$).

Any spectroscopic line has a finite width and ESR lines are no exception. However, to understand the causes of line broadening one must first understand the relaxation process. In the absence of any external field, transitions are always occurring between the electron spin states. This can only be accomplished by an exchange in energy with the surroundings (lattice). The time (T_1) which characterizes this interaction is called the 'spin-lattice relaxation time' and will cause a 'natural' or 'inherent' line width. The interaction between the unpaired electrons will give rise to the so-called 'spin-spin relaxation time ' (T_2); obviously spin-spin interactions depend on the dipole concentration and their homogeneity. Two more processes can lead to line broadening (mainly in systems with T_1 unimportant). The first is called secular broadening and is caused by processes that generate a varying

local magnetic field. The variation of local magnetic field can be dynamic or spatial: in the former case (homogeneous broadening) each paramagnetic centre experiences a local field that fluctuates with time, whereas in the latter case (inhomogeneous broadening) the local magnetic field varies from one paramagnetic centre to another but remains constant with time for a given paramagnetic centre. The second source of line broadening is called life-time broadening and is a pure quantum mechanical term. By virtue of a finite lifetime term (Δt) of a spin state the energy of that state will have a finite width (ΔE) determined by the Heisenberg uncertainty principle :

$$\Delta E \Delta t \sim \hbar \quad \text{or} \quad \Delta\nu\Delta t \simeq \frac{1}{2\pi} \qquad 2.4.21$$

$$\text{since} \quad \Delta\nu = \frac{g\beta}{h}\Delta H \qquad 2.4.22$$

$$\text{then} \quad \Delta H \sim \frac{1}{\gamma\Delta t} \qquad 2.4.23$$

and this will be the ultimate minimum of the line width.

There are other interactions which cause the line to broaden, such as (i) electron spin exchange (the unpaired electrons of two free radicals exchange their spin states), (ii) electron transfer (the unpaired electron is transferred between a radical and a diamagnetic species), and (iii) proton exchange.

The fine structure of the ESR spectrum arises from the fact of the presence of more than one unpaired electron. Application of a magnetic field (external or internal) will split the energy levels into $2J + 1$ magnetic levels and transitions between these levels will occur according to the selection rule, if an oscillating field perpendicular to the static field is present as well. The term zero-

field splitting states the case in which an internal magnetic field (such as a crystal field) is already present in the molecule. In this case the degeneracy of the levels is removed regardless of the application of an external magnetic field.

ESR spectra can be split into many characteristic patterns by the hyperfine phenomenon, which is the interaction of an unpaired electron with a nuclear magnetic moment. The interaction of the nucleus with a magnetic field is much smaller than that of the electron, so to a first approximation each electronic sublevel is further split into $2I + 1$ nuclear sublevels by a nucleus of spin I. Accordingly, if there are n interacting nuclei the maximum number of hyperfine lines will be 2^n; however, the symmetry of the electronic orbitals frequently reduces the number of levels considerable and hence the number of lines.

2.4.4 Quantitative Applications of ESR Spectroscopy

Next in importance to the observation of an ESR signal in a sample and to an identification of the responsible molecular species is a quantitative measurement of how many ESR centres are present.

The determination of spin concentrations requires great care if good accuracy is to be attained. The usual output of an ESR spectrometer is an approximation of the derivative of the resonance absorption with respect to the magnetic field. Signal distortions, aside from random noise and drifts, are produced by application of the microwave power on the test sample and magnetic field modulation, both of which are inherent in contemporary instrumentation. On the other hand, the signal amplitude at low power and modulation is directly proportional to the field modulation

and increases with microwave power. The signal used in the determination of spin concentrations is assumed to be distortion-free.

Relative concentration for species with the same spectral line width and shape function are readily determined by measuring the ratio of peak heights (h_1/h_2) on the first derivative curves, for samples of identical sizes measured under identical conditions. If N_1 and N_2 are the number of unpaired electrons in two samples :

$$N_1/N_2 = h_1/h_2 \qquad 2.4.24$$

If the line shape is the same (e.g. both gaussian) but the line-width differs, the equation

$$N_1/N_2 = h_1\Delta H_1^2/h_2\Delta H_2^2 \qquad 2.4.25$$

(where ΔH_1 and ΔH_2 are the linewidths) is the basis of comparison. Otherwise the full integrated absorption intensity must be used.

Absolute measurements, i.e. those relating the recorded signal to the susceptibility of the sample, are not practicable because they demand knowledge of parameters which are not easy to measure. Consequently, the problem of determining spin concentrations may be divided into three parts : (i) a suitable material for use as standard must be found, (ii) the number of spins in the standard must be determined, and (iii) the number of spins in the standard must be related to the number of spins in the sample of interest.

The required properties for a suitable standard and the methods for determination of the number of spins in it have been summarized by Hyde (151). For solid samples, 'Varian Strong Pitch' has been the preferred standard.

Since the recorded ESR signal is approximately the first

derivative (f'(x)) of the absorption signal (f(x)), the spin evaluation must involve determination of the second integral of the spectrometer output. Andrew (152) has pointed out that a graphical estimation of the first moment of the signal is equal to the double integral :

$$\iint f'(x)\ dx^2 = \int x\ f'(x)dx \qquad 2.4.26$$

Halbach (153) has proven that the first moment is proportional to the modulation amplitude times the number of spins, N, independent of whether overmodulation or other modulation effects are occurring :

$$\int x\ f'(x)dx \propto MN \qquad 2.4.27$$

Thus the area under the absorption curve (or the second integral of the derivative signal as approximation) can be obtained by computing the first moment (142), by electronic double integration (154), by digital integration or graphical integration (155).

The graphical method consists of dividing the magnetic field, H, into n intervals each of length h, the value of f'(x) at the centre of each interval, y, is measured, the first moment of the first derivative spectrum about its mid-point, A, is given by :

$$A = \tfrac{1}{2}h^2 \sum_{r=1}^{n} (n-2r+1)y_r \qquad 2.4.28$$

Providing that A has been determined for the standard k, and for the unknown u, the spin concentration N of the sample is given by :

$$N_u = \frac{N_k\ A_u\ SR_u^2\ G_k\ M_k\ g_k^2\ S(S+1)_k}{A_k\ SR_k^2\ G_u\ M_u\ g_u^2\ S(S+1)_u} \qquad 2.4.29$$

where SR is the horizontal scale in gauss per unit length on the chart paper, G is the relative gain of the signal amplifier and M is the modulation amplitude.

2.5 The Microcatalytic Technique

The beginning of the microcatalytic technique followed quickly on introduction of gas chromatography. Less than three years after James, Martin and Smith (156) had successfully separated gaseous compounds by GC, Kokes, Tobin and Emmett (157) attached a gas chromatograph to a small catalytic reactor, so originating the microcatalytic technique.

2.5.1 The Systems

There are two types of microcatalytic reactor. The chromatographic column reactor (158) in which the catalyst bed also serves as chromatographic column was the pioneer in this technique but is no longer used very much and will not be considered here. The second, and now more usual type, consists of a small fixed bed catalytic reactor placed between a sampling valve and a GC unit. Pulses or slugs of reactant introduced through the sample port are mixed with the carrier gas and swept towards the catalyst bed. The reaction mixture is immediately analyzed by the GC unit.

In such a system the contact time is fixed by the flow rate of the carrier gas. In order to have versatility in controlling and varying this flow rate without deterioration of the resolution of the chromatograms, the carrier gas can be split into two streams, one of which is varied and passes through the reactor (stream 1) and the other is usually fixed and passes through the gas chromatographic

column (stream 2). In this case it is necessary to transfer the raction mixture from stream 1 to stream 2. This can often be done by collecting the reaction mixture in a cold trap and having an appropriate set-up of switching valves to permit isolation of stream 1 while vaporizing the reaction mixture into stream 2. This arrangement also solves the problem of asymmetric chromatographic peaks due to tailing of the pulse caused by slow desorption from the catalyst bed.

There are several methods for pulse injection. For gases, a metal valve with a fixed volume doser connected directly to the gas handling system has been most useful. For liquid injection a saturator in line with the carrier gas stream has been extensively used.

The reactor, usually tubular, can be of any shape as long as the catalyst bed length is kept small compared with the pulse width. It needs to be provided with a means of controlling and measuring temperature.

2.5.2 Remarks

A great advantage of the microcatalytic technique is in its ability to provide information about initial interactions which reactants undergo with a catalyst while the surface is still in a relatively uncontaminated state. With this technique one can also determine the fate of reactant molecules with fresh catalyst surfaces. One may additionally examine the exchangeability of atoms from the formed residue (if any on the catalyst) and incoming molecules.

A further advantage is that it is possible in principle to determine the total number of active sites by a titration made by

alternating pulses of reactants and known amounts of some strongly adsorbed poison.

The ease with which the reactor can usually be converted into a steady state flow reactor permits extensive information to be derived from the combined results. A final advantage worthy of mention is that the small amount of reactant and catalyst makes this technique very suitable for use of radioactive tracers and with it all their kinetic applications.

The main limitation of the pulse technique lies in the interpretation of the kinetic data. This stems primarily from the uncertainty of the partial pressures of reactants and products which are continuously changing as the pulse goes through the bed. Moreover, it is likely that components will be separated to some extent according to their adsorption-desorption parameters. This also complicates the judgement of the residence time since it could be different for different molecules. Therefore it is not possible to interpret accurately such data as the pressure dependence of the reaction rate.

These limitations are increasingly complicated by the order of reaction. The effects of reaction order on microcatalytic results as compared with those obtained from flow technique have been studied by Hattori and Murekami (159). Most agreement has been found between the flow technique and the microcatalytic technique for first order reactions.

CHAPTER III

3. METHODS AND RESULTS

3.1 Double Carbonates of Calcium and Strontium

3.1.1 Preparation

The preparation of the mixed carbonates was carried out by precipitation of the solution of the mixed nitrates with ammonium carbonate. 2M solutions of $Ca(NO_3)_2$ and $Sr(NO_3)_2$ were prepared by dissolving $CaCO_3$ and $SrCO_3$ ('Specpure' from Johnson and Matthey Chemicals Ltd.) in dilute HNO_3 (Aristar from BDH). 2M solution of $(NH_4)_2CO_3$ was prepared by dissolving ammonium carbamate in distilled water :

$$2NH_4HCO_3NH_2COONH_4 + H_2O \longrightarrow 3(NH_4)_2CO_3 + CO_2\ (g)$$

The solutions of the nitrates were then mixed in the required proportions and precipitation was carried out under continuous stirring by four different methods :

Method I : Series Q. The mixed nitrate solution was slowly dripped into a large excess of the ammonium carbonate solution at 298 K and the precipitate was immediately filtered.

Method II : Series R. As Method I but ageing the precipitate for 16 hours before filtering.

Method III : Series S. As Method I but precipitation was carried out at 370 K.

Method IV : Series T. The ammonium carbonate solution was added to the mixed nitrate solution at 370 K and filtered immediately.

The coprecipitated carbonates were then washed free of ammonium and nitrate ions and dried in a vacuum desiccator at room temperature.

The strontium content was varied in 10% increments (molar percentage). Method I was used for the range 0 - 40% Sr content, Methods II and III were used for the complete range (0 - 100%) and Method IV for only 0 - 30% Sr. Additionally Methods I and II were used to investigate the low Sr content range (0.001 - 1%).

Samples are named by the letter of the Series corresponding to the method employed followed by a symbol stating the mol % of Sr content. Thus, for example, R.30 refers to a sample prepared by Method II with a nominal Sr content of 30%.

3.1.2 Characterization

X-Ray characterization of the coprecipitated carbonates of calcium and strontium was performed employing three different techniques. X-Ray powder photographs were taken using a 114.6 mm Nonius Guinier focusing camera (G) and a 114.6 mm Philips Debye-Scherrer camera (DS) with the film mounted in the Straumanis position. Samples were exposed to Mn filtered Fe Kα radiation for four hours at room temperature. Powder diffractometry was carried out on a Philips PW 1050/25 instrument using Ni filtered Cu Kα radiation from a Philips PW 1010/80 generator.

Structure identification, measurement of d-spacings and lattice constant calculations were performed. Phase identification was mainly based on the observation of the strongest lines in the respective diffraction patterns, namely the lines corresponding to the following d-spacings in the pure carbonates :

Calcite (C) : 3.035 Å (d_{104})

Aragonite (A) : 3.396 Å (d_{111})

Vaterite (V) : 3.296 Å (d_{101})

Strontianite (A) : 3.535 Å (d_{111})

The d-spacings are naturally slightly different for the mixed carbonates. Results are listed in Table 3.1.1 and 3.1.2. Full analysis of the diffraction pattern was then performed in appropriate cases in order to determine lattice constants.

Although quantitative determinations of the relative amounts of the different phases were not carried out, qualitative information can be gained from visual observation of the pattern. Thus Q.0 showed a very small amount of calcite which increased at Q.10 and decreased from Q.20 to Q.30; the vaterite amount in all of these solids decreased with increasing Sr content. For R, S and T samples the amount of the calcite phase decreased with increasing Sr concentration.

Series Q samples showed a preferential formation of vaterite-type structure carbonates, and the variation of the d_{101} for this phase is listed in Table 3.1.3. However, an aragonite phase was also present from Q.20 and the changes in the d_{111} spacing are shown in Table 3.1.4.

The Sr content is distributed in two phases for samples R.20 to R.50 but preferential distribution in the aragonite phase was observed as evidenced by the change in the d-spacing shown in Table 3.1.5. This table includes the complete set of samples where an aragonite phase was present.

Series S samples received greatest attention in view of the extensive solid solutions reported for aragonite-type carbonates. The three parameters of the orthorhombic unit cell were calculated as follows :

1. Reflections with $\ell = 0$ were firstly used to calculate c_o from :

$$c_o = \frac{\ell d_{hko} \; d_{hk\ell}}{(d^2_{hko} - d^2_{hk\ell})^{\frac{1}{2}}} \qquad 3.1.1$$

Table 3.1.1 Structural Identification of $(Ca_{1-x}Sr_x)CO_3$ for $0<x<1$ in 0.1 increments

Series	X-Ray Analysis Method	mol % Sr: 0	10	20	30	40	50	60	70	80	90	100
Q	DS	V	V	V								
		C	C	C	C							
				A	A	A						
R	DS	C	C	C	C	C	C					
				A	A	A	A	A	A	A	A	A
S	G,Df	C	C	C	C							
		A	A	A	A	A	A	A	A	A	A	A
T	G,Df	C	C	C	C							
			A_1	A_1	A_1							
			A_2	A_2	A_2							

Table 3.1.2 Structural Analysis of $(Ca_{1-x}Sr_x)CO_3$ at Low Concentration of Sr

mol % Sr	Series Q	Series R
0.001	V	V,C
0.01	V	V,C
0.1	V	V,C
1	V,C	V,C

Table 3.1.3 d_{101} of Vaterite Phase for Series Q

Sample	d_{101}/Å
Q.0	3.285
Q.10	3.306
Q.20	3.292

Table 3.1.4 d_{111} of Aragonite Phase for Series Q

Sample	d_{111}/Å
Q.20	3.433
Q.30	3.439
Q.40	3.444

Table 3.1.5 d_{111}, d_{102} and d_{201} of Aragonite Phase for Series R

Sample	d_{111}/Å	d_{102}/Å	d_{201}/Å
R.20	3.436	3.344	2.740
R.30	3.454	3.359	2.750
R.40	3.456	3.368	2.756
R.50	3.472	3.421	2.790
R.60	3.456	3.386	2.761
R.70	3.472	3.408	2.787
R.80	3.514	3.424	2.801
R.90	3.524	3.448	2.823
R.100	3.535	3.450	2.859

2. The average value of c_o was then used to calculate a_o from reflections with $k = 0$ from :

$$a_o = \frac{h}{\left(\frac{1}{d^2_{ho\ell}} + \frac{\ell^2}{c_o^2}\right)^{\frac{1}{2}}} \qquad 3.1.2$$

3. The average values of a_o and c_o were then used to calculate b_o using all the observed reflections using the relation :

$$b_o = \frac{k}{\left(\frac{1}{d^2_{hk\ell}} - \left(\frac{h^2}{a_o^2} + \frac{\ell^2}{c_o^2}\right)\right)^{\frac{1}{2}}} \qquad 3.1.3$$

4. Finally, the volume of the unit cell was calculated from :

$$V = a_o b_o c_o \qquad 3.1.4$$

The films from the Guinier photographs were calibrated by using the data for $CaCO_3$ and $SrCO_3$ as references. Eleven reflections were used to calculate the lattice constants, and results are reported in Table 3.1.6. Plots of the d-spacings vs mol % Sr are shown in Figures 3.1.1, 3.1.2 and 3.1.3 for each reflection. These plots will later be used as calibrations for determining the composition of unknown aragonite phases. Data in Table 3.1.6 will render plots of the same type as Figures 3.1.1, 3.1.2 and 3.1.3 with a marked discontinuity in the 20 - 40% Sr range. The Guinier photographs are shown in Fig. 3.1.4.

Series T samples were studied by both Guinier and powder diffractometer techniques. The d-spacings of the aragonite phase were used to determine the composition by referring to Figures 3.1.1, 3.1.2 and 3.1.3, and results are listed in Table 3.1.7.

A calcite phase was always present at certain compositions, regardless of the method of coprecipitation used. The variation of

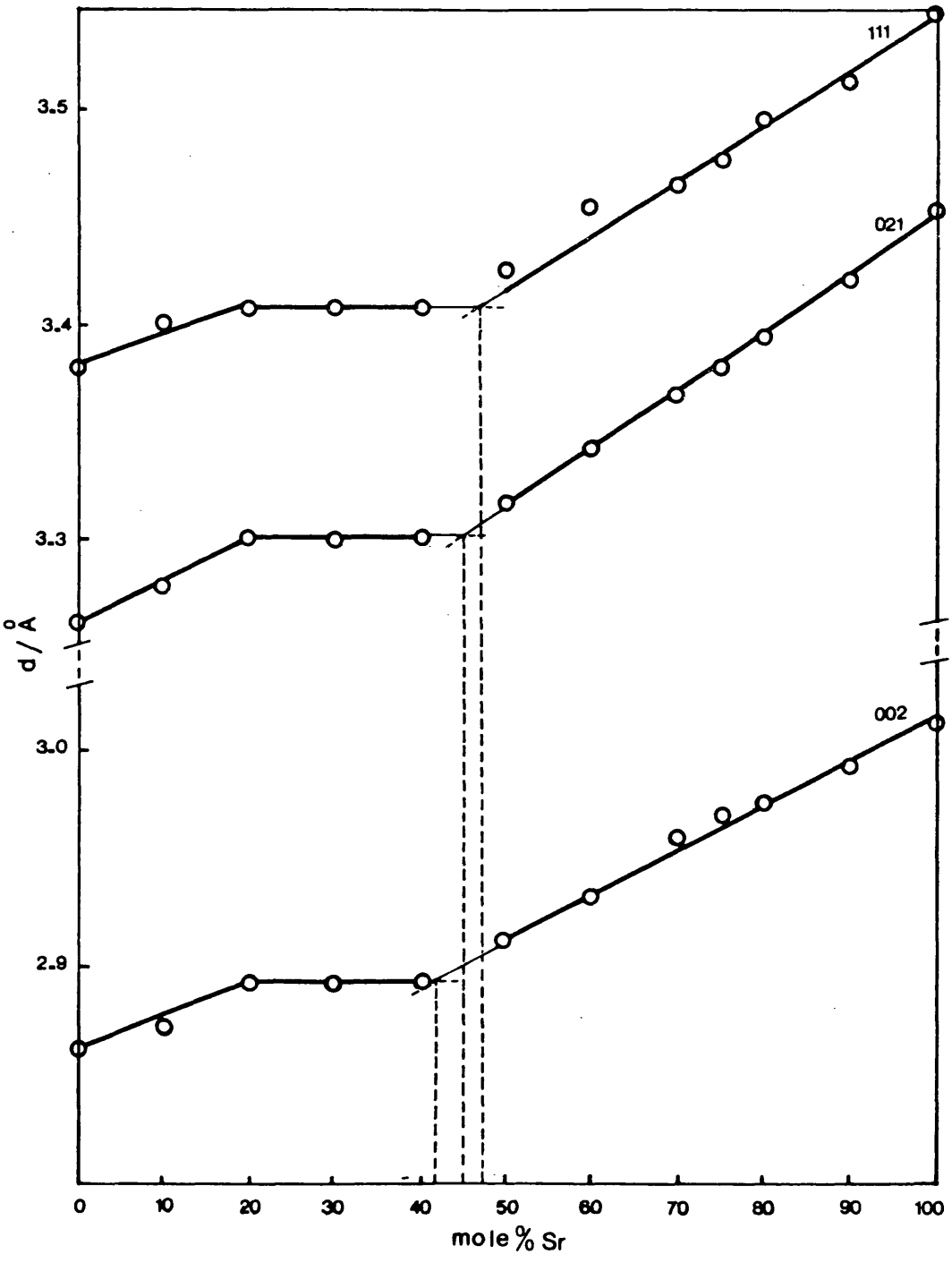

Figure 3.1.1

d-spacing vs Sr Concentration for $CaCO_3$ - $SrCO_3$ Double Carbonates

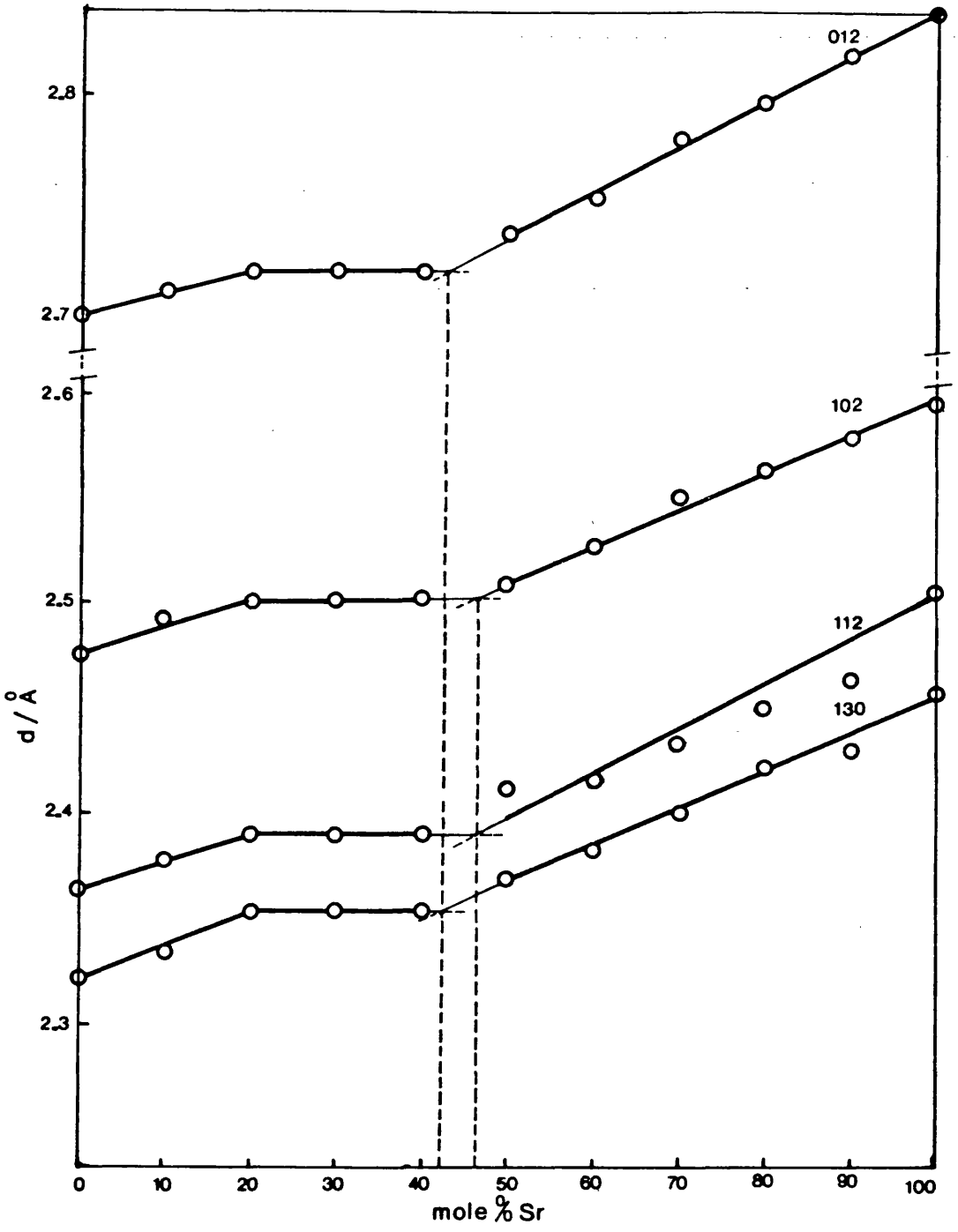

Figure 3.1.2

d-spacings vs Sr Concentration for $CaCO_3$ - $SrCO_3$ Double Carbonates

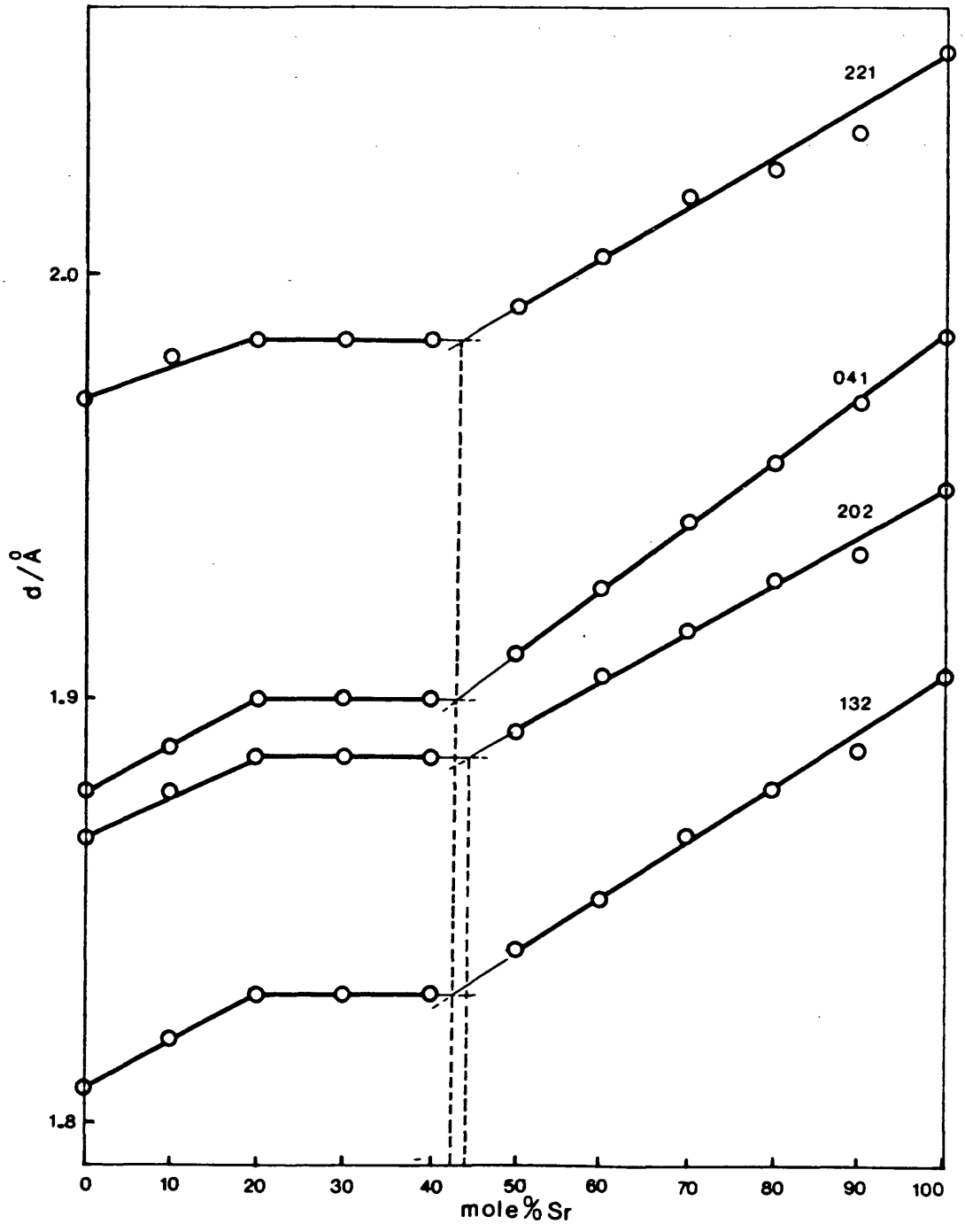

Figure 3.1.3

d-spacings vs Sr Concentration for $CaCO_3$ - $SrCO_3$ Double Carbonates

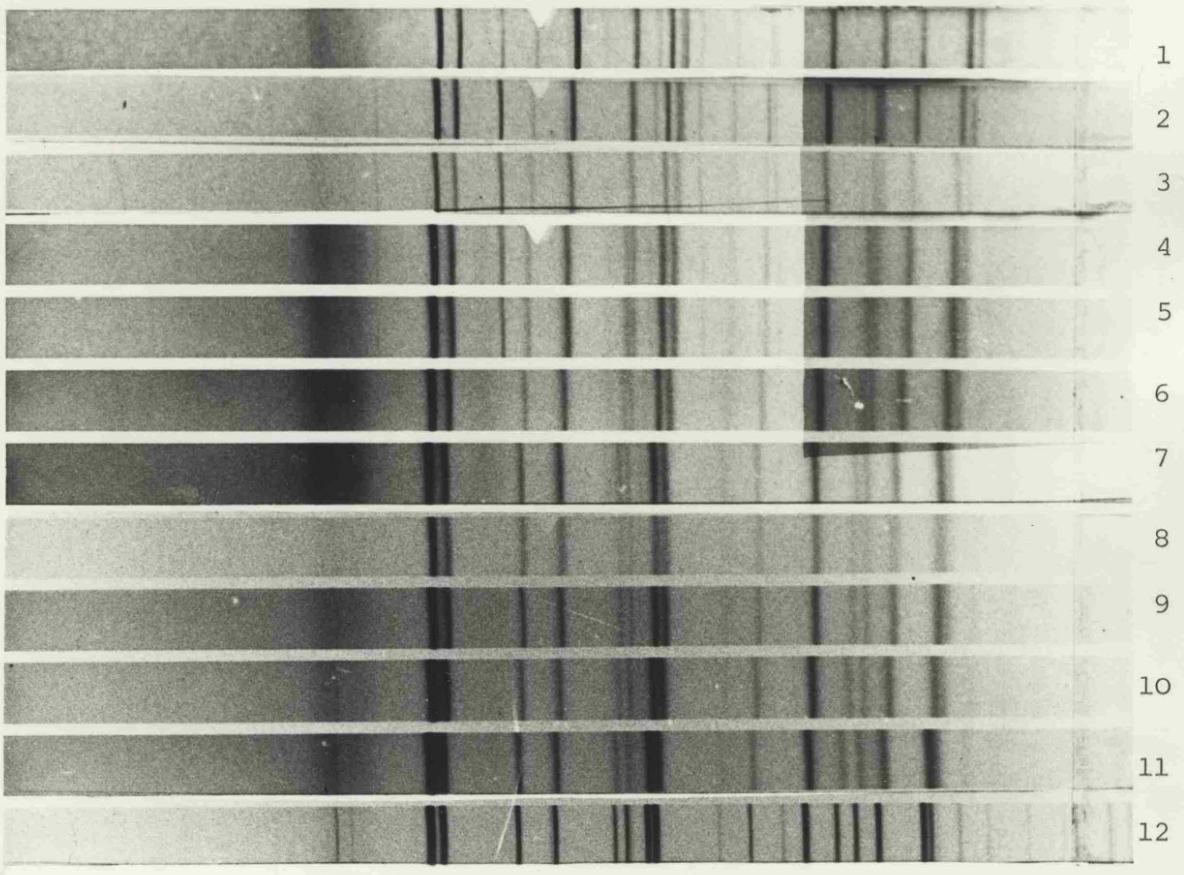

Figure 3.1.4

Guinier Photographs of $(Ca_{1-x}Sr_x)CO_3$

for x = 1. 0.0; 2. 0.1; 3. 0.2; 4. 0.3; 5. 0.4; 6. 0.5; 7. 0.6;

8. 0.7; 9. 0.75; 10. 0.8; 11. 0.9; 12. 1.0

Table 3.1.6 Lattice Parameters and Unit Cell Volume for Series S Samples

Sample	a_o/Å	b_o/Å	c_o/Å	V/Å^{3}x10^2
S.0	5.740	4.961	7.967	2.268
S.10	5.757	4.988	8.004	2.298
S.20,S.30,S.40	5.797	4.999	8.081	2.342
S.50	5.835	5.007	8.121	2.373
S.60	5.871	5.022	8.165	2.407
S.70	5.928	5.034	8.212	2.469
S.75	5.946	5.050	8.250	2.477
S.80	5.958	5.060	8.310	2.505
S.90	5.994	5.079	8.326	2.535
S.100	6.029	5.107	8.414	2.545

Table 3.1.7 Composition of Aragonite Phase of Series T

Nominal % Sr	10	20	30
% Sr in Phase A_1	60	50	50
% Sr in Phase A_2	10	20	45

Table 3.1.8 Variation of d_{104} for Calcite Phase

Series	X-Ray Analysis Method	mol % Sr 0	10	20	30	40	50
Q	Df	3.046	3.048	3.050	3.057		
R	DS	3.028	3.029	3.031	3.039	3.043	3.039
S	G	3.035	3.037	3.040	3.045		
T	Df	3.046	3.050	3.050	3.050		

the d_{104} for this phase is reported in Table 3.1.8.

3.2 CaO-SrO Solid Solutions : Preparation and Phase Characterization

CaO-SrO solid solutions were obtained by thermal decomposition of the Series S coprecipitated carbonates as follows :

1. Outgassing for 3 hours at a pressure of approximately 10^{-4} torr and room temperature.

2. Programmed heating treatment as sketched in Figure 3.2.1 at a pressure of approximately 10^{-4} torr until the temperature reached 1423 K, when annealing was carried out at a pressure of approximately 10^{-6} torr.

In order to avoid contamination by silica at high temperature the carbonates were placed in a platinum bucket. Due to the high surface reactivity of the finely divided materials it was desirable to avoid exposure of the specimens to the atmosphere, so special devices were designed for the preparation of the solid solutions, particularly to attempt the experiment 'in situ' whenever possible.

The oxide solid solutions are designated OS.x where x represents the mol % of SrO. Thus, for example, OS.60 represents $(Ca_{0.4}Sr_{0.6})O$.

Due to the high reactivity of these solids, the determination of accurate lattice parameters requires that the x-ray capillaries be filled with the sample and sealed off when still under vacuum. For this purpose the greaseless system (160) shown in Figure 3.2.2. was used. It allowed the preparation of the sample in a reaction tube and its transfer into a grinder compartment which contained a sliding pestle. This pestle could be manipulated externally so as to grind the powder in vacuo prior to inversion of the apparatus

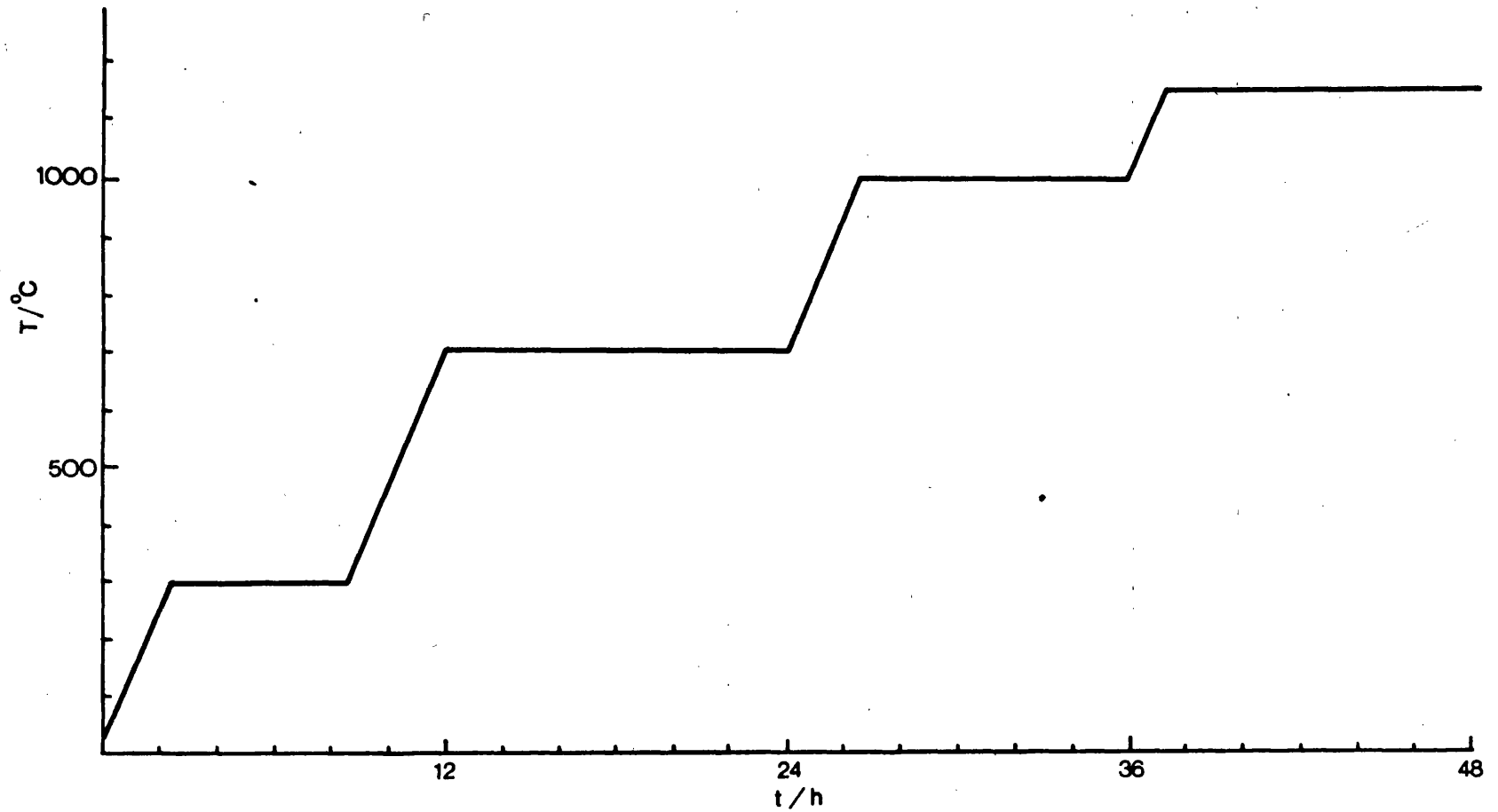

Figure 3.2.1

Heating program for the preparation of CaO - SrO Solid Solutions

1. Furnace
2. Silica tube
3. Platinum bucket
4. Greaseless joints
5. Greasless tap
6. EPR tube
7. Sample reservoir
8. Grinder
9. O-ring vacuum seals
10. Sliding pestle
11. X-ray capillary tube

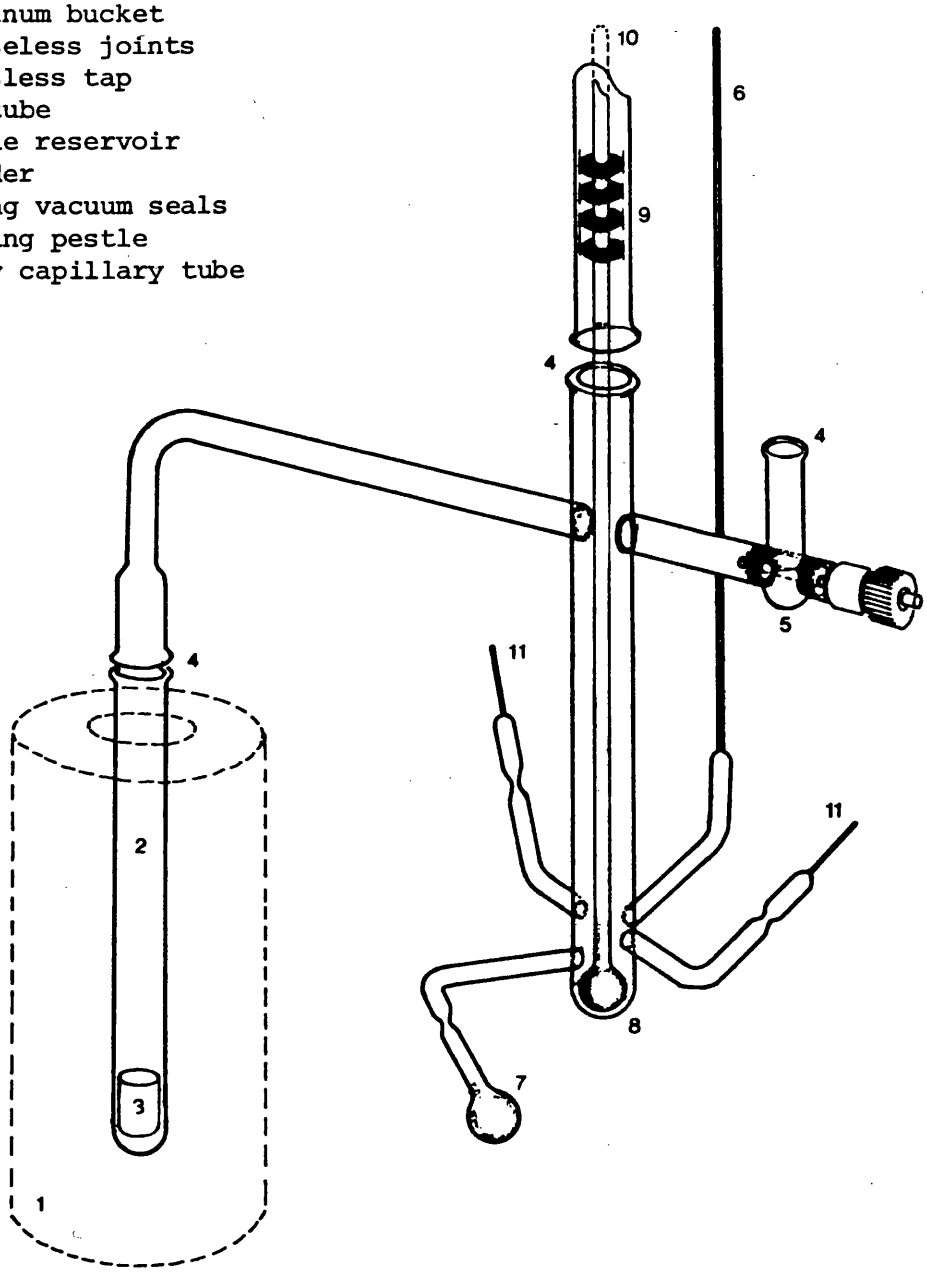

Figure 3.2.2

Apparatus for preparation of CaO - SrO samples

for measurements of X-Ray Diffraction and

ESR spectra in vacuo

in order to fill the thin-walled x-ray capillary tubes (2 for each sample). The capillaries were then sealed in vacuo and detached.

X-Ray powder photographs were taken for each capillary by the Debye-Scherrer method at room temperature using Ni filtered Cu Kα radiation and a 114.6 mm camera. The film was placed in the Straumanis position. a_o was calculated from the high angle lines using Nelson and Riley plots for extrapolation.

Figures 3.2.3 and 3.2.4 show the x-ray diffraction patterns for all the samples where a single-phase solid solution was achieved. This is evidenced by the presence of single lines in the NaCl-type pattern. OS.20 and OS.30 did not form solid solutions when subjected to this method of preparation.

Figure 3.2.5 shows a linear dependence of the lattice parameter with composition. This adherence to Vegard's law confirms that single-phase solid solutions have been formed.

3.3 CaO-SrO Solid Solutions : Surface Characterization

3.3.1 Surface Area Determination

The specific surface area of the CaO-SrO solid solutions (and also pure CaO and SrO) prepared in situ, were measured by the krypton BET method at 78 K. Results are shown in Fig. 3.3.0 and in Table 3.3.1.

3.3.2 Reflectance Studies

A Pye Unicam SP 700C fitted with the standard commercial Pye Unicam reflectance attachment was used. The optics of the instrument are those of a standard double beam spectrometer. A detailed diagram of the reflectance attachment is shown in Fig. 3.3.1.

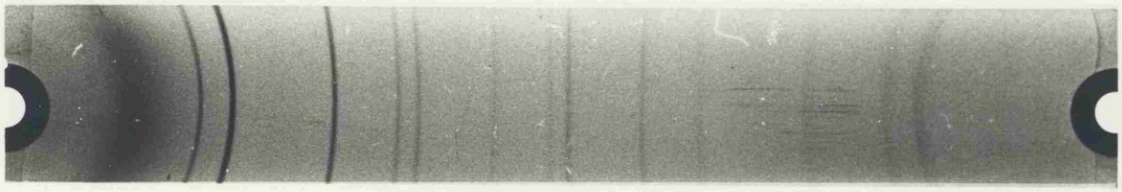

OS.O

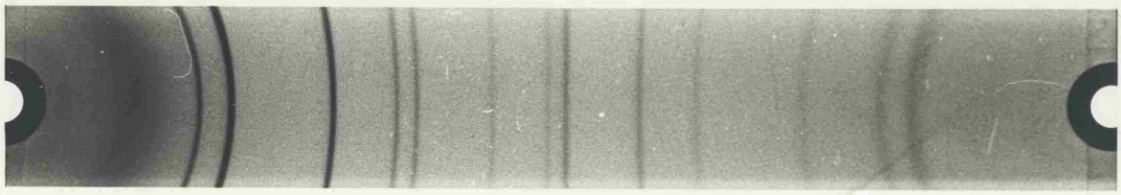

OS.10

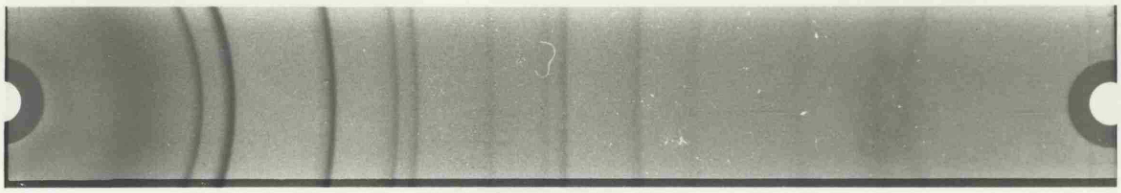

OS.20

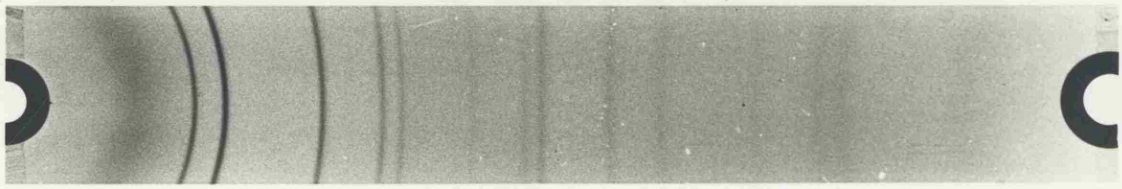

OS.40

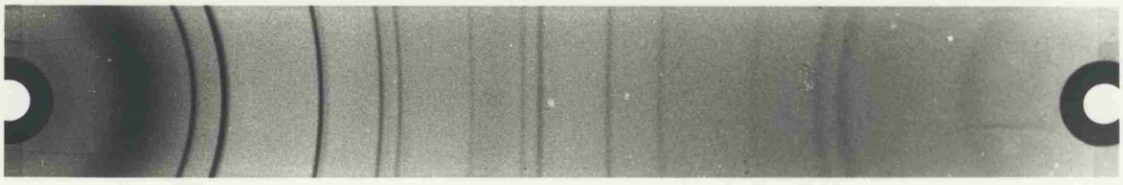

OS.50

Figure 3.2.3

Debye-Scherrer Photographs of CaO - SrO Solid Solutions

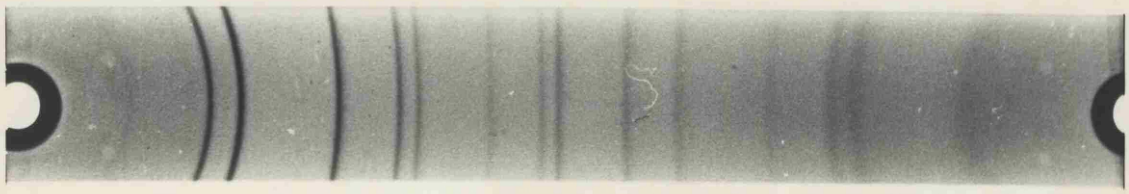

OS.60

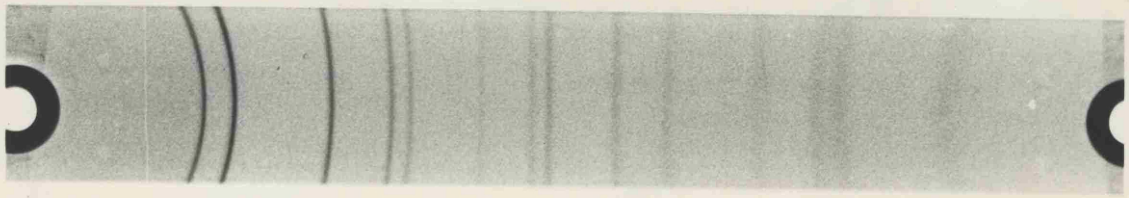

OS.70

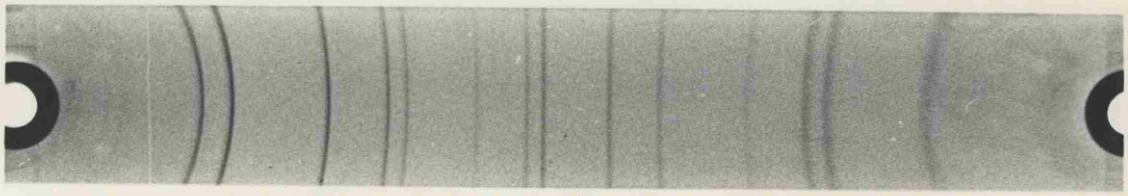

OS.80

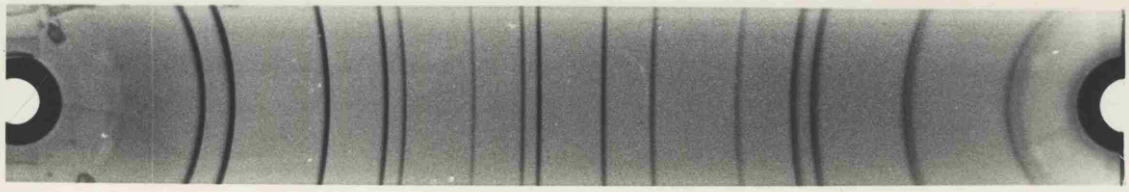

OS.90

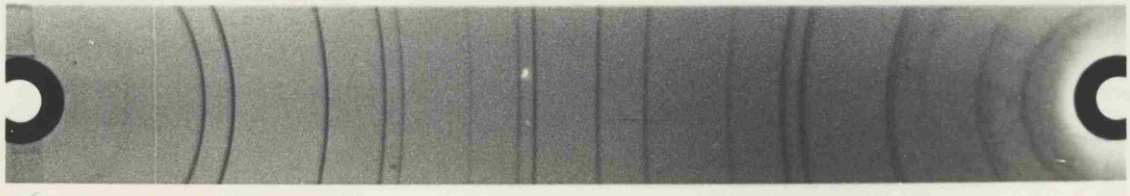

OS.100

Figure 3.2.4

Debye-Scherrer Photographs of CaO - SrO Solid Solutions

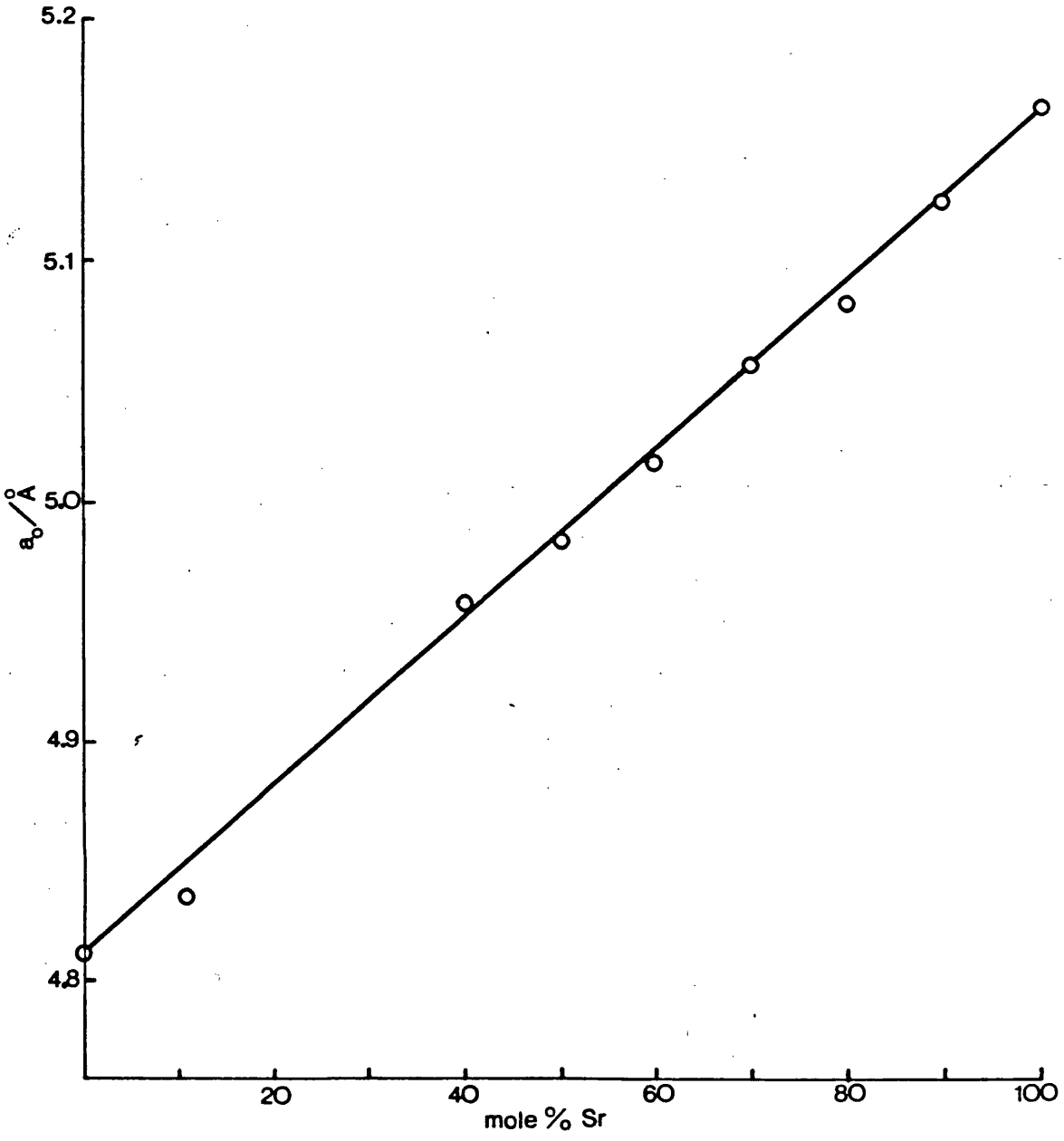

Figure 3.2.5

Variation of the lattice parameter with Sr Concentration for

CaO - SrO Solid Solutions

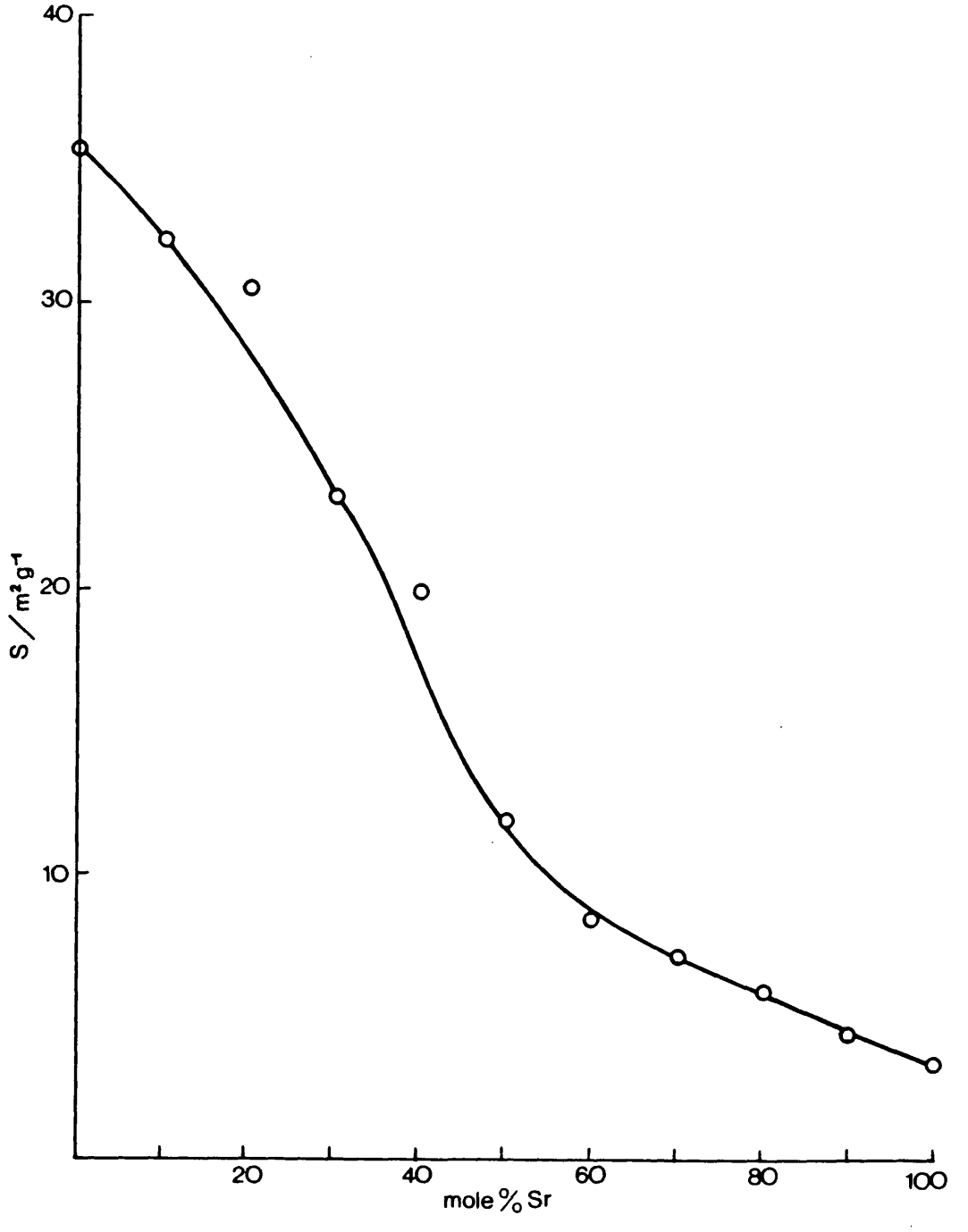

Figure 3.3.0

Variation of Surface Area with Sr Concentration for CaO - SrO Solid Solutions

Table 3.3.1 Surface Area of CaO-SrO

Sample	S/m^2g^{-1}
OS.100	3.5
OS.90	4.6
OS.80	6.0
OS.70	7.4
OS.60	8.5
OS.50	12.0
OS.40	20.1
OS.30	23.3
OS.20	30.7
OS.10	32.3
OS.0	35.5

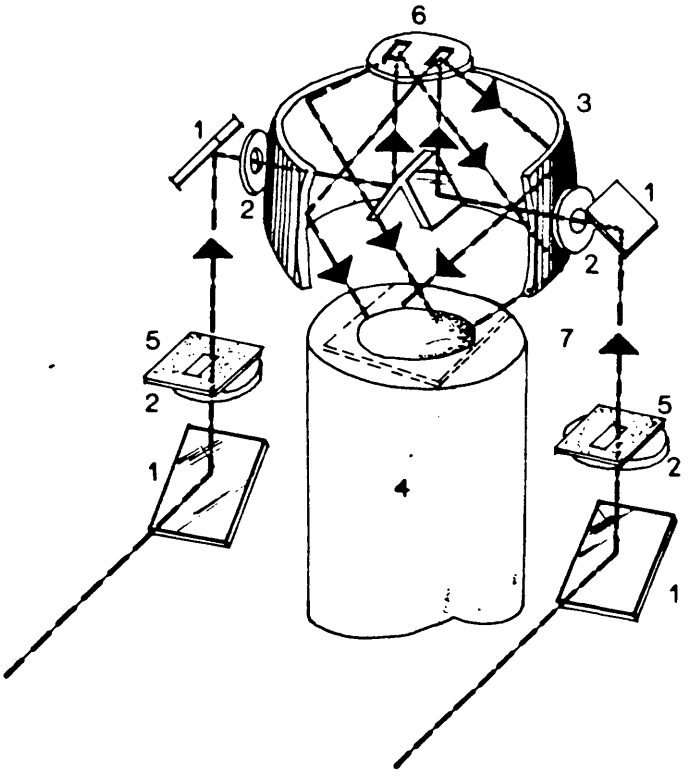

1. Reflecting mirror
2. Lenses
3. Ellipsoidal reflecting mirror
4. Photomultiplier tube
5. Aperture place
6. Light patches on reference and sample
7. Lead sulphide detector

Figure 3.3.1

Reflectance Attachment

The spectrometer has a linear scan with respect to energy and time and it ranges from 52,000 cm^{-1} to 4,000 cm^{-1}. To cover the full range two detectors are used, a photomultiplier above 15,000 cm^{-1} and a lead sulphide cell below 15,000 cm^{-1}. The reflectance range employed was the 0 - 110% reflectance scale.

The reflectance cell described by Zecchina, Lofthouse and Stone (15) was slightly modified for carrying out the present work. Since the oxides were prepared in situ in the cell, it was necessary to ensure not only that all the sample was heat treated but also that it was completely contained in the platinum bucket to guarantee a homogeneous and reproducible preparation. Thus the cell was separated into two vertical halves, one consisting of the reflectance cell itself and the other the reaction tube for sample preparation (Fig. 3.3.2). The top of the sample tube comprised a greaseless tap and a large rubber 'O' ring ball joint. The cell could be connected using the corresponding cup joint and a suitable retaining clip. Two 'O' ring joints fused to each other in a z-shaped piece allowed freedom of movement of the cell in the vertical plane facilitating the placing of the cell on the spectrometer porthole. The author is indebted to Mr. M. Lock who very skilfully made the cell.

Trevethan (21) has described the method for making up the reference compartment by using 'Suprasil' powder, a spectroscopically pure silica, and the same method has been adopted here.

A diagram of the reflectance frame is shown in Fig. 3.3.3. This was a conventional greasefree frame comprising the vacuum system, the pressure readers and the gas handling system. The vacuum system consisted of a mercury diffusion pump backed by a standard two-stage belt-driven Edwards rotary pump. The pressure readers comprised

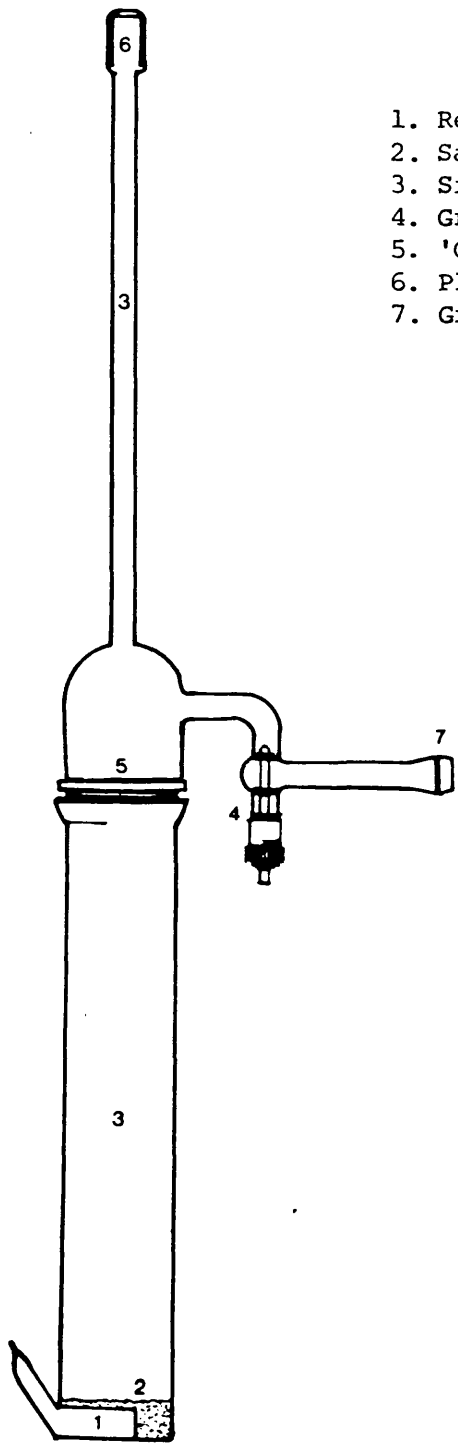

1. Reference compartment
2. Sample
3. Silica tube
4. Greaseless tap
5. 'O'-ring joint
6. Platinum bucket
7. Greaseless joint

Figure 3.3.2

Reflectance cell

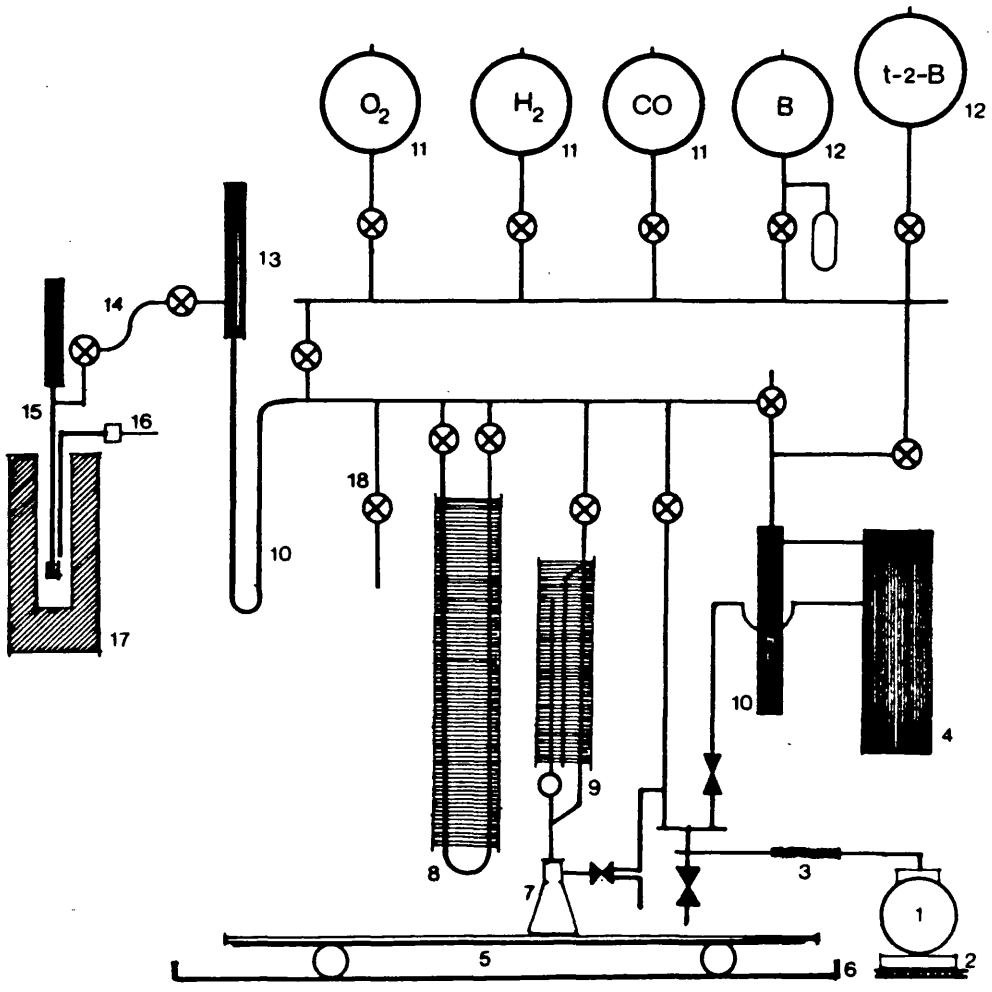

1. Rotary pump
2. Foam rubber base
3. Flexible hose connection
4. Mercury diffusion pump
5. Wooden base
6. Metal rails
7. Mercury cut-offs
8. Mercury manometer
9. McLeod gauge
10. Liquid nitrogen traps
11. Grade 'X' gas storage bulbs
12. Gas storage bulbs having cold finger
13. Ionisation head
14. 'Z'-piece connection
15. Reflectance cell
16. Thermocouple
17. Furnace
18. Inlet connection point

Figure 3.3.3

Reflectance Frame

a U-tube mercury manometer, a McLeod gauge and a Metrovac ionization gauge. On the gas handling system were placed some British Oxygen grade X bulbs (O_2 and CO) and also glass bulbs with a side finger which were used to store 1-butene and trans-2-butene supplied by Air Products in small cylinders.

The complete assembly was constructed as a large trolley which ran on a pair of rails. This arrangement allowed the withdrawal of the reflectance cell from the spectrometer so that a furnace could be easily placed around the cell for the heat treatment. Thus, each sample could be prepared 'in situ' in the cell at the inverted position and when ready be transferred to the reflectance part. The cell was then moved on to the porthole while still under vacuo and thereafter the reflectance cell remained on the spectrometer porthole for all the adsorption-desorption studies at room temperature.

The corner of the laboratory in which the reflectance frame and the spectrometer were situated was curtained off from the remainder of the room using heavy black curtains. The frame and reflectance cell were further covered by black curtains to minimize the risk of extraneous light reaching the spectrometer detectors.

The reflectance spectra of the oxide solid solutions and also the pure oxides were studied in the ultraviolet-visible range (50,000 - 15,000 cm^{-1}). The effect of some adsorbates on the spectra has been studied as well. A freshly prepared sample was used for each experiment. Adsorption experiments were carried out at intervals of increasing pressure obtained by making successive doses of the adsorbate. Desorption experiments were performed by taking a freshly-prepared sample, admitting a single dose of gas to

reach a pressure of about 50 torr, allowing to stand for about 3 hours to achieve equilibrium (or until the spectrum did not show any significant change), and the gas phase was then withdrawn stepwise by expansion into an outgassed adjacent volume in the frame, further outgassing being achieved by using the pumping system directly. For the experiments involving interaction between gases, a high pressure of the first adsorbate (50 torr) was allowed to attain equilibrium for 3 hours, the excess gas phase was withdrawn from the system leaving a pressure of approximately 1 torr in the isolated reflectance cell, and successive doses of the second adsorbate were then allowed into the cell to interact with the preadsorbed molecules.

All spectra were recorded after equilibrium was reached.

The results reported here are reflectance spectra obtained by direct tracing of the experimentally recorded spectra. Five separate sections will be considered : (a) high vacuum spectra (HVS) and oxygen effect, (b) adsorption and desorption of CO, (c) adsorption and desorption of 1-butene, (d) effect of CO on preadsorbed 1-butene, and (e) effect of 1-butene on preadsorbed CO.

(a) High vacuum spectra and effect of oxygen

Figs. 3.3.4 to 3.3.9 show the spectra obtained in high vacuum (10^{-6} torr), under a low oxygen pressure (3 torr) and after removing the oxygen. The HVS showed an apparently high reflectance value at energies higher than approximately 30,000 cm^{-1} due to fluoresence to which the detector also responds (15).

In all cases oxygen had two effects, the first one to quench the fluoresence above the region 30,000 cm^{-1} and the second to move the edge to higher energy. Thus, by quenching the fluorescence,

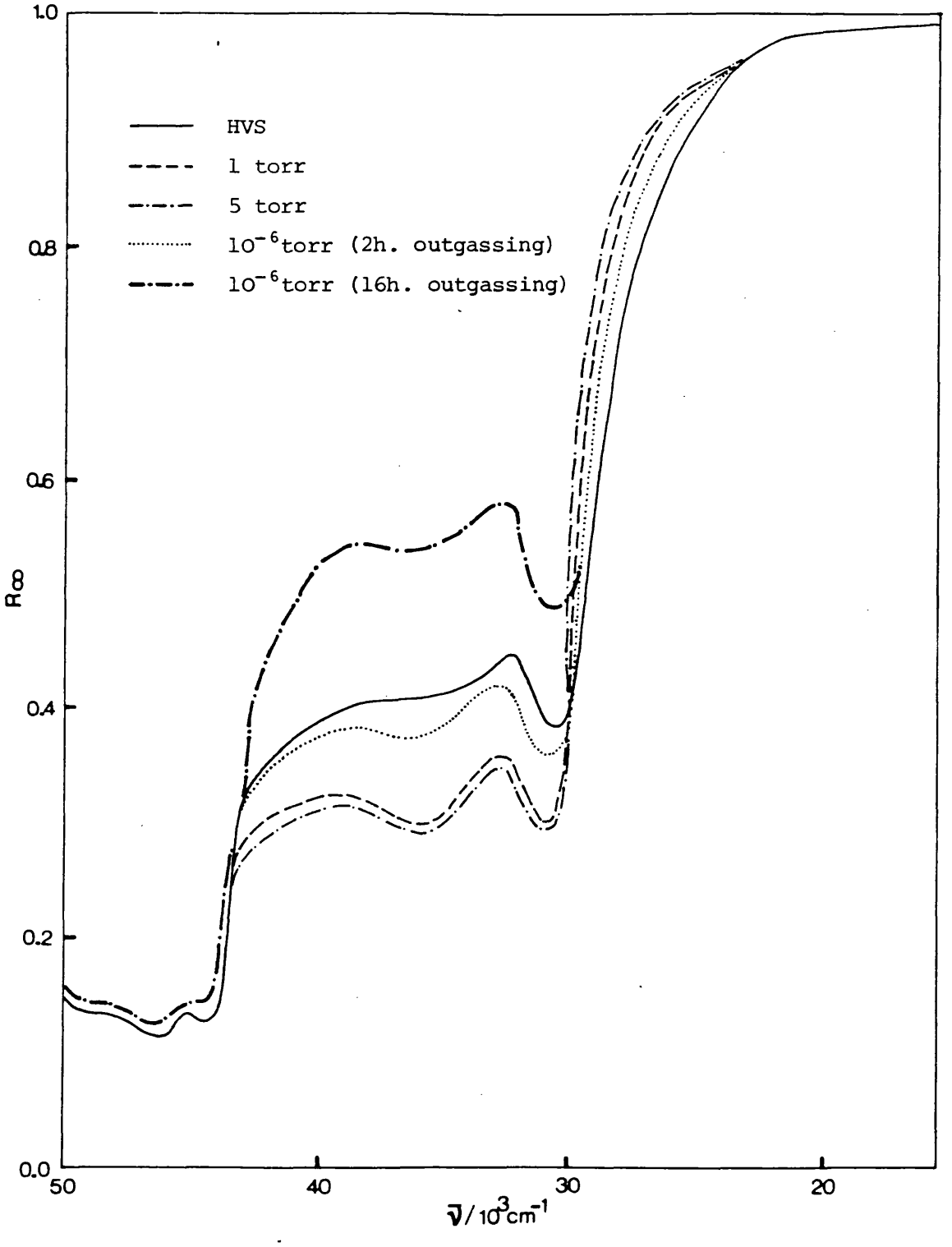

Figure 3.3.4

Oxygen effect on OS.100

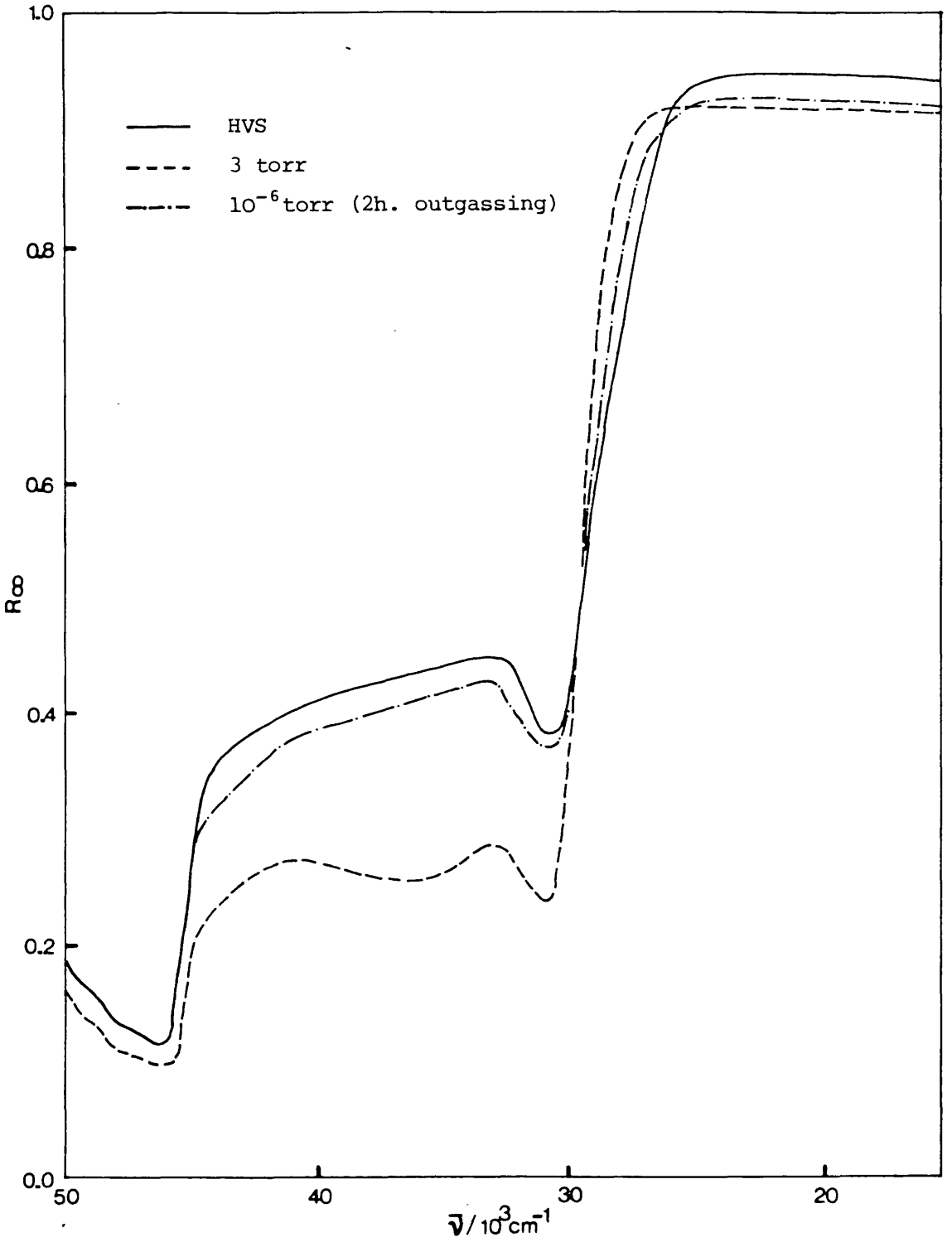

Figure 3.3.5

Oxygen effect on OS.80

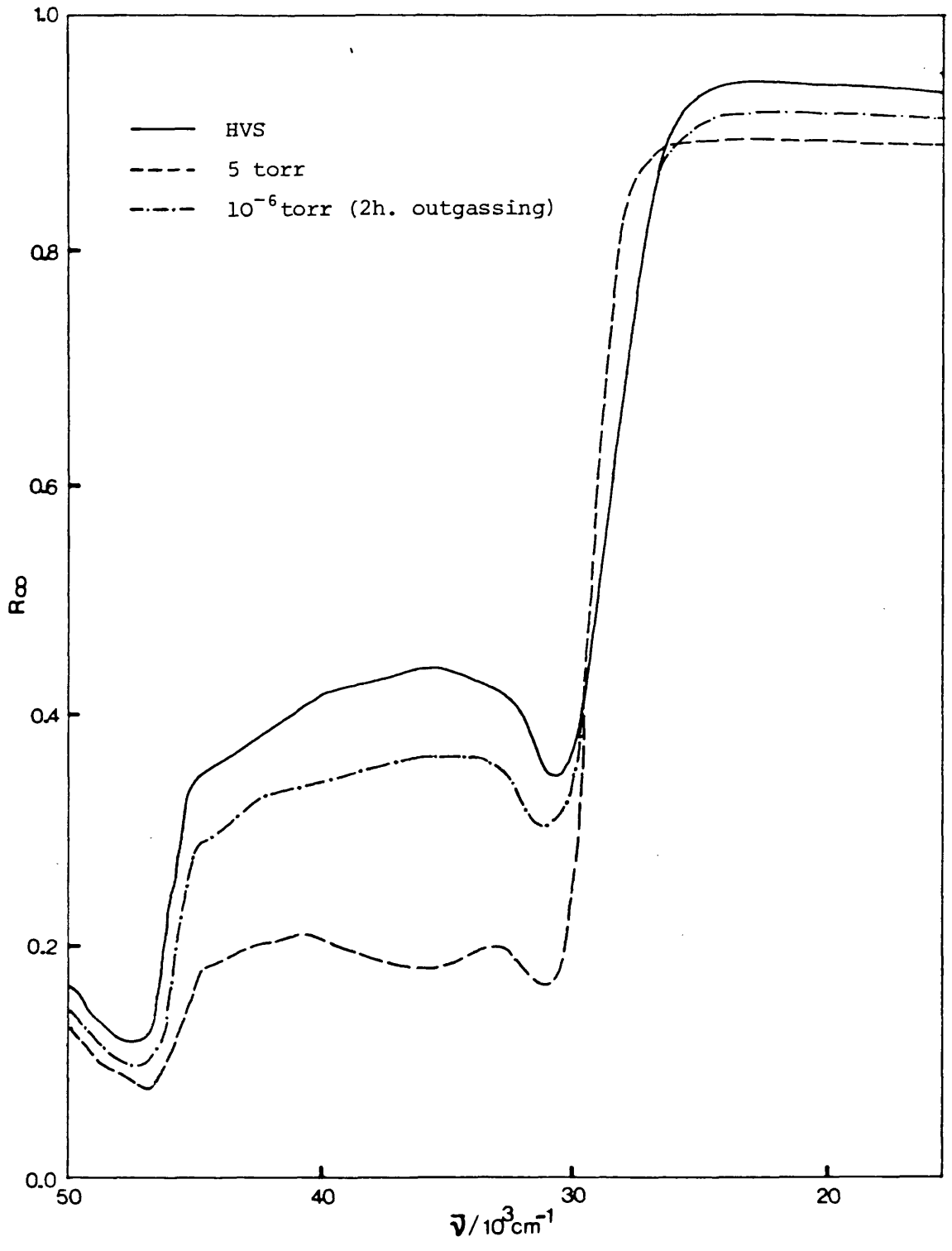

Figure 3.3.6

Oxygen effect on OS.60

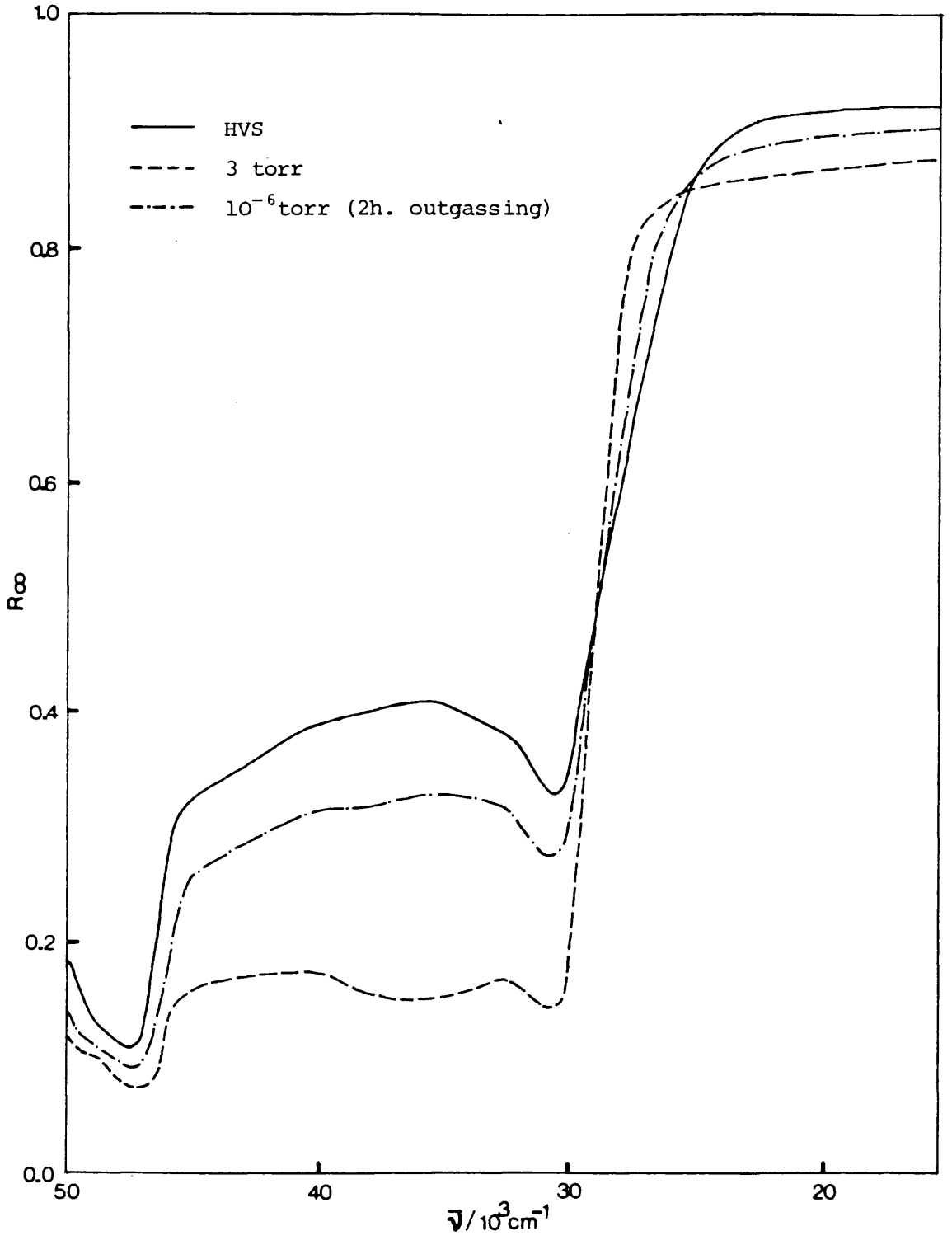

Figure 3.3.7

Oxygen effect on OS.40

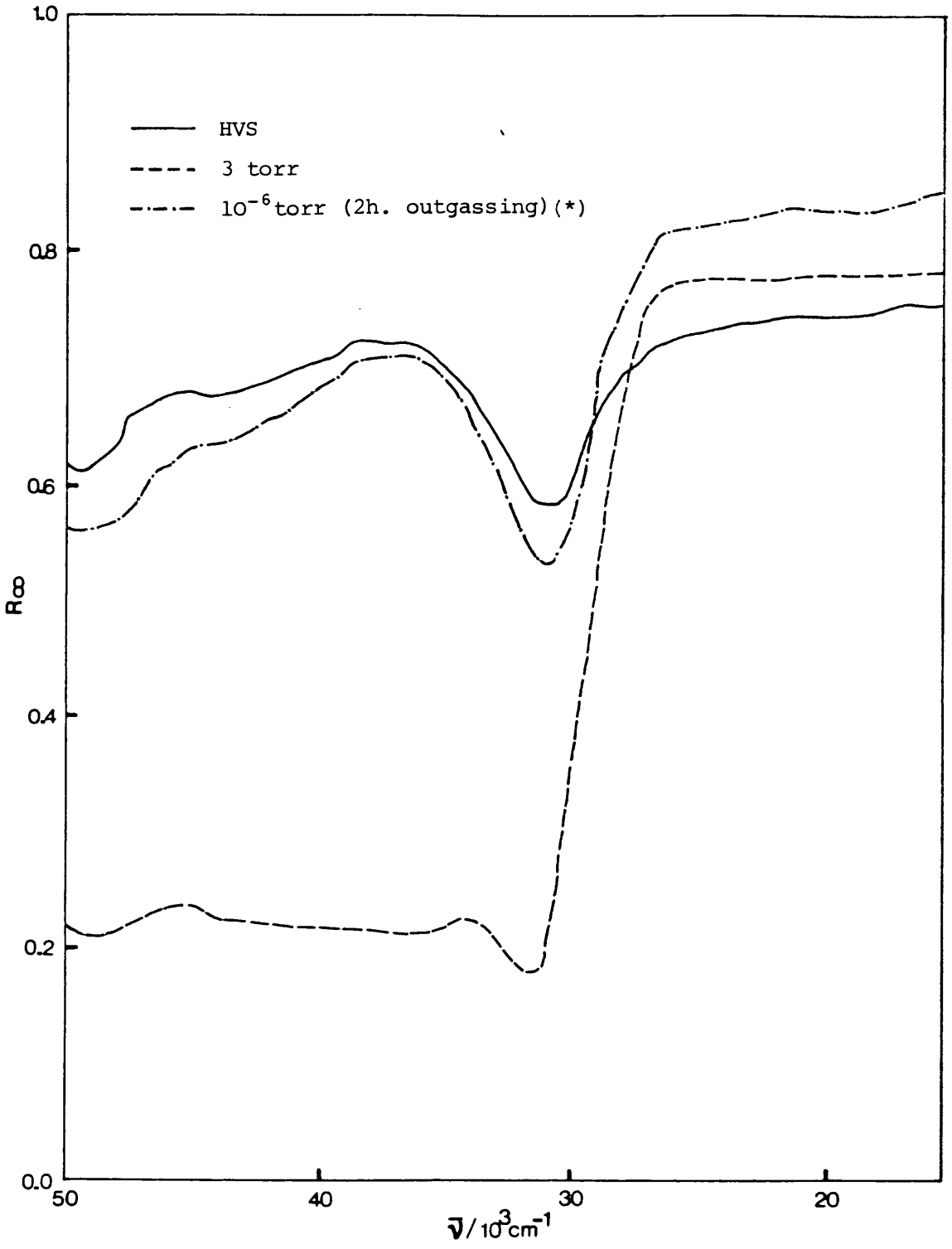

Figure 3.3.8

Oxygen effect on OS.10

(*) these spectra have been displaced downwards

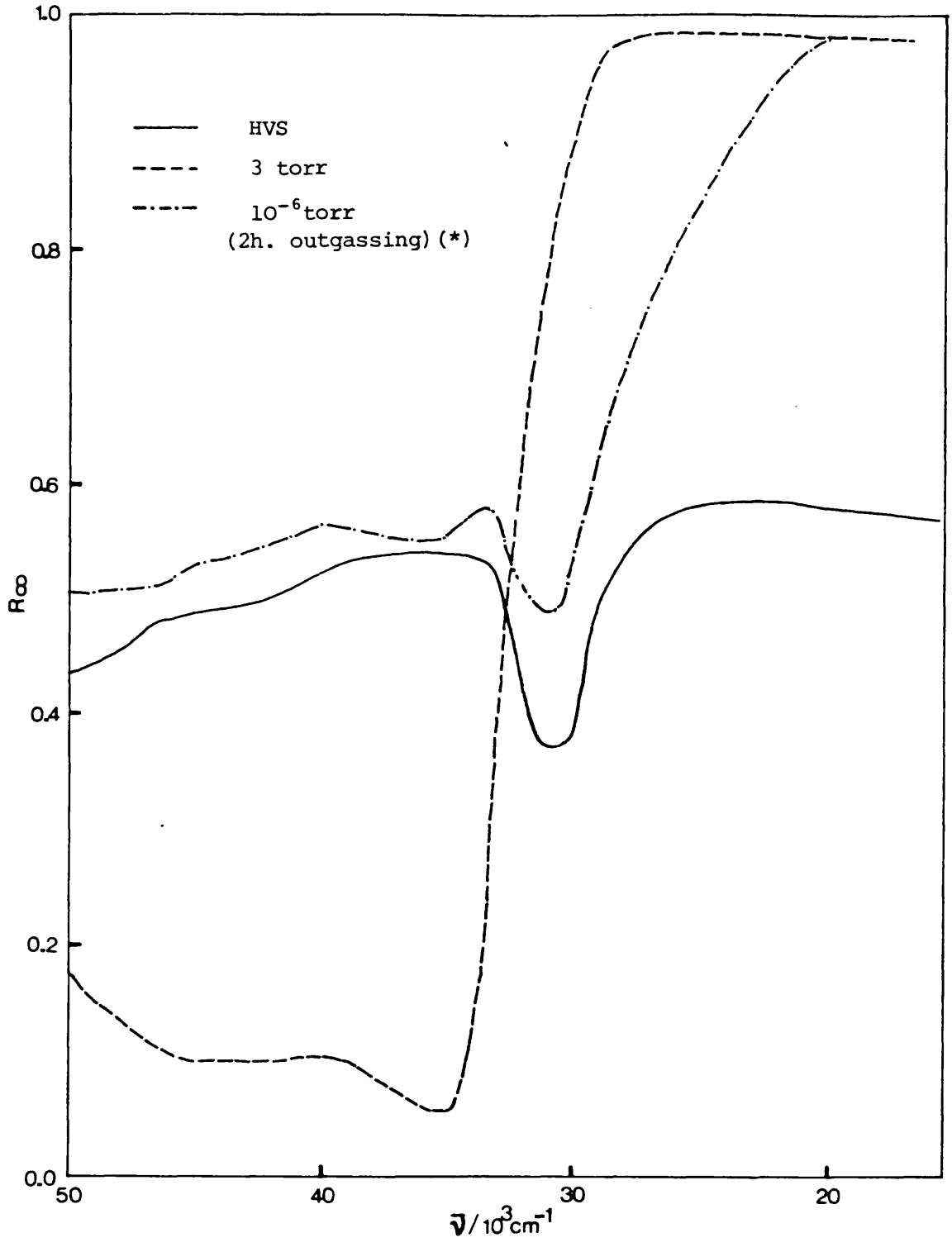

Figure 3.3.9

Oxygen effect on OS.O

(*) these spectra have been displaced downwards

oxygen can be used to reveal the true spectra in which the position of the bands is as indicated in Table 3.3.2. These bands have been already classified into bulk and surface excitons following the assignment given for CaO (15) and SrO (16) by Zecchina and co-workers with whose results the present spectra are in very good agreement.

The surface transitions are characterized by two bands, except for OS.10 where three bands are observed. The low energy band, being narrower and more clearly defined than the high energy band, can be measured with greater accuracy.

OS.60 exhibited the highest exciton energies, not only for the bulk transitions but also for the surface transitions.

(b) Adsorption and desorption of CO

The spectra due to the chemisorption of CO are shown in Figures 3.3.10 to 3.3.15. The effect of the adsorption of CO is to erode immediately the surface spectra and to generate two bands whose intensities increase with increasing pressure. The pure oxides can be seen as extreme cases where the changes in intensity with coverage of each band is slightly different, while the solid solutions can be regarded as intermediates smoothly changing towards the extremes.

In SrO at low CO coverage the high energy band is more intense than the low energy band and the separation interval is small. The low energy band increases faster with pressure (coverage) than the high energy one causing overlapping to occur at medium coverages. At high coverage a third band positioned at even higher energy begins to develop but again is quiclky overlapped giving rise to a single very broad band which seems to enclose the previous three bands.

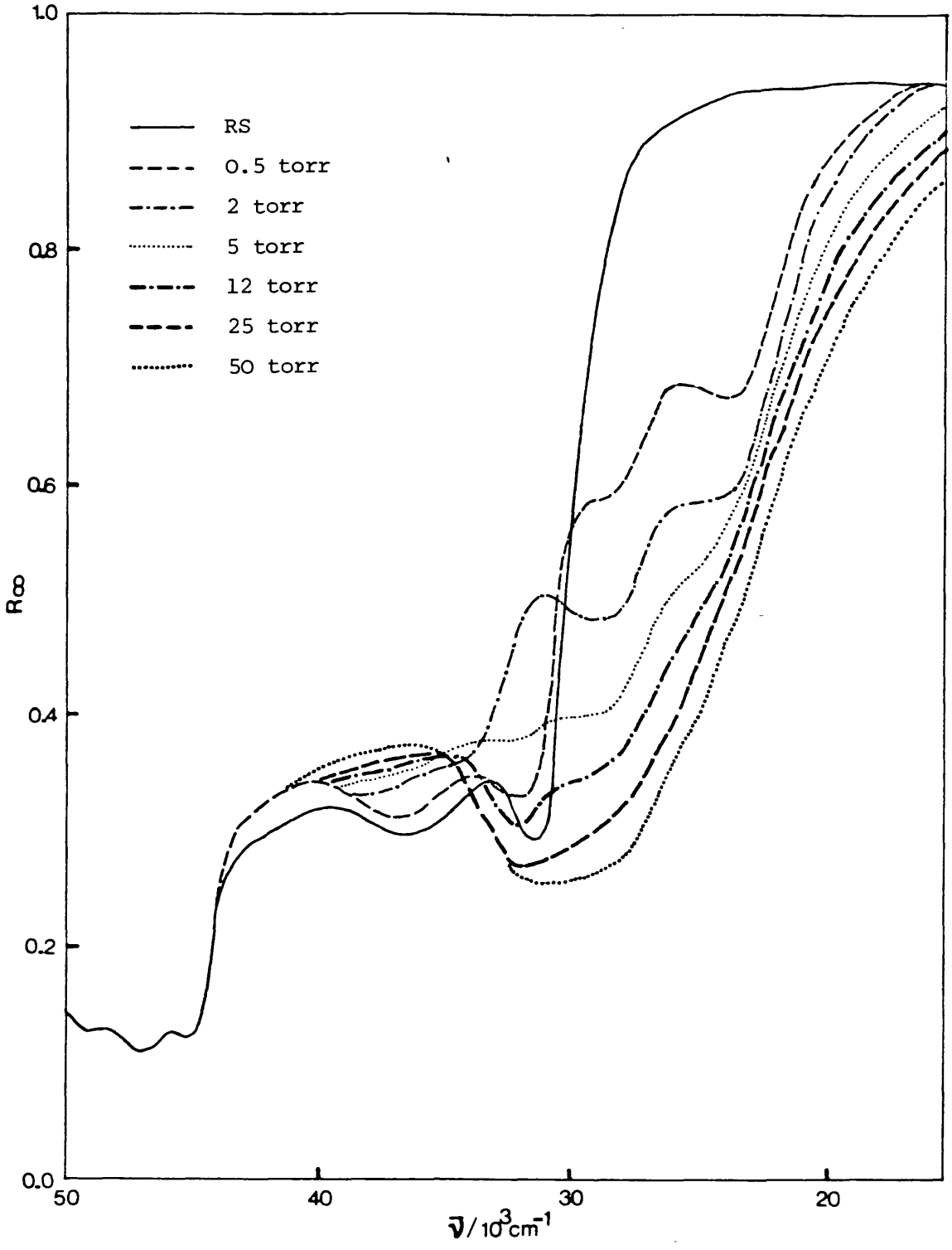

Figure 3.3.10

CO Adsorption on OS.100

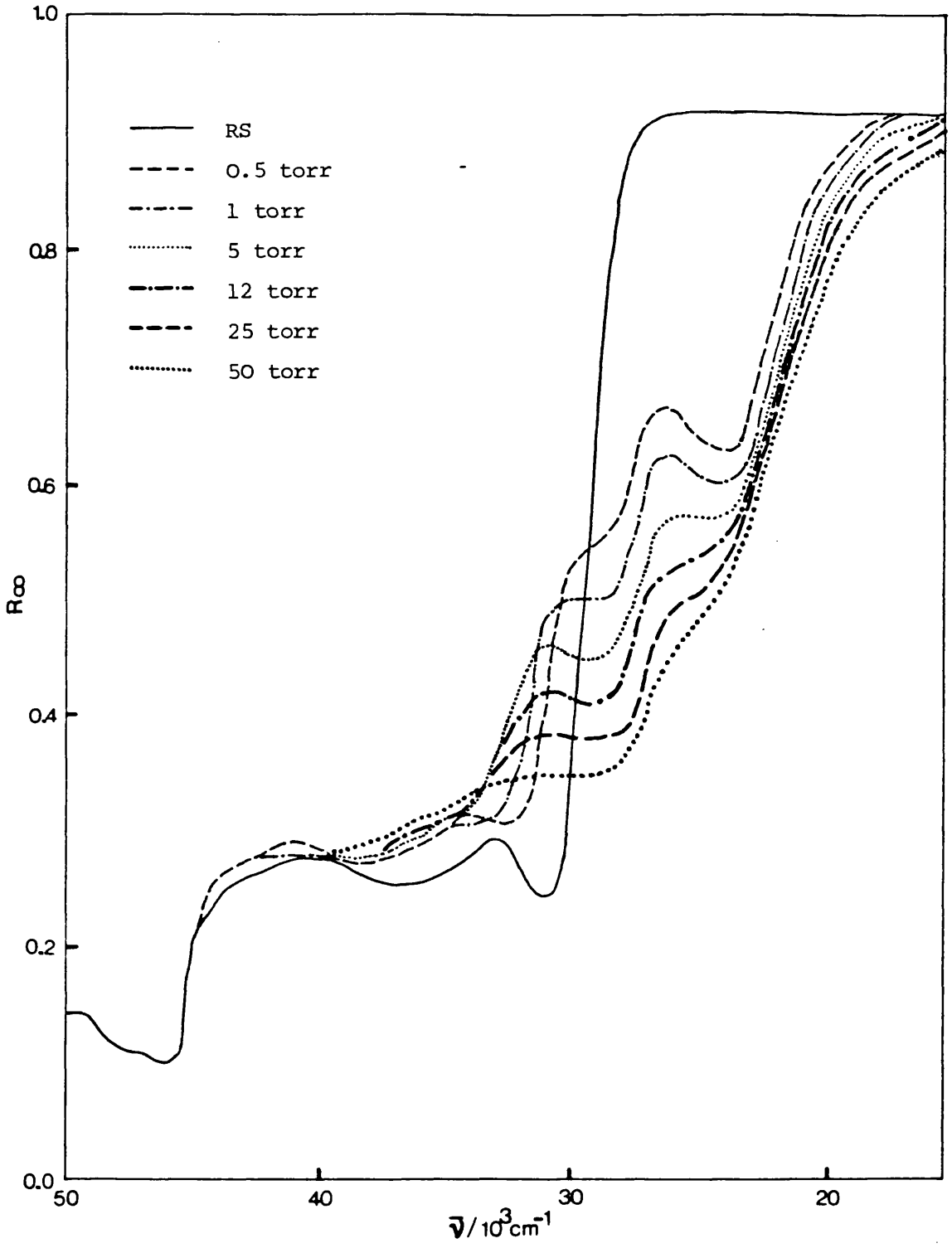

Figure 3.3.11

CO Adsorption on OS.80

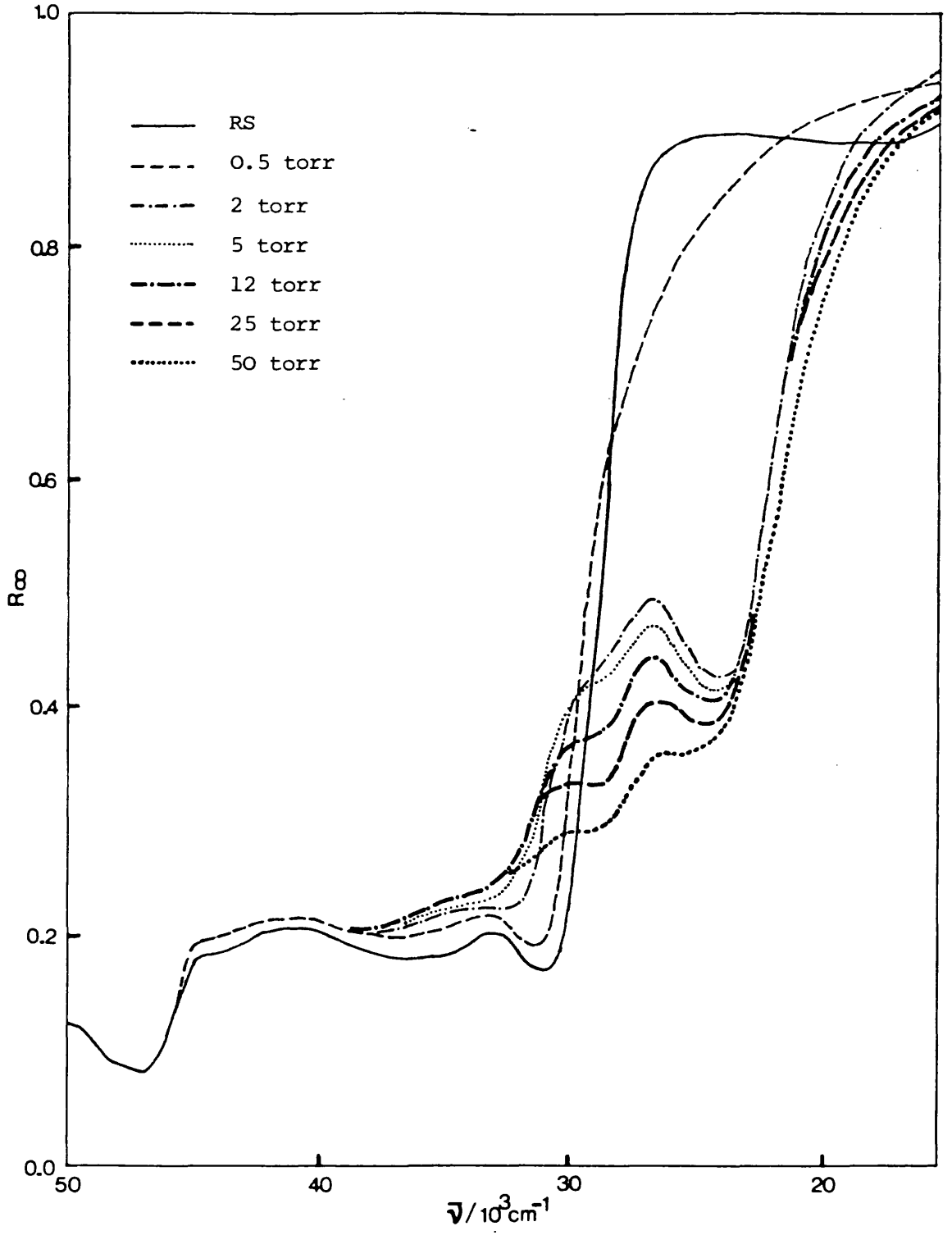

Figure 3.3.12

CO Adsorption on OS.60

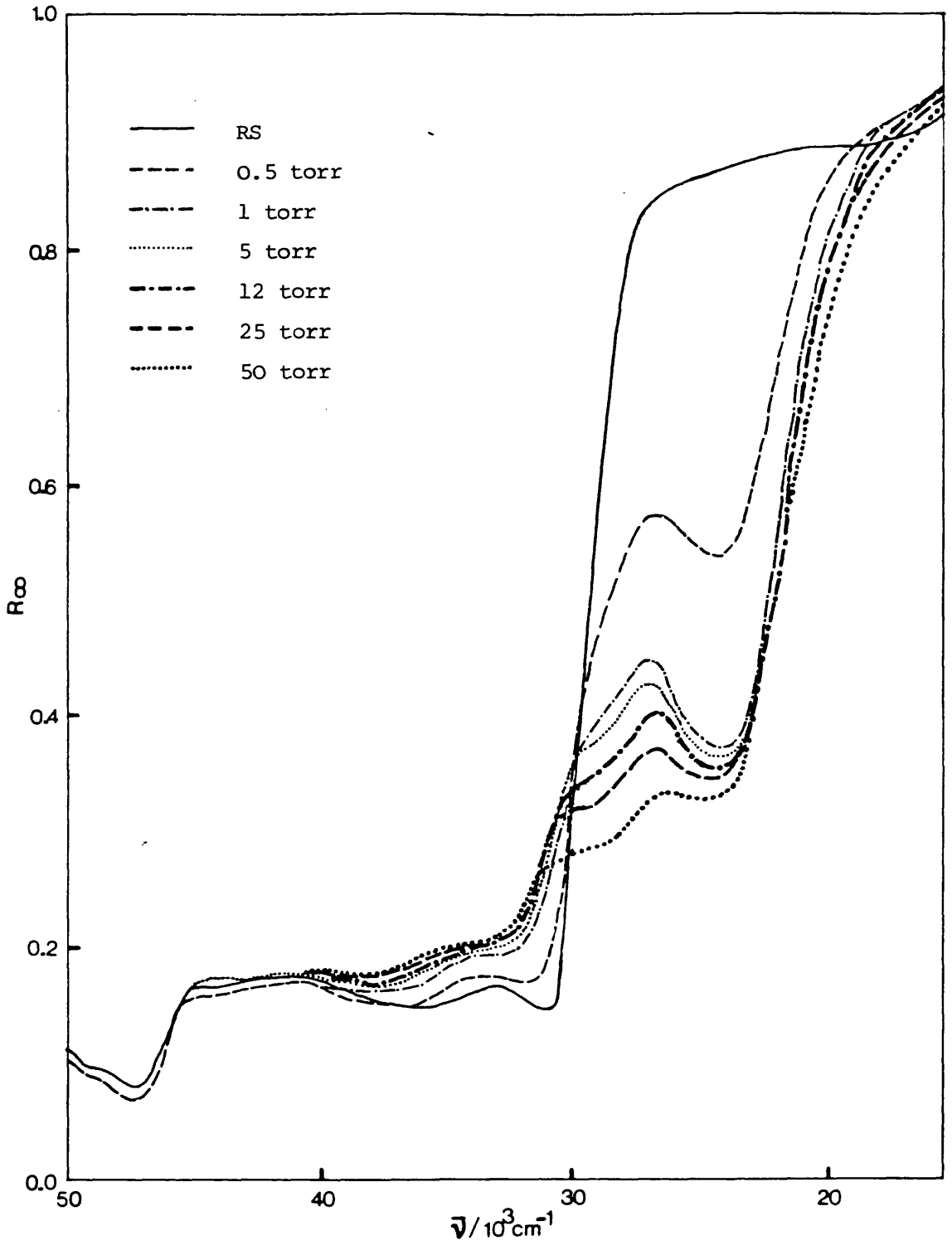

Figure 3.3.13

CO Adsorption on OS.40

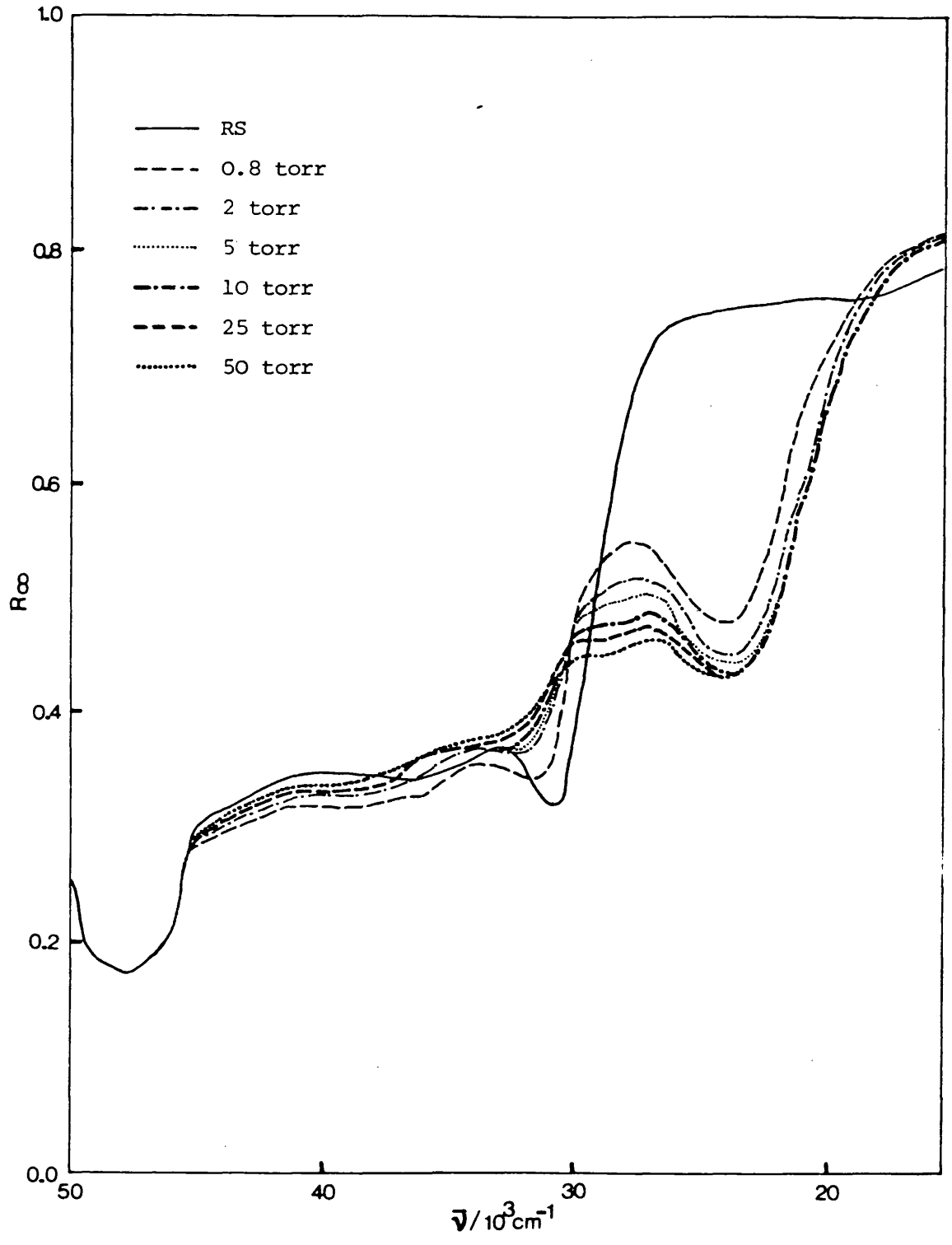

Figure 3.3.14

CO Adsorption on OS.10

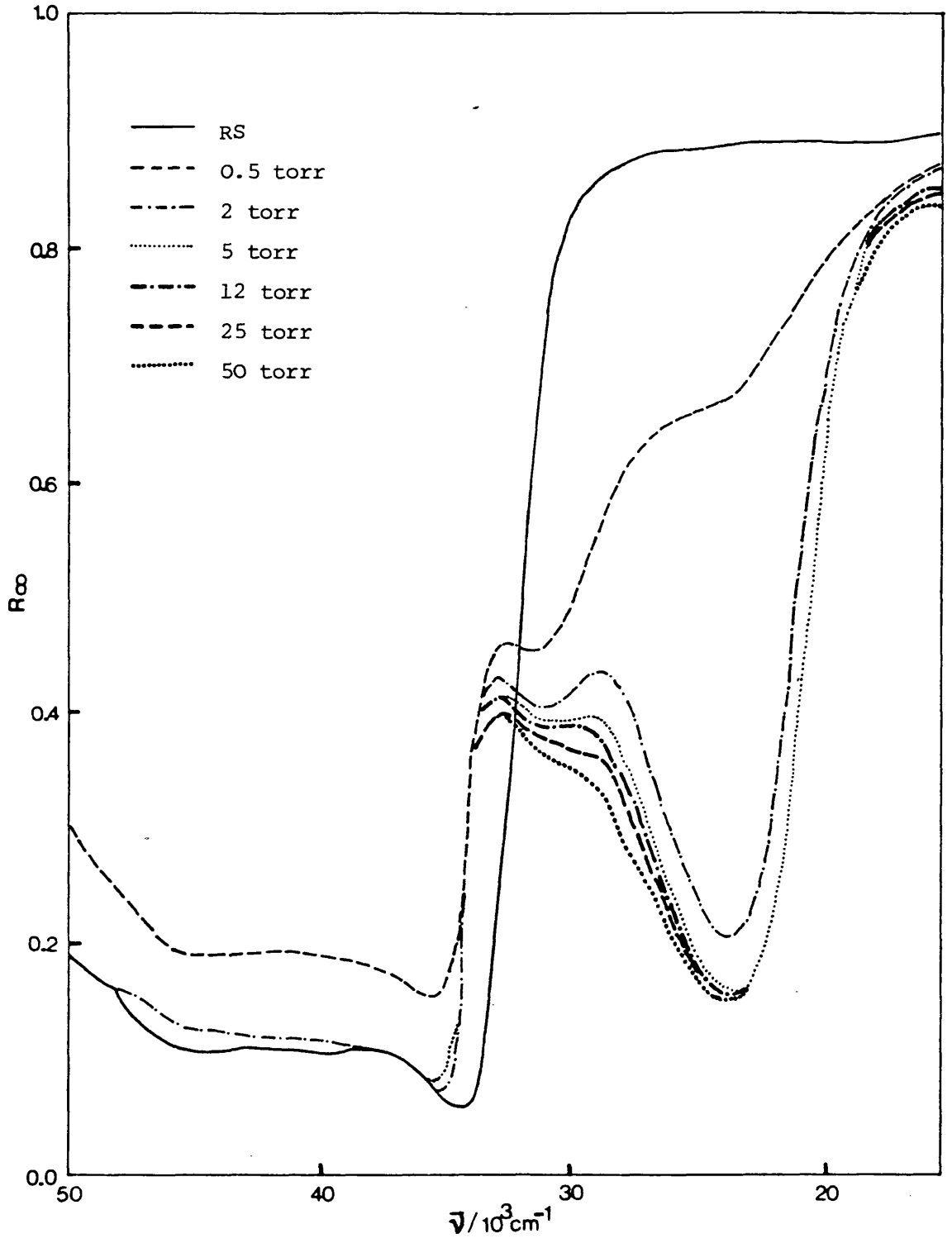

Figure 3.3.15

CO Adsorption on OS.O

Table 3.3.2 Reflectance Spectra of CaO - SrO Solid Solutions

Sample	Band maxima/cm^{-1}					
	Bulk Excitons			Surface Excitons		
OS.100	44,600	46,700	49,100	31,100	36,000	
OS.80	46,250	47,800	49,470	31,140	36,300	
OS.60	47,200	48,350	49,700	31,340	36,700	
OS.40	47,300	49,500		31,000	36,500	
OS.10	48,850			31,000	36,400	43,350
OS.0					35,350	45,150

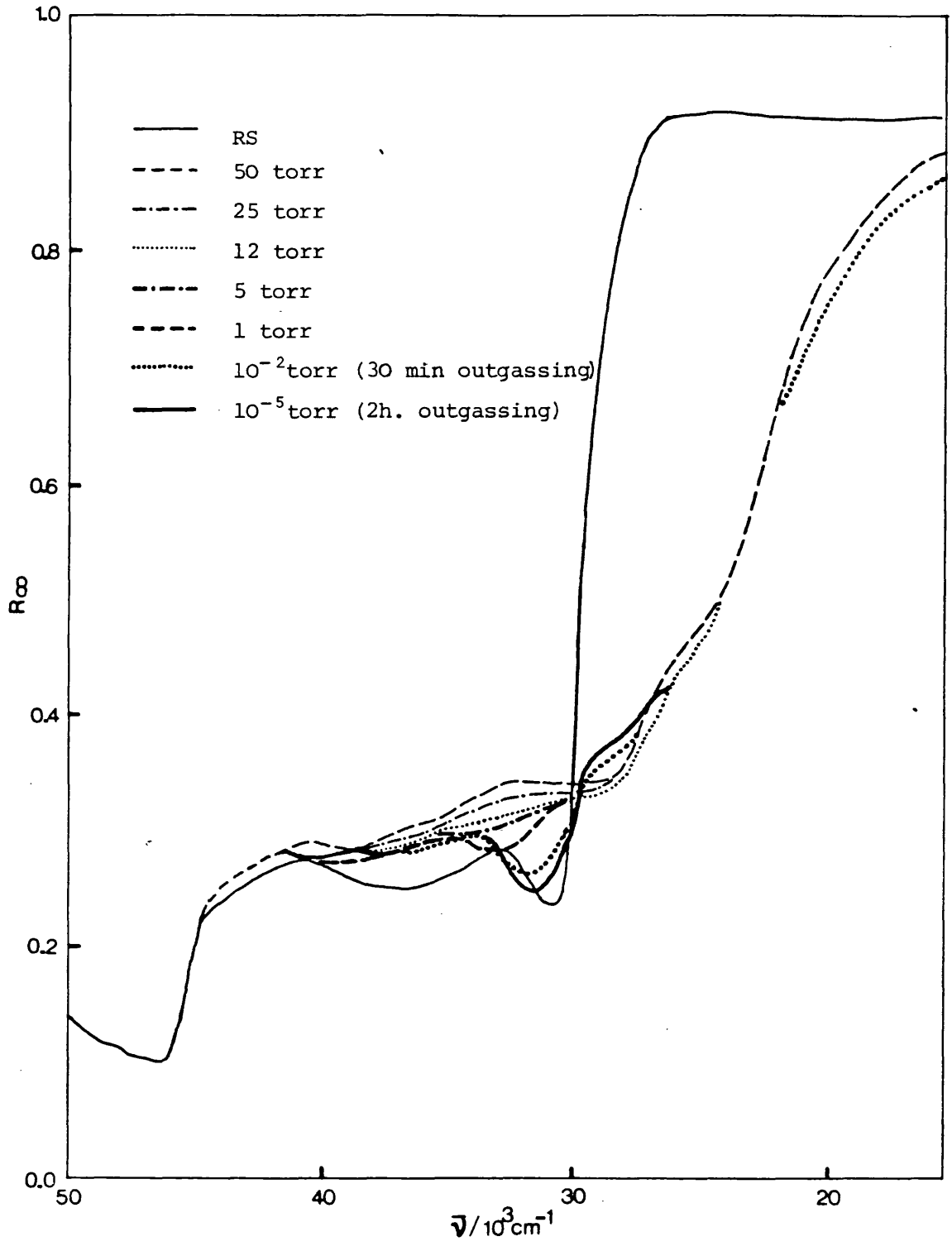

Figure 3.3.16

CO Desorption, OS.80

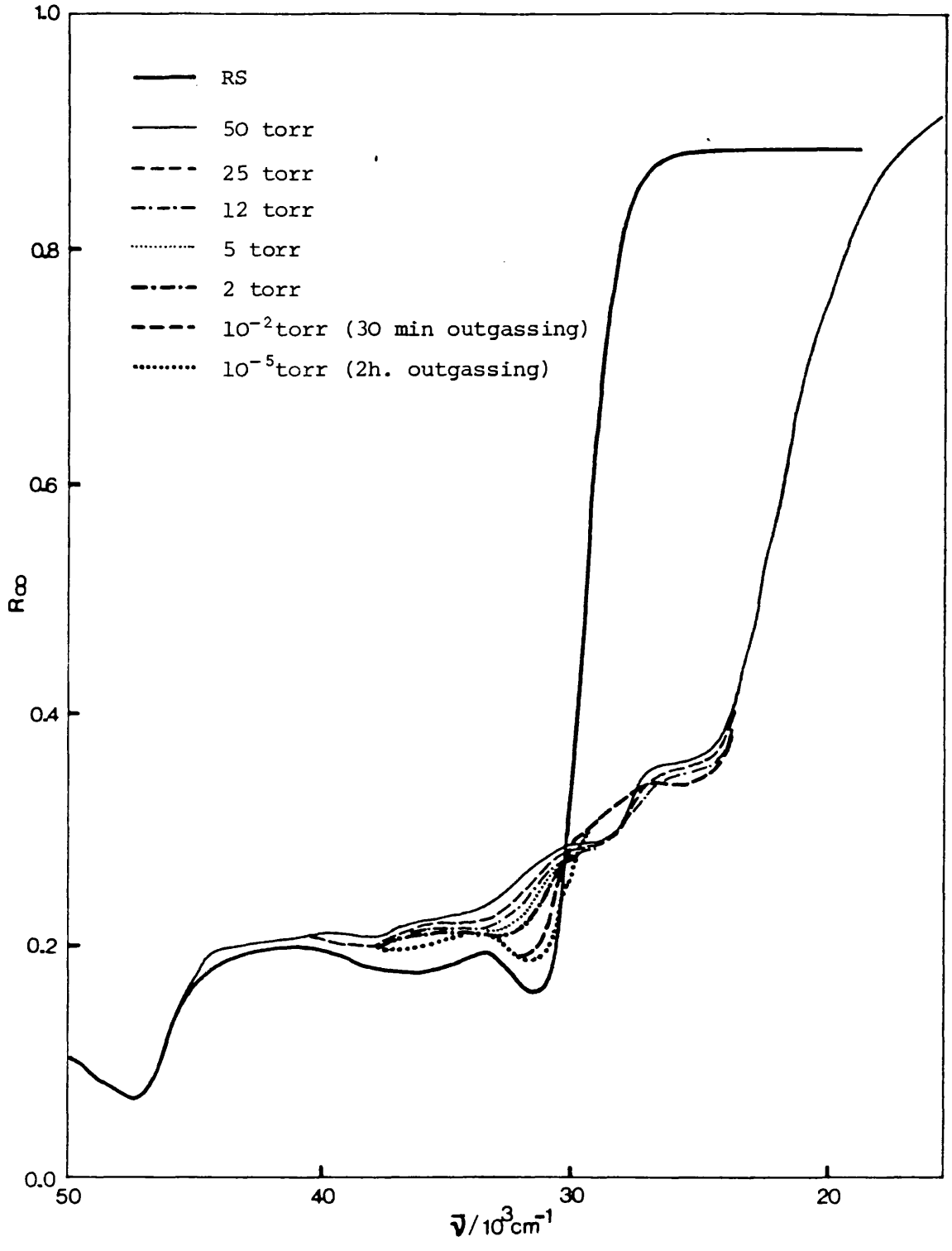

Figure 3.3.17

CO Desorption, OS.60

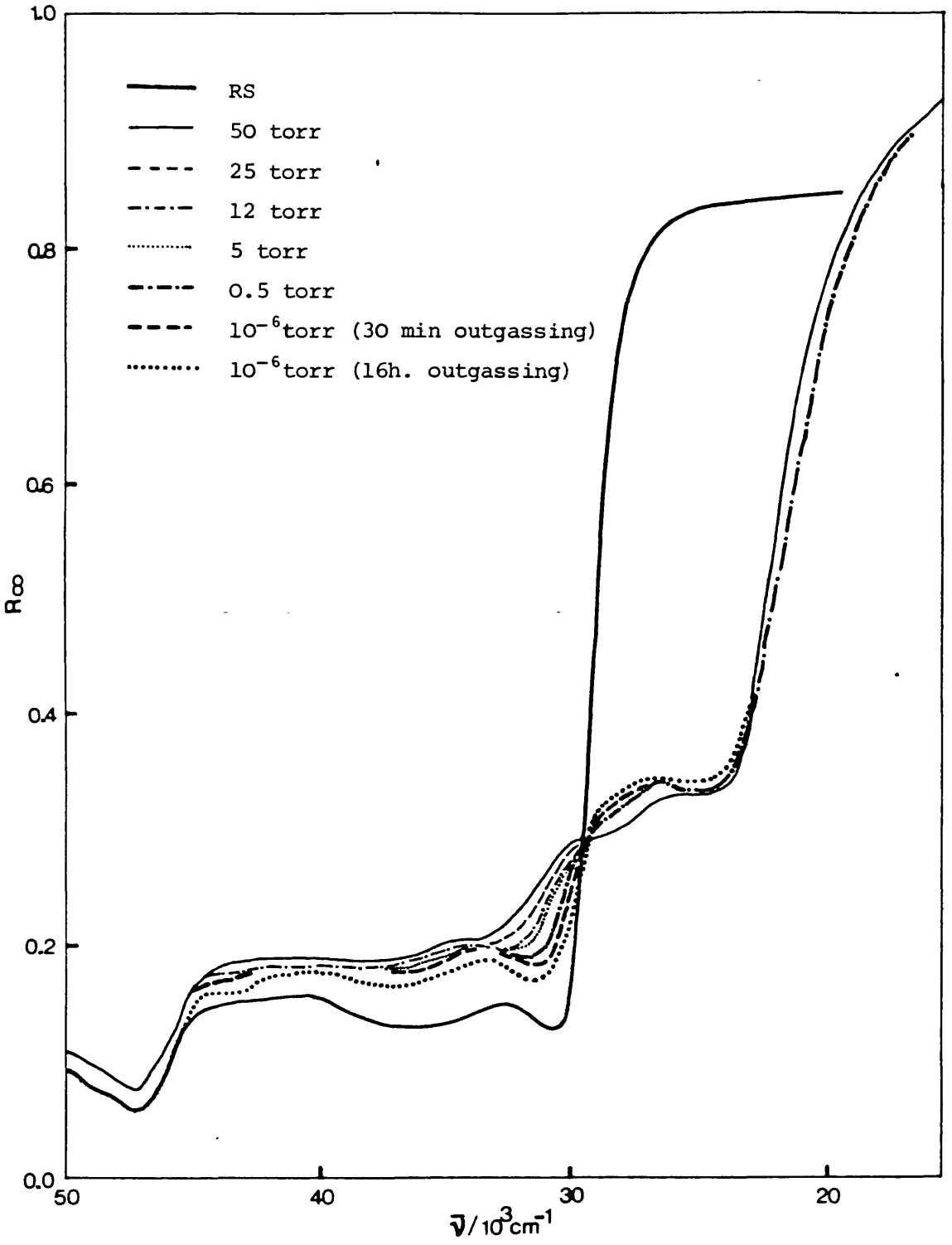

Figure 3.3.18

CO Desorption, OS.40

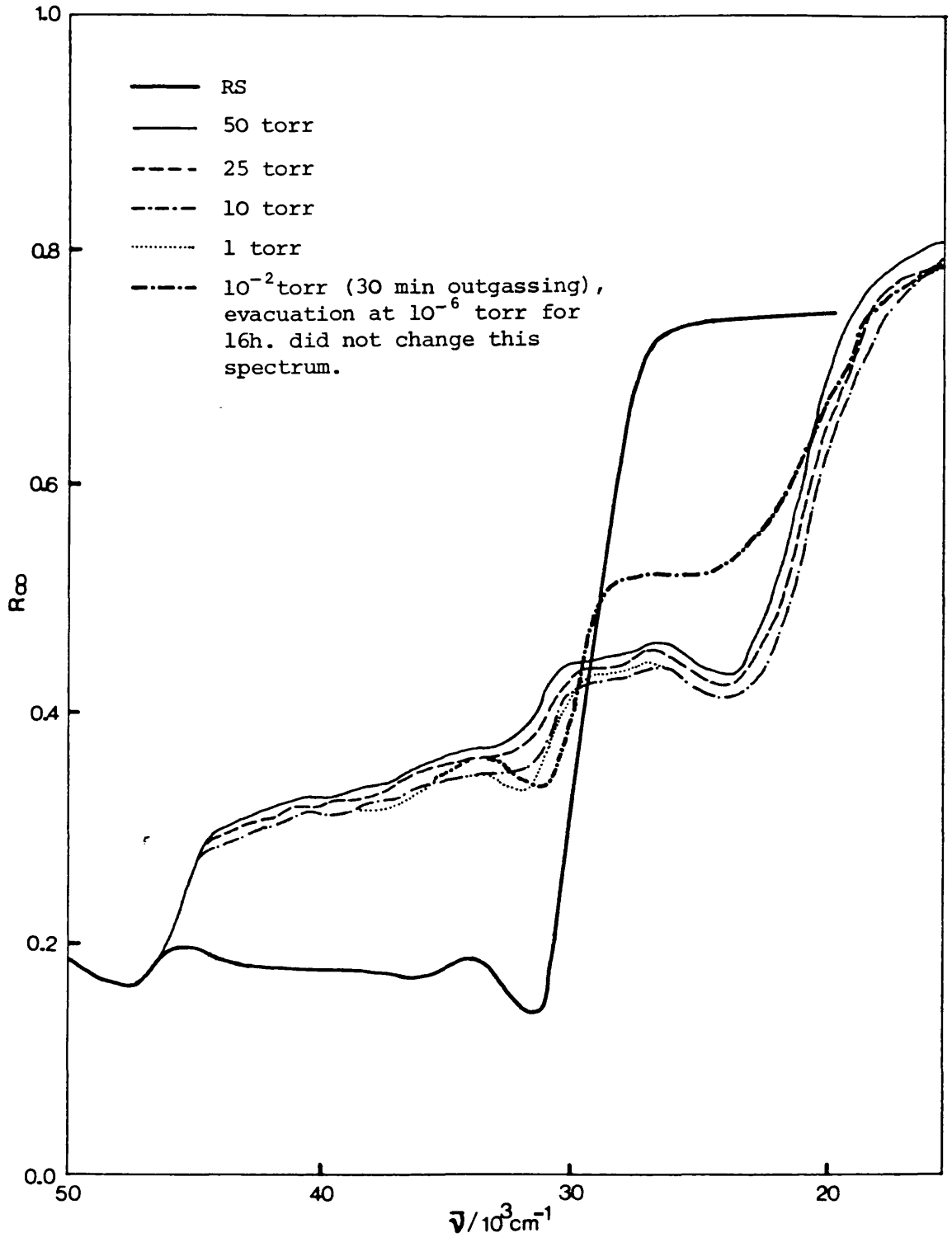

Figure 3.3.19

CO Desorption, OS.10

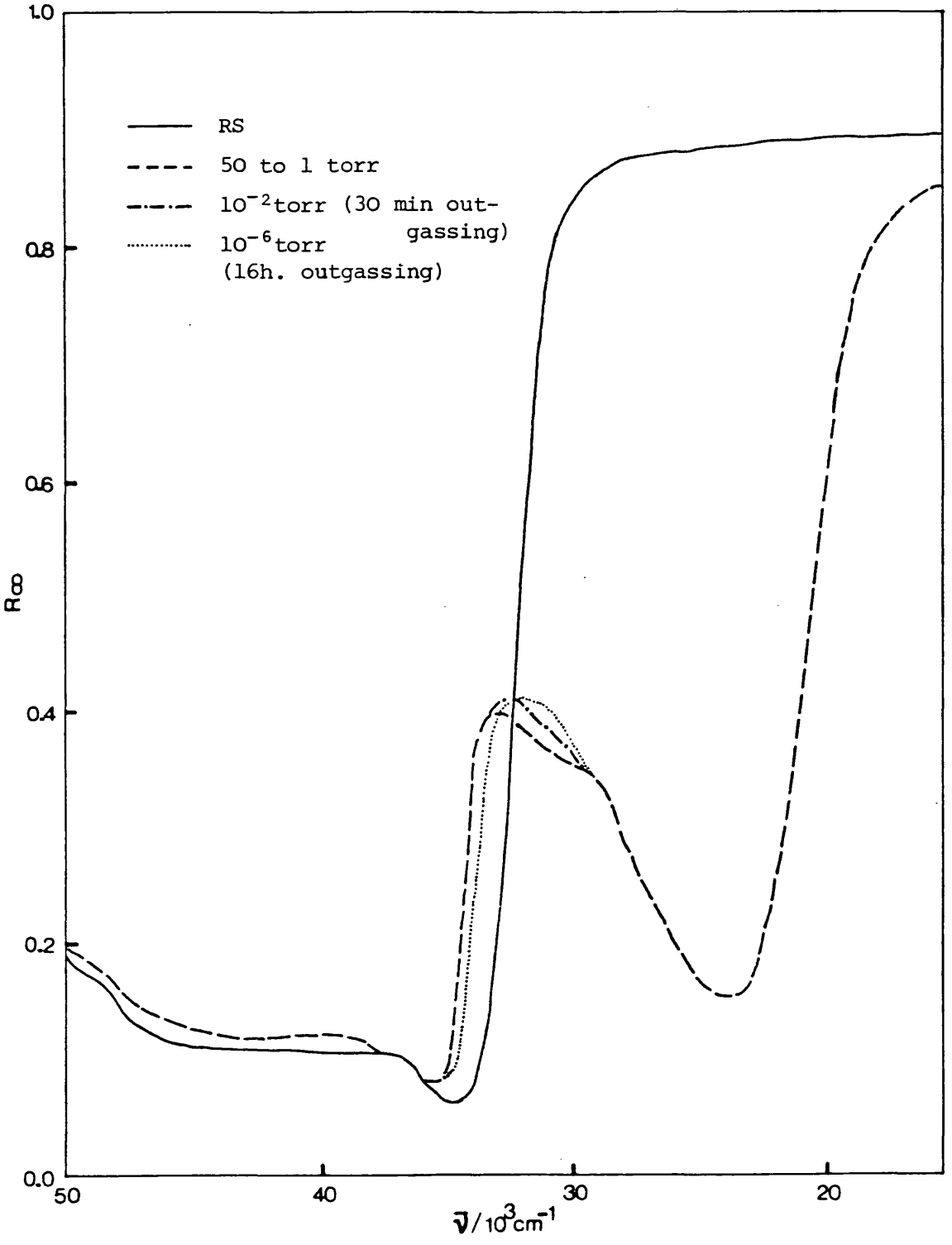

Figure 3.3.20

CO Desorption, OS.O

In CaO the low energy band increases faster with pressure than the corresponding band in SrO, becoming more intense than the high energy band at medium coverage. This time complete overlapping did not occur even at 50 torr, so the high energy band remained as a shoulder on the low energy band at high coverage.

Table 3.3.3 summarizes the positions of the bands. The band positions do not vary monotically with composition of the solid solutions. The position of the low energy band passes through a maximum energy at 60% Sr. The high energy band also shows a maximum energy at 60% Sr as the Sr content is decreased between 100% Sr and 10% Sr, but there is then a sharp rise at 0% Sr content (pure CaO) to give the highest energy in the series.

The behaviour of the bands on evacuation at room temperature is shown in Figures 3.3.16 to 3.3.20. OS.100 has been omitted since the spectrum of chemisorbed CO did not change even after 16 hours outgassing at a pressure of 10^{-6} torr. The general tendency with decreasing pressure is an increase in the intensity of band 1 and a decrease of band 2, whose complete destruction can be achieved under prolonged outgassing.

(c) Adsorption and desorption of 1-butene

Adsorption of 1-butene does not produce as drastic a change as the adsorption of CO; the corresponding spectra are shown in Figures 3.3.21 to 3.3.26.

At low pressure the first effect is to quench the fluorescence so giving a spectrum very similar to that obtained with oxygen. The destruction of the surface excitons requires higher coverage.

At low coverage weak bands are observed; increasing the pressure has the effect of gathering the bands into a single broad

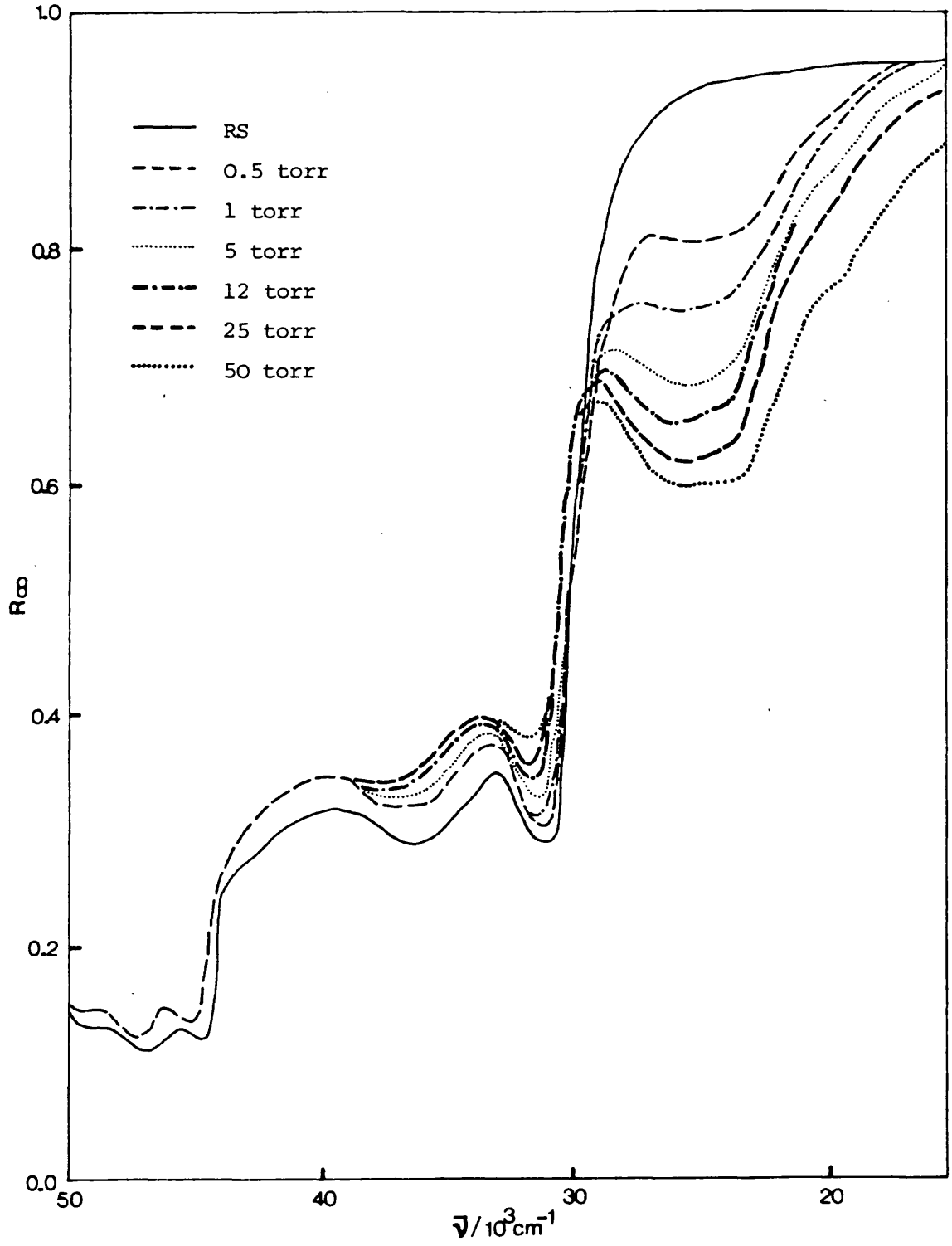

Figure 3.3.21

1-Butene Adsorption on OS.100

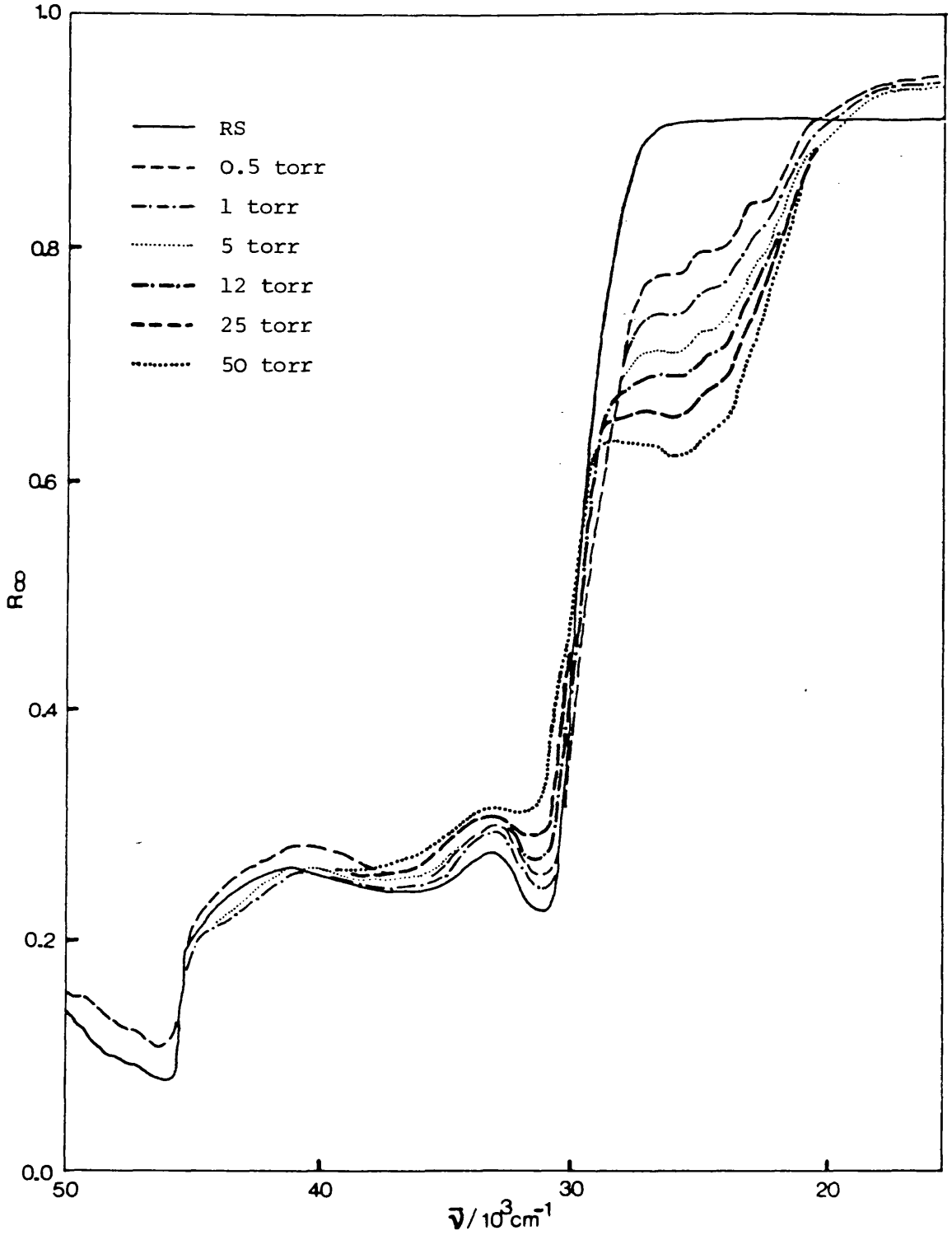

Figure 3.3.22

1-Butene Adsorption on OS.80

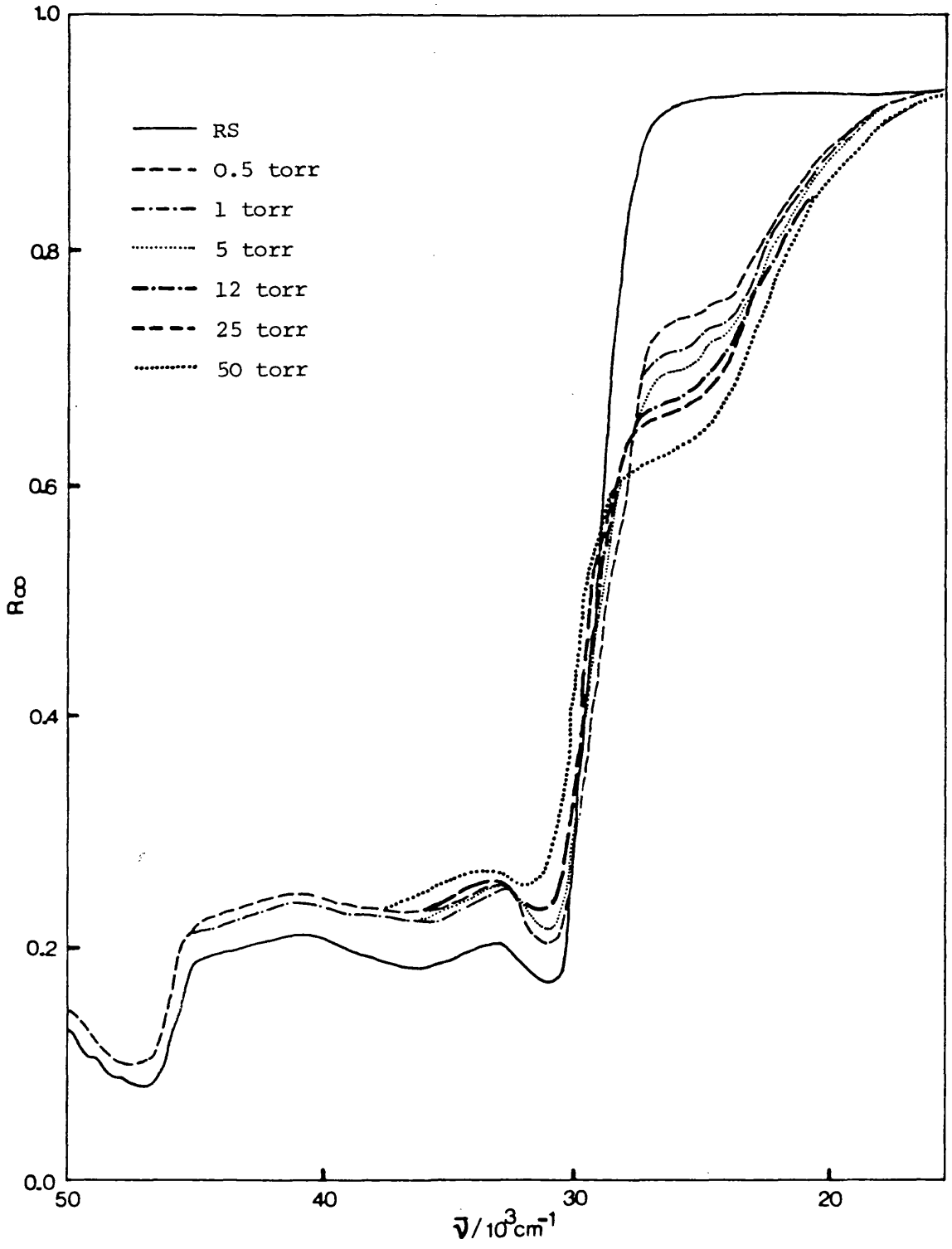

Figure 3.3.23

1-Butene Adsorption on OS.60

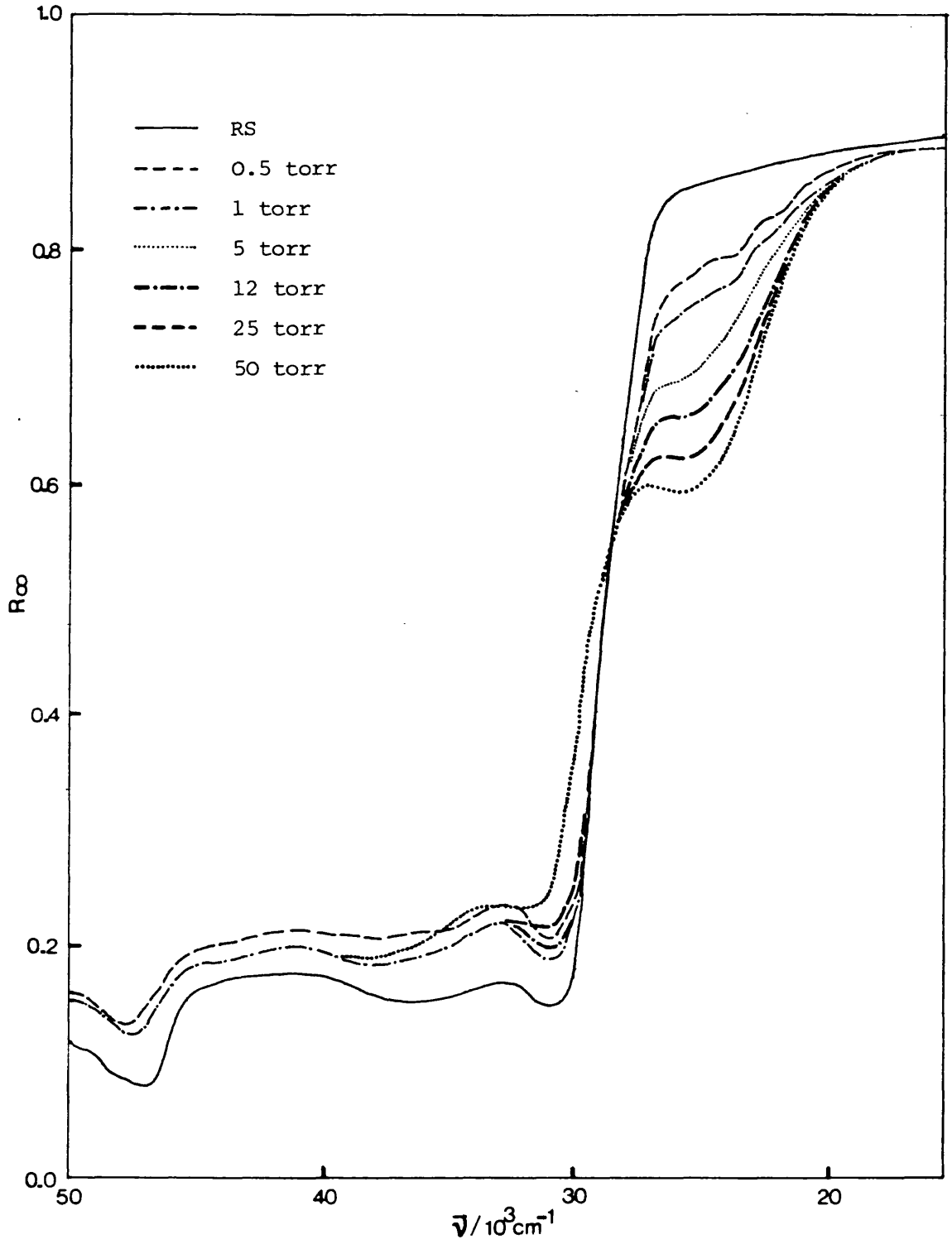

Figure 3.3.24

1-Butene Adsorption on OS.40

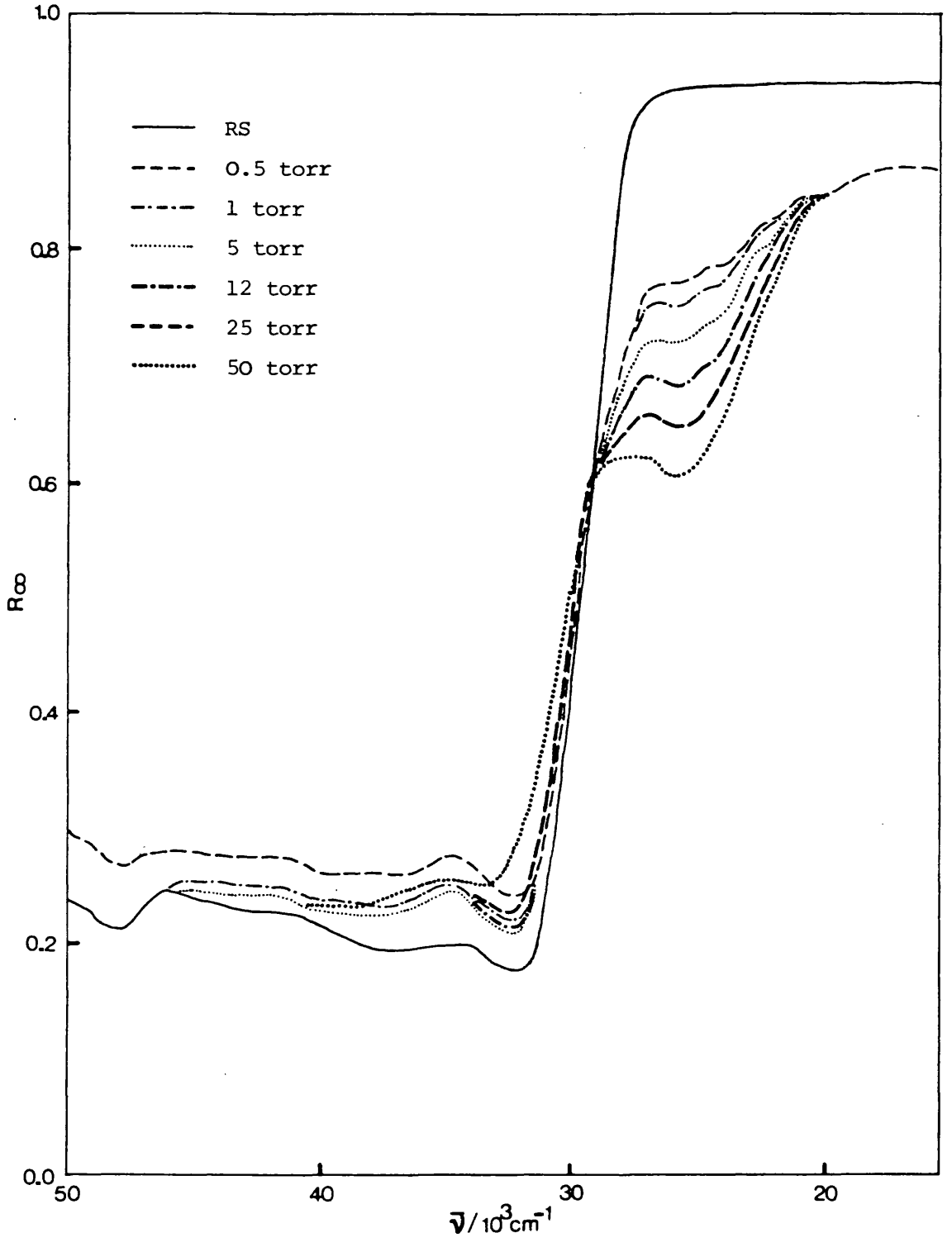

Figure 3.3.25

1-Butene Adsorption on OS.10

Table 3.3.3 Band Positions of Chemisorbed CO/cm^{-1}

Sample	Band 1	Band 2	Band 3
OS.100	24,050	28,950	32,400
OS.80	24,200	29,600	
OS.60	24,500	29,800	
OS.40	24,450	29,300	
OS.10	24,300	29,100	
OS.0	24,200	31,750	

band and then at high coverage a strong band with a shoulder at lower energy develops. This band is stronger and narrower in OS.O (pure CaO) than it is in OS.100 (pure SrO). In the intermediate range (the solid solutions) increasing Sr content broadened the band and shifted its position as reported in Table 3.3.4.

Outgassing at room temperature readily restores the surface exciton spectra; however, after long evacuation a strong absorption below 30,000 cm^{-1} is still present. The recorded spectra are shown in Figures 3.3.27 to 3.3.32.

On OS.100, partial outgassing decreases the intensity of the spectrum but the broad band becomes resolved into three bands positioned at 20,850, 24,000 and 26,650 cm^{-1}. On OS.O at very low pressure the band is shifted to higher energy at approximately 29,000 cm^{-1}. Neither of these effects are observed in the solid solutions but the persistent strong absorption below 30,000 cm^{-1} seems to be composed of weak and small bands which complicate the appearance of the spectra.

Hence, although strong outgassing restores the surface exciton spectra, it is evident that a residue remains on the catalyst (causing the absorption below 30,000 cm^{-1}) which does not interact with the surface sites responsible for the exciton spectra.

(d) CO interaction with preadsorbed 1-butene

CO rapidly destroys the spectra due to chemisorption of 1-butene generating the two bands typical of chemisorbed CO already described. For the range of pressure studied, the behaviour of these two bands is comparable with the behaviour observed when the clean surface of the oxides is exposed solely to CO; however, this time the bands are better defined and clearly separated, and their positions are

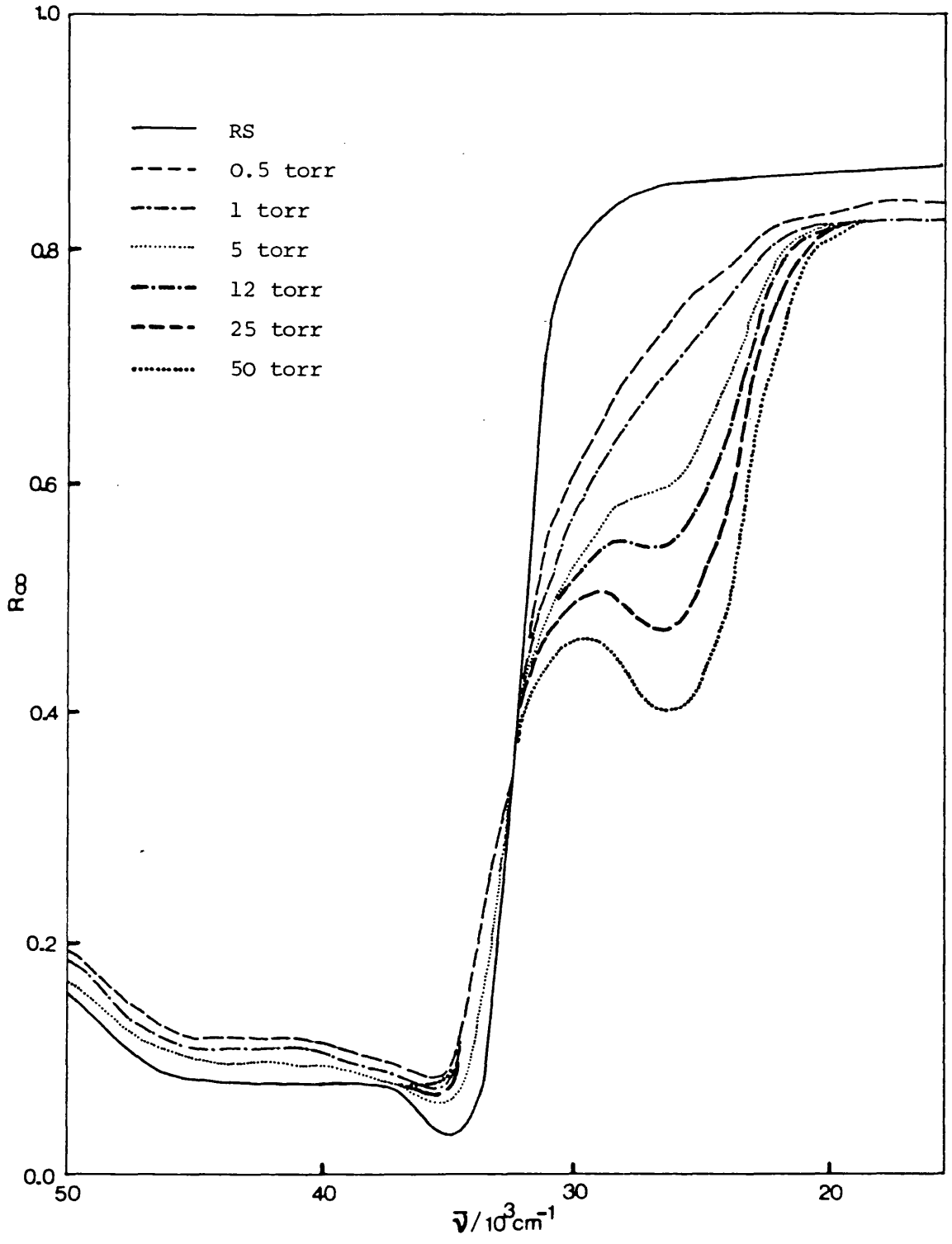

Figure 3.3.26

1-Butene Adsorption on OS.O

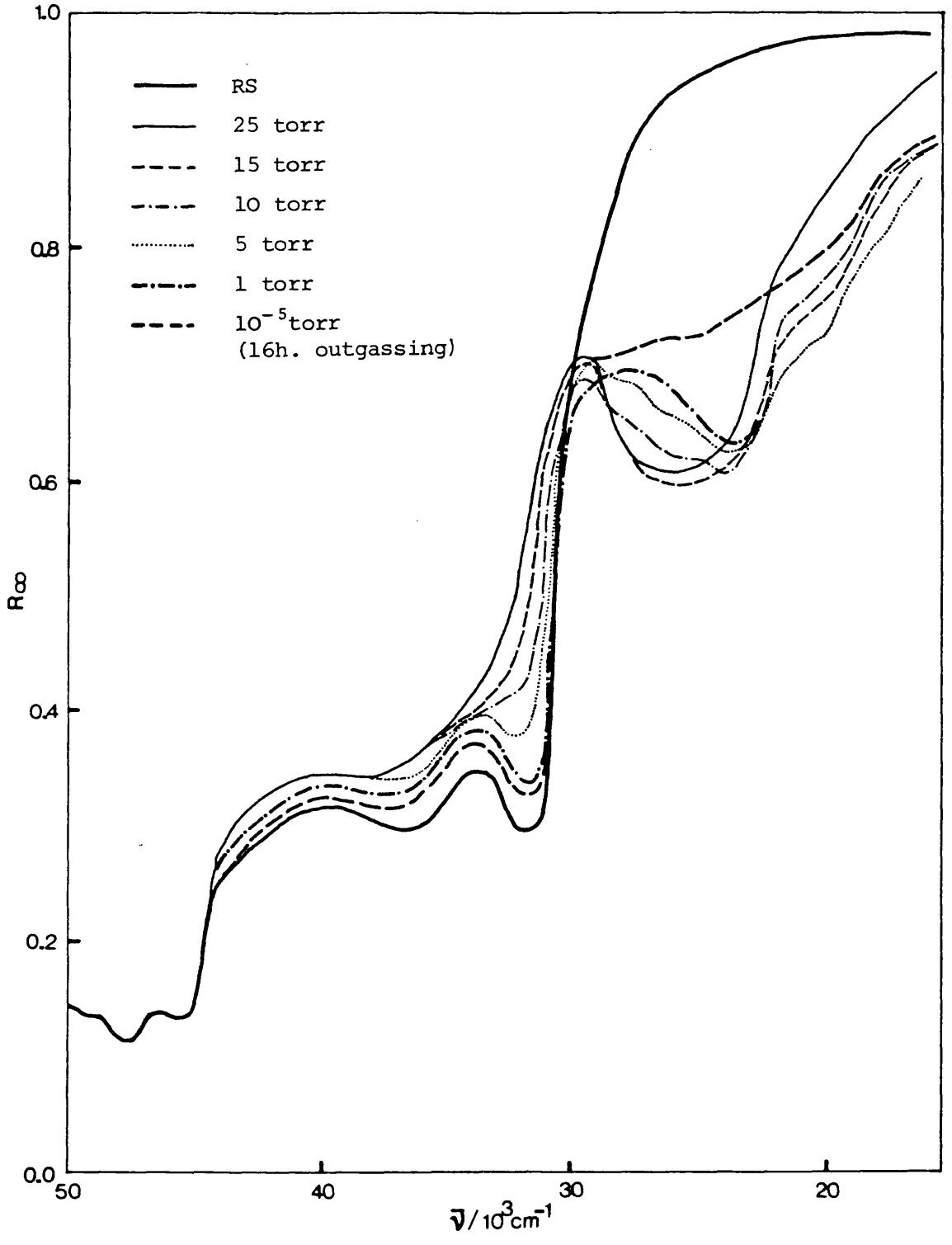

Figure 3.3.27

1-Butene Desorption, OS.100

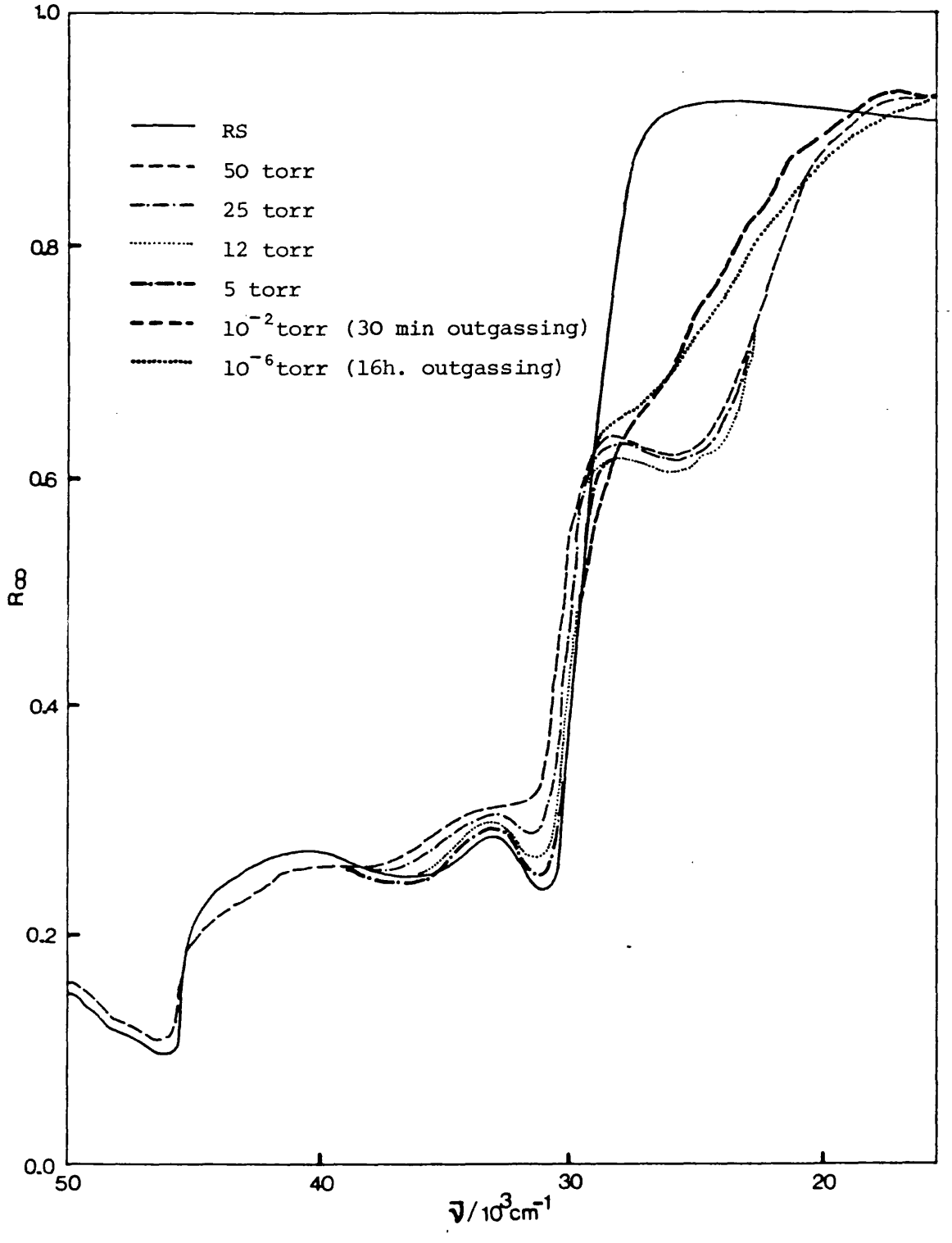

Figure 3.3.28

1-Butene Desorption, OS.80

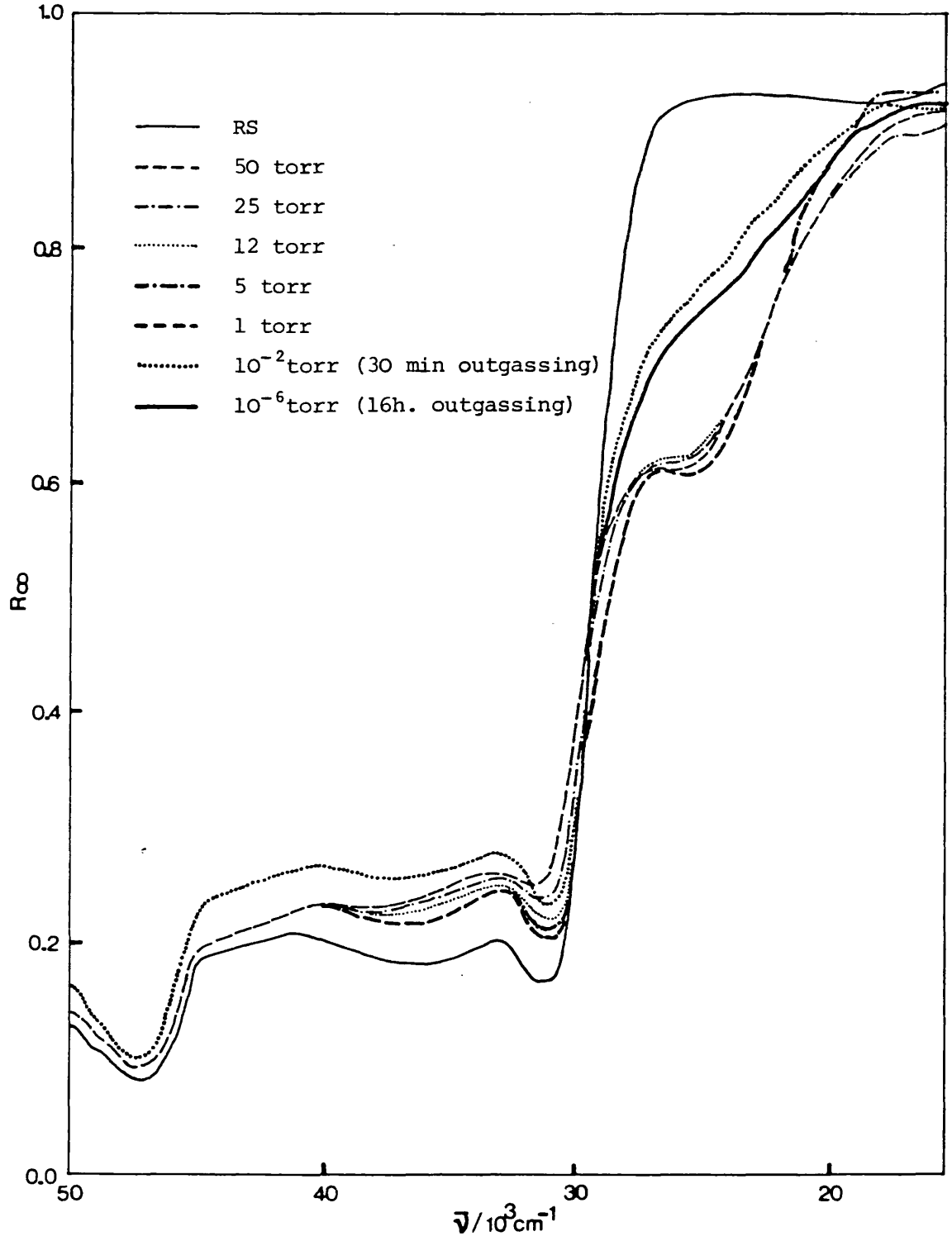

Figure 3.3.29

1-Butene Desorption, OS.60

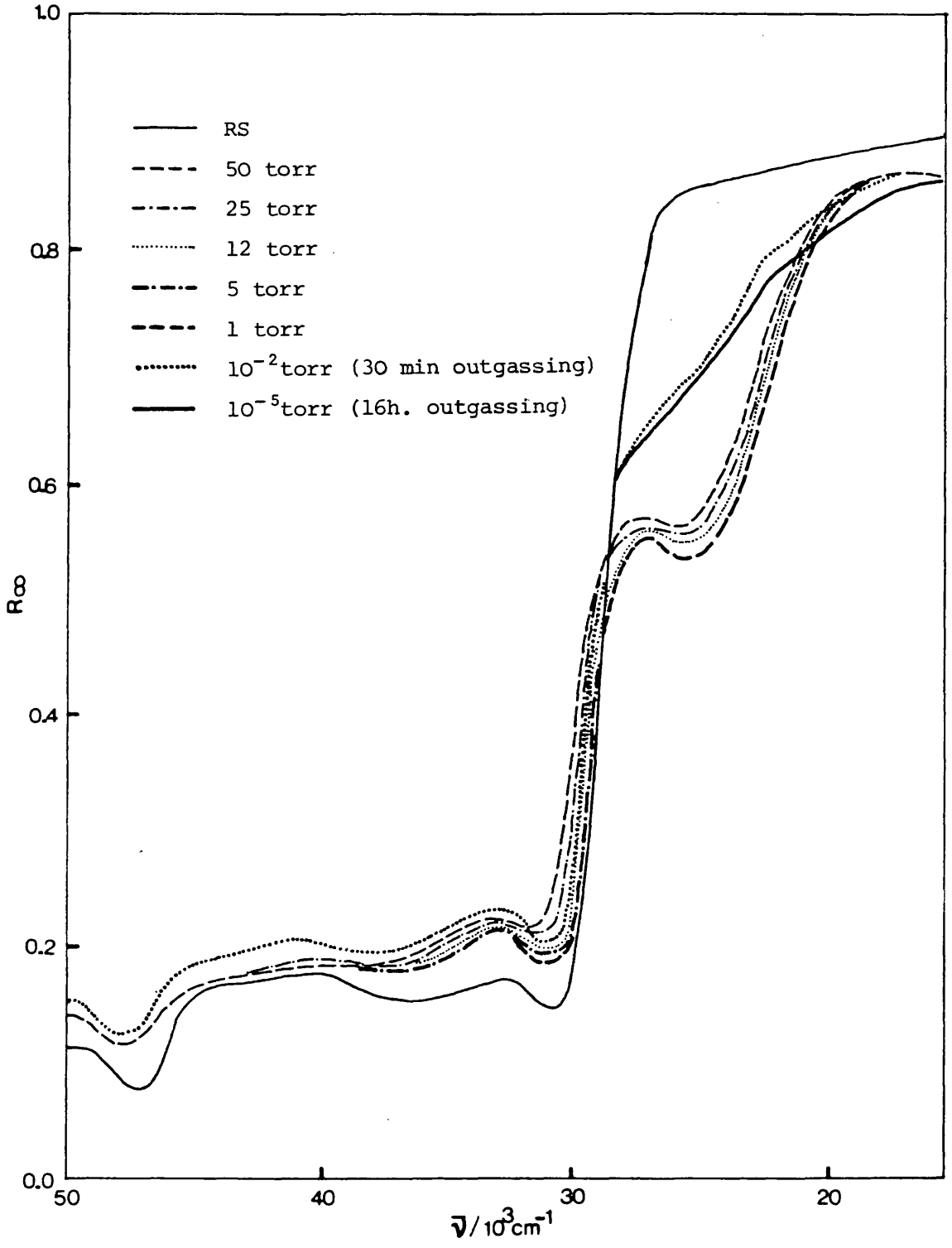

Figure 3.3.30

1-Butene Desorption, OS.40

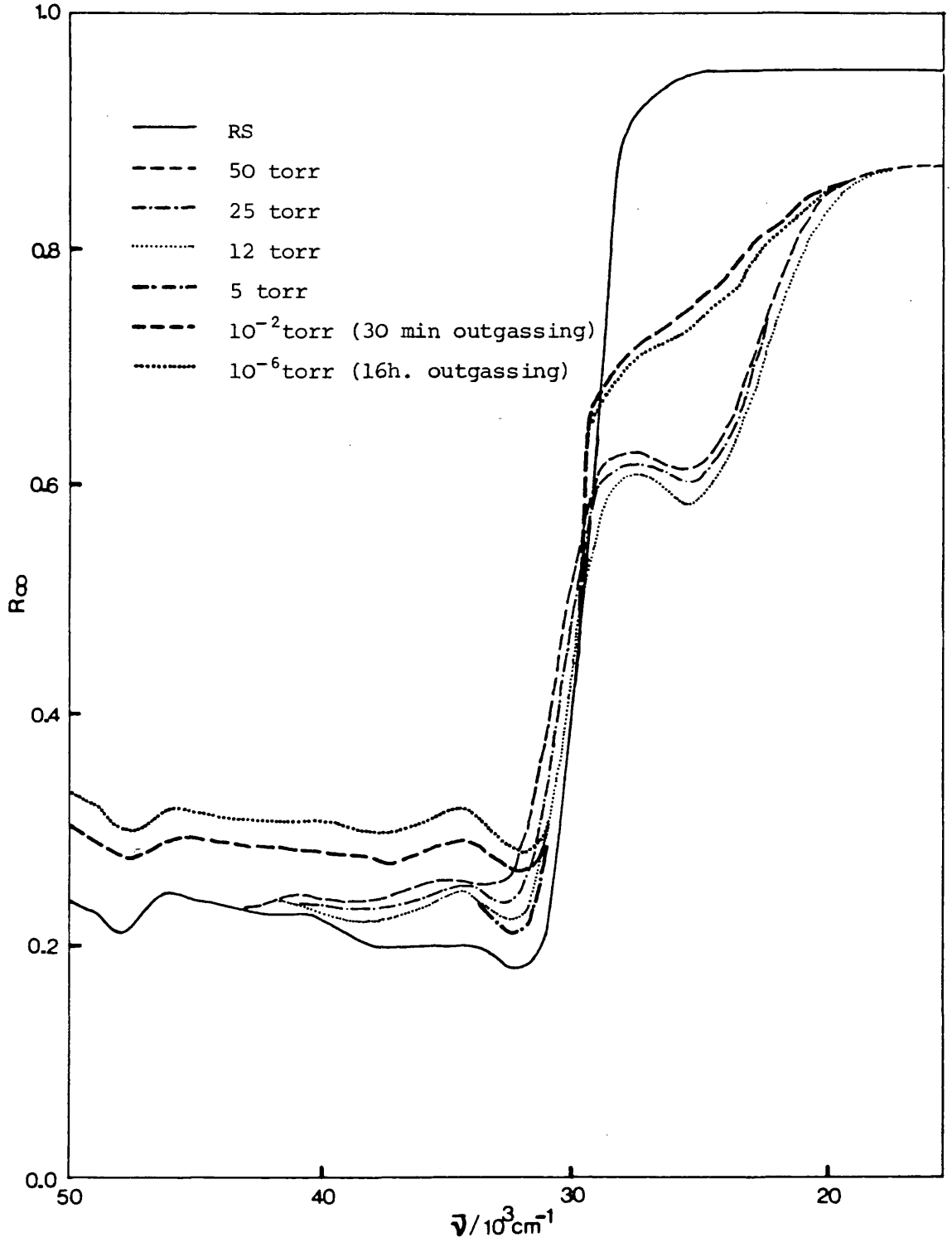

Figure 3.3.31

1-Butene Desorption, OS.10

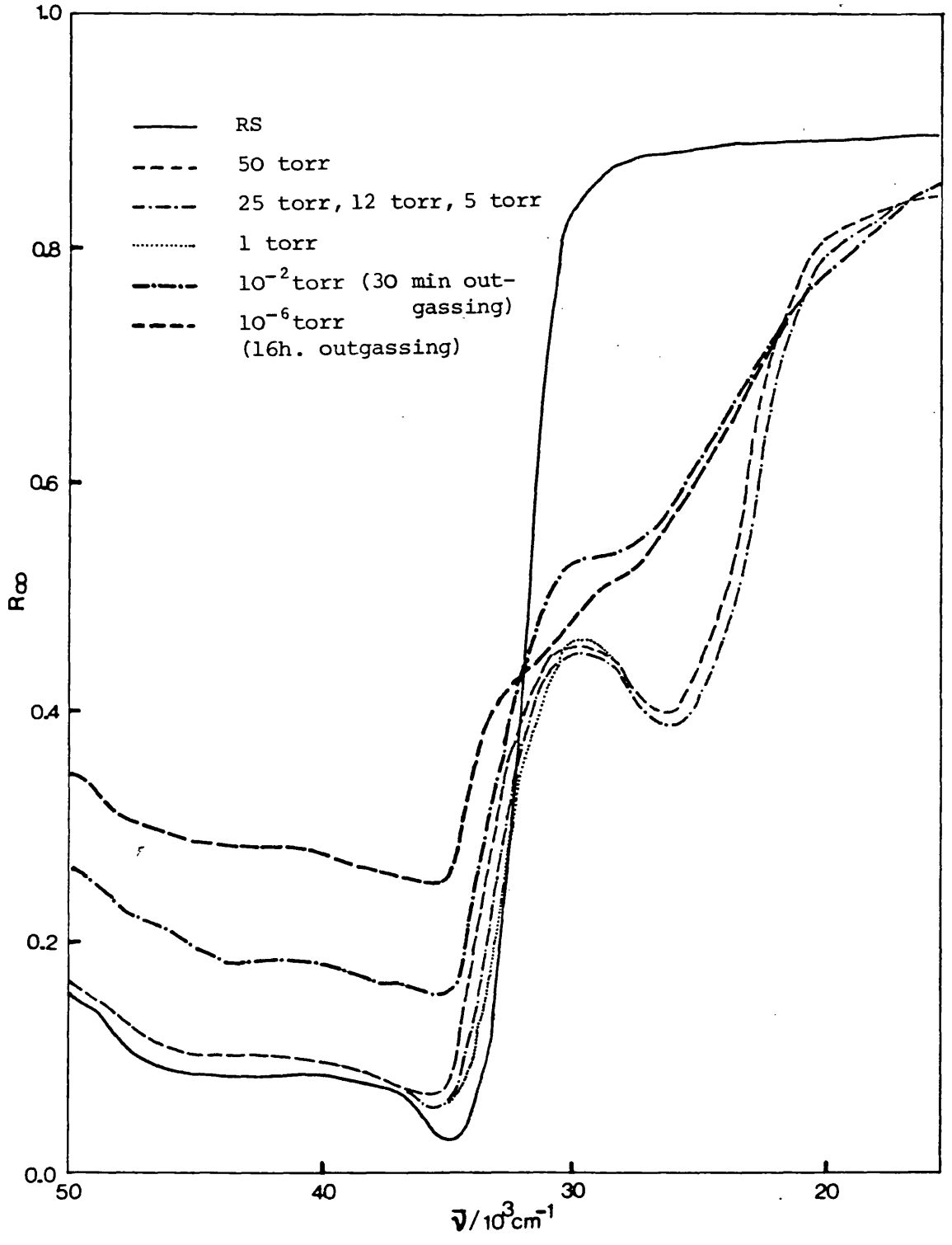

Figure 3.3.32

1-Butene Desorption, OS.O

Table 3.3.4 Band Position of Chemisorbed 1-Butene/cm^{-1}

Sample	High Coverage		Low Coverage		
OS.100	19,650	24,900	20,800	24,350	26,000
OS.80	24,100	26,250	22,170	24,170	26,500
OS.60	22,170	25,600		24,600	26,000
OS.40	22,800	26,000	21,850	23,900	26,170
OS.10	22,000	26,300	22,500	24,300	26,400
OS.0	22,400	26,500		24,300	26,850

summarized in Table 3.3.5.

It is manifest that the effect of Sr is to shift the low energy band towards higher energy. On OS.O it remains at the same position but the shift increases with increasing Sr concentration, showing a shift of approximately 2,000 cm^{-1} on OS.100, but it is important to mention at this point that this band is observed only with the first dose of CO, becoming rather quickly overlapped by the high energy band, and also there is no third band observed at high coverage. No shift occurs for the high energy band, and within the limits of the experimental error this band is at the same position as on pure CO chemisorbed spectra.

The recorded spectra are shown in Figures 3.3.33 to 3.3.38. For CaO, comparison of Figures 3.3.15 and 3.3.38 reveals that the CO spectrum in the presence of adsorbed 1-butene is less intense than in the absence of butene. It can be inferred that the effect of increasing Ca concentration is to decrease the intensity of the spectra yet this effect is less noticeable than the shift caused by Sr on the low energy band.

Further weak bands can also be observed below the region 22,000 cm^{-1}, the number of bands varying with the solid surface exposed and with coverage. However, the bands are so weak that it has been difficult to assign an accurate position for them.

(e) 1-Butene interaction with preadsorbed CO

1-Butene has little effect on the spectra of chemisorbed CO, the main observation being a decrease in the intensity, but keeping the features of the CO spectra.

Under the conditions of the experiment (outgassing to remove gas-phase CO) the high energy band of chemisorbed CO was already

Table 3.3.5 Band positions for CO interaction with preadsorbed 1-butene/cm^{-1}

Sample	Band 1	Band 2
OS.100	26,000	28,700
OS.80	25,000	29,200
OS.60	24,850	29,500
OS.40	24,600	29,350
OS.10	24,350	29,000
OS.0	24,200	31,170

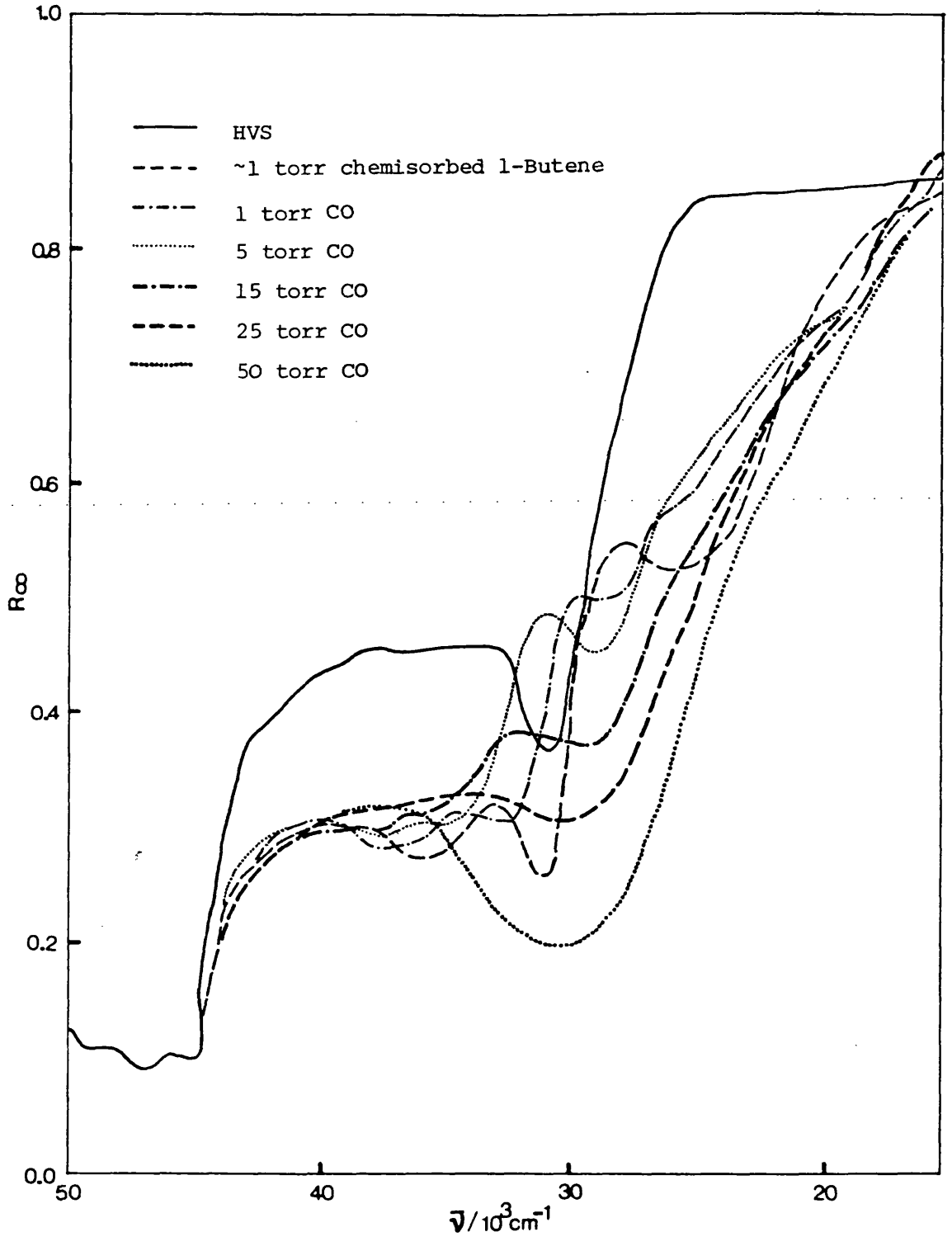

Figure 3.3.33

Effect of CO on chemisorbed 1-Butene on OS.100

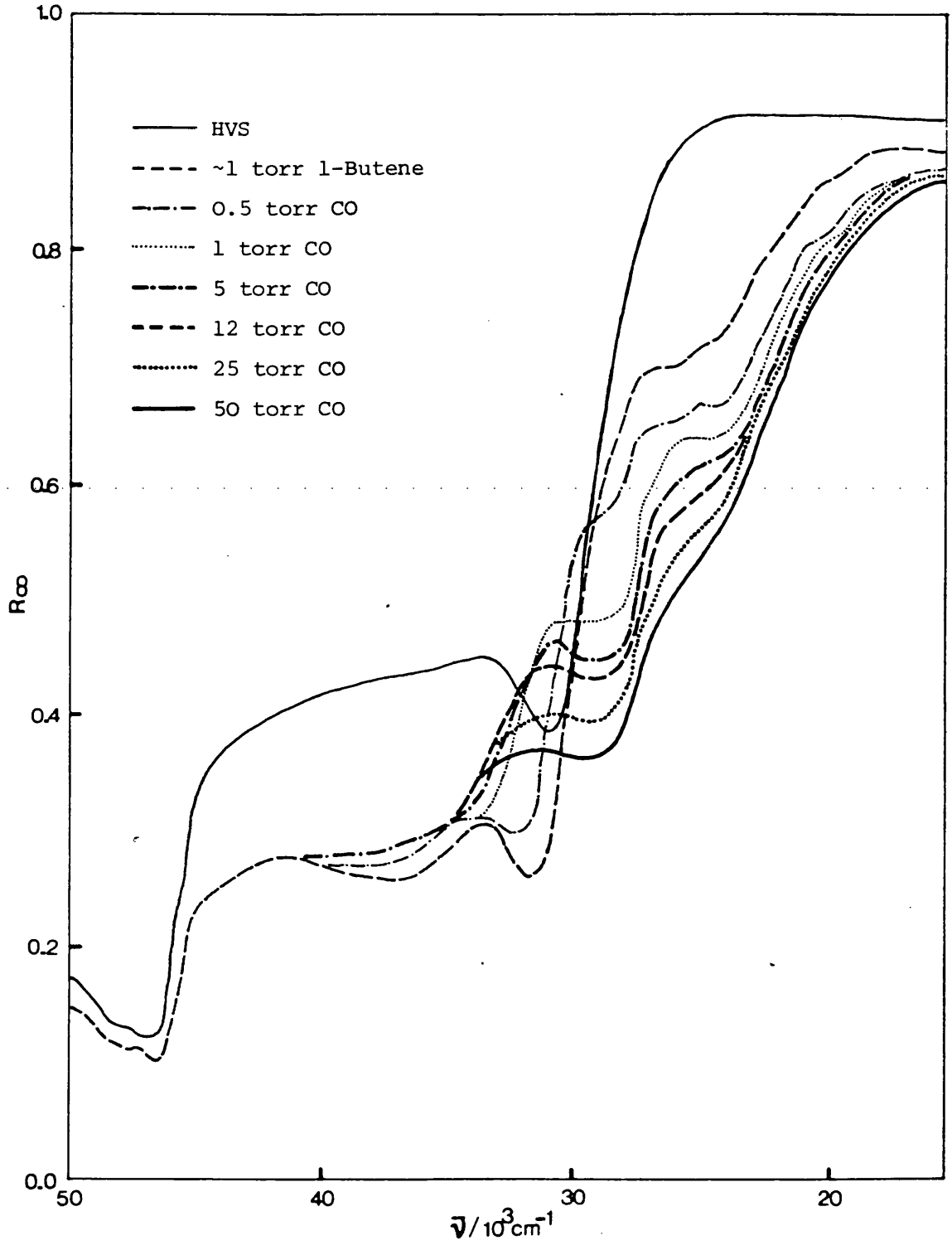

Figure 3.3.34

Effect of CO on chemisorbed 1-Butene on OS.80

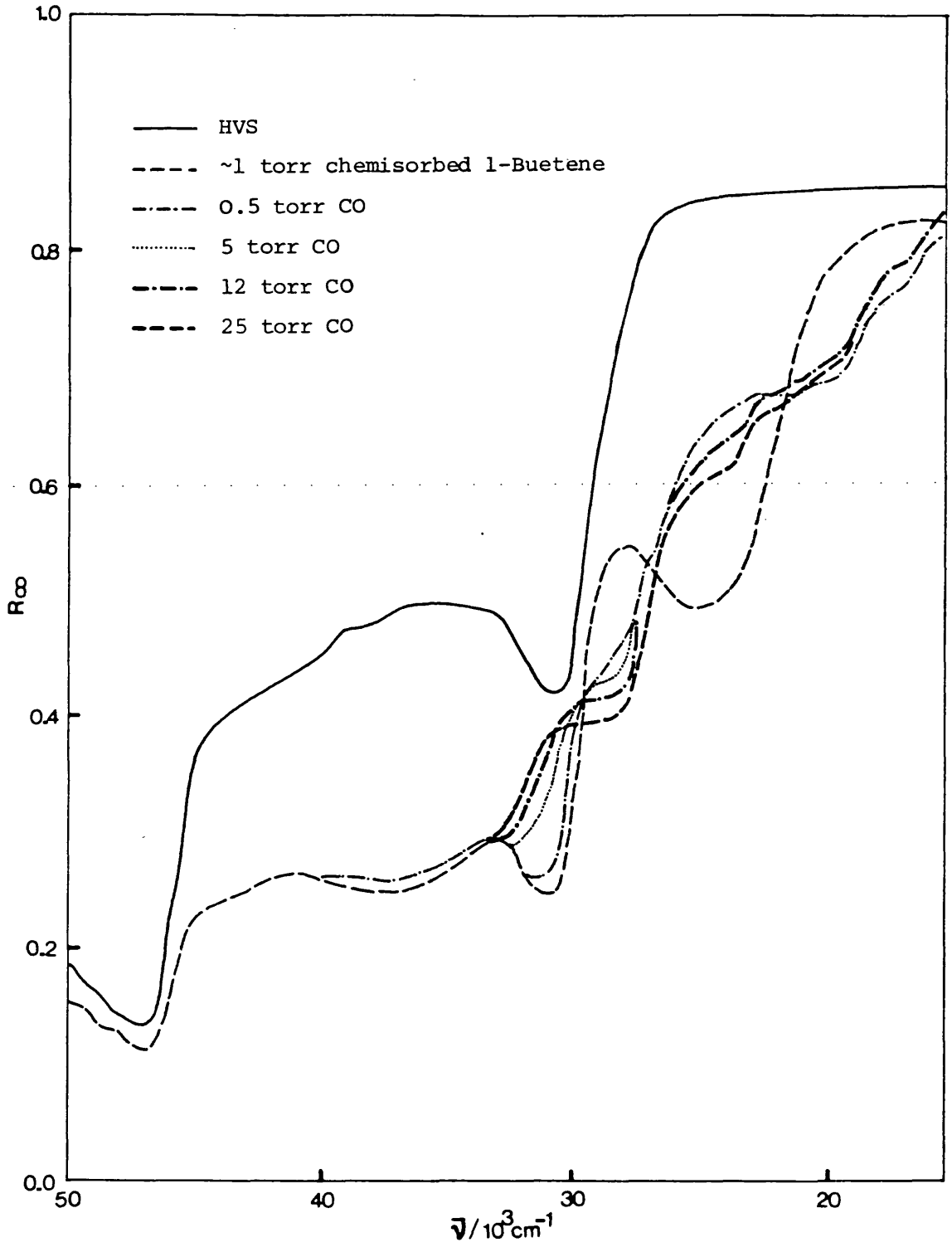

Figure 3.3.35

Effect of CO on chemisorbed 1-Butene on OS.60

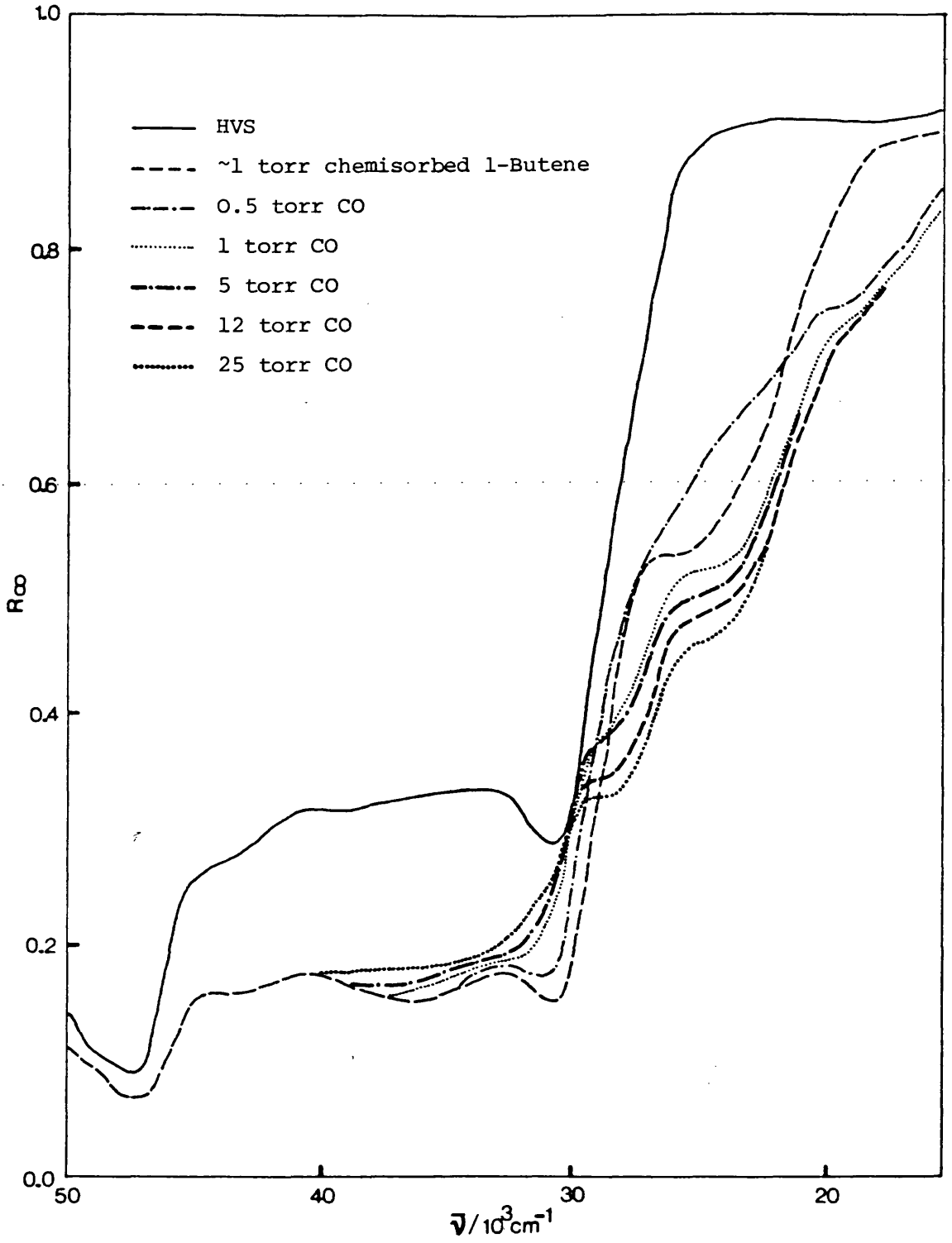

Figure 3.3.36

Effect of CO on chemisorbed 1-Butene on OS.40

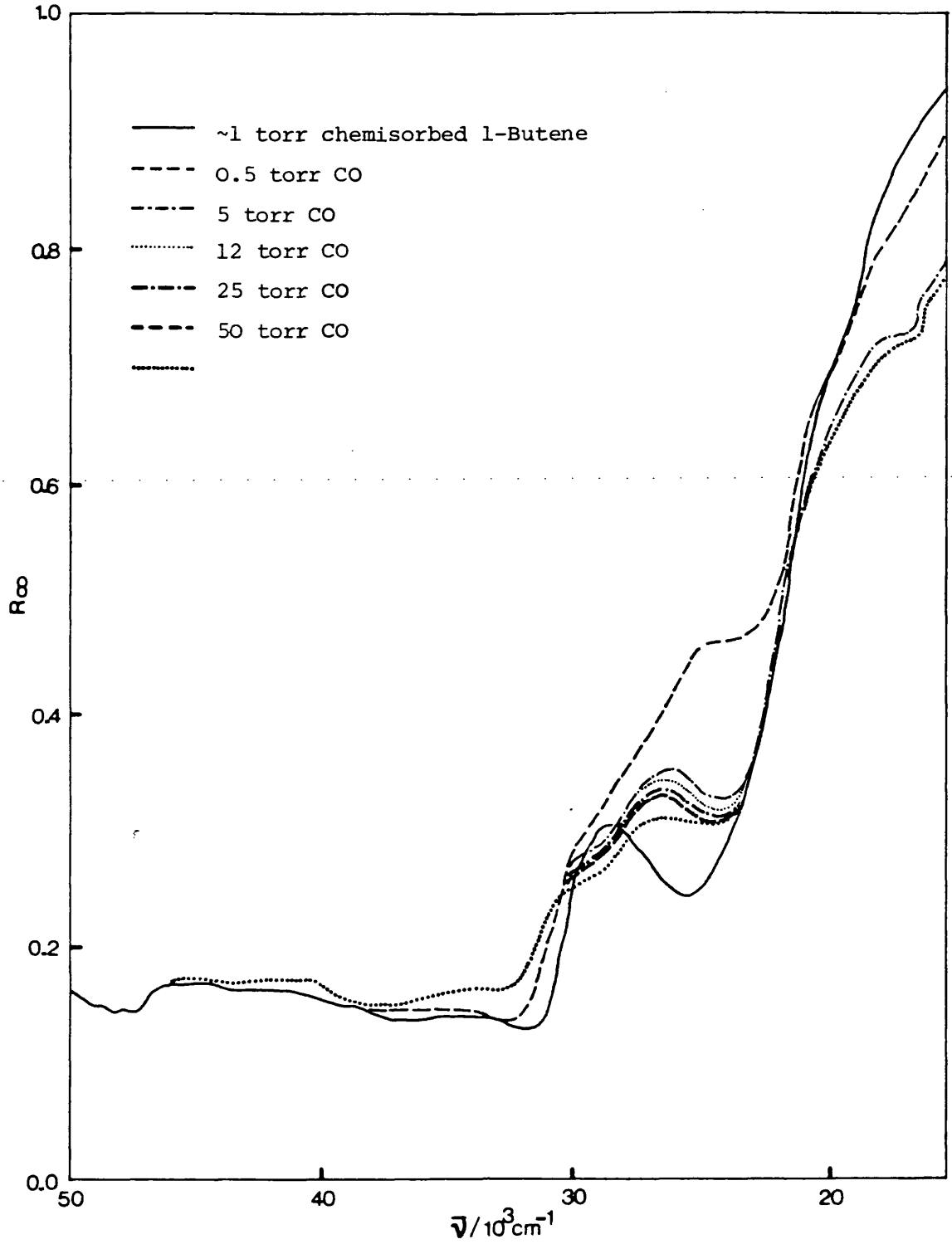

Figure 3.3.37

Effect of CO on chemisorbed 1-Butene on OS.10

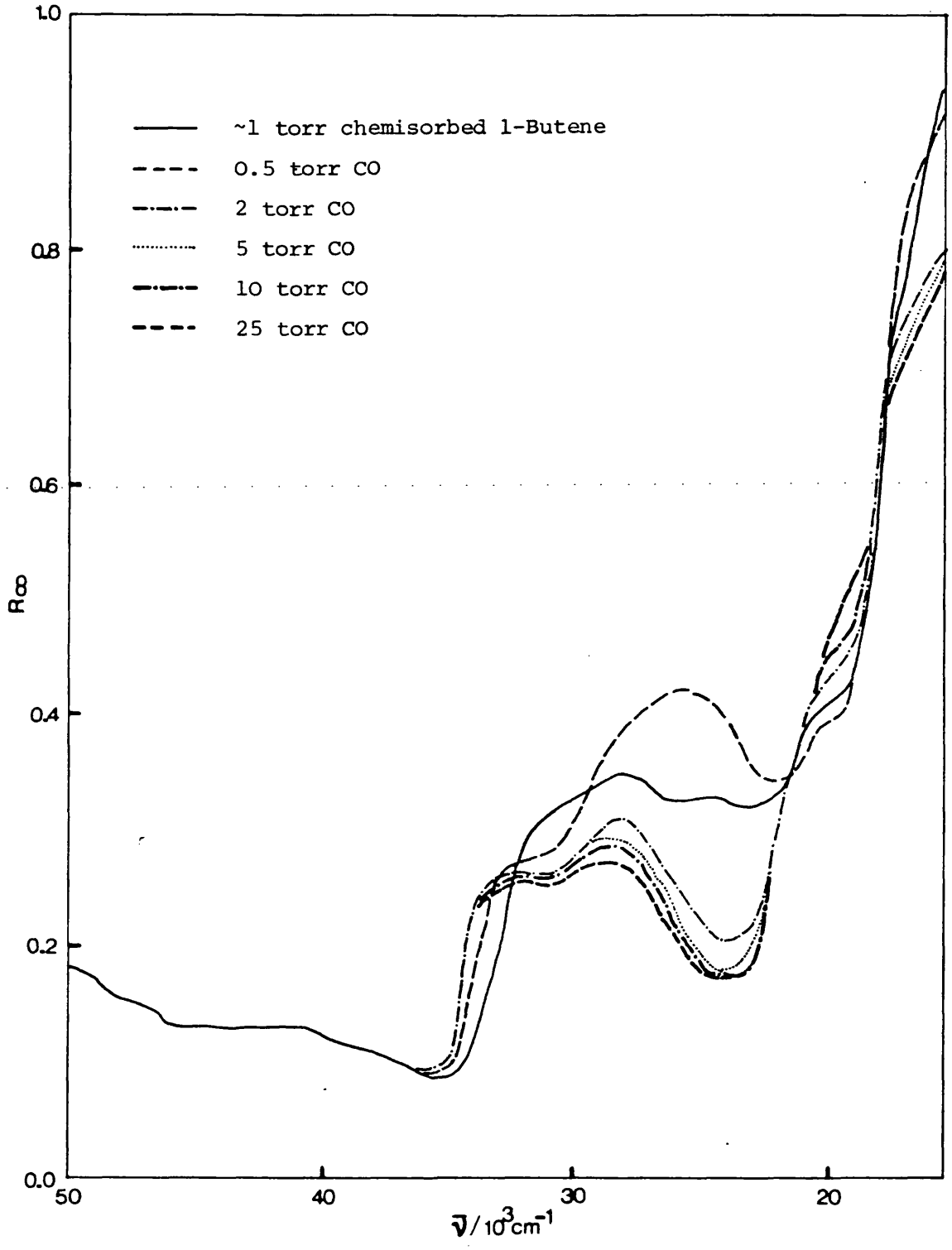

Figure 3.3.38

Effect of CO on chemisorbed 1-Butene on OS.O

diminished when the 1-butene was admitted into the system. Thus it is impossible to determine any effect on this band which in turn being more susceptible to changes in pressure may be also more sensitive to interaction with other gases.

Since there was no other remarkable consequence during the interaction of 1-butene with preadsorbed CO than the decrease in intensity, the corresponding spectra are not shown.

3.4 E.S.R. Studies

3.4.1 The E.S.R. Spectrometer and the E.S.R. Cell

Spectra were recorded with a Varian E-3 spectrometer using X-band microwave radiation provided from a klystron tube. The magnetic field was controlled by a Varian field dial unit connected to a Hall effect magnetic sensor. A small 100 kHz modulating field provided the output signal from which resonance was observed as the first derivative of the absorption curve. A block diagram of the spectrometer is shown in Figure 3.4.1.

The ESR cell (Fig. 3.4.2) consists of two silica arms and a greaseless vacuum tap for the connection to the appropriate frame. The wide arm contains a platinum bucket for sample preparation. The side arm for containing the sample during the recording of the ESR spectra had a diameter of 2 mm and was made of 'Spectrosil'.

3.4.2 Experimental Determination of g-Values and Linewidth

The g-value of Varian Strong Pitch (VSP) was determined by calibration against the free radical diphenyl-picryl-hydrazyl (DPPH). The spectra of freshly made solutions of DPPH in benzene at different concentrations (0.05, 0.01, 0.001 and 0.0001 M) were compared with the spectra of VSP recorded under the same conditions. From the

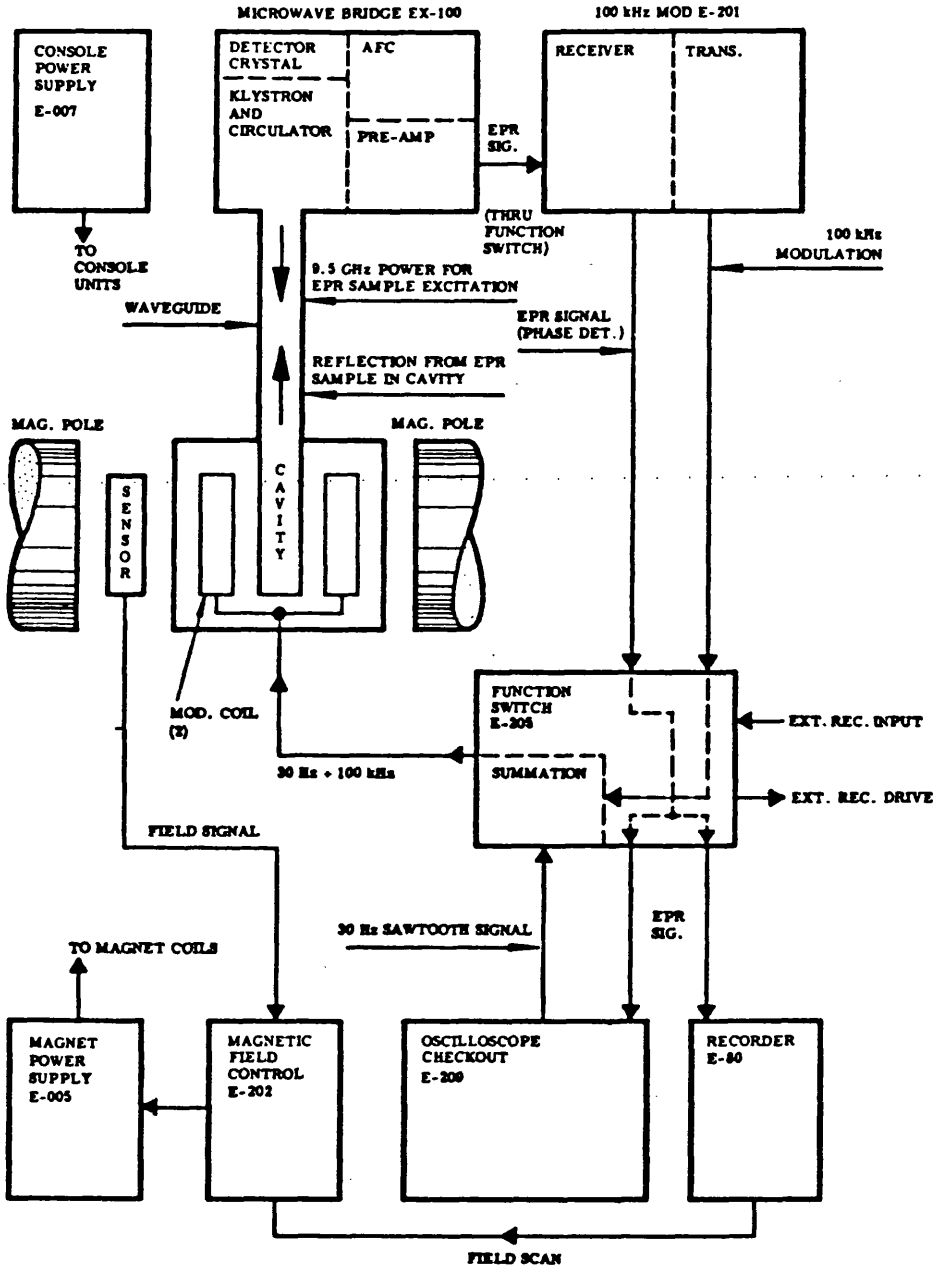

Figure 3.4.1

Block Diagram of Varian E-3

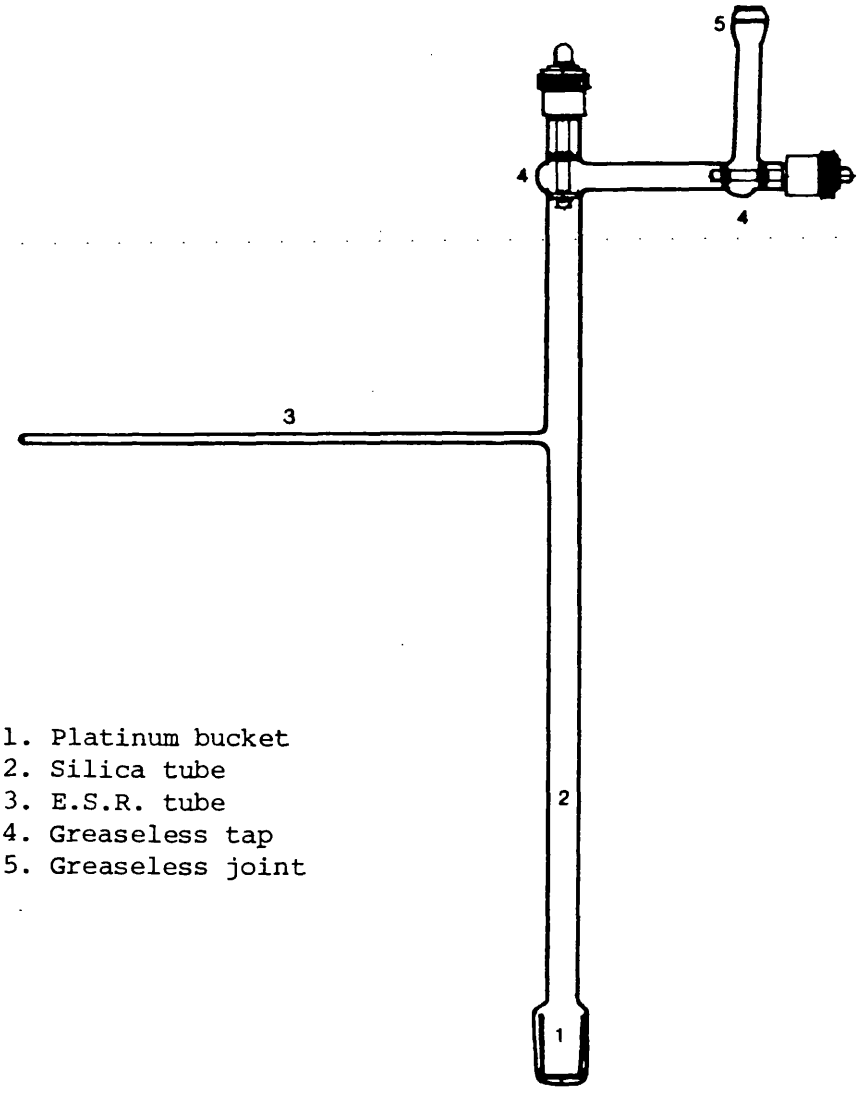

1. Platinum bucket
2. Silica tube
3. E.S.R. tube
4. Greaseless tap
5. Greaseless joint

Figure 3.4.2

E.S.R. Cell

known g-value of DPPH (161, 162), g_{ref}, the g-value of VSP, g_{std}, was evaluated as :

$$g_{std} = g_{ref}\left(1 - \frac{(H_{ref} - H_{std})}{H_{std}}\right) \qquad 3.4.1$$

The g-value of the sample, $g_{unknown}$, was then found by calibration against VSP using the corresponding equation :

$$g_{unknown} = g_{std}\left(1 - \frac{H_{std} - H_{unknown}}{H_{unknown}}\right) \qquad 3.4.2$$

The linewidth was measured as the peak to peak difference of the resonance line in gauss.

3.4.3 Adsorption Studies

A. Nitrobenzene

Nitrobenzene (NB) adsorption was carried out in a separate frame to avoid contamination of the preparation frame. NB was admitted to the adsorption frame using a pyrex bulb containing the 'Specpure' liquid clasped to the frame. The liquid was then subjected to freeze-thaw cycles to remove the dissolved air.

A freshly prepared sample was used for each experiment. Six samples covering the range 0 - 100% Sr content at 20% intervals were studied. These are designated OS.0, OS.20, OS.40, OS.60, OS.80 and OS.100, respectively, where the number represents mole % Sr. A vacuum spectrum was recorded for each sample prior to adsorption. Then the powder was transferred back into the wide arm and placed on the adsorption frame. This was necessary because of the gradual light to dark colour change which occurred when the sample was kept in the narrow side arm during exposure to NB. The vapour was allowed

to contact the powder sample at room temperature for 1 to 2 hours. The excess gas phase was removed by evacuation at room temperature for 2 hours. The sample was transferred again to the side arm for the recording of the corresponding spectra. All the spectra were recorded at room temperature.

B. Oxygen

Adsorption of oxygen was carried out on OS.0, OS.10, OS.50, OS.70, OS.90 and OS.100, where the number again represents mole % Sr. A freshly prepared sample was contacted with 10 torr O_2 at 298 K for 1 hour. Excess oxygen was pumped out for 5 minutes at 298 K; in some cases, which will be specified later, the gas phase was not removed. The sample was then transferred to the sidearm and the ESR tube was sealed off while still under vacuum. ESR spectra were recorded immediately at 298 K and about 1 month later at 77 K and 298 K. These last spectra were recorded on a Varian V-4502 spectrometer at X-band with 100 kHz field modulation. The author is indebted to Dr. A.J. Tench for allowing her the use of the V-4502 spectrometer at A.E.R.E., Harwell.

3.4.4 Results

The g-value of VSP was determined as explained in Section 3.4.2 using several spectra, a typical one being shown in Figure 3.4.3. A value of g_{std} = 2.0019 was found. These spectra were also used for evaluating the errors involved in the double integration method and in the determination of number of spins when using a single cavity spectrometer such as the Varian E-3. Double integration was performed by Wyard's method as described in Section 2.4.4. The maximum error was not greater than 5%. The error introduced by the fact that having a single cavity instrument the sample spectrum and

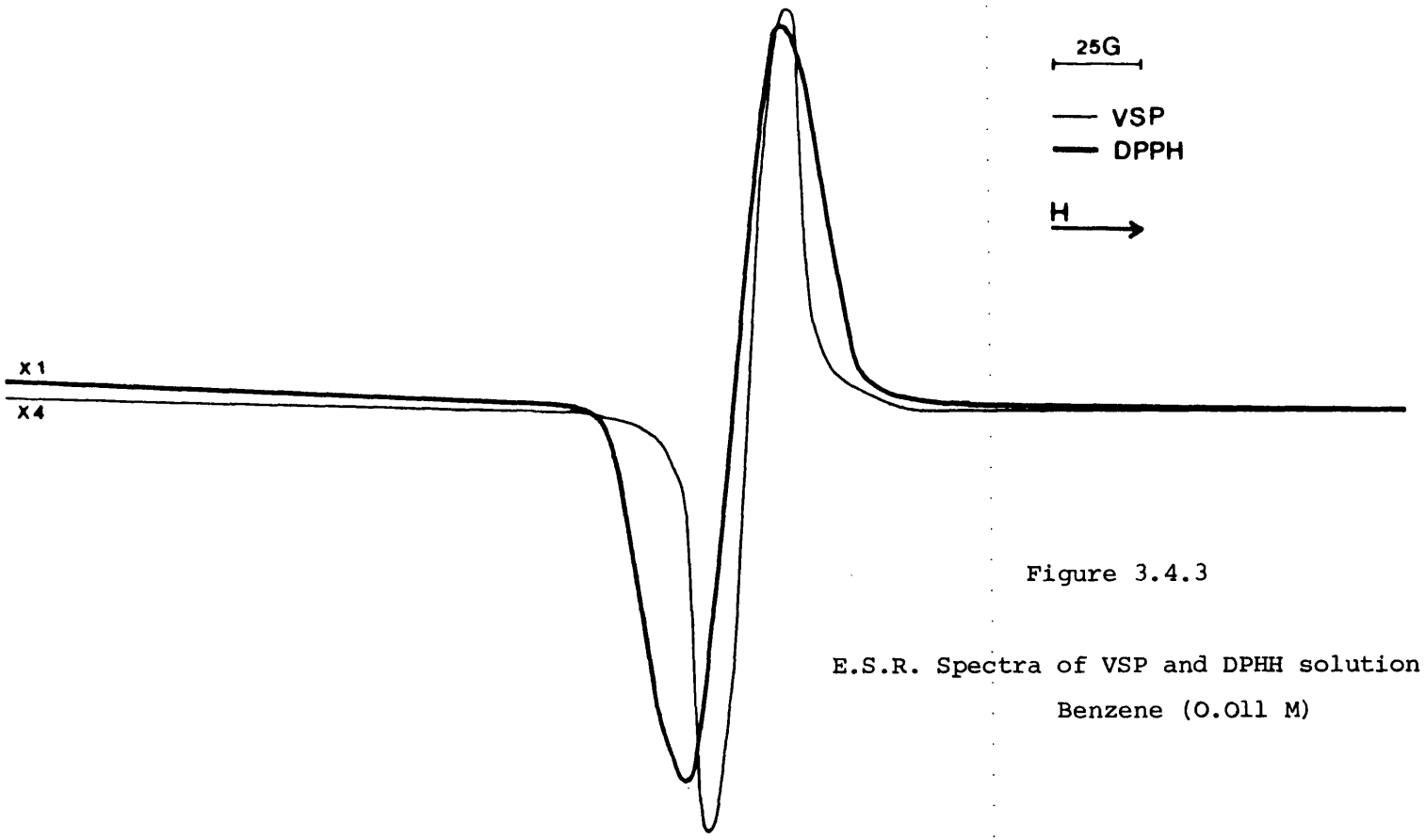

Figure 3.4.3

E.S.R. Spectra of VSP and DPHH solution in Benzene (O.Oll M)

the standard spectrum have to be recorded at different times was evaluated by checking the reproducibility for determination of the number of spins for DPPH solutions in benzene. The concentrations of the solutions were checked by UV-Vis spectrophotometry. Each spectrum was recorded several times, testing the effect of replacing the ESR tube in the spectrometer cavity and the different set-up of the spectrometric parameters. This error was not larger than 15%.

The vacuum spectrum of the CaO-SrO solid solutions and of the pure oxides showed the 6-line spectrum of the Mn^{2+} ion present as impurity, but no other features of significance.

When CaO-SrO solid solutions and the pure oxides were exposed to nitrobenzene vapour at 298 K the powder turned to a grey-green colour immediately and a three-line anisotropic ESR signal was observed. If the adsorption was allowed to continue, the powder finally turned to a yellow colour as excess of NB was adsorbed. The ESR signal showed a decrease in resolution, becoming broadened into a single line. These colour changes could not be reversed by evacuation at room temperature nor could the ESR signal be destroyed. Typical spectra obtained at low coverage (short contact time) are shown in Figures 3.4.4 to 3.4.6. The spectra are not symmetrical suggesting that both g and hyperfine anisotropic contributions are present. The g-values of the middle hyperfine line and of the satellites of the triplet, as sketched in Figure 3.4.7, were calculated by using Equation 3.4.2 and are summarized in Table 3.4.1 together with the linewidth values (ΔH_{pp}). OS.20, OS.40 and OS.60 were not studied at low coverage, so their values are not included in Table 3.4.1. The g-values (g_{av}) and the linewidth of the singlet observed at high coverage (long exposure) are collected in Table 3.4.2 and a typical

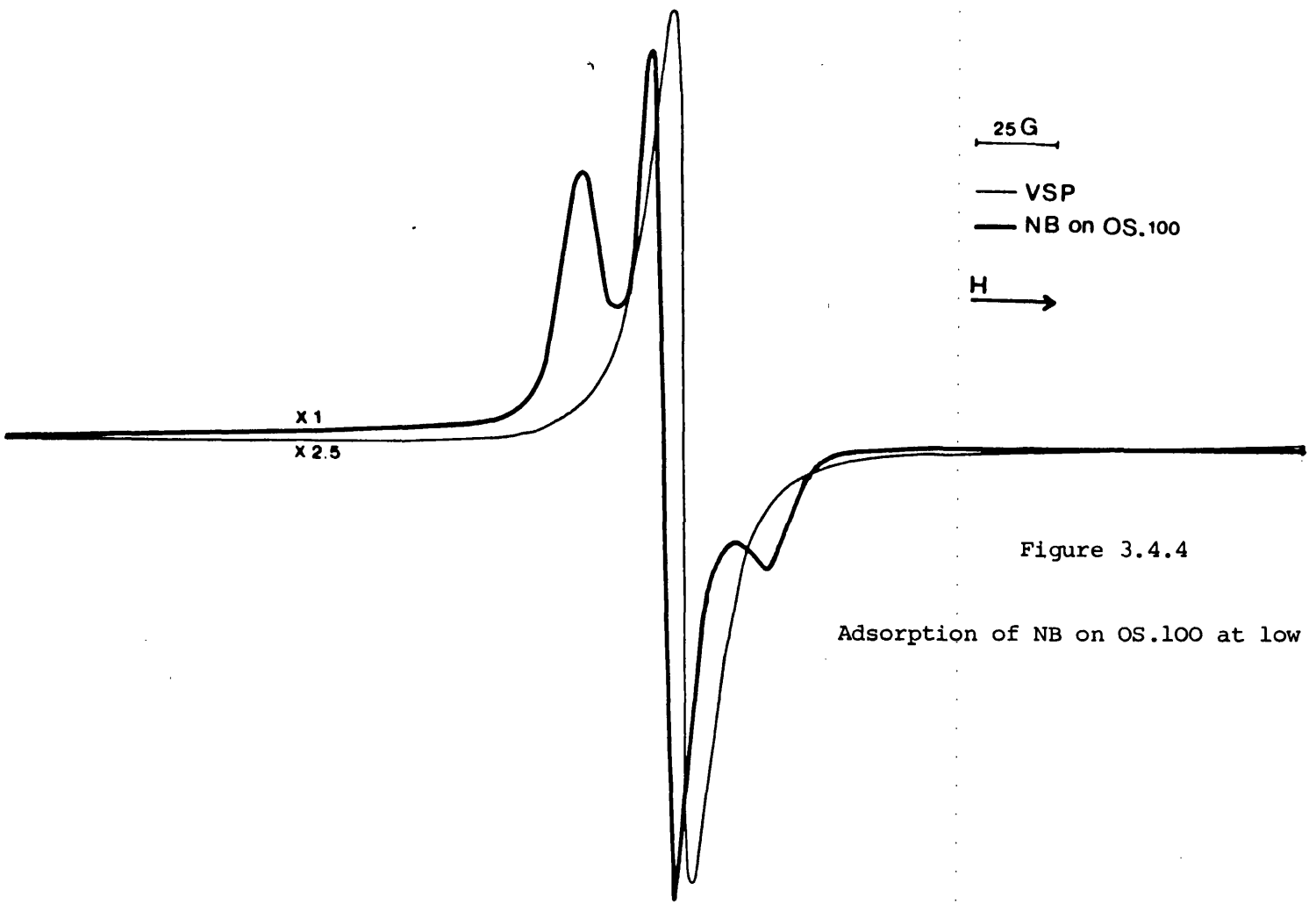

Figure 3.4.4

Adsorption of NB on OS.100 at low coverage

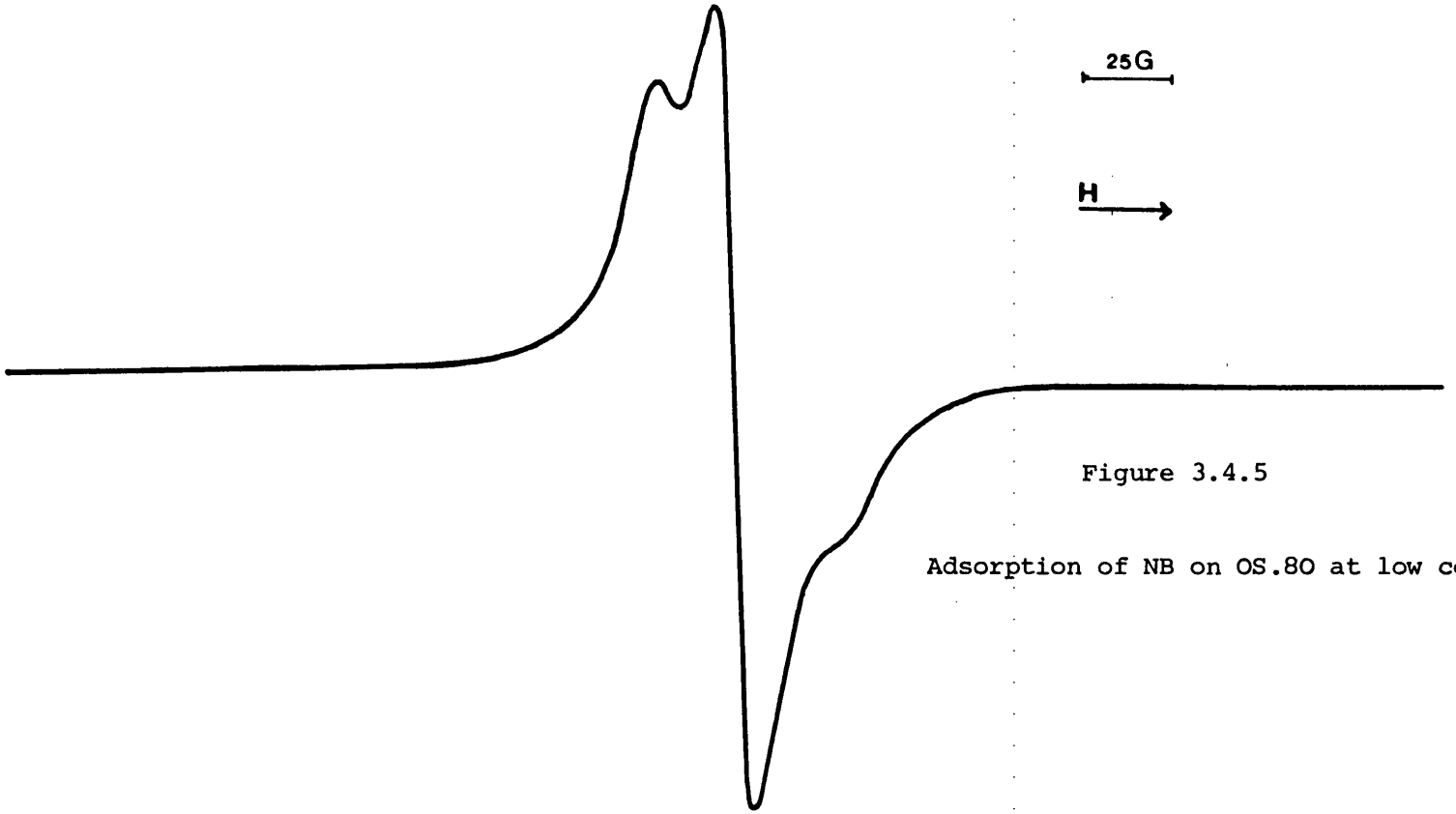

Figure 3.4.5

Adsorption of NB on OS.80 at low coverage

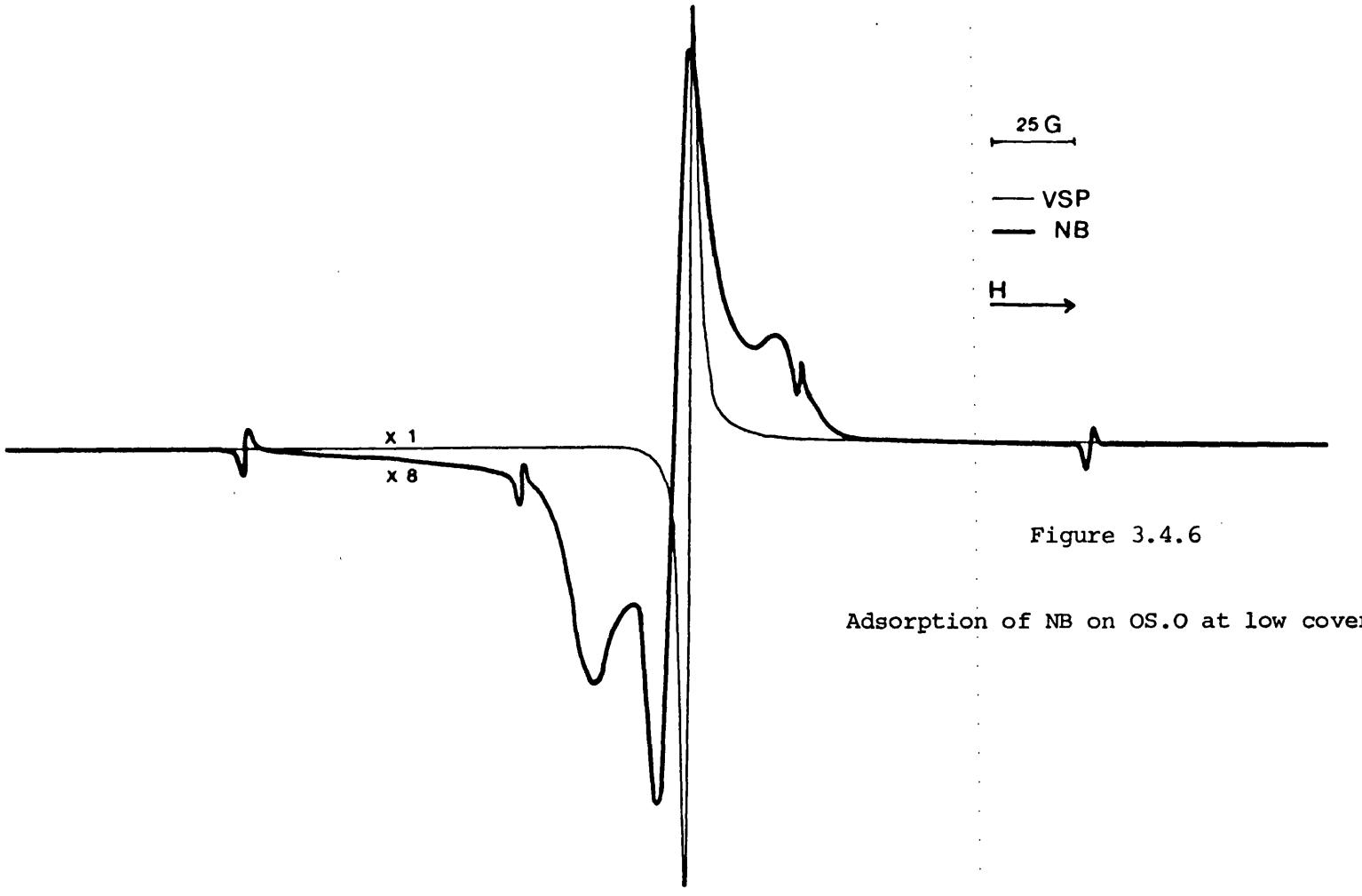

Figure 3.4.6

Adsorption of NB on OS.O at low coverage

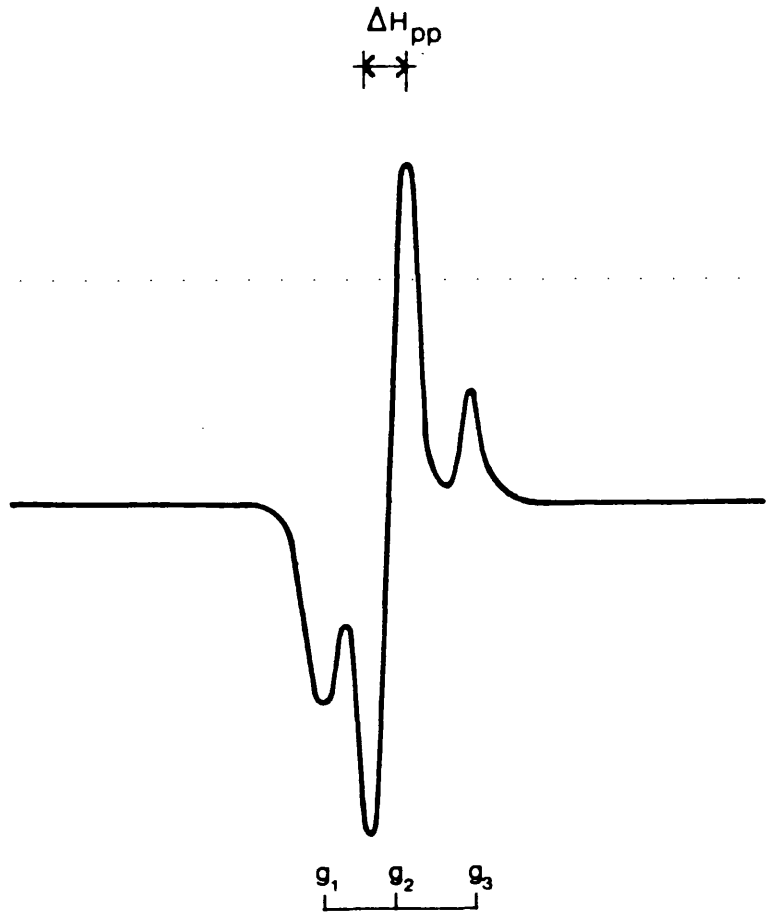

Figure 3.4.7

Determination of g-values and linewidth of chemisorbed NB

Table 3.4.1 ESR Parameters of Adsorbed Nitrobenzene at Low Coverage

Sample	g_1	g_2	g_3	ΔH_{pp}/gauss
OS.0	2.0123	2.0046	1.9822	12.5
OS.80	2.0186	2.0048	1.9840	12.5
OS.100	2.0227	2.0052	1.9857	10.0

Table 3.4.2 ESR Parameters of Adsorbed Nitrobenzene at High Coverage

Sample	g_{av}	ΔH_{pp}/gauss
OS.0	2.0025	18.8
OS.20	2.0049	17.5
OS.40	2.0049	15.0
OS.60	2.0040	17.5
OS.80	2.0025	20.0
OS.100	2.0037	18.8

spectrum is shown in Figure 3.4.8. These singlet signals have been integrated using Wyard's equation (Equation 2.4.28) to obtain the area under the absorption curve. These areas were then used for the evaluation of the number of spins (using Equation 2.4.29) which can be converted to surface concentrations (spin m^{-2}) using weight, length and surface area of the sample in the ESR tube. The results are shown in Table 3.4.3 and Figure 3.4.9.

When the powder samples were contacted with oxygen a strong ESR signal was immediately observed. The spectra (Figs. 3.4.10 to 3.4.15) are rather complex, the number and relative intensity of the lines depending on the sample concerned. The measured g-values as sketched in the respective figures are summarized in Table 3.4.4. OS.O showed a clear resolution which allowed the measurement of 5 g-values, and this spectrum is shown in a wider span for clarity in Fig. 3.4.15. The other samples only allowed the measurement of three g-values. The presence of the gas phase caused the lines to broaden and also to change their relative intensity. This effect was studies on OS.100, OS.90 and OS.O and can be seen by comparison of Figs. 3.4.10, 3.4.11 and 3.4.15 with 3.4.16, 3.4.17 and 3.4.18, respectively. The linewidth of the central line of OS.90 and OS.O increased, as a result of which it overlapped the first line and prevented the measurement of g_1. The observed g-values are summarized in Table 3.4.5.

The effect of time on the oxygen spectra was qualitatively studied by recording the spectra of the sealed ESR tubes one month after the oxygen adsorption was carried out. The signal diminished, reaching the noise level for OS.90 and OS.100 at 298 K and preventing the recording of any spectra. Figures 3.4.19 to 3.4.22 showed the

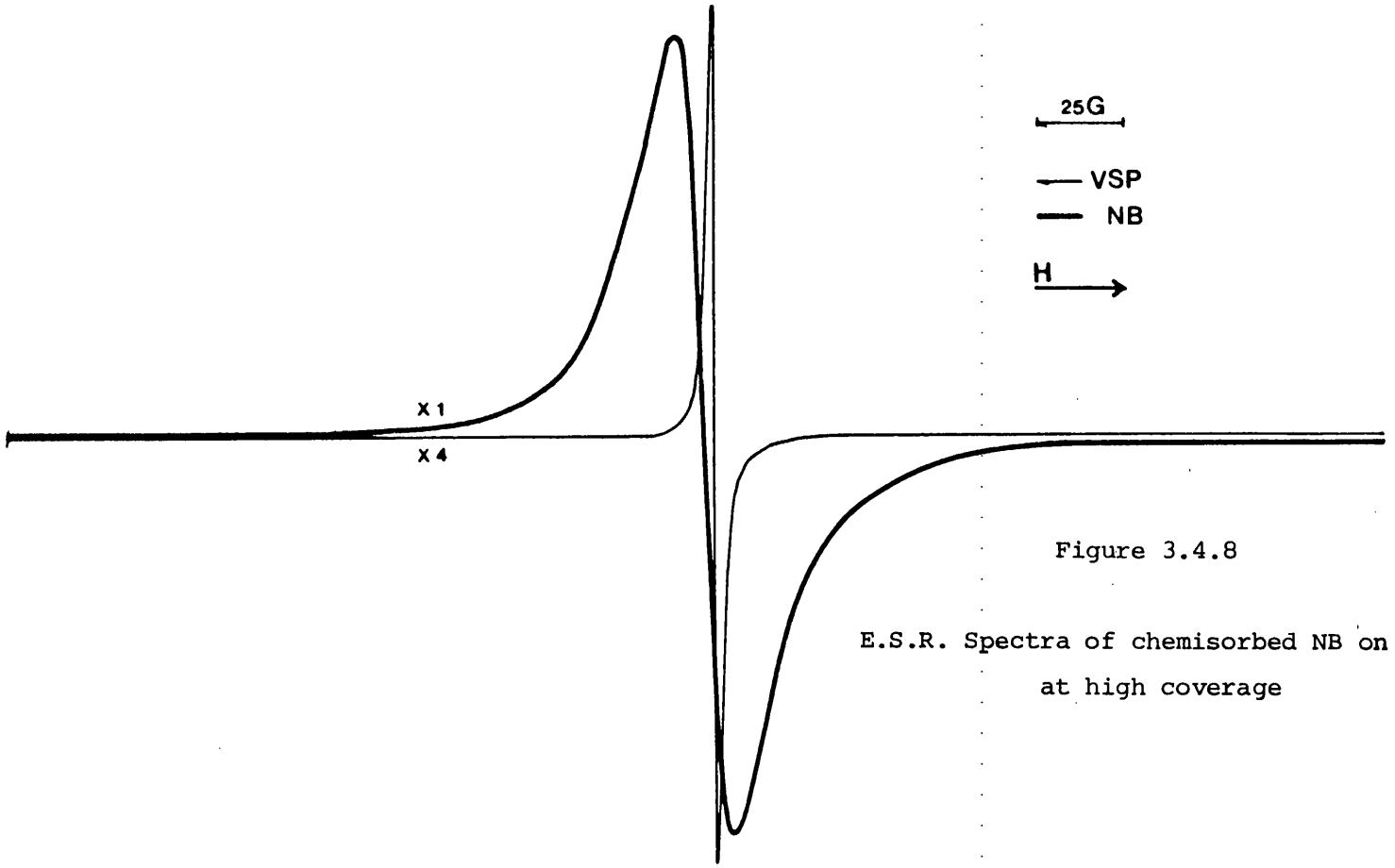

Figure 3.4.8

E.S.R. Spectra of chemisorbed NB on OS.60 at high coverage

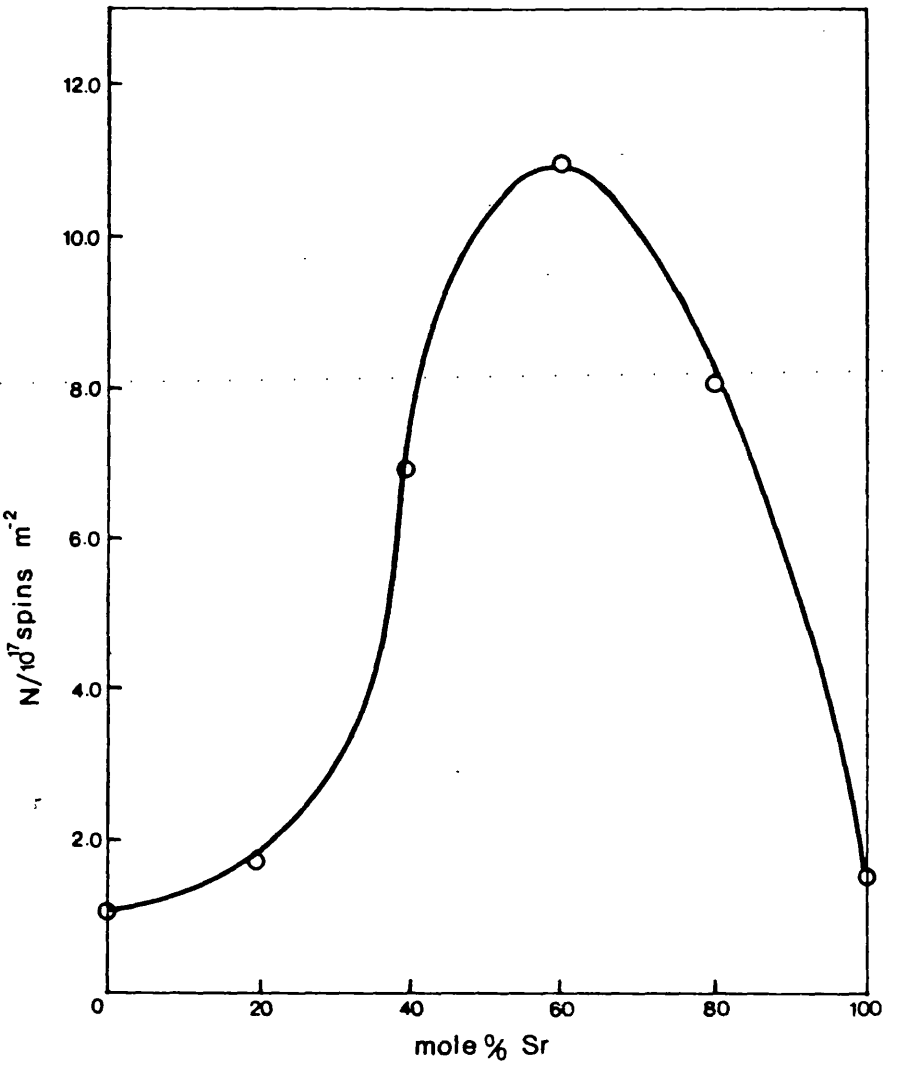

Figure 3.4.9

Surface Concentration of Nitrobenzene Anion Radical vs Composition of CaO - SrO Solid Solutions

Table 3.4.3 Surface Concentration of Adsorbed Nitrobenzene

Sample	$N/10^{17}$ spins m^{-2}
OS.0	1.06
OS.20	1.69
OS.40	6.98
OS.60	11.00
OS.80	8.06
OS.100	1.51

Table 3.4.4 g-values of Adsorbed Oxygen (298 K)

Sample	g_1	g_2	g_3	g_4	g_5
OS.0	2.0156	2.0114	2.0084	2.0068	2.0019
OS.10	2.0153	2.0094	2.0021		
OS.50	2.0197	2.0130	2.0034		
OS.70	2.0139	2.0079	2.0028		
OS.90	2.0131	2.0078	2.0019		
OS.100	2.0144	2.0086	2.0028		

Table 3.4.5 g-values of Adsorbed Oxygen (298 K, gas phase present)

Sample	g_1	g_2	g_3
OS.0		2.0082	2.0015
OS.90		2.0082	2.0019
OS.100	2.0175	2.0090	2.0028

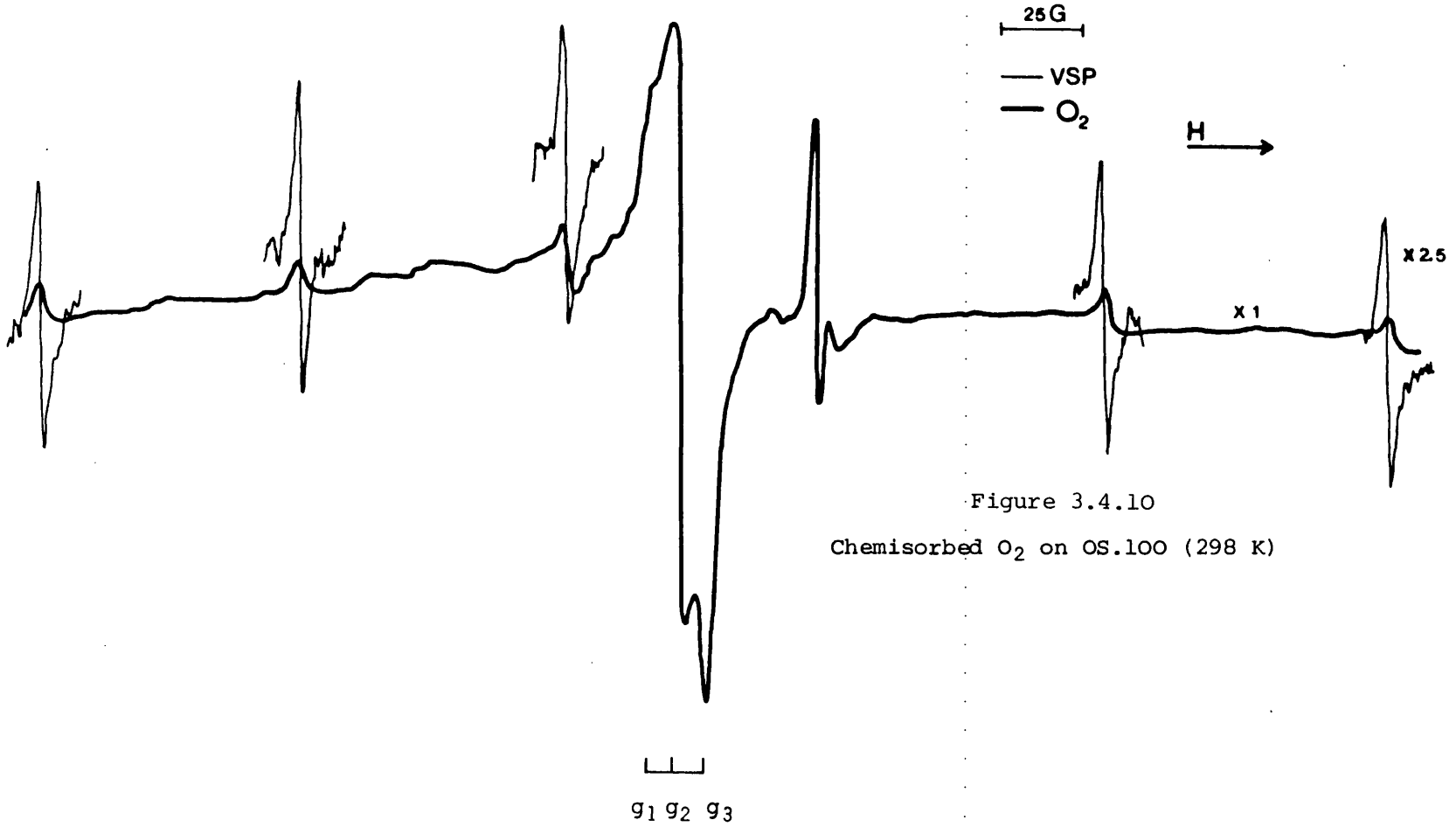

Figure 3.4.10

Chemisorbed O_2 on OS.100 (298 K)

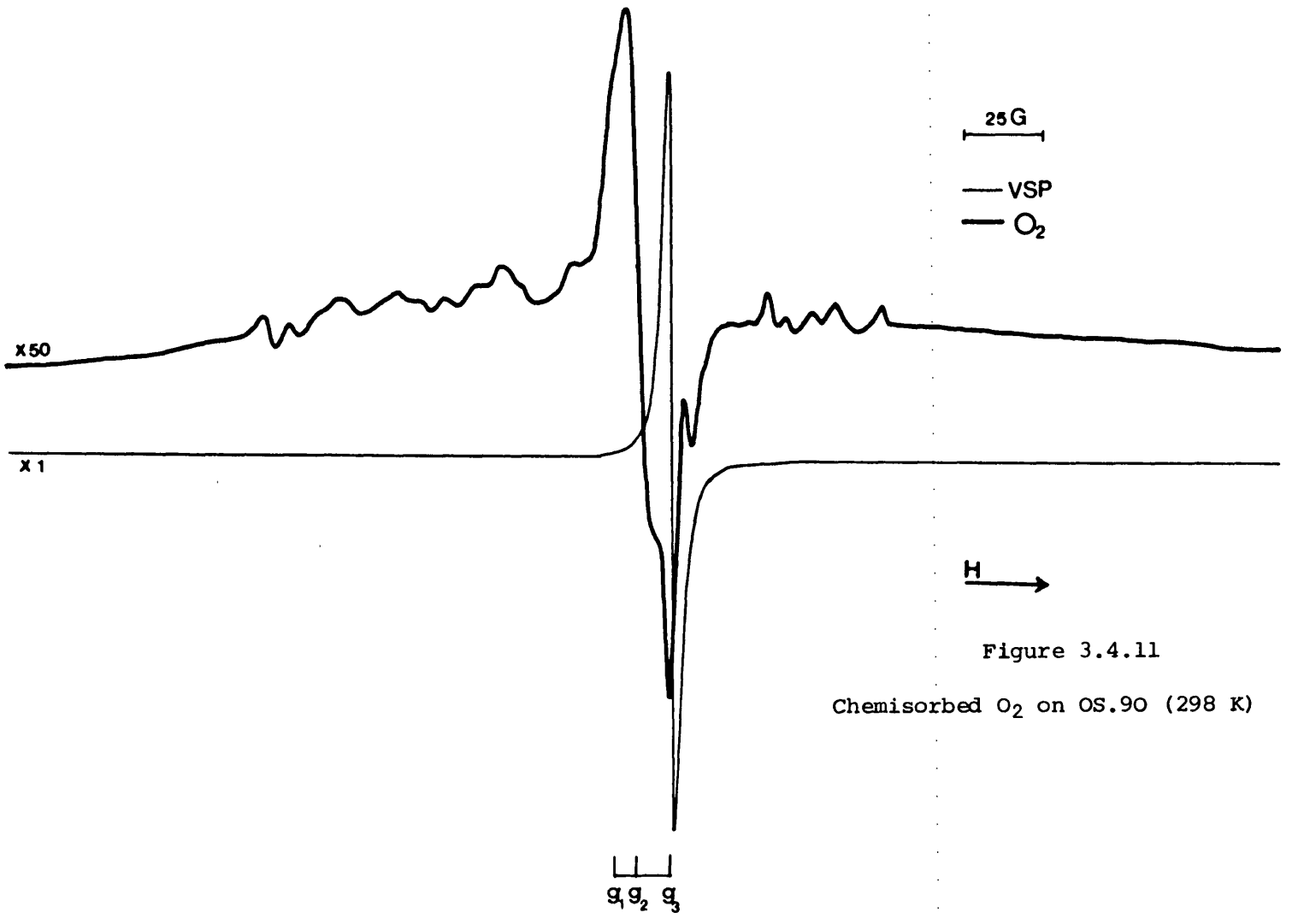

Figure 3.4.11

Chemisorbed O_2 on OS.90 (298 K)

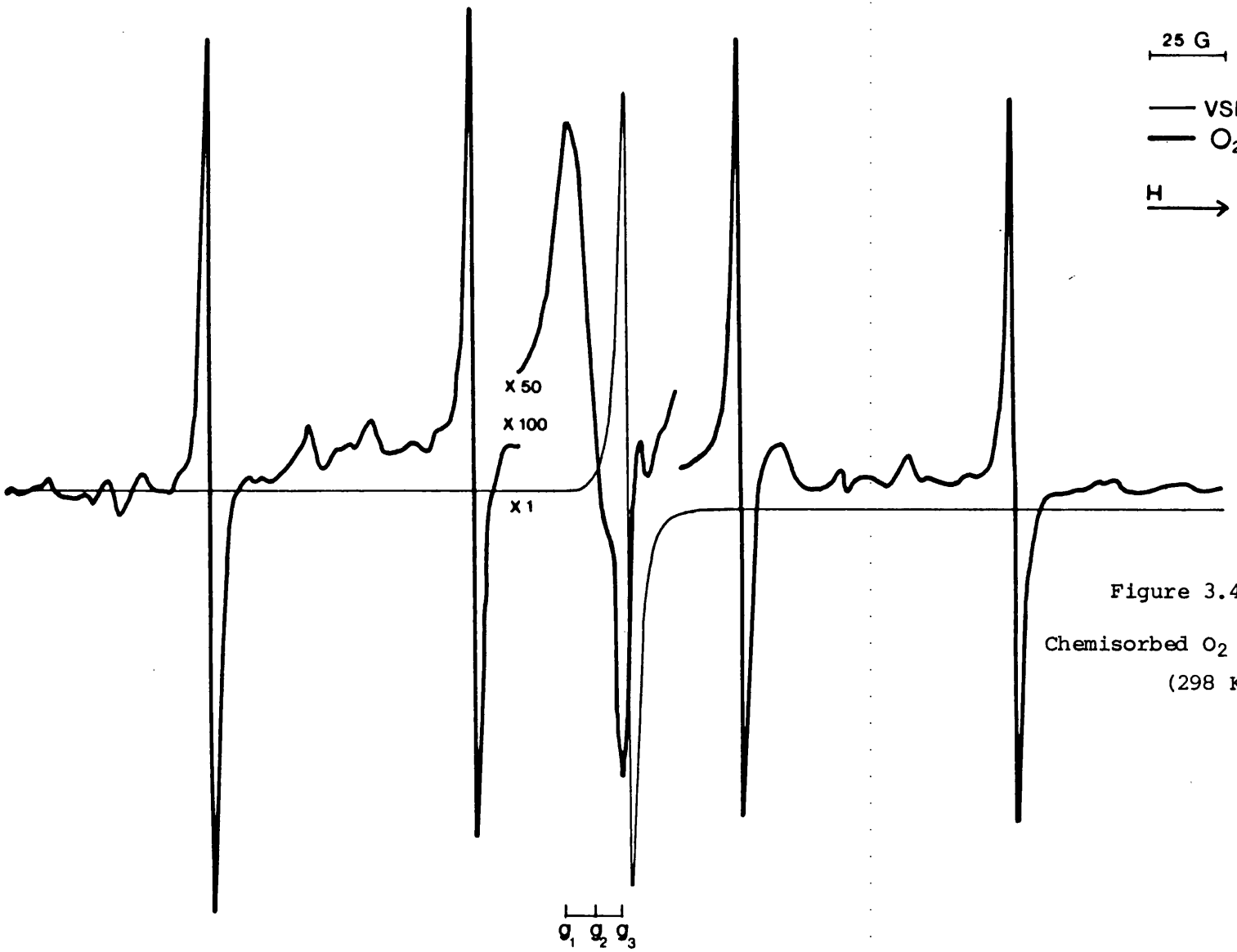

Figure 3.4.12

Chemisorbed O_2 on OS.70

(298 K)

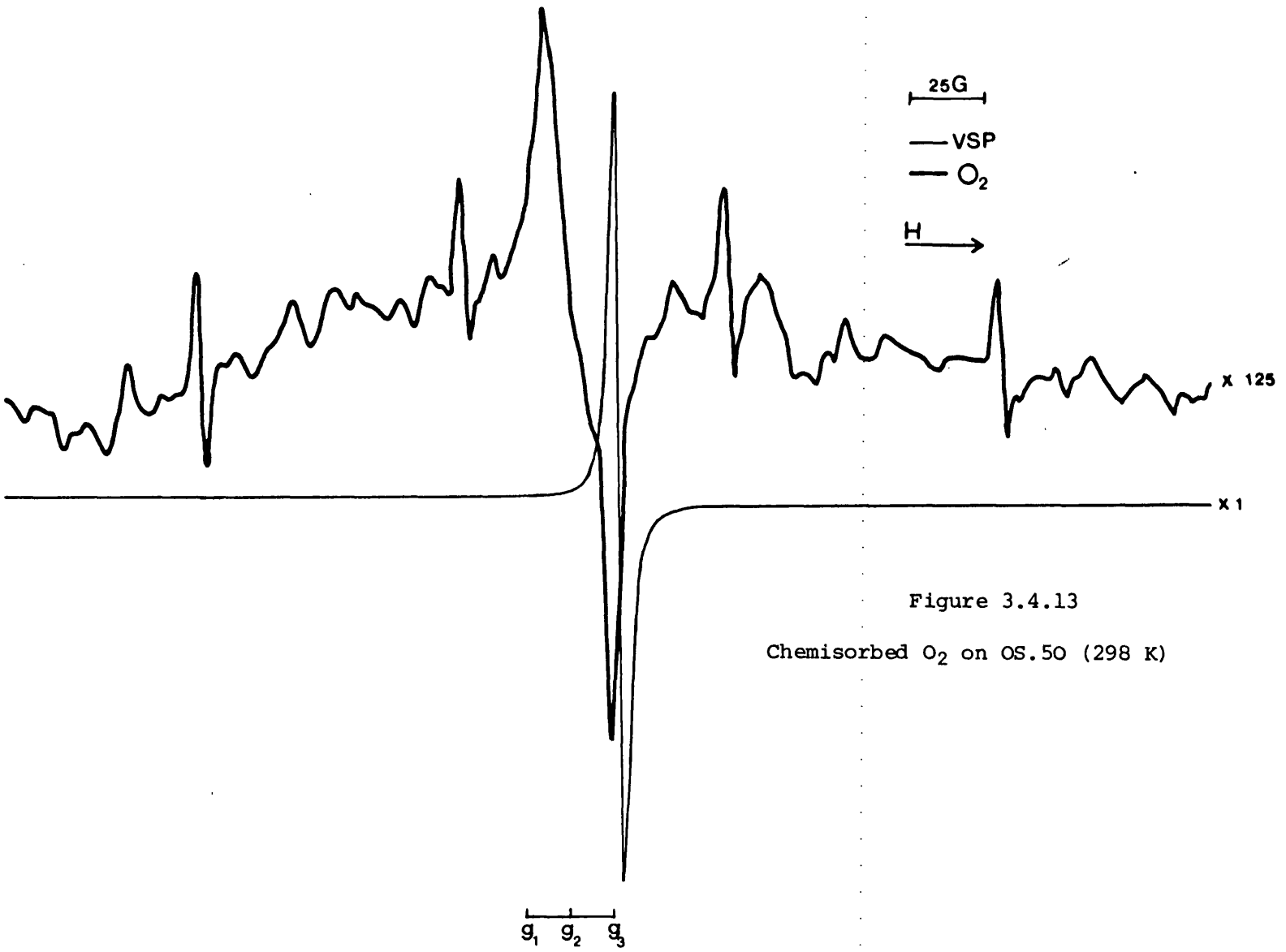

Figure 3.4.13

Chemisorbed O_2 on OS.50 (298 K)

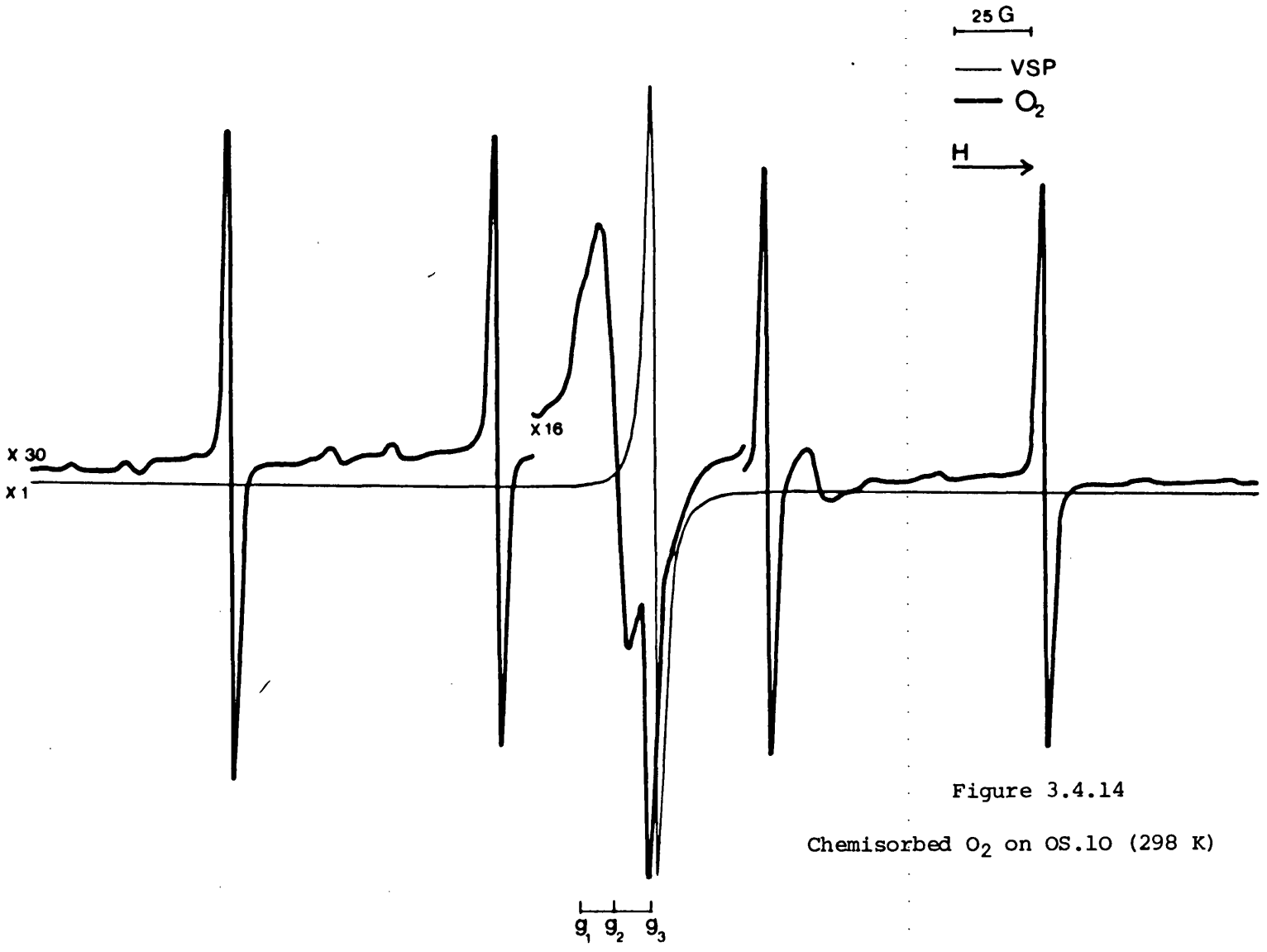

Figure 3.4.14

Chemisorbed O_2 on OS.10 (298 K)

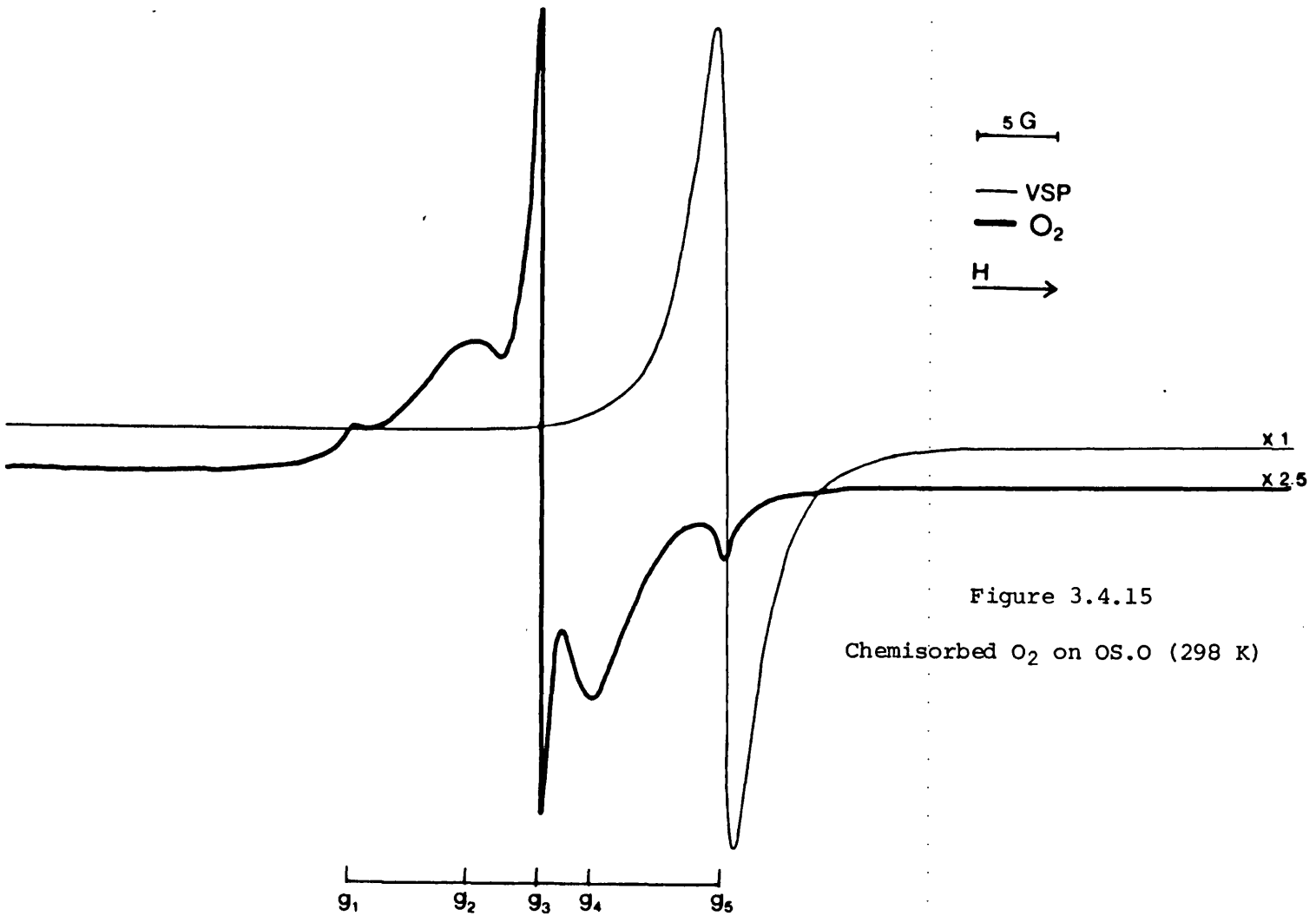

Figure 3.4.15

Chemisorbed O_2 on OS.O (298 K)

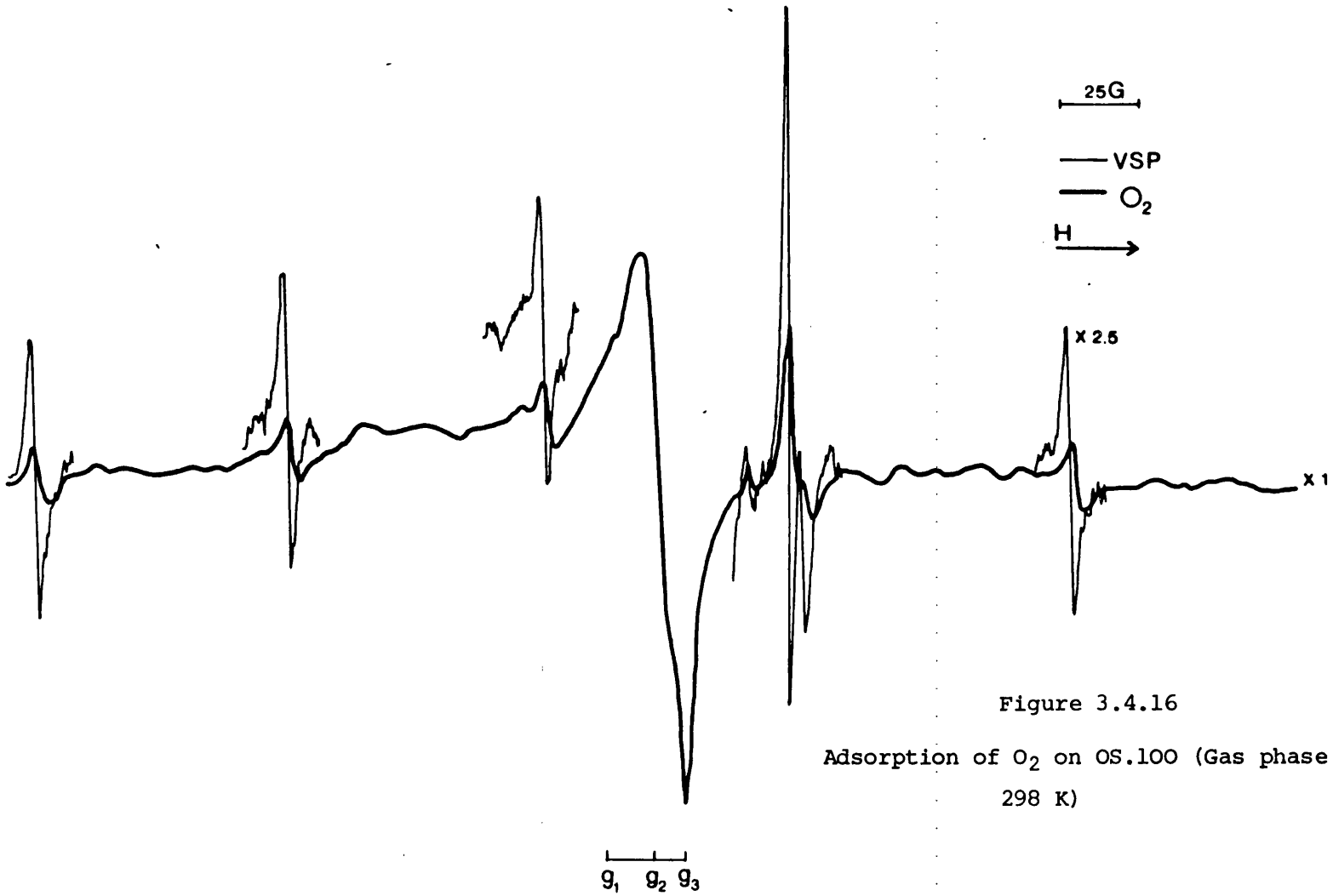

Figure 3.4.16

Adsorption of O_2 on OS.100 (Gas phase present, 298 K)

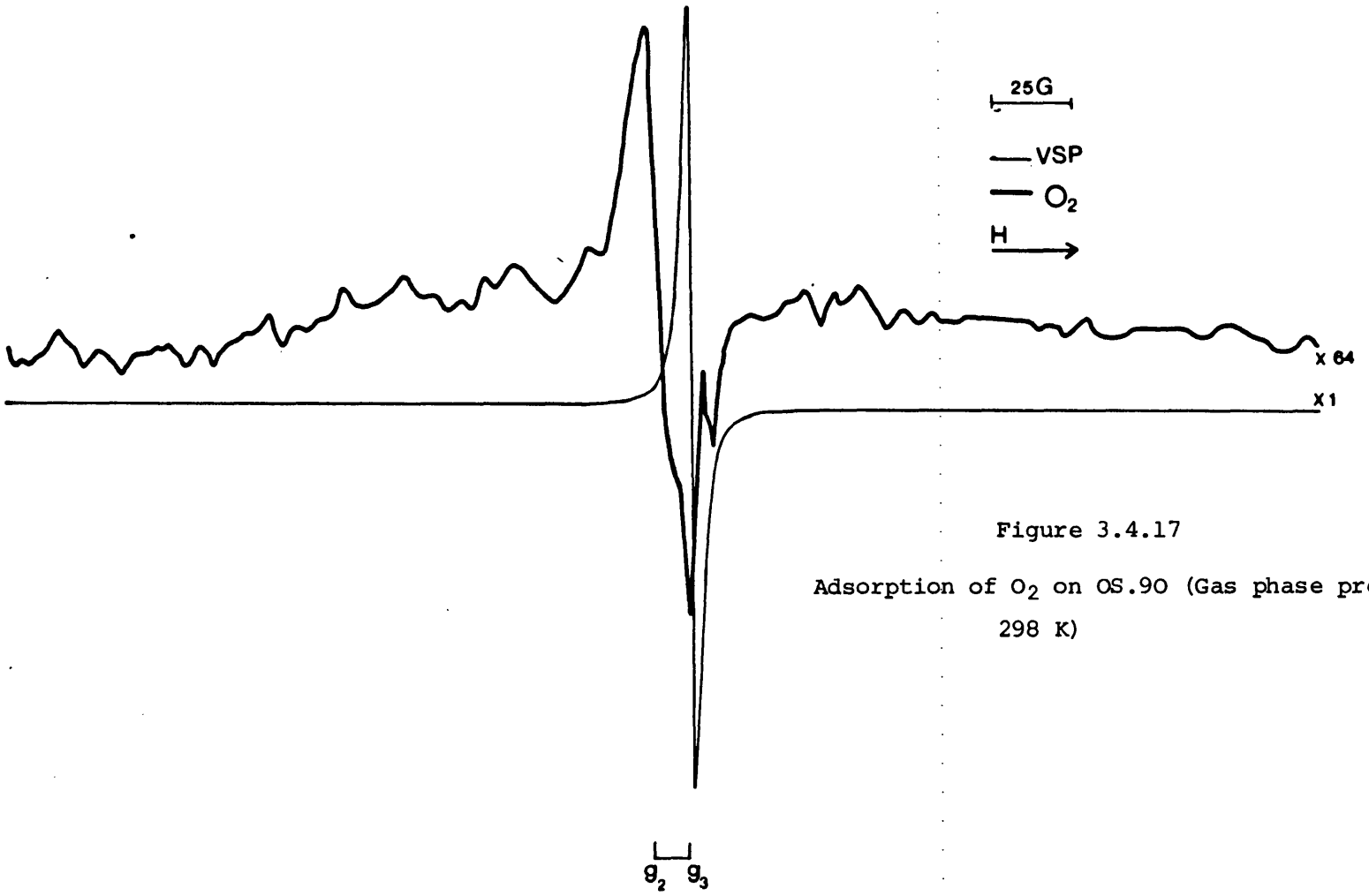

Figure 3.4.17

Adsorption of O_2 on OS.90 (Gas phase present, 298 K)

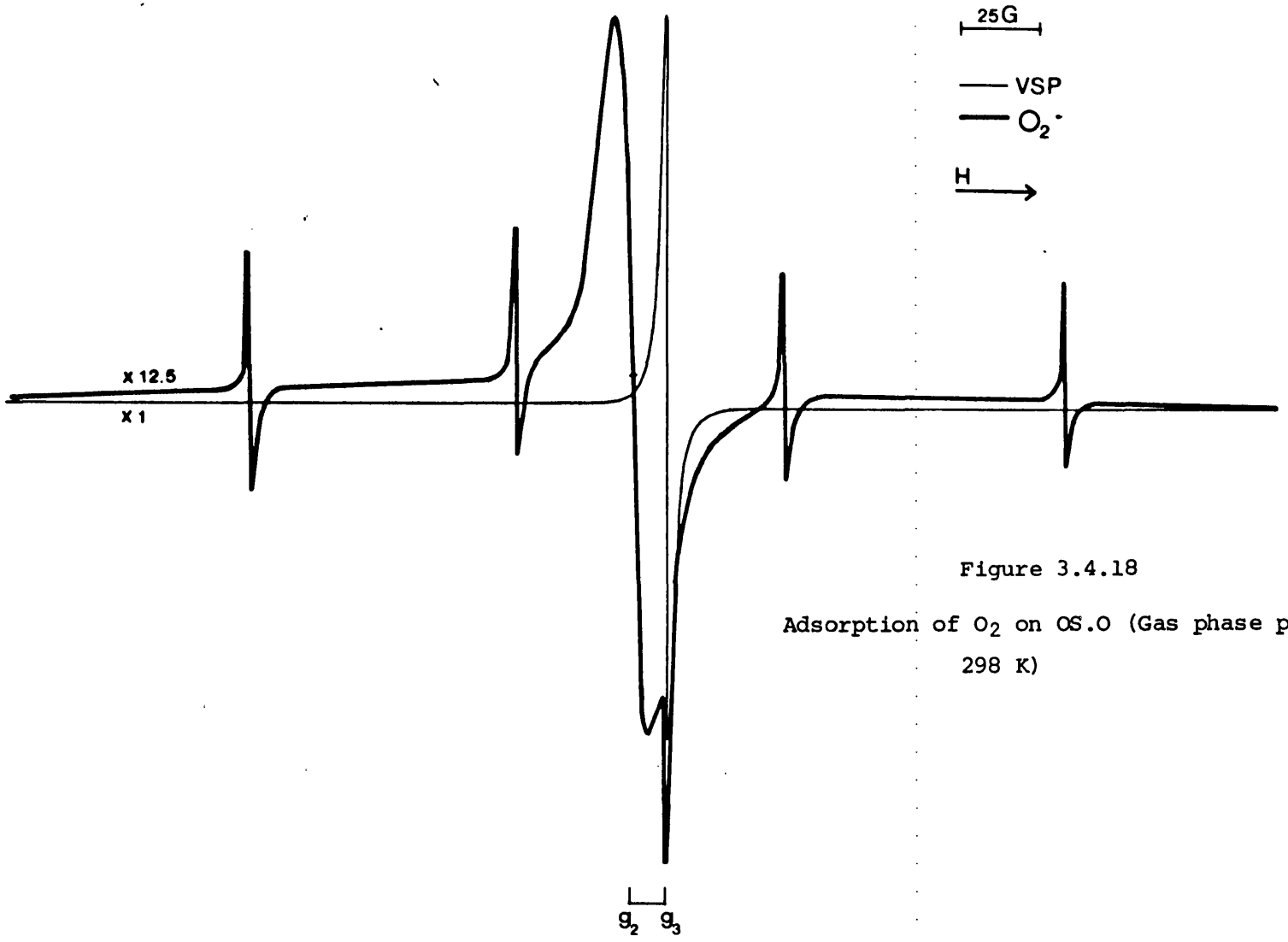

Figure 3.4.18

Adsorption of O_2 on OS.O (Gas phase present, 298 K)

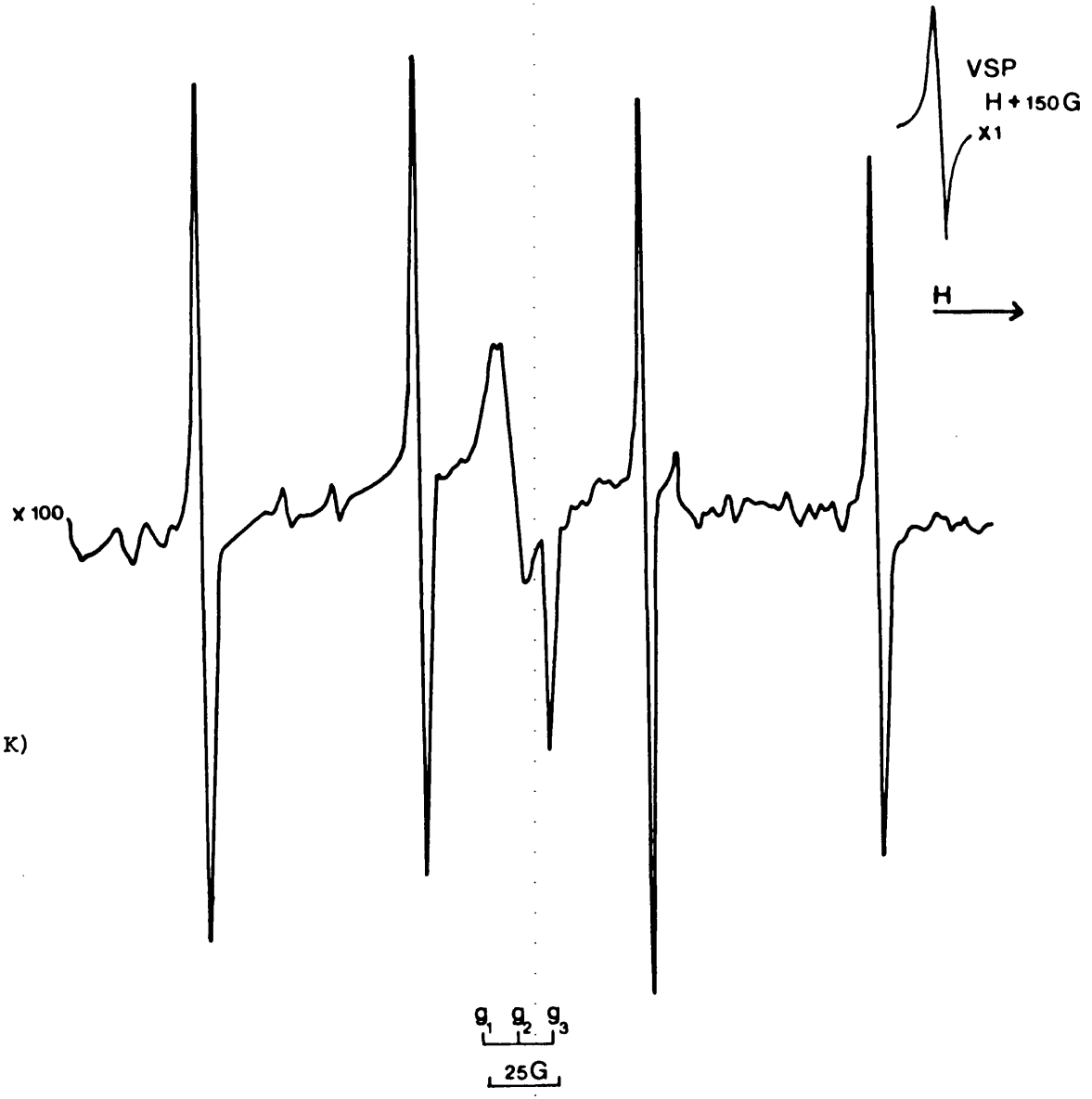

Figure 3.4.19

Chemisorbed O_2 on OS.O

(1 month after adsorption, 298 K)

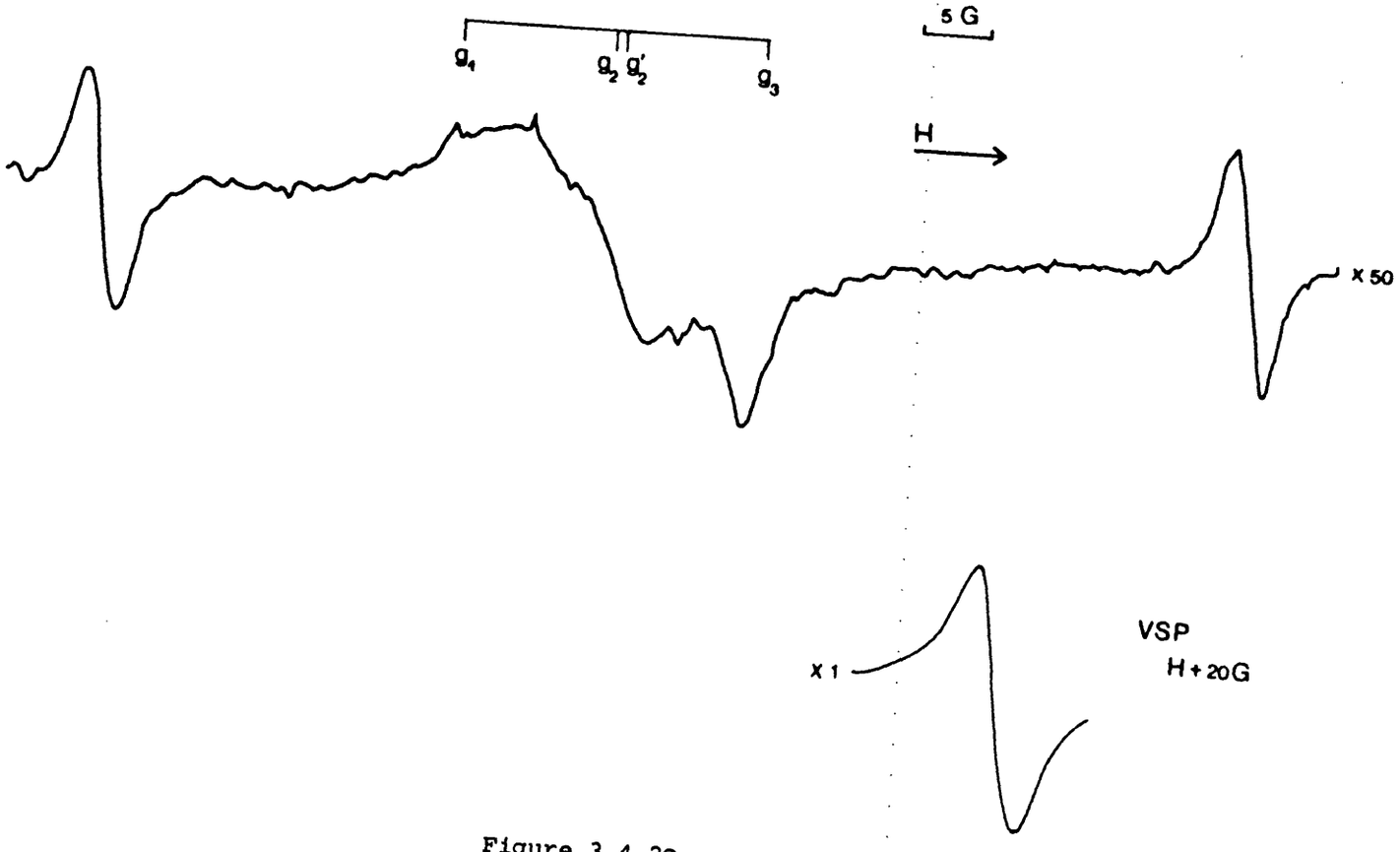

Figure 3.4.20

Chemisorbed O_2 on OS.10
(1 month after adsorption, 298 K)

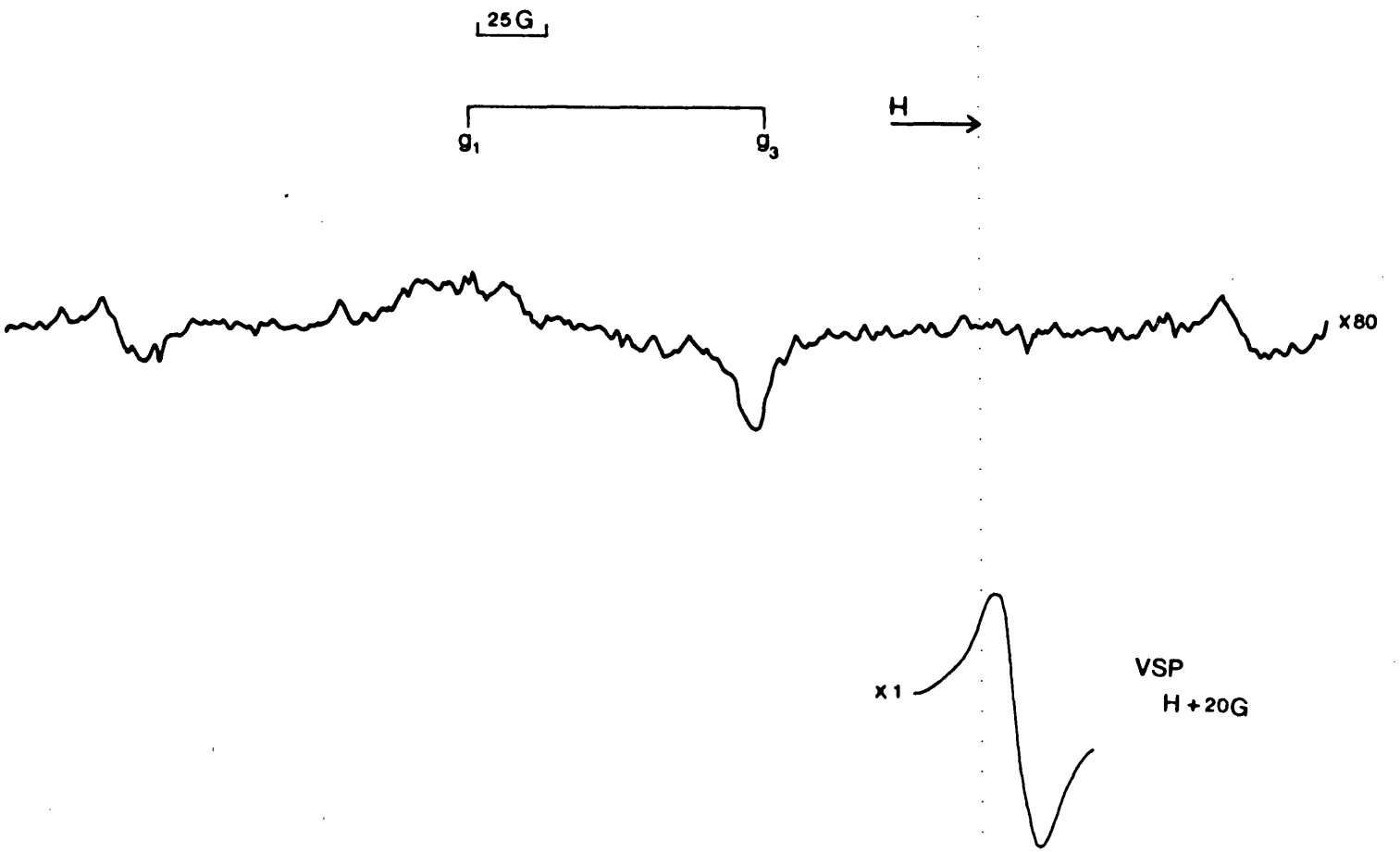

Figure 3.4.21

Chemisorbed O_2 on OS.50

(1 month after adsorption, 298 K)

Figure 3.4.22

Chemisorbed O_2 on OS.70
(1 month after adsorption, 298 K)

recorded spectra for the other samples (OS.0, OS.10, OS.50, OS.70) and their g-values are collected in Table 3.4.6. The strongest change was registered for OS.0, where the clear resolution of 5 lines disappeared completely; the line became broader and more similar to the signal observed for the other samples. It seemed also that the species responsible for the lines giving g_2 and g_4 has decayed to extinction or else those values have been overlapped into the signal which is now observed.

Lowering the temperature of the sample to 78 K during the recording of the spectra revealed a more intense signal and moved it to lower field. There is also a decrease in resolution between g_2 and g_3. The measured g-values are reported in Table 3.4.7 and the recorded spectra are shown in Figures 3.4.23 to 3.4.28.

3.5. Isomerization of Trans-but-2-ene

3.5.1 The Microcatalytic System

The isomerization of trans-but-2-ene has been studied by using the microcatalytic system shown in Figure 3.5.1. It consisted of (a) a gas handling system, (b) a doser, (c) a microreactor, (d) a trapping system, and (e) a chromatographic unit. Details are as follows :

(a) Gas handling system

Four gas supplies were required. Trans-but-2-ene (99.95%) was connected to the system with the appropriate regulator through a needle valve. Helium (high purity) was used as carrier gas. Two lines were employed. The first one passed through the reactor and had a finely controlled flow rate previously calibrated with a slow flow rotameter connected in line; this arrangement permitted one

Table 3.4.6 g-values of Adsorbed Oxygen (298 K, 1 month after adsorption)

Sample	g_1	g_2	g_3
OS.0	2.0152	2.0087	2.0019
OS.10	2.0153	2.0085	2.0019
OS.50	2.0150		2.0019
OS.70	2.0175	2.0081	2.0013

Table 3.4.7 g-values of Adsorbed Oxygen (77 K, 1 month after adsorption)

Sample	g_1	g_2	g_3
OS.0	2.0109	2.0019	1.9972
OS.10		2.0019	1.9966
OS.50	2.0120	2.0024	2.0000
OS.70	2.0111	2.0026	1.9980
OS.90	2.0097	2.0012	1.9968
OS.100	2.0134	2.0019	1.9978

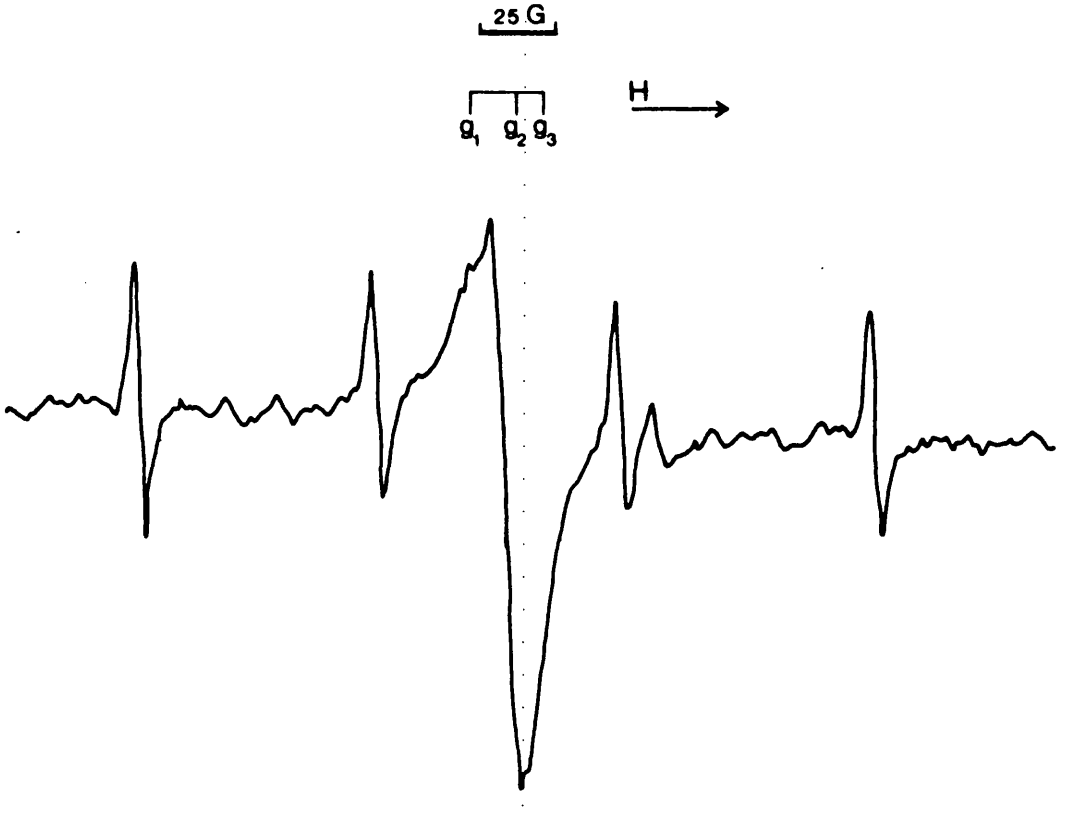

Figure 3.2.23

Chemisorbed O_2 on OS.O

(1 month after adsorption, 78 K)

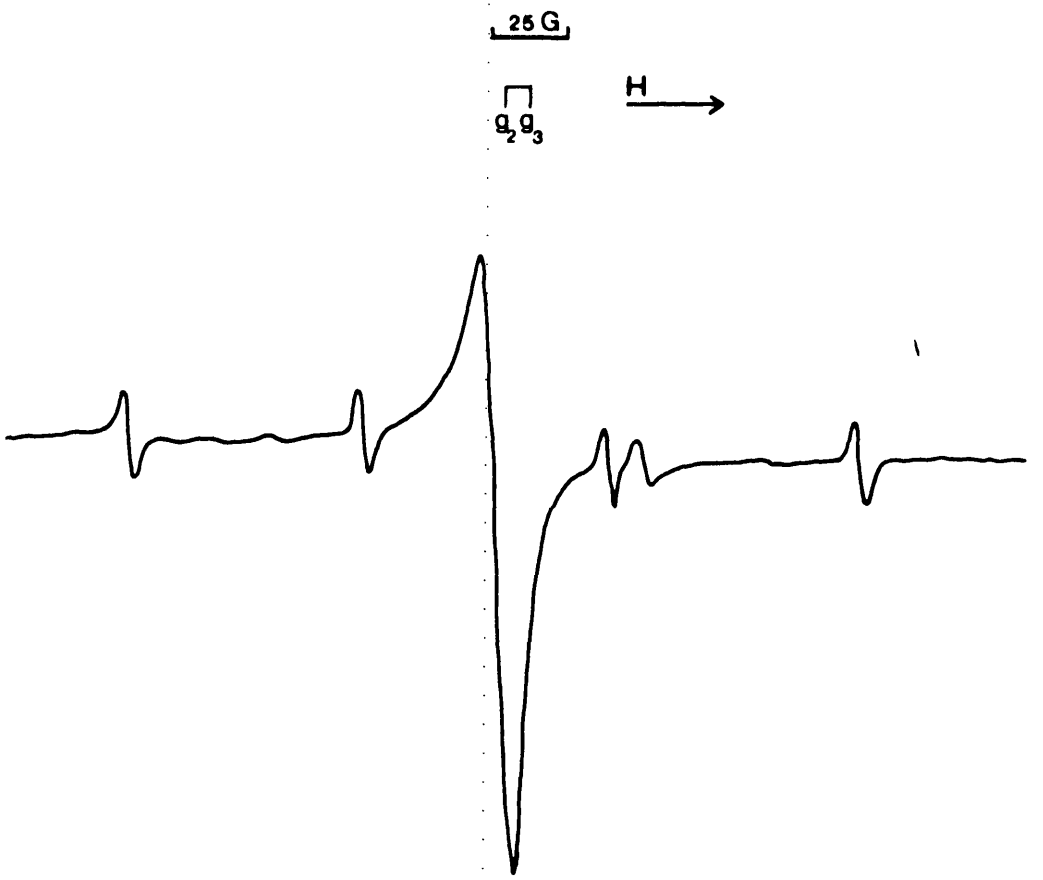

Figure 3.4.24

Chemisorbed O_2 on OS.10

(1 month after adsorption, 78 K)

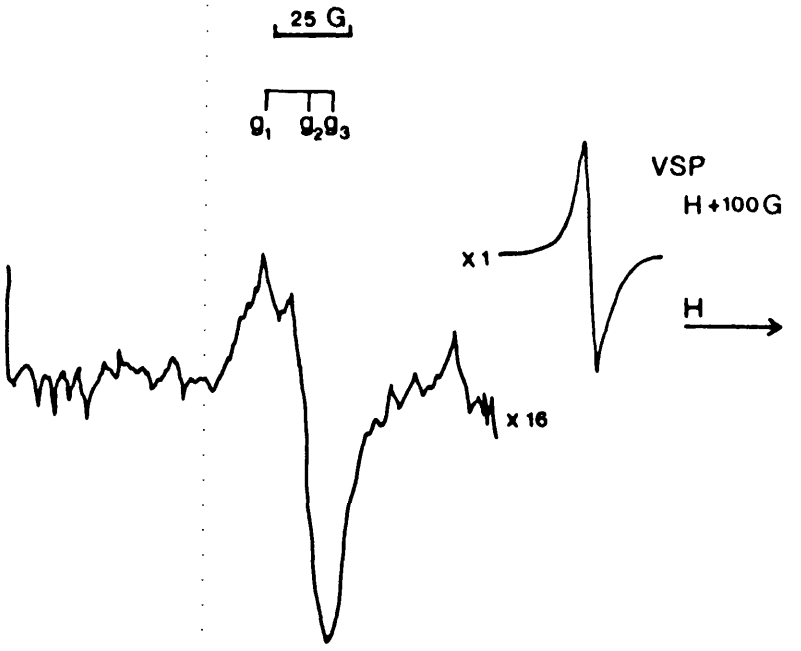

Figure 3.4.25

Chemisorbed O_2 on OS.50

(1 month after adsorption, 78 K)

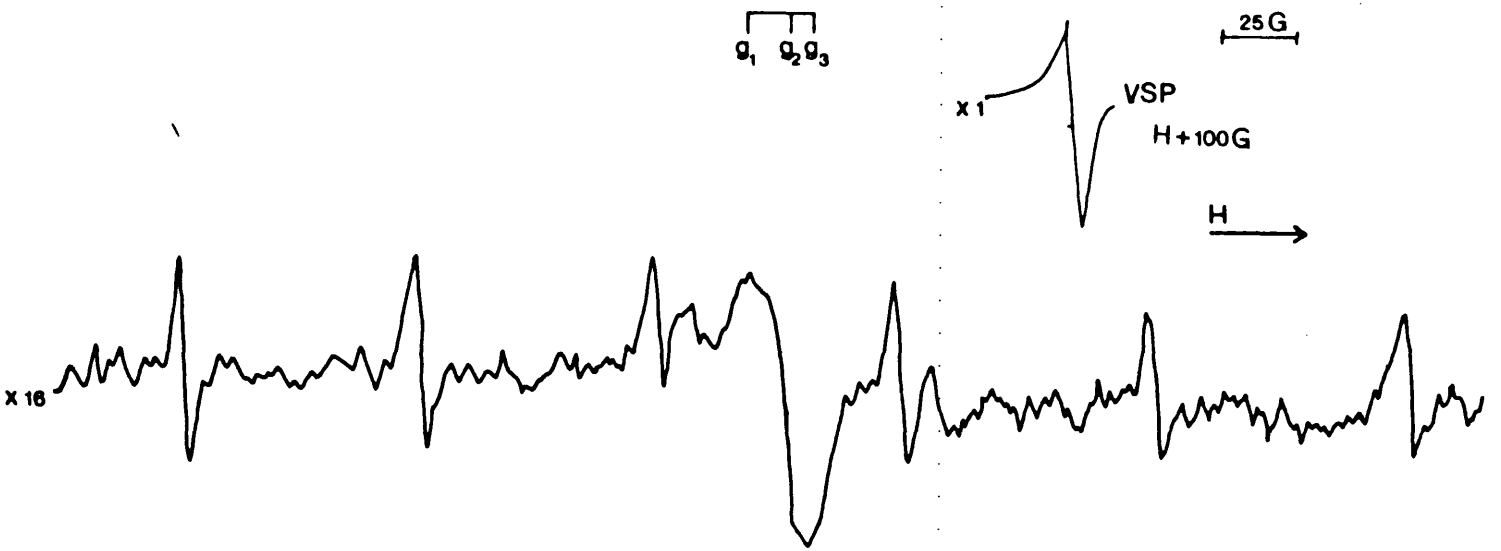

Figure 3.4.26

Chemisorbed O_2 on OS.70
(1 month after adsorption, 78 K)

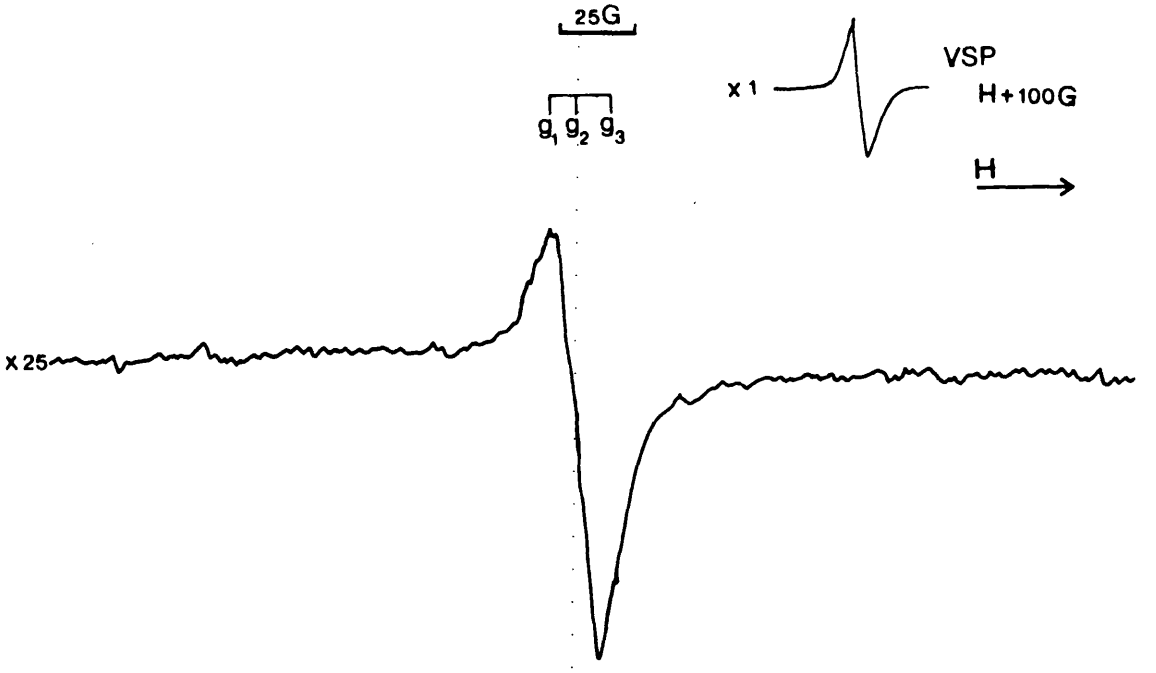

Figure 3.4.27

Chemisorbed O_2 on OS.90
(1 month after adsorption, 78 K)

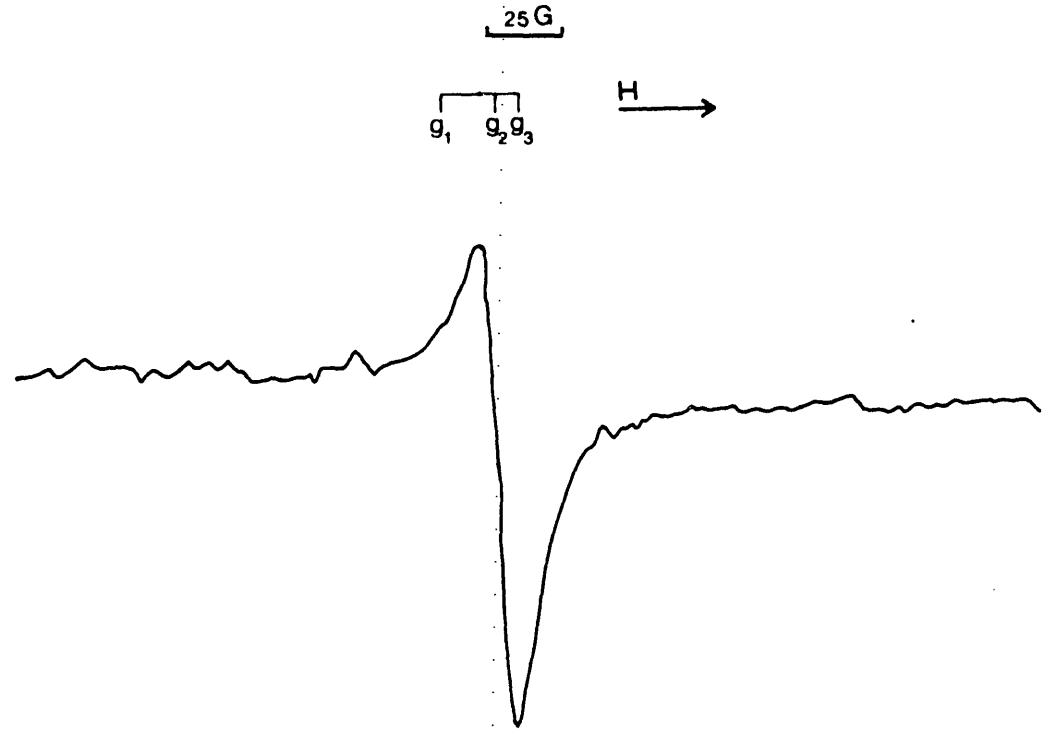

Figure 3.4.28

Chemisorbed O_2 on OS.100
(1 month after adsorption, 78 K)

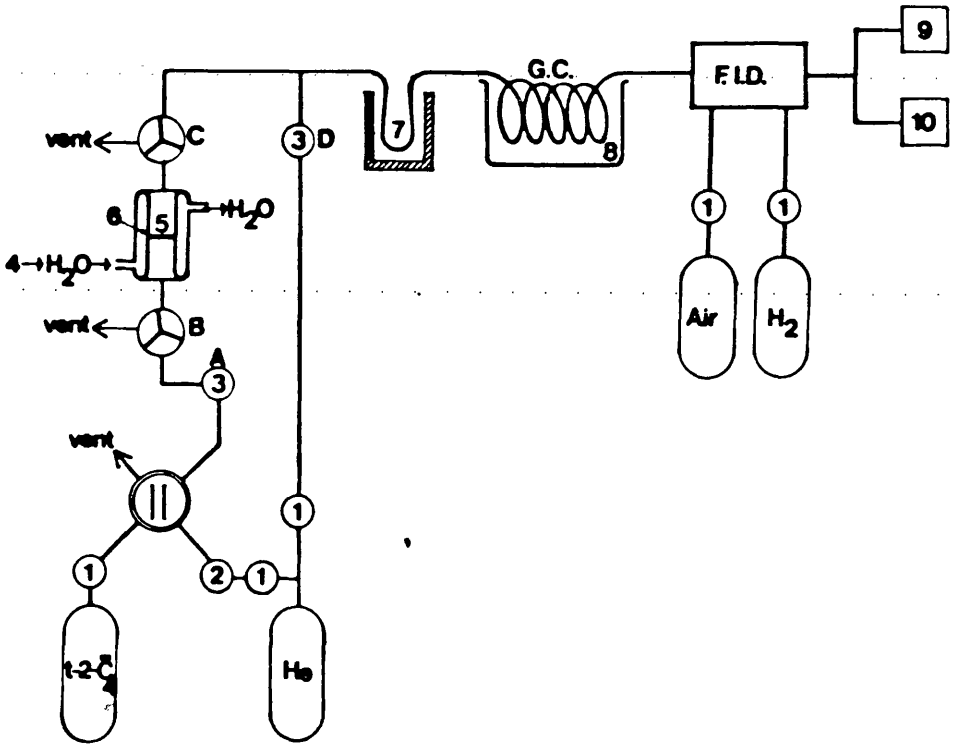

1. Flow controllers
2. Rotameter
3. Switch valve (A and B)
4. Thermostat
5. Catalyst
6. Sintered glass plate
7. Cold trap
8. Ice water bath
9. Recorder
10. Integrator

B and C : two-way taps

Figure 3.5.1

Microcatalytic System

to vary the flow rate to obtain different contact times of the reactant with the catalyst sample. The second line was also finely controlled and was used to fix the optimum gas flow for the resolution of peaks in the gas chromatographic unit. It passed through the cold trap where the mixture to be analyzed was flash-evaporated into the chromatographic column (see later). Air and hydrogen (high purity) were used for supplying the flame ionization detector (see below). All the gases were supplied by Air Products Co. and were dried by passage through a tube containing molecular sieve 5A activated at 500 K.

(b) Doser

A Pye 6-port gas valve was used to inject the reactant (trans-but-2-ene) into the carrier gas stream ahead of the reactor. A calibrated volume of 0.125 cm^3 was contained between two ports which could be by-passed either to the trans-but-2-ene line (for filling the doser) or to the helium line (for carrying the reactant towards the reactor). The doser was filled at 1 atmosphere and 295 K. The other four ports were connected to the trans-but-2-ene line, to the helium line, to the reactor through a switch valve, and to the external vent respectively.

(c) Microreactor

The microreactor was made of pyrex and is shown in Figure 3.5.2. The catalyst was placed on a sintered glass plate in the middle of the reactor. The temperature was regulated by a water jacket fed from a thermostat at the desired temperature. Two two-way taps (B and C) connected it to the remainder of the system. These were used to load the catalyst in an inert atmosphere and to isolate it while still in this environment prior to being transported and fixed

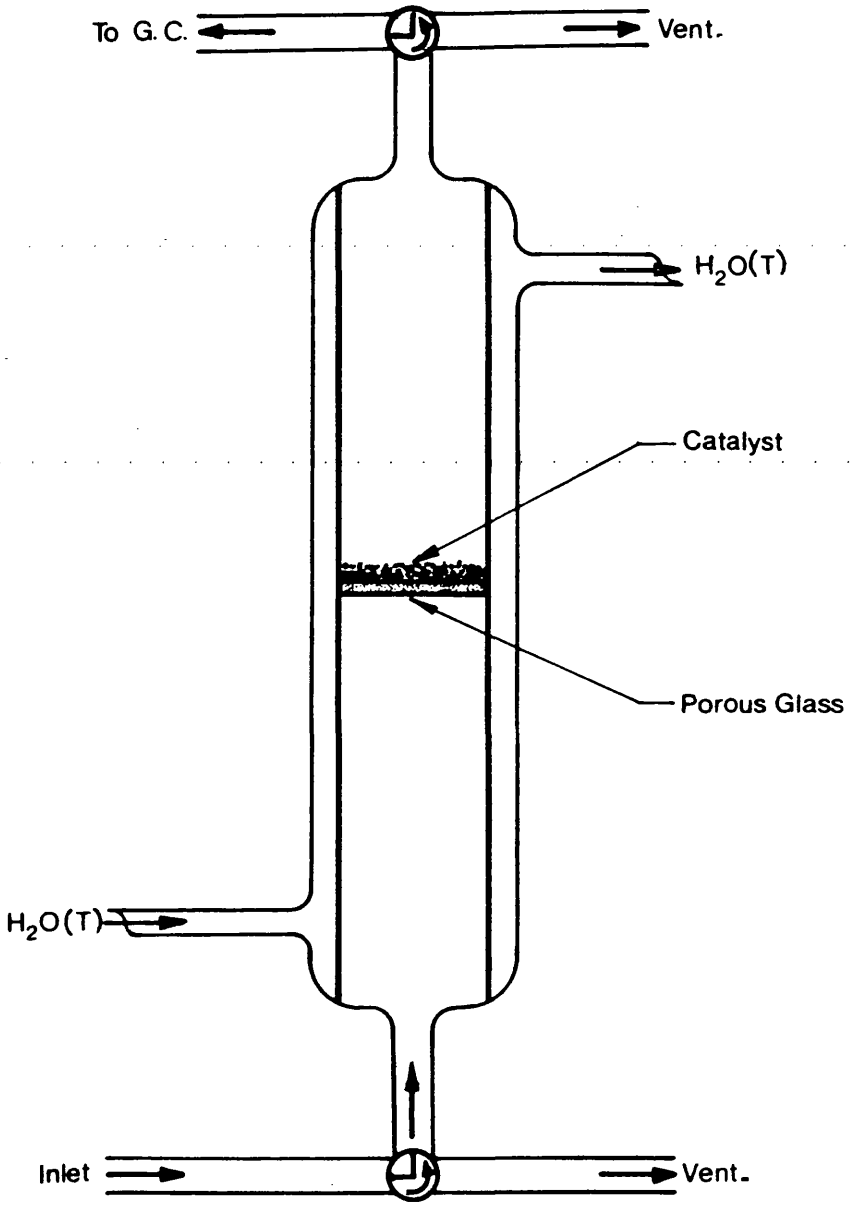

Figure 3.5.2

Microcatalytic Reactor

in the flow system.

(d) Trapping system

A cold trap made of $^1/_4$" o.d. copper tubing as a single round coil was incorporated between the exit from the reactor and the entry to the chromatographic column. In order to collect the reaction mixture the trap was kept at 78 K, and to inject the mixture into the column the trap was heated very rapidly by means of a 1000 W blower.

(c) Chromatographic unit

A column of 20' x $^1/_4$" o.d. stainless steel packed with 20% 2:1 dimethylsulpholane:hexamethylamide on diatomite S-NAW 30-60 mesh provided by Field Instruments Co. was used. This column achieved complete separation of the butene isomers (but-1-ene, cis-but-2-ene and trans-but-2-ene) under the conditions specified below. After activation at 303 K overnight in a helium flow, the column was operated at 273 K (immersed in an ice-water bath) with a helium carrier gas flow rate of 45 cm^3 min^{-1}. Elution was completed in about 23 minutes with the retention times reported in Table 3.5.1. A flame ionization detector (FID) from a Pye 104 gas chromatograph was used. Its output was connected to both a potentiometric recorder and an electronic integrator.

3.5.2 The Method

Prior to studying the catalyzed isomerization of trans-but-2-ene the possibility of homogeneous reaction was examined. It was found that even at 350 K it did not undergo any reaction. Temperatures higher than 350 K were not examined because the activities of the catalysts used in the present work were such that all reactions could be conducted below 345 K.

Table 3.5.1 Retention Times of Butene Isomers

	tR/min
But-1-ene	13.5
Trans-but-2-ene	16
Cis-but-2-ene	19.5

OS.0, OS.10, OS.40, OS.60, OS.80 and OS.100 were used as catalysts. The catalyst sample was loaded into the reactor inside a dry-box. High purity nitrogen, dried by using two 25" x 2" o.d. tubes filled with P_2O_5, was used as the purge gas for the dry-box. Inside the dry-box there were two more driers filled with the same desiccant. After purging for a period of 16 hours, a freshly prepared catalyst sample, brought under vacuum to the dry-box, was loaded into the perfectly dried reactor and isolated by the taps. The reactor was then removed and connected to the system and all the lines were purged free of air with a high purity helium flow by turning taps B and C to vent for 30 minutes.

The catalyst was preconditioned at 345 K in a helium flow for 16 hours by turning taps B and C in line with the system. All the catalysts were found to be very active for the first pulses (approximately 20), but then the activity dropped abruptly to reach a constant level for approximately 70 more pulses when it began to slowly decrease again. For this reason a treatment of 25-30 pulses of reactant was applied to each catalyst sample before definitive measurements of the rate of isomerization were made.

The reaction temperature was set and allowed to stabilize for 16 hours. The contact time was fixed by establishing a given flow rate through the reactor (tap A open, B and C in line, and D closed). The cold trap was filled with liquid nitrogen and allowed to stabilize for 30 minutes.

A reactant pulse was injected and the reaction mixture was collected in the cold trap for 30 minutes. The reaction mixture was then flash-evaporated into the gas chromatographic carrier gas stream (A,B and C closed and D open). The mixture was separated into its components and the output from the FID displayed on a recorder.

Only three peaks were observed, and these were readily identified as but-1-ene (B), trans-but-2-ene (T) and cis-but-2-ene (C). Each peak was electronically integrated and their areas used to calculate the molar conversion as :

$$X_B = \frac{A_B}{A_B + A_C + A_T} \qquad 3.5.1$$

$$X_C = \frac{A_C}{A_B + A_C + A_T} \qquad 3.5.2$$

$$X'_T = \frac{A_T}{A_B + A_C + A_T} \qquad 3.5.3$$

whence

$$X_A + X_B + X'_T = 1 \qquad 3.5.4$$

$$X_T = 1 - X'_T = X_A + X_B \qquad 3.5.5$$

where X_B and X_C are the molar conversion of trans-but-2-ene into but-1-ene and cis-but-2-ene, respectively, X_T is the total conversion of trans-but-2-ene, X'_T is the molar fraction not converted of trans-but-2-ene and A_i is the area of the ith peak.

The contact time was calculated as the inverse of the flow rate (F). Six different contact time values were examined and not less than three injections were evaluated for each one. Each catalyst sample was studied at three different reaction temperatures.

3.5.3 Results

The information extracted from the microcatalytic system comes in the form of molar conversion of trans-but-2-ene to cis-but-2-ene (X_C or molar fraction of cis-but-2-ene) and to but-1-ene (X_B or molar fraction of but-1-ene) as a function of time (contact time or

Table 3.5.2 Molar Conversion of Trans-but-2-ene

Sample	$S \times W/m^2$	Temp/K	$X_c \times 10^2$	$X_b \times 10^2$	$t/min \times 10^2$
OS.0	3.7914	342	19.29	4.11	3.95
			18.11	3.73	2.92
			17.14	3.56	2.60
			16.42	3.46	2.30
			15.28	3.23	2.04
			13.51	2.95	1.54
		322.5	13.67	2.48	4.20
			12.16	2.24	3.11
			11.53	2.12	2.76
			10.17	1.89	2.46
			9.00	1.71	2.04
			7.87	1.46	1.52
		303	9.91	1.50	4.20
			8.32	1.29	3.02
			7.79	1.20	2.60
			7.18	1.13	2.41
			6.65	1.00	2.11
			6.02	0.93	1.71
OS.10	5.2261	342	18.10	3.71	4.20
			15.95	3.28	3.20
			14.88	3.08	2.80
			13.74	2.82	2.40
			12.58	2.56	2.02
			12.00	2.43	1.81

Table 3.5.2 (contd.)

Sample	S x W/m^2	Temp/K	X_c x 10^2	X_b x 10^2	t/min x 10^2
		326	12.43	2.18	4.20
			11.58	2.03	3.81
			9.83	1.69	3.02
			8.93	1.53	2.60
			8.46	1.46	2.41
			7.98	1.38	2.19
			7.05	1.23	1.82
		305.5	7.00	0.99	4.20
			6.25	0.88	3.58
			5.48	0.79	3.02
			4.93	0.72	2.60
			4.65	0.68	2.41
			4.08	0.60	2.02
			3.55	0.51	1.58
OS.40	2.2693	343	15.82	2.89	4.05
			14.71	2.75	3.10
			13.77	2.49	2.60
			13.16	2.42	2.27
			11.55	2.19	1.71
			10.48	1.95	1.47
		321.5	12.95	2.07	4.22
			11.67	1.89	3.28
			10.87	1.84	2.76
			9.82	1.59	2.17
			8.89	1.41	1.72
			8.45	1.35	1.54

Table 3.5.2 (contd.)

Sample	S x W/m^2	Temp/K	$X_c \times 10^2$	$X_b \times 10^2$	t/min x 10^2
		302	10.03	1.58	4.76
			9.31	1.44	4.20
			8.89	1.34	3.95
			7.75	1.21	2.92
			7.62	1.10	2.60
			6.61	0.98	2.16
OS.60	0.9223	344.5	20.44	4.30	3.95
			19.89	4.19	3.40
			19.46	4.14	3.11
			18.19	3.95	2.60
			16.58	3.64	2.16
			15.39	3.49	1.71
		325.5	16.05	2.95	4.00
			15.79	2.91	3.51
			14.99	2.86	2.84
			13.92	2.61	2.52
			12.75	2.36	2.04
			11.82	2.20	1.81
		303	13.65	2.06	4.20
			12.97	1.93	3.31
			12.12	1.82	2.75
			11.21	1.69	2.37
			10.18	1.51	2.04
			9.38	1.42	1.81
OS.80	0.7206	342	12.84	2.81	3.50
			12.11	2.68	2.92

Table 3.5.2 (contd.)

Sample	S x W/m^2	Temp/K	X_c x 10^2	X_b x 10^2	t/min x 10^2
			11.43	2.57	2.60
			10.61	2.39	2.30
			9.70	2.26	1.96
			8.96	2.12	1.67
		325	10.35	2.08	4.20
			9.70	1.94	3.70
			9.05	1.81	2.92
			8.14	1.70	2.52
			7.52	1.61	2.16
			6.62	1.46	1.71
		304	7.07	1.24	3.70
			6.31	1.12	2.92
			5.89	1.04	2.60
			5.33	0.97	2.16
			5.00	0.93	1.92
			4.52	0.83	1.71
OS.100	0.5702	344	22.88	4.63	3.95
			22.39	4.59	3.11
			22.07	4.57	2.76
			21.68	4.47	2.46
			21.09	4.35	2.04
			20.25	4.22	1.71
		321	19.91	3.47	4.07
			19.61	3.42	3.30
			18.88	3.29	2.92
			18.44	3.28	2.46

Table 3.5.2 (Contd.)

Sample	S x W/m^2	Temp/K	X_c x 10^2	X_b x 10^2	t/min x 10^2
			17.88	3.15	2.11
			17.49	3.11	1.71
		306	18.51	2.89	4.20
			18.23	2.77	3.30
			17.52	2.64	2.76
			17.03	2.57	2.46
			16.84	2.47	2.11
			15.92	2.40	1.71

reaction time). These data are collected in Table 3.5.2 for all the samples used as catalysts.

As explained in Section 1.4.2, considering the reaction system as a first order reversible reaction leads to Equation 1.4.20. This equation has been used for the treatment of data. Straight lines were obtained by plotting Ln $(X_e - X'_T)$ versus time and then rate constants were evaluated from the slopes and normalized per unit surface area. These plots are shown in Figures 3.5.3 to 3.5.5. The rate constants were plotted according to the Arrhenius equation (Fig. 3.5.6) and the activation energy was evaluated. Results were processed by least square linear regression and are summarized in Table 3.5.3.

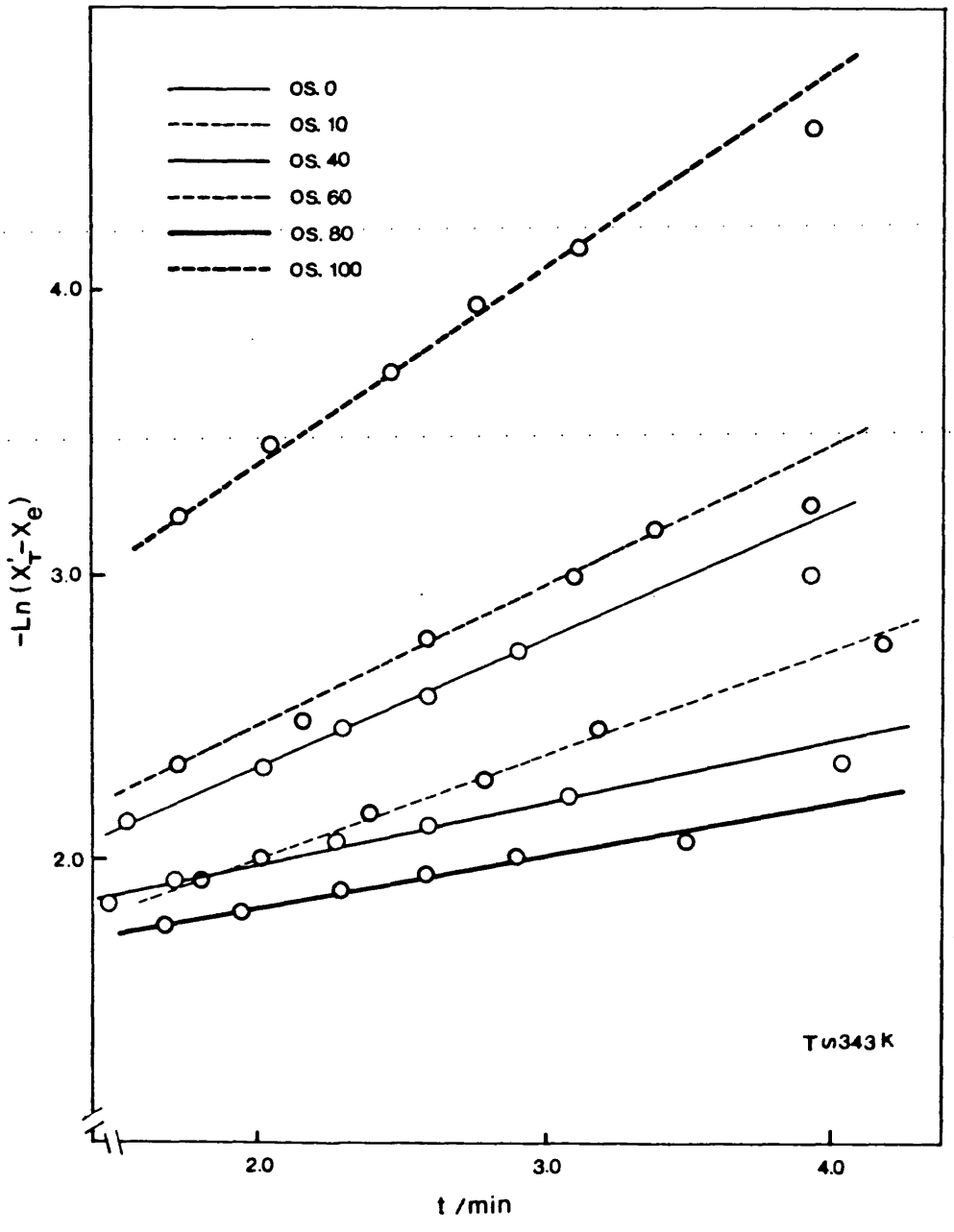

Figure 3.5.3

First order reversible reaction approximation for the isomerization of trans-but-2-ene at 343 K

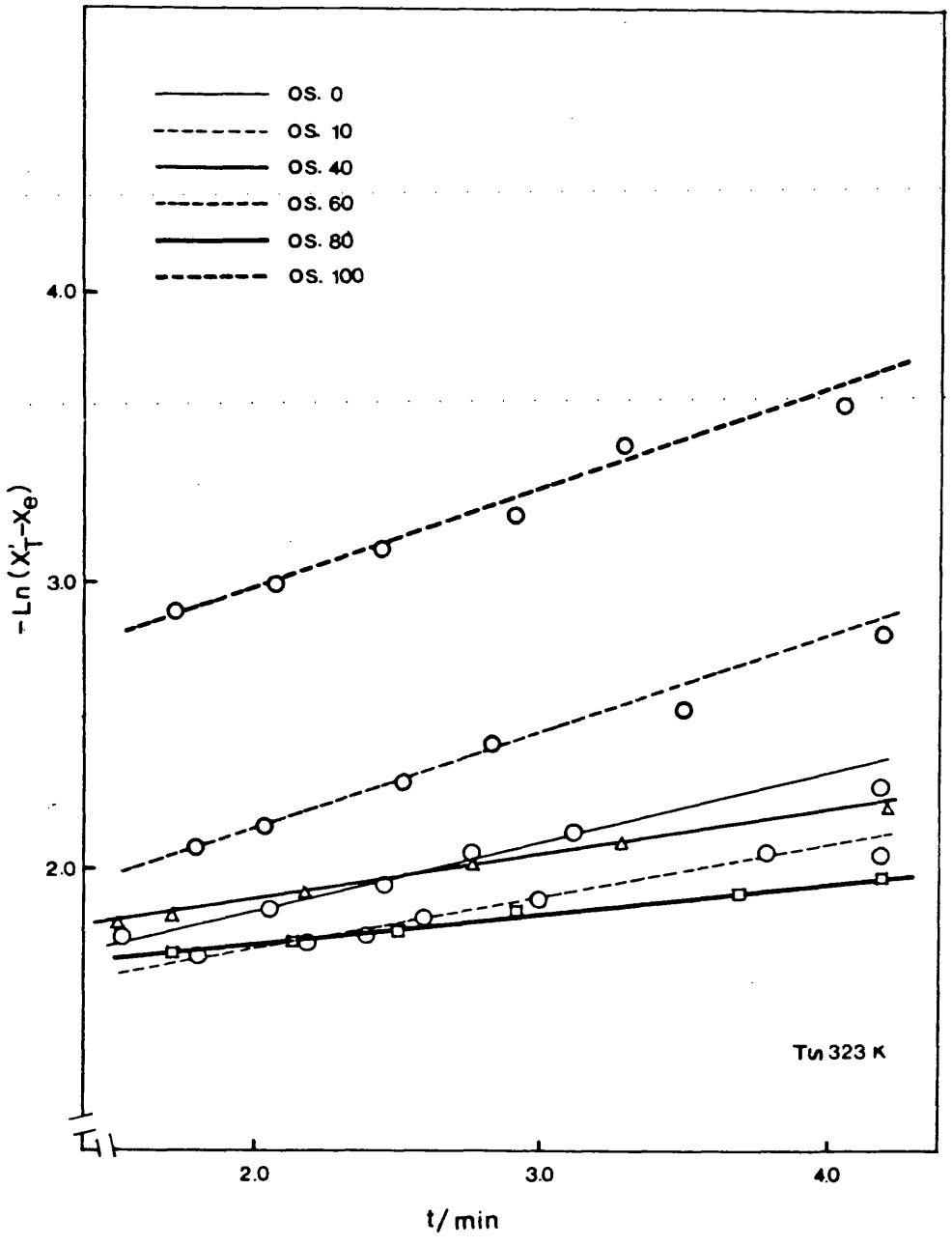

Figure 3.5.4

First order reversible reaction approximation for the isomerization of trans-but-2-ene at 323 K

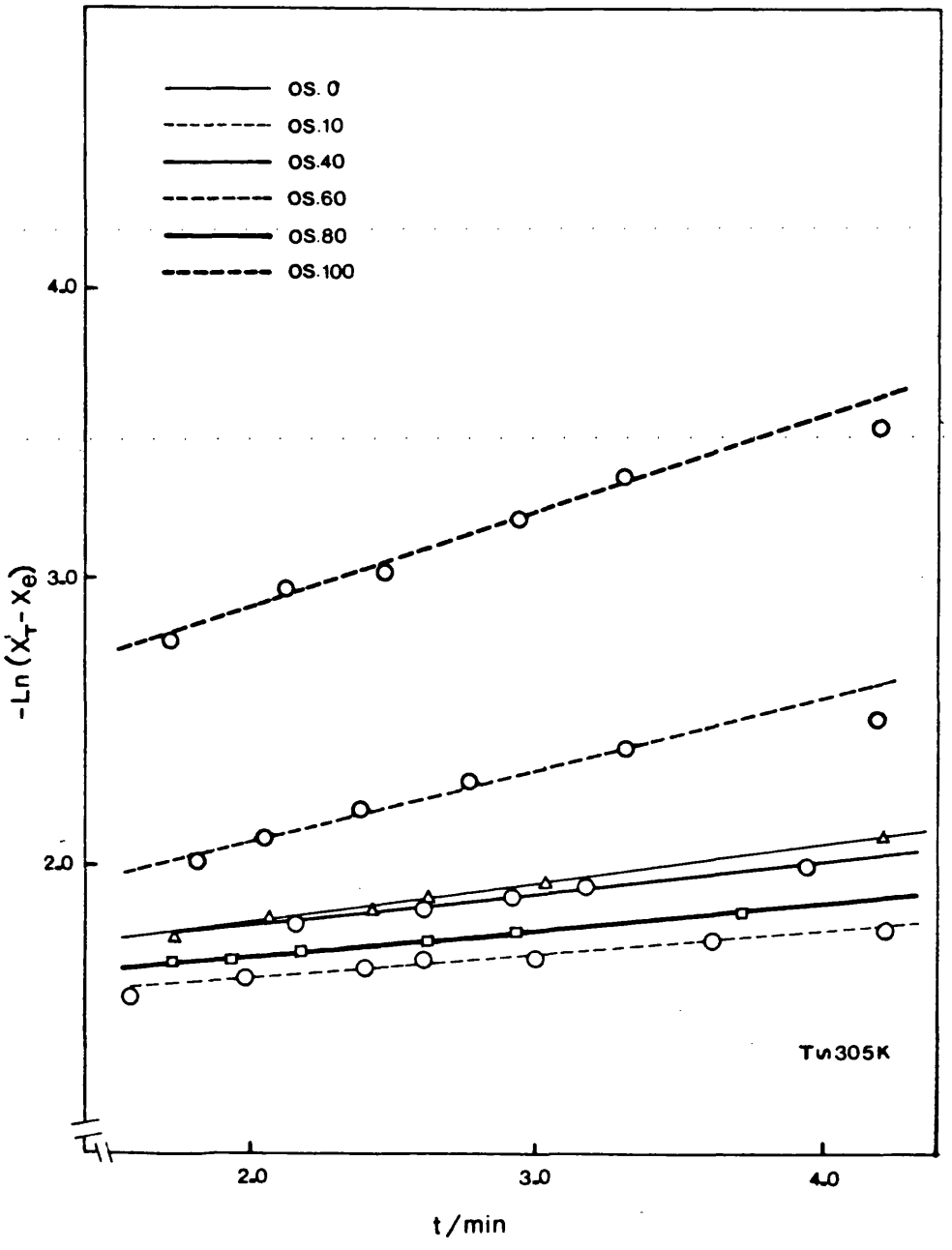

Figure 3.5.5

First order reversible reaction approximation for the isomerization of trans-but-2-ene at 305 K

Table 3.5.3 First order reversible reaction approximation : Results

Sample	Temp/K	$k/min^{-1}m^{-2}$	Ea/kJ mol^{-1}
OS.0	342	11.54	27.88
	322.5	6.03	
	303	3.26	
OS.10	342	6.24	33.10
	326	3.40	
	305.5	1.55	
OS.40	343	9.95	16.67
	321.5	6.70	
	302	4.49	
OS.60	344.5	53.43	14.01
	325.5	37.04	
	303	27.15	
OS.80	342	24.13	16.05
	325	14.71	
	304	11.68	
OS.100	344	107.30	16.76
	321	74.56	
	306	51.49	

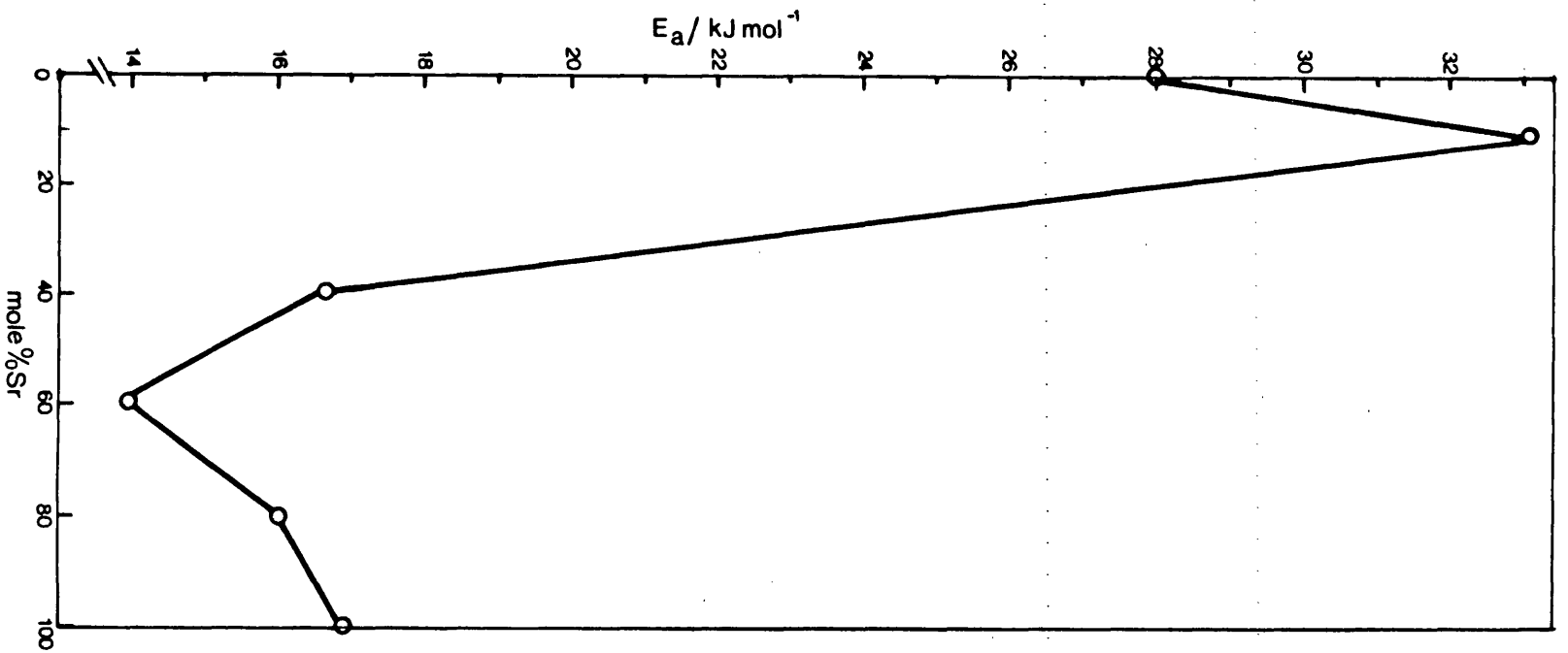

Figure 3.5.6

Apparent activation energy for the isomerization of t-but-2-ene on CaO - SrO Solid Solutions vs Composition

CHAPTER IV

4. Discussion

4.1 Double Carbonates of Calcium and Strontium

As already mentioned, the principal application of the double carbonates of calcium and strontium in the present work is on the preparation of calcium oxide-strontium oxide solid solutions for surface studies and catalysis. Consequently the investigation has focused on the possibility of achieving their conversion into the oxide solid solutions at the lowest practicable temperature, so as to yield specimens with the highest surface area. For this reason, it was important to attain a continuous single phase solid solution for the system $CaCO_3$-$SrCO_3$ and thereby have the best prospect that there would be ready transformation into CaO-SrO solid solutions.

Previous research in this field has brought out certain information about the preferential existence of the different crystallographic phases of the pure carbonates. This can be summarized in the following statements (for full details, see Section 1.1.3) :

(a) The predominance of one isomorphic form of $CaCO_3$ over another is governed by kinetic control rather than thermodynamic control (41).

(b) The calcite structure of $CaCO_3$ is favoured by slow precipitation at 290-300 K (163), by ageing (44) and by keeping supersaturation conditions (59). Ammonia inhibits the nucleation of calcite (59).

(c) Aragonite formation is favoured by slow precipitation at the boiling point of the aqueous solution (58) and by the incorporation of large cations which crystallize in the same type of structure.

(d) Vaterite is favoured by fast precipitation at 273-283 K

(163). Ageing in the mother liquor will cause it to transform into calcite.

(e) Strontianite will always precipitate at room temperature.

The present work has examined the effect of ageing, temperature and supersaturation on the coprecipitated carbonates.

(i) Series Q

Method I produced preferentially vaterite-type structure carbonates. It is very likely that the nucleation of this unstable μ-form of $CaCO_3$ is a rather fast process, faster than the nucleation of calcite or aragonite. However, in the presence of mother liquor its transformation into calcite can take place through the solubility equilibrium which in turn favours the most insoluble structure (i.e. calcite), also the most stable structure (see Table 1.1.6). The concomitant small amount of calcite in Q.0 is explained in these bases.

It can be seen in Table 3.1.2 that the incorporation of a very small amount of Sr^{2+} (0.001 to 0.1 mol %) produced a single phase of vaterite-type. So either the precipitation of calcite has been hindered or the nucleation and growing of vaterite has been assisted, or perhaps both effects have occurred. However, increasing the Sr content to more than 1% caused this effect to vanish and calcite to reappear.

The nature of a crystal nucleus is such that adsorption of additives can have a great influence in preventing the development of a nucleus of a particular structure. In many cases, also the incorporation of a foreign body can lead to the formation of an unstable solid solution with surface effects such as to preclude its growth. A third possibility is that the shape and configuration

of a particular foreign ion wil assist the rapid formation of nuclei of unstable phases which in other circumstances would not be formed. In this case a very small amount of the foreign species can be sufficient to provoke the nucleation from which the large crystals grow.

Thus, it might be possible that small amounts of Sr^{2+} helped the nucleation of vaterite but that increasing the Sr concentration caused this phase to take up an amount of strontium which produced an unstable solid solution and thus prevented the vaterite nuclei growing any further. Consequently, with the majority of the Sr^{2+} ions having become associated with the vaterite phase, nucleation of the calcite structure is no longer hindered and thus calcite began to precipitate. The change in the d_{101} of the vaterite phase was about 0.015 Å for an increase of 20% Sr content whilst the same variation in concentration only changed the d_{104} of calcite by 0.004 Å. This seems to indicate that vaterite can dissolve Sr^{2+} better than calcite. However, this vaterite would be unstable and so a limited amount of Sr can be lodged in it without hindering its formation.

Since $SrCO_3$ has an aragonite-type structure, the main effect of Sr^{2+} ions is to induce the formation of an aragonite-type phase. Thus, even in adverse conditions a concentration of 20 mol per cent of Sr or higher could provoke the formation of an aragonite phase. Table 3.1.4 reports a change in the d_{111} of this aragonite phase of 0.011 Å for an increase in Sr concentration from 20% to 40%. This indicates that Sr not only assists in the formation of the phase but also that it forms part of it.

Finally, from observation of Table 3.1.1 it can be inferred

that by Method I, more than 30 mol per cent of Sr will produce a single phase material of the aragonite type but less than 30% will yield a mixture of two or three phases with different crystallographic structures, namely vaterite and calcite, and in some cases also aragonite.

(ii) Series R

In Method II, an investigation has been made of the effect of ageing when precipitation is carried out as in Method I (series Q). However, the presence of Sr has its own effects which must be taken into consideration. Firstly, the calcite phase cannot take up much Sr and secondly it favours the formation of an aragonite phase. In other words, since ageing will favour the formation of a calcite phase and the obligatory presence of Sr will oppose it we are dealing with a method which only partially assists the formation of calcite phase.

Examination of Table 3.1.1 shows that ageing of Q.0, Q.10 and Q.20 transformed all the vaterite phase into calcite. At low Sr concentration (0.001-0.1%), where no calcite was formed by Method I, there was a calcite phase present in series R (Table 3.1.2). Thus, ageing converts the kinetically formed vaterite phase into calcite.

For Q samples with an Sr content of more than 30 mol % we should expect to obtain only one phase (of aragonite type) in the absence of ageing. However, for series R it was observed that R.40 and R.50 consist of two phases, one of calcite type and one of aragonite type. Hence, it can also be stated that ageing can also transform aragonite into calcite.

Thus, the effect of increasing Sr concentration cannot

completely annul the effect of ageing. Nevertheless, the observed decrease in the amount of precipitated calcite revealed that the increasing Sr concentration diminished the effect of ageing to a certain extent. Furthermore, increasing the Sr content from 30% to 40% could never force the calcite phase to accept more Sr than it has probably already incorporated at 30%, and so the rest has gone to enrich the aragonite phase.

Table 3.1.5 shows an interesting feature of the aragonite phase of the R series samples, mainly due to the precipitation of a calcite phase which cannot dissolve much Sr. Thus, in R.30 the d-spacing of the A-phase corresponds to a solid solution containing approximately 55 mol % Sr, whilst for R.40 it is rather less than 60% and for R.50 it is less than 70%. This tendency, of course, was expected in view of the decreasing amount of calcite phase which was precipitated. Hence these two facts together reassure that the calcite phase precipitated at 30 nominal mol % Sr corresponds to the maximum possible Sr content for that phase.

Finally, the phase distributions observed for the series R samples showed good agreement with those prepared by Ostapchenko (56), although he carried out his experiments at 363 K. We have prepared the series S samples at that temperature, but as we discuss later, our results differ from his below 40 mol per cent in Sr content. Another contradiction with his work was his affirmation that precipitation of pure $CaCO_3$ at 363 K using $(NH_4)_2CO_3$ produces calcite while Na_2CO_3 produces aragonite, whereas it has been widely demonstrated that precipitation at that temperature preferentially yields aragonite.

(iii) Series S

Method III rendered a full range of samples with the aragonite phase. Even with no Sr present mainly aragonite was formed, although some calcite was also present.

Unfortunately, this method permits the calcite phase to accommodate more Sr than the other two methods, but it must still be only a small amount since the change of the d_{104} reflection was slight (from Table 3.1.8 $\Delta d = 0.01$ Å for 30% increase in Sr concentration). The presence of calcite will cause an error in the actual composition of the aragonite phase, which is estimated as the composition of the starting nitrate solution. This minor extraction of Ca from the mixture was ignored when plotting Figs. 3.1.1, 3.1.2 and 3.1.3, so the points for the A-phase should be displaced slightly to the right. However, for all the reflections measured a good fit of their d-spacing vs. composition was observed. Hence, the amount of calcite must be small.

Regarding the A-phase itself, examination of Figs. 3.1.1, 3.1.2 and 3.1.3 and Table 3.1.6 clearly establishes that, in spite of the common structure, a continuous series of single phase solid solutions cannot be prepared across the full range of composition. These results unequivocally emphasize that a miscibility gap exists between 20 and about 40 mol per cent Sr content. There is one solid solution range from 0% to 20% Sr content (solution of Sr in aragonite) and another back from 100% to about 45% Sr content (solution of Ca in strontianite).

(iv) Series T

In Methods I-III a condition of supersaturation prevailed guaranteeing almost immediate precipitation for each drop of mixed nitrate falling into the ammonium carbonate solution. Reversing the order of mixing the solutions, as in Method IV, prevented this supersaturation condition. Thus, Method IV was expected to hinder calcite precipitation. This was also to be anticipated from the choice of 363 K as the precipitation temperature. The results, however, are rather complicated. There were always three phases present, one C-phase and two A-phases. The C-phase can be regarded as pure $CaCO_3$ as evidenced by Table 3.1.8 where no appreciable change of the d_{104} of this phase can be seen. The two A-phases constitute the most interesting feature of this preparation method. By comparing their unit cell sizes with those of series S samples (Figs. 3.1.1, 3.1.2 and 3.1.3), the Sr contents of phases A_1 and A_2 were evaluated (Table 3.1.7). We note that this attempt to force a content of 30% Sr into the A-phase results in a low limit strontianite at 50% Sr (phase A_1) confirming the position of the discontinuity in the miscibility.

The observed trends of these two A-phases on increasing Sr concentration seems to indicate that each phase has grown from different nuclei. In other words, an aragonite nucleus grows to be finally converted into what we have called phase A_2, whilst on the other hand a strontianite nucleus grows to become the A_1 phase. However, probably at 30% Sr no aragonite nuclei are formed but strontianite and calcite nuclei are produced. Thus the strontianite nuclei withdraw as much Ca as they can from

the unstable calcite aggregates (because of the temperature) giving rise to two A-phases very close in composition to the miscibility gap.

Conclusions

General consideration of precipitation reactions, which involve the kinetic aspects of nucleation and growth of crystals, suggests that there need be no direct relationship between thermodynamic stability and the order of appearance of the possible phases.

The present results on the effects of temperature and solution composition confirm this. They indicate that the form of calcium carbonate precipitated responds to favourable kinetics of vaterite nucleation and to a favourable environment for aragonite nucleation, and that production is enhanced by calcite growth inhibition. However, ageing causes the isomorphic phases to change into the rhombohedral structure of calcite, except at high Sr content where the strontianite structure prevails. This effect of ageing is in accordance with thermodynamics, since calcite is the most stable structure and also the least soluble. Thus ageing, which obviously leads to an equilibrium state, will also lead to the thermodynamically most favoured phase. First, a precipitate is formed which is rich in two phases, namely vaterite and aragonite, which will leave the liquid phase poor in Sr. Secondly, under this condition of low Sr concentration, at room temperature and with no stirring, nucleation of calcite will take place. Once the calcite nuclei are formed they will grow with no inhibition and with the limited

amount of Sr available from solution.

The presence of Sr^{2+} ions for the coprecipitation of the $CaCO_3$-$SrCO_3$ double carbonates favours the nucleation and growing of an aragonite-type phase. At 373 K calcite nucleation does not seem to be induced on free particles in solution or on glass surfaces but to occur on the surface of aragonite-like nuclei. Calcite growth probable takes place on point or line defects at locations which can give rise to the rhombohedral form.

The present experimental observations enable us to state that :

(a) $CaCO_3$ in the form of both calcite and vaterite can accommodate only small amounts of Sr^{2+} ions;

(b) increasing the temperature increases the solubility of Sr^{2+} ions in the calcite matrix.

However, the most important feature of the present investigation on the $CaCO_3$-$SrCO_3$ system is the proved existence of a miscibility gap which impedes the preparation of continuous single phase solid solutions in the full range of composition.

4.2 CaO-SrO Solid Solutions

4.2.1 Formation of the Solid Solutions

Figure 3.2.5 shows the dependence of lattice parameter with composition. There is a linear increase in lattice parameter with Sr content. This together with the fact that in the diffraction pattern no lines other than those of the expanded CaO lattice were observed is a good indication of solid solution formation.

Table 4.2.1 shows a comparison of the lattice parameters

obtained in the present work with those reported by Huber and Wagener (53), Heinz and Muenchberg (63) and the theoretical values predicted by Vegard's law. Our values are in good agreement with both Huber and Wagener and the theoretical ones, but not with those of Heinz and Muenchberg which showed a negative deviation from the theoretical values (Fig. 1.2.1). Huber and Wagener prepared their solid solutions by a method similar to the one adopted here. However, Heinz and Muenchberg prepared their CaO-SrO solid solutions by decomposing the mixed carbonates at 1873 K. As explained in Section 1.2.3, their smaller values of lattice parameter correspond to solid solutions whose compositions differ from those of the starting carbonates because of a preferential vaporization of SrO at the very high temperature which they employed.(63).

However, Heinz and Muenchberg (63) successfully attained single phase solid solution over the whole range of composition. In contrast, the present method of preparation did not yield a single phase for samples having 20 and 30 mol per cent Sr. The lower temperature seems to be the reason. A sample of OS.20 which was accidentally heated at approximately 1850 K for an unknown period of time produced an x-ray diffraction pattern with single lines of the NaCl-type. The Debye-Scherrer photograph has been included in Figure 3.2.3 as comparison, but the observed lines were so broad that the calculated lattice parameter was subject to a very high error and this introduced a large discrepancy with those reported in Table 4.2.1 and Figure 3.5.2. The conclusion seems to be that for 20 and 30% Sr a higher temperature is required for the formation of a single phase solid solution.

Table 4.2.1 Lattice Parameter of CaO-SrO Solid Solutions

% Sr	Theoretical	This Work	Ref. 53	Ref. 63
0	4.8105	4.813		4.80
10	4.8455	4.835	4.835	4.83
20	4.8804		4.843	4.85
30	4.9154			4.87
40	4.9503	4.959	4.969	4.90
50	4.9853	4.984		4.92
60	5.0202	5.021	5.020	4.96
70	5.0552	5.058		4.99
80	5.0901	5.084	5.075	5.04
90	5.1251	5.127		5.10
100	5.160	5.168		5.14

However, this would inevitably decrease surface area to a very low value, and make the solids less suitable as members of a set.

To understand the decomposition it is useful to refer again to the work of Zemtsova et al. (62) and Hall and Sharp (61). Zemtsova et al. prepared 40:60 $SrCO_3$-$CaCO_3$, obtaining a mixture of two phases, one of calcite-type and one of aragonite-type, the latter being a solid solution containing appreciable amounts of both strontium and calcium. On decomposition up to 1000 K, the highest temperature studied, they observed two stages. The first stage was the preferential destruction of the calcite-type phase. The second stage, at higher temperature, involved extraction of calcium oxide from the aragonite-type phase, producing a residue of $CaCO_3$- $SrCO_3$ enriched in strontium. The work of Hall and Sharp (61), although only very briefly reported, involved thermal analysis (DTA,TG) of the aragonite-strontianite phase. They report a small exotherm at 772 K, a loss in weight at 823-1023 K and an endotherm at 1193 K. This latter peak is characteristic for the transition of pure $SrCO_3$ from the aragonite (strontianite) structure to the calcite structure, and thereby indicates that the loss in weight stage was enriching the residue in $SrCO_3$.

On this basis it would appear that $SrCO_3$-$CaCO_3$ does not transform into SrO-CaO in a single decomposition mode. The stages involved during the decomposition procedure described in Section 3.2 can be explained as follows :

(i) decomposition of the calcite phase, if present, at 850-900 K;

(ii) partial decomposition and reorganisation of the aragonite-strontianite phase (the A phase) at 900-1000 K, yielding CaO and a residue of A phase enriched in strontium, possibly even pure $SrCO_3$ itself;

(iii) transformation of the residual A phase to the rhombohedral calcite-type structure at approximately 1200 K, followed by decomposition to the strontium-rich oxide beginning at approximately 1300 K;

(iv) homogenization of the CaO and the strontium-rich oxide into a single phase of SrO-CaO substitutional solid solution.

Conclusions

A complete range of single-phase solid solutions can be prepared for the system CaO-SrO. However, when starting from the mixed carbonates and following the heating treatment described in Section 3.2 (dynamic vacuum) a minimum temperature of 1450 K is required. Under these conditions single phase solid soultions containing 20-40 mol per cent of Sr cannot be prepared. They probably could be prepared by increasing the temperature to 1800 K, but for chemisorption and catalytic purposes a specimen heated at that temperature would experience such a reduction of specific surface area that its applicability would be greatly diminished.

4.2.2 Specific Surface Area Study

The variation of the specific surface area for CaO-SrO solid solutions is shown in Table 3.3.1. The observed change is not linear with composition but is a smooth S-shaped curve (Fig. 3.3.0). The total change is about one order of magnitude, ranging from 3.5 m^2g^{-1} to 35.5 m^2g^{-1}.

The main trend of CaO-SrO solid solutions in this regard

is to have low surface area. On producing a specimen by decomposition, physical changes take place which greatly affect its resulting surface area :

1. formation of a new pseudo-lattice from a decomposing lattice;
2. recrystallization of the formed pseudo-lattice to the most stable lattice;
3. sintering.

In practice stage 3 is operative not only in the material newly formed in stage 1, but also in the recrystallized material and the starting material which has not decomposed.

Regarding pure CaO, the value of 35.5 m^2g^{-1} is in good agreement with that reported by Glasson (164) and reveals that the heat treatment did not cause a great reduction in surface area. Glasson studied the changes associated with specific surface area during the decomposition of $Ca(OH)_2$ and $CaCO_3$ in vacuo and in air, from room temperature to 1273 K. Higher surface areas were present for CaO obtained from $Ca(OH)_2$ than those present when CaO was obtained from $CaCO_3$. During the decomposition of $CaCO_3$, CaO formed at 973 K showed a surface area of 36 m^2g^{-1} but a maximum value of 43.2 m^2g^{-1} was attained when heating at 1023 K. Assuming a value of 45 m^2g^{-1} for the specific surface area of CaO prepared by decomposing $CaCO_3$ at 1023 K, we infer a reduction of 10 m^2g^{-1} due to the heating treatment at further high temperatures.

Our results show that the initial introduction of Sr into the CaO matrix does not have a significant effect on its sintering rate. For the first 20%, Sr did not much affect the specific surface area of CaO, probably because the surface can still be rich in CaO. This can be attributed to the fact that a low

Sr content can be easily accommodated in the bulk leaving the surface with a lower content than overall. Moreover, SrO can be vaporized (53) enhancing the enrichment of the surface in Ca^{2+} ions.

From the other end, however, introduction of Ca into the SrO matrix affects its surface area to a greater extent. Addition of only 30% Ca already doubled the specific surface area. This can also be explained in terms of an enrichment of the surface in Ca. A non-homogeneous distribution of ions at the surface is suggested by the fact that the change in specific surface area did not follow a linear behaviour with composition.

It should be remembered that the OS.20 and OS.30 samples were not single-phase specimens, so their values of surface area represent an average of the two phases present. A quantitative method for the evaluation of the amount of each phase can be suggested. If surface area measurements are carried out in conjunction with x-ray diffraction analysis it is possible to identify the composition of each phase and assign them their corresponding surface area values, say S_1 and S_2. Thus, having measured the average surface area, S, if X_1 and X_2 are the molar fraction of phases 1 and 2 respectively, then,

$$X_1 = \frac{S - S_2}{S_1 - S_2} \qquad 4.2.1$$

where S has been taken as :

$$S = X_1S_1 + X_2S_2 \qquad 4.2.2$$

Hence the amount of that first phase is

$$w_1 = \frac{X_1wM}{M_2X_2 + M_1X_1} \qquad 4.2.3$$

where w is the total weight of sample and M_1 and M_2 are the average molar weights of phases 1 and 2 respectively, calculated as :

$$M_i = (1-\alpha)M_{CaO} + \alpha M_{SrO} \qquad 4.2.4$$

for a specimen with formula $(Ca_{1-\alpha}Sr_{\alpha})O$.

This method avoids having to calibrate by x-ray powder photography which would be very tedious for a system that has to be kept in vacuo and subjected to a high error. Also it would be very difficult to know the total amount of sample in the x-ray tube in order to assure the reproducibility of the calibration.

Conculsions

The specific surface areas of the CaO-SrO solid solutions are quite low, and a change of one order of magnitude was observed in the full range of composition. Introduction of Ca into the SrO matrix greatly increases the surface area. The observed change has been attributed to an enrichment of the surface in Ca due to the possible vaporization of SrO. A method has been suggested for the quantitative evaluation of samples consisting of two phases of known composition.

4.2.3 Reflectance Studies

(a) High Vacuum Spectrum and Effect of Oxygen

High reflectance values at energies higher than 30,000 cm^{-1} was a common feature of the high vacuum spectra of the CaO-SrO solid soultions. Zecchina, Lofthouse and Stone (15) have attributed this effect to fluorescence which can reach the detector because there is no monochromator between the sample and the detector. Since, the fluorescence can be quenched readily by contacting the

sample with a low oxygen pressure, it has been ascribed to a surface process and not to the presence of activator ions (Mn, Cr, etc.) dispersed in the matrix of the host material (21).

Following the Franck-Condon principle (165), excitation leads to population of the excited vibrational states of the excited electronic level. Emission of phonons returns the exciton to the minimum in the potential energy curve of the excited electronic state. Radiative decay from this condition appears as fluorescence and the emitted light has a smaller frequency than the excitation radiation (negative Stokes shift).

Two mechanisms can be considered as plausible for the quenching of the fluorescence by oxygen. The first is by a collisional (residence time) effect whereby the gas molecules interact with the excited state and merely suppress fluorescence; in other words, collisions of gas molecules with the surface allow the exciton to dissipate its energy by a non-radiative pathway (15). The second is that chemisorbed oxygen species attenuate the excitonic absorption associated with the adsorption site and therefore destroy the fluorescence (21).

Chemisorption of oxygen on CaO has been indicated by Cordischi, Indovina and Occhiuzzi (26) who confirmed the formation of O_2^- and O_3^- radicals at room temperature. In general, oxygen adsorption is associated with a part of the surface which is oxygen deficient (e.g. anion vacancies) or has a local excess of cations. O_2^- and O_3^- commonly present a hyperfine interaction in their ESR spectra on oxides with cations of non-zero nuclear spin, indicating that they are associated with a nearby cation on the surface (166). Based on this argument, Coluccia, Deane and

Tench (17) suggested that the sites of the surface responsible for the fluorescence emission are those which are oxygen deficient or have local excess of cations. The Levine and Mark model (167) has been found to be appropriate for the description of the luminescence. Edge and corner sites with coordination less than five were suggested to be responsible for this effect. Spectroscopic observation of the formation of chemisorbed oxygen species is below the limits of detection of our instrument, and as a result their bands occurring at 23,000 cm^{-1} for O_2^- (168) and 22,000 cm^{-1} for O_3^- (169) did not appear in the recorded spectra.

Hence the evidence is that oxygen interacts chemically with the surface and thus the mechanism of quenching by collisional deactication (15) can be discarded. However, in view of the low coverage O_2 adsorption does not destroy the surface states but helps to dissipate the excess energy through a non-radiative pathway by attenuating the excitonic absorption.

Garrone, Zecchina and Stone (170) have applied the theoretical model of Levine and Mark (167), and the analytical methods of Ivey and of Hilsch and Pohl (171) to the band maxima position of the reflectance spectra of the alkaline earth oxides. They arrived at the conclusion that the surface transitions are excitonic in nature. The highest energy surface exciton (bound exciton) is associated with the lowest index surface plane, while the lower energy excitons are trapped electron centres associated with higher index surface planes.

Surface exciton formation can be described most simply by the process

$$O^{2-}(2p^6) \rightarrow O^{2-}(2p^5 3s^1) \qquad (1)$$

but depending upon the extent of admixture of anion and cation wavefunction in the excited state it can also extend to include full charge transfer

$$M^{2+}(3s^{0})O^{2-}(2p^{5}3s^{1}) \rightarrow M^{+}(3s^{1})O^{-}(2p^{5}) \qquad (2)$$

The true description will vary depending upon the degree of coordinative unsaturation. The lower the coordination around the surface oxide ion, the lower will be the frequency of the surface exciton associated with it. This is because the Madelung potential is progressively reduced as coordination decreases and the overall process (1 and 2) requires less energy.

Our results in terms of exciton energies are reported in Table 4.2.2 (they have been previously shown in Table 3.3.2 as the band maxima position in cm^{-1}). A comparison with the values reported in the literature (which have been discussed in Section 1.1.2) is given in Table 4.2.3, and there is seen to be good agreement.

Regarding the bulk excitons, the effect of introduction of Ca into the SrO matrix is to move the exciton energy to higher values. This can be explained as due to the polarizing effect of Ca^{2+} ions in decreasing the ionicity of the metal-oxygen bond. The variation of exciton energy with composition for the bulk exciton absorption is shown in Figure 4.2.1 (a). The bulk exciton energies smoothly increase with Ca content in agreement with a homogeneous distribution of ions in the bulk.

However, the tendency observed for the surface excitons is quite different as can be seen in Figure 4.2.1 (b). Furthermore, the behaviour of the low energy surface exciton is slightly different

Table 4.2.2 Exciton Energies/eV

	Absorption Maxima					
Sample	Bulk Exciton			Surface Exciton		
OS.100	5.53	5.79	6.09	4.46	3.86	
OS.80	5.73	5.93	6.13	4.50	3.86	
OS.60	5.85	5.99	6.16	4.55	3.89	
OS.40	5.86	6.14		4.53	3.84	
OS.10	6.06			4.51	3.84	(5.37)
OS.0				4.38		(5.60)

Table 4.2.3 Comparison of CaO and SrO Surface Exciton Energies/eV

Oxide	This Work	Ref.(15)(16)	Ref.(14)	Ref.(21)
CaO	4.38	4.4		
	5.60	5.5	5.3	
SrO	3.86	3.9		3.97
	4.46	4.9	4.9	4.59

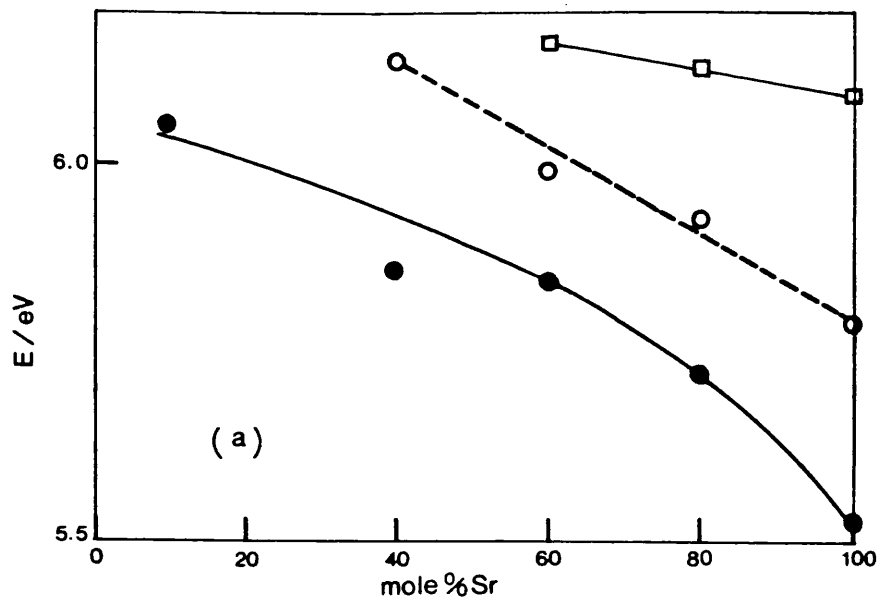

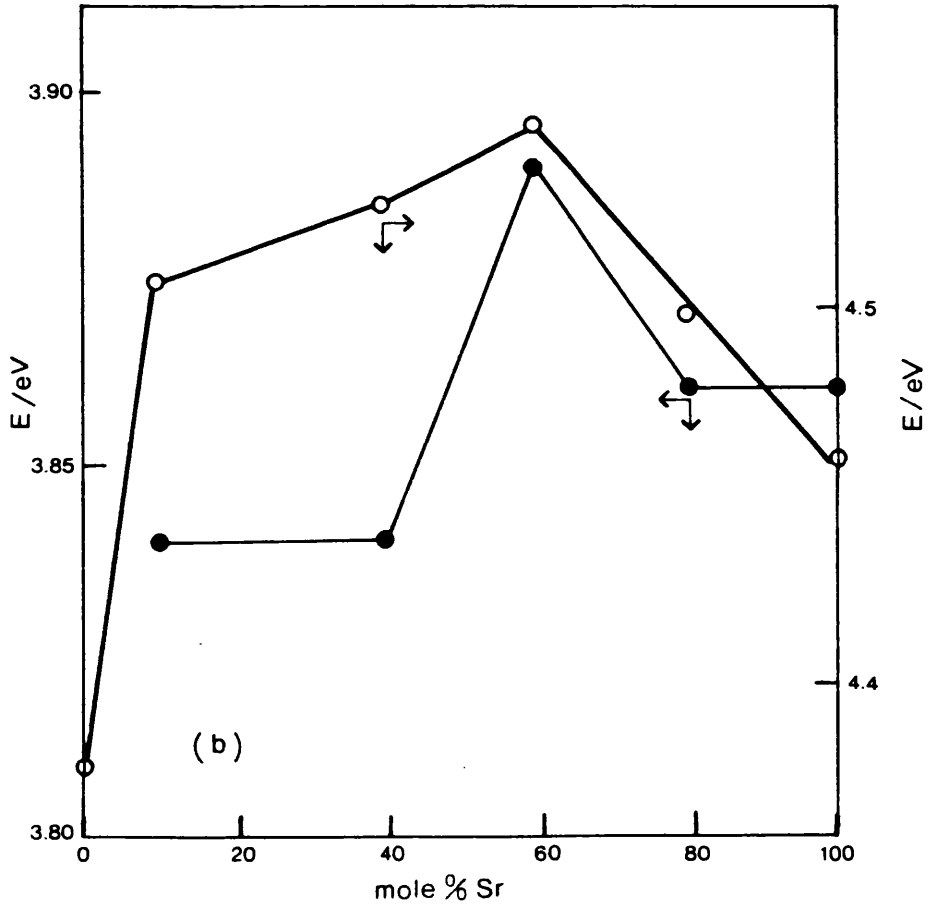

Figure 4.2.1

Band Maxima of the Reflectance Spectra of CaO - SrO Solid Solutions

a) Bulk Excitons; b) Surface Excitons

from the behaviour of the high energy surface exciton, although a common feature is observed in both of them, we come back to it later.

The higher energy surface exciton is associated with a 5-fold coordinated O^{2-} (15, 16). Six possible arrangements of cations surrounding the O^{2-} anions can occur, namely : 5 Sr, 4 Sr + 1 Ca, 3 Sr + 2 Ca, 2 Sr + 3 Ca, 1 Sr + 4 Ca, and 5 Ca. Naturally, the composition of the solid solution will determine which combination will be most common, e.g. for OS.6O the combination 2 Ca + 3 Sr would be the most probable. Similarly, the lower energy surface exciton which is associated with a 4-fold coordinated O^{2-} would have five possible combinations. From this point of view statistically the influence on the energy of the surface excitons due to the inclusion of a foreign ion in the oxide matrix would be greater on the higher energy surface exciton than on the lower energy surface exciton.

The first conclusion we can draw from an immediate examination of Figure 4.2.1 (b) is the presence of some heterogeneity on the surface. It can either be of physical or of chemical origin.

If the composition of the surface were the same as that of the bulk one would expect a continuous increase in the energy of the surface excitons with compositionon going from one end member of the series to the other (SrO to CaO). Certainly one would not expect the maximum in the energy which is observed.

To interpret these results, we may recall that the specific surface area increases froL SrO to CaO (Table 3.3.1). An increase in surface area can be interpreted as an increase in the proportion of higher index planes. Hence increasing the surface area will

increase the proportion of lower coordinative unsaturation. The primary consequence will be an increase in the intensity of the lower energy surface exciton band. This is in fact observed when Ca is introduced at increasing concentration in the SrO matrix (Fig. 3.3.4 to 3.3.9); as the specific surface area increases so does the surface exciton intensity. However, since an ion cannot be isolated from the rest of the lattice, there will be an influence on neighbour ions. Thus, as a secondary consequence, the increase in the proportion of anions with lower exciton energy (lower coordinative unsaturation) will cause a redistribution of charge (which will decrease the surface Madelung potential) and we suggest that the overall shift of the surface exciton energy to lower values is a consequence of this. This effect dominates at the Ca-rich end of the range where the specific surface areas rise steeply towards CaO.

As mentioned before, the polarizing effect is smaller for Sr^{2+} ions than for Ca^{2+}. Thus, introduction of Ca in the SrO matrix decreases the ionicity of the metal-oxygen bond and accordingly the exciton energy moves toward higher energy. For Sr-rich samples, the vaporization of SrO will have more effect than for Ca-rich samples. The surface will be richer in Ca than the bulk composition would suggest. The polarisation effect will therefore be strong, and the energy of the surface excitons will move toward higher values. However, decreasing Sr concentration will diminish this effect and a surface area effect becomes more important making the energy move back toward lower values.

Conclusions

Fluorescence has been shown to be common in the high vacuum spectra of CaO-SrO solid solutions. The quenching of the fluorescence by O_2 has been explained in terms of a chemical interaction. Chemisorbed oxygen species by attenuating the exciton absorption and creating a non-radiative pathway of energy dissipation can quench the observed fluorescence.

The bulk exciton energy increases continuously with composition from pure SrO to pure CaO which seems to indicate a homogeneous random distribution of ions in the bulk. Hence, this bulk property confirms again a substitutional solid solution formation.

The change in the surface exciton energy with composition showed a maximum at 60% Sr content. This has been interpreted as due to the simultaneous effect of the specific surface area, the polarization effect of one foreign cation in the pure oxide matrix influencing the ionicity of the metal-oxygen bond and the enrichment of the surface with Ca.

In general, the electronic structure of the solid solutions can be thought of as ranging in characteristics between those of pure CaO and SrO. Although, the electronic properties of the bulk for a solid solution can be expected to have an intermediate behaviour, the surface properties cannot be predicted beforehand. This fact indicates that each solid solution has its own surface characteristics and properties which make it a new chemical entity.

(b) CO Adsorption-Desorption Studies

The chemisorption of CO on the CaO-SrO solid solutions produced a two-band spectrum, and on SrO there was an additional band.

Table 4.2.4 collects the energy values corresponding to the band maxima. The characteristics of the bands have already been detailed in Section 3.3.2 (b) and can be summarized as follows :

- at low coverage the intensity of band B is greater than the intensity of band A
- on increasing coverage, band A grows faster than band B
- on outgassing, band B grows in the initial stages, whilst band A is preferentially destroyed.

The presence of these two bands A and B and their behaviour are in very good agreement with the results of Zecchina and Stone (20). They cannot be attributed to simple anionic species such as CO^-, CO_2^-, carboxylate, carbonate and oxalate since those species do not have absorption below $\bar{\nu}$ = 40,000 cm^{-1} (172). Paramagnetic species can also be ruled out since there is no ESR spectrum produced. A weak ESR signal has been observed when CO is adsorbed on MgO (173, 174), but the paramagnetic species present are anionic radicals (174) of the type $(CO)_2^-$ and $(CO_2)^-$ whose concentration was found to increase with increasing electron-donor capacity of the solid (CoO-MgO solid solutions in this case).

Zecchina and Stone (20) have considered anionic CO clusters to be responsible for the observed absorptions. The high energy band was attributed to a simple dimeric anionic form stabilized by the electrical field of the cations :

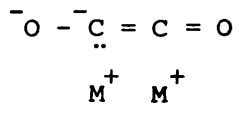

On this basis, it has been predicted that a decrease in

cation radius will increase the energy of the n → π* transition since as the ionic radius of the cation decreases the charge-radius ratio increases and so therefore does the field strength.

Thus, forms of the type :

$$\bar{O} - C = C = O$$
$$M^{+} \quad M$$

become important in the stabilization of the carbanion and consequently the energy of the non-bonding ground state is reduced.

The low energy band has been ascribed to the more complex carbanions $(CO)_n^{x-}$ where n > 2. In order to account for the low-$\bar{\nu}$ absorption, stabilization by resonance and large values of n (e.g. 4 to 7) have been introduced. Some of the proposed forms are :

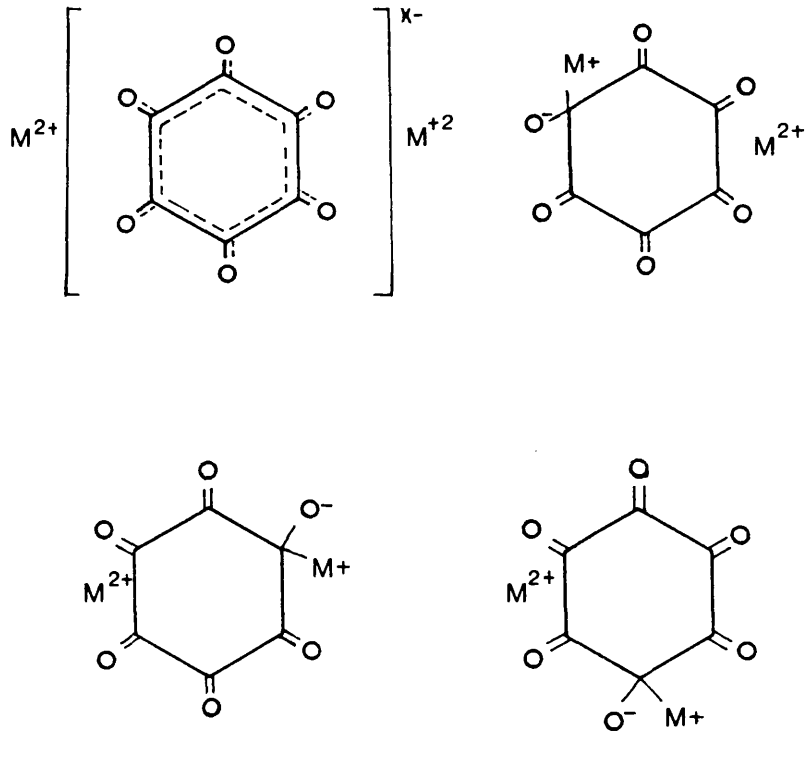

Table 4.2.4 CO Adsorption : Band Maxima/eV

	A	B	C
OS.100	2.98	3.58	4.02
OS.80	3.00	3.67	
OS.60	3.04	3.69	
OS.40	3.03	3.63	
OS.10	3.01	3.61	
OS.0	3.00	3.94	

Table 4.2.5 Ionicity fraction I and charge-lattice parameter ratio for CaO-SrO Solid Solutions (q=2+)

	I		
	(177)	(178)	q/a
OS.0	.913	.868	.416
OS.10	.914	.874	.414
OS.20	.916	.880	.410
OS.30	.917	.885	.407
OS.40	.918	.891	.403
OS.50	.920	.897	.401
OS.60	.921	.903	.398
OS.70	.922	.909	.395
OS.80	.923	.914	.393
OS.90	.925	.920	.390
OS.100	.926	.926	.387

The predicted behaviour of this band with increasing cationic size is opposite to that of the first band. The larger size of this species requires more than one surface cation to stabilize it. Increasing the lattice parameter (or, more significantly, the cationic size) will decrease the stabilization by resonance because of the steric effect necessary to accommodate the large cyclic species. It was found that MgO had the optimum lattice parameter for a good overlapping of wavefunctions.

Infrared studies on CO adsorption on MgO performed by Zecchina and co-workers (175) have produced more evidence. They postulated 10 possible adsorbed species, namely CO molecule, CO transient entities, anionic stabilized dimers $(CO)_2^{2-}$, anionic stabilized clusters $(CO)_n^{x-}$ and carbonate-like anions. It was predicted that a six-membered ring required 3 Mg^{2+} ions for stabilization and the dimers could be stabilized either by 1, 2 or 3 Mg^{2+} cations giving rise to 6 different species depending on the steric arrangement.

Anionic species of the type proposed by Zecchina et al. (20, 175) have undoubtedly been formed on the surface of CaO-SrO solid solutions. Thus, band A is ascribed to the cyclic polymeric form $(CO)_n^{x-}$ and band B to the dimeric form $(CO)_2^{2-}$. It has also been observed that the position of the band changes with the composition of the oxide solid solution, as can be seen in Figure 4.2.2 A maximum value, for both bands A and B, is again observed on OS.60, as was the case with the exciton spectra.

This time the position of the band is an indication of how well the anions are stabilized by the cationic field. Different effects have to be taken into account. A geometric factor can be stated in terms of the lattice dimensions. The cation-cation distance (and hence the lattice parameter) will determine how many cations can

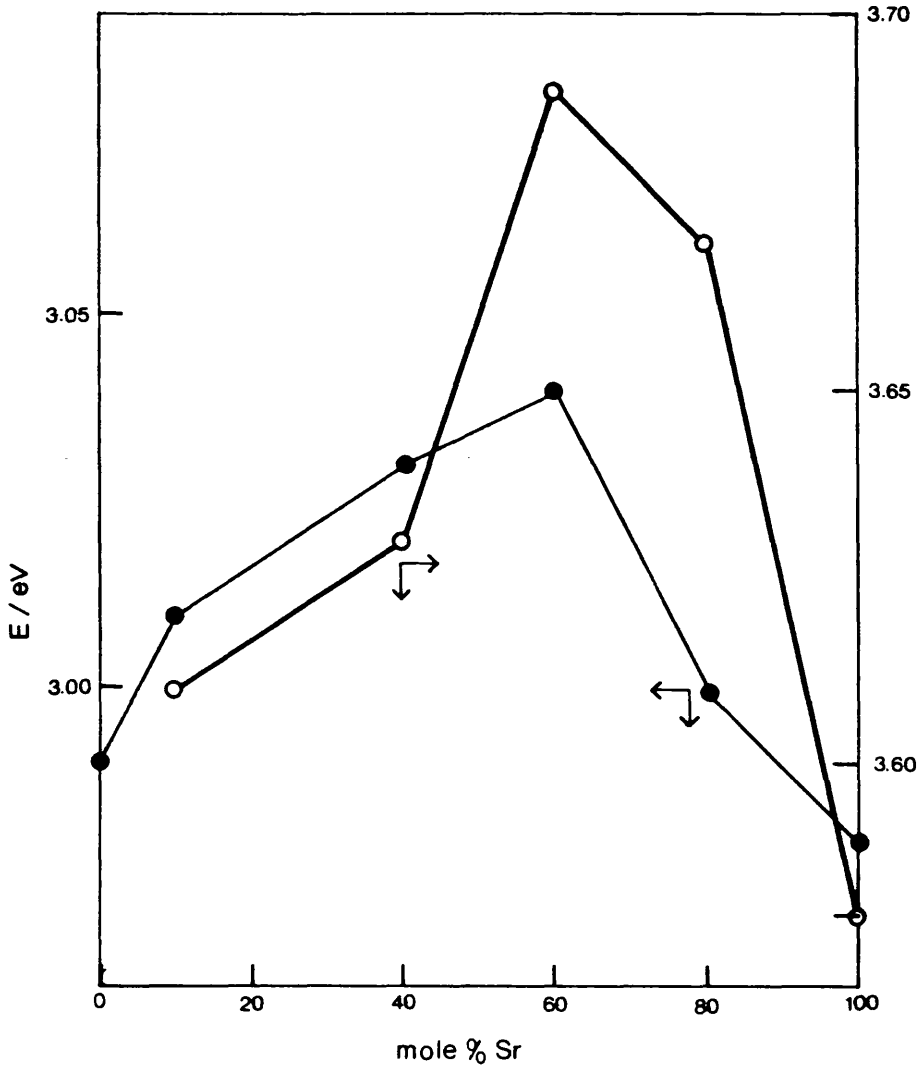

Figure 4.2.2

Band Maxima of the Spectra of Chemisorbed CO on CaO - SrO Solid Solutions

participate in the stabilization of the CO anions without causing too much steric hindrance or possibly causing the ring to open. The more cations involved the lower will be the energy of the band. However, opening of the ring will move the band to higher frequencies.

Electric field effects are also present, and they can be explained as follows. Two interrelated factors can be considered,; the ionicity of the M - O bond and the charge-radius ratio. Increasing covalency of the M - O bond will decrease the net charge on the cation. Also, as has been pointed out above (last section), the polarizing effect (and hence the charge-radius ratio) is greater for Ca^{2+} than for Sr^{2+}. These two effects influence each other. Three ionicity scales have been proposed, namely those of Pauling (176), Phillips (177) and Goyal and Tripathi (178). The Pauling scale does not indicate any change in the ionic character of the M - O bond of the solid solutions with the concentration change because $I_{CaO} = I_{SrO}$. However, the Phillips and the Goyal and Tripathi scales indicate that there is an observable change in the ionicity through the solid solution range. The predicted average ionicity from each scale, defined as :

$$I_{(Ca_{(1-x)}Sr_x)O} = (1-x)I_{CaO} + xI_{SrO} \qquad 4.2.1$$

is compiled in Table 4.2.5. Thus increasing Sr concentration increases the ionic character of the metal-oxygen bond and so the net charge on the cation (consequently the charge-radius ratio) also increases, thereby giving rise to an overall increase in the electric field strength on the cations.

The preferential vaporization of SrO from the surface layers, as explained in the last section, implies an increase in the influence of the ionic factor. We found that for Ca-rich samples the geometric factor (such as surface area) was the most important whilst on Sr-rich solid solutions it was the ionic factor. Hence, one would expect an increase in $\bar{\nu}$ due to the inclusion of Sr^{2+} in the CaO matrix (geometric factor preponderant) but $\bar{\nu}$ will begin to decrease towards Sr-rich samples where the ionic factor dominates. This is what we have observed.

Conclusions

Adsorption of CO on the CaO-SrO solid solutions leads to the formation of anionic species. A mechanism for their formation has been already proposed by Zecchina and Stone (20). The clear participation of the unsaturated coordinative surface oxygen is a decisive step in the formation of the species. However, as a charged species is being formed, it needs to be stabilized and steric requirements have to be satisfied by the surrounding cations.

A maximum for the energy of the transition involved in each band has been found to correspond to the species formed on OS.60 and has been explained in terms of ionic and geometric effects. However, this maximum is also an indication of the 'tightness' by which the species is fixed to the surface. Hence, OS.60 provides the least stabilized species and consequently the species least tightly held to the surface and so probably the most likely species to undergo further reactions.

From this point of view we could anticipate a high catalytic

activity for OS.60 because for catalytic purposes the requirement is to have chemisorbed species with a certain degree of stability but without too strong a bonding to the surface in order to permit facile surface reaction and ultimate desorption.

(c) Butene Adsorption-Desorption Studies

The effect of the initial dose of butene is to quench the fluorescence, but then additional doses destroy the absorption bands due to the surface excitons. The quenching of the fluorescence without affecting the surface exciton transition can be attributed to a physical adsorption. The butene molecules, in these circumstances, interact with the excited states and simply supress the fluorescence, probably by a collisional mechanism.

Increasing the pressure produced the spectrum of chemisorbed butene. At low coverage three bands were observed at approximately 20,000, 24,000 and 26,000 cm^{-1}, but as adsorption proceeded they merged into a single broad band at about 26,000 cm^{-1}. The positions of the band maxima are shown in Table 3.3.4. Table 4.2.6 gives the positions of the band maxima for the adsorbed butene from the present work. Also in this table are listed absorption maxima for the three butene isomers in the gas phase, as reported in the literature (179). Examination of this table shows a shift in the bands of more than 200 nm, which must imply strong chemical interaction with the surface.

Simple theory predicts the same excitation energy for the carbanion, the corresponding carbonium ion and the radical. The absence of an ESR signal when butene is adsorbed in MgO (180)

Table 4.2.6 Band Maxima Position for Chemisorbed Butene and Gas Phase Butene Isomers

λ_{max}/nm								
Chemisorbed Butene						Gas Phase Butene (179)		
OS.100	OS.80	OS.60	OS.40	OS.10	OS.0	But-1-ene	Trans-but-2-ene	Cis-but-2-ene
509	415	451	439	455	417	187	202	200
402	308	390	385	380	377	181	187	196
						175	175	175

rules out the formation of radical species. Based on the similar character of MgO, CaO and SrO it is very likely that the absorptions observed here will not be due to a butene radical.

Let us therefore consider next the electronic distribution and theoretical predictions for carbanions. The presence of an olefinic group in simple anions decreases the separation between the highest filled and lowest vacant orbitals and so reduces the excitation energy. As a result many conjugated carbanions absorb in the visible region although their corresponding parent molecules absorb only in the UV region. A basic reason for the long-wavelength absorption lies in the fact that many conjugated carbanions are odd alternant systems and consequently possess a non-bonding molecular orbital, in this case doubly filled (Fig. 4.2.3). Huckel molecular orbital (HMO) theory predicts an increase in energy of the highest energy (π) filled orbital and a lowering of the energy of the lowest energy unoccupied (π^*) molecular orbital (LUMO). Thus the presence of a non-bonding filled orbital (the highest occupied molecular orbital, HOMO) effectively halves the energy gap for the carbanion as compared to the parent olefin (Fig. 4.2.3). HMO theory can be used to justify the observed excitation energies of carbanions, but as mentioned before the magnitude of the excitation energy is not itself a criterion to make a definite assignment between carbanions, carbonium ions or radicals.

Regarding carbonium ions, HMO theory predicts a 1.4β energy gap between HOMO and LUMO in allylic cations, corresponding to a λ_{max} for the $n \rightarrow \pi^*$ transition of 275-315 nm. This is about 100 nm below the values obtained in this work but this is also a theoretical

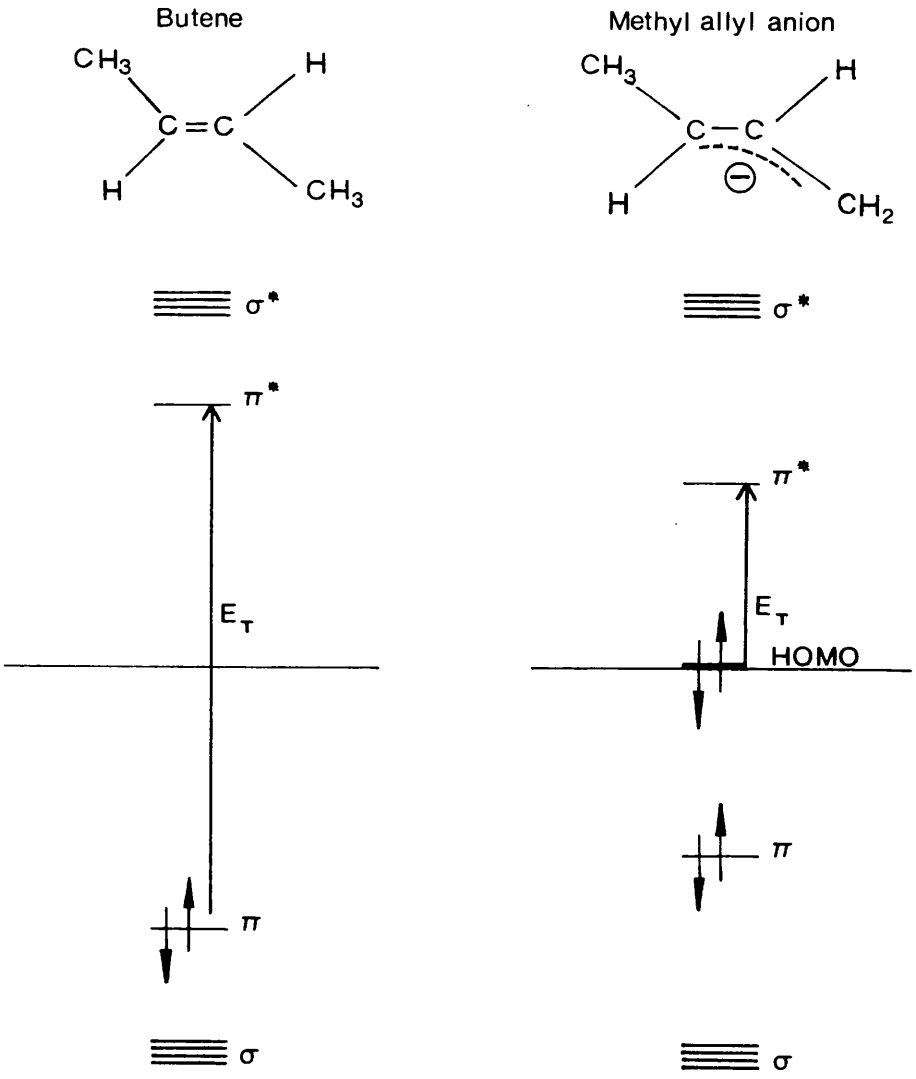

Figure 4.2.3

Energy Level Diagram for Butene and Methyl Allyl Anion

estimate which cannot be used to rule out the possible formation of carbonium ions. However, a value of λ_{max} = 290 nm has been reported for the methyl allyl carbonium ion (181) and this is certainly very low compared with our results. Triphenylmethane is one of the few systems for which spectral data are available for the molecule and for the corresponding carbonium ion and carbanion (182):

	λ_{max}/nm		
	Carbonium ion	Molecule	Carbanion
Triphenylmethane	331	256,262,269	488

It is thus evident that in spite of the theoretical predictions, differences do exist between the carbonium ion and carbanion absorption energies, and certainly stability plays a very important role in the position of the band maxima.

The disctinction between carbonium ion and carbanion cannot be made for butene on spectral grounds because of lack of data. However, we are inclined to consider the chemical nature of the surface (i.e. the strong basic character of CaO and SrO) and firmly propose that the adsorbed species correspond to methyl allyl carbanions. On this basis we attribute the observed absorptions to the $n \rightarrow \pi^*$ transitions (HOMO $\rightarrow$ LUMO) of the methyl allyl carbanion.

One may expect that this carbanion will require certain ionic and steric conditions from the surface, not only for its formation but also for its stabilization.

Theoretical calculations (107) have revealed that there are no significant differences in the charge distribution for the syn and anti conformations. This implies that the electrical

field of the surface will not influence which carbanionic conformation will be most stable. It is accordingly the geometric arrangement of cations at the solid surface which must play the decisive role in determining the preferred conformation. Thus, we can state that the formation of the carbanion is achieved by the participation of the strongly basic O^{2-} at the surface and its stabilization is then effected by a specific arrangement of cations.

The absorption remaining after prolonged outgassing indicates that a residue is left on the surface. This absorption did not consist of individual and separate bands, which suggests a possible polymeric nature for that residue.

Conclusions

Based on the chemical nature of the solid surfaces under study and on the low energy of the absorptions observed when butene is adsorbed on CaO-SrO solid solutions we have suggested carbanionic species to be responsible for the electronic transitions of the UV-Vis results. These UV-Vis absorptions have been assigned to the HOMO → LUMO ($n \rightarrow \pi^*$) electronic transitions. A residue of possible polymeric nature is formed and observed to reamin on the surface even after prolonged outgassing.

(d) Interaction of CO with Preadsorbed Butene

Before going into the details of this section, a remark on an experimental detail is appropriate. It has to be borne in mind that the amount of chemisorbed butene left on the surface prior to the admission of CO was not enough to destroy completely the surface states responsible for the exciton absorptions.

The effects of CO on the chemisorbed spectrum of butene were

detailed in Section 3.3.2, and can be summarized as follows :

- the first dose of CO immediately destroys the spectrum of the chemisorbed butene and the surface exciton absorptions and generates its own typical two-band spectrum,

- the high energy band is developed at the same position as for pure chemisorbed CO,

- the low energy band is shifted, the shift increasing with increasing Sr concentration,

- increasing Ca concentration decreases the intensity of the spectrum.

The fact that CO immediately destroys the absorption due to the carbanionic-butene species can be explained in two ways. First, it might be that the carbanionic charge is used to form the anionic $(CO)_n^{x-}$ species but that butene molecules remain on the surface interacting with the CO species in some way. Their absorption is either masked by the bulk exciton bands or lies beyond the spectroscopic range studies. Secondly, it could be that the carbanions are displaced from the surface (as butene) leaving only polymeric species whose absorption can be easily masked by the CO spectrum. To discriminate between these two possibilities it is necessary to take into account the other observations, particularly the shift of the low energy band.

Since the newly developed spectra resemble those of directly chemisorbed CO, we attribute the bands to the same type of species already discussed in Section 4.2.3 (b), namely CO-dimer anions and CO-polymeric anions. Regarding the high energy band, its position indicates that the dimeric anionic species are formed in the same surface sites in the butene-plus-CO experiment and in

the pure CO experiments. This can be easily understood if one considers that the formation and stabilization of these anionic dimers do not have strong electronic and geometric requirements. Moreover, they are the first species to be formed and could have been adsorbed on probably any of the surface sites which were available when CO was first admitted to the system.

However, the picture is much different for the polymeric species responsible for the low energy band absorption. Table 4.2.7 lists the positions of this band and the observed shift, and the variation of the shift with composition is shown in Figure 4.2.4. The fact that the band has moved toward higher energy indicates that the polymeric anions are not as well stabilized as they were when CO was adsorbed on the clean surface of the solid solutions. The electronic and geometric requirements which this species demands from the surface are rather specific.

The first possibility we will consider is that the electron transfer takes place from the butene-carbanions, i.e., the new anion charge is not directly stabilized by the surface cation field but develops by using the carbon chain as an intermediate. This can provide a better electronic delocalization and hence a better resonance stabilization. Therefore, it is difficult to discern, only on this basis, whether this mechanism of electron transfer would explain the observed shift. We accordingly turn to consider the possible effects of increasing Sr concentration and how this can affect the position of the band. Increase in Sr concentration increases the lattice dimensions and also the electron-donor character of the surface O^{2-} ions. Each of these effects leads to the same consequence. The polymeric anion will have greater net charge the greater the electron-donation. The greater the net charge the

Table 4.2.7 Low energy absorption band of chemisorbed CO when CO is solely adsorbed and when CO is added to preadsorbed butene on CaO-SrO solid solutions

	$\bar{\nu}/cm^{-1}$		$\bar{\nu}/cm^{-1}$
	CO	CO+ad-Butene	
OS.100	24,050	26,000	1,950
OS.80	24,200	25,000	800
OS.60	24,500	24,850	350
OS.40	24,450	24,600	150
OS.10	24,300	24,350	50
OS.0	24,200	24,200	0

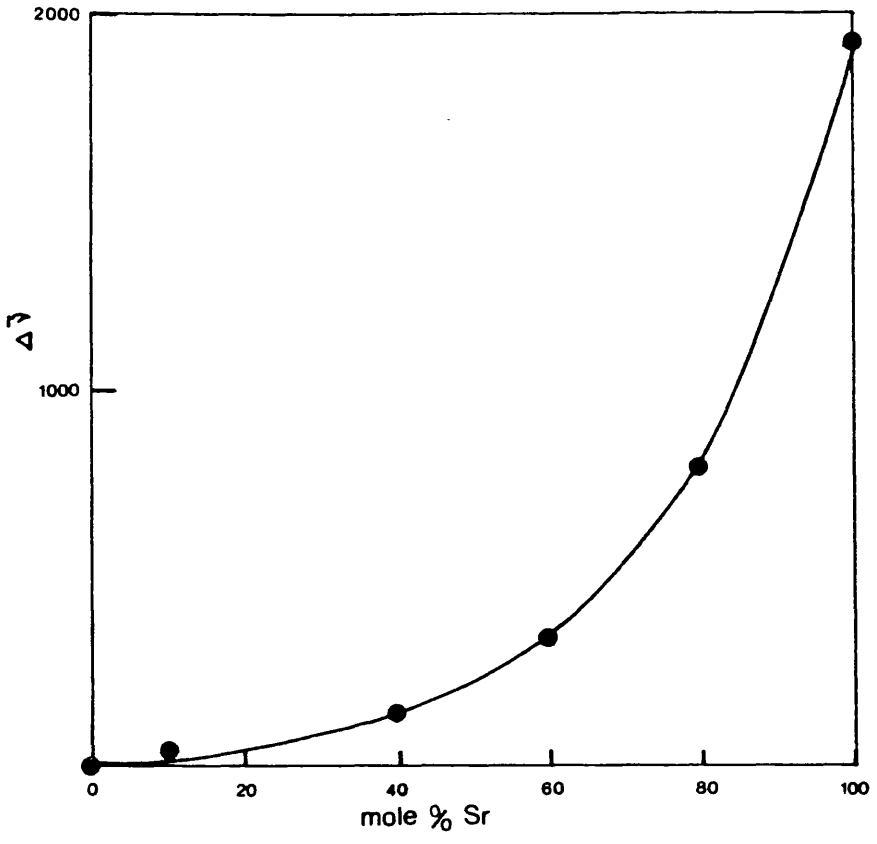

Figure 4.2.4

Spectral Shift of the Low Energy Band of Chemisorbed CO on CaO - SrO Solid Solutions carrying Preadsorbed Butene

greater the electric field needed for its stabilization. Also, the greater the lattice dimension the greater the distance between the cation and the CO-anion charges and accordingly steric hindrance will involve less stabilization. These facts together imply that the greater the Sr concentration the greater the destabilization of the CO-anions.

However, when CO was adsorbed on the virgin surface of the solid solutions we observed that this shift tendency was balanced in the Sr-rich samples by an ionic effect which was most important at high Sr content. What we are observing here is that the preadsorption of butene destroys this effect; thus the increase in the lattice dimensions has now become more important and dominates through the whole range of composition. Thus the residual butene is adsorbed on those sites where the ionic effect was dominant or is hindering their accessibility. If this hindrance is taken together with the increasing destabilization due to the increasing dimensions of the lattice, it can also cause the polymeric anion rings to open and move the band to even higher frequencies the greater the Sr concentration.

If the electron transfer were to take place from the carbanionic-butene, one would expect that the anionic-CO cluster, being further away from the surface effects, will be more unstable but also the influence of the lattice dimensions (and in general all the geometric factors which disfavour the formation of the CO-anions on the solutions with high Sr concentration) will be smaller. Thus, an effect such as the one observed would not be expected. We therefore postulate that there is no electron transfer from the carbanionic-butene species.

This leaves the second possibility mentioned earlier, namely that butene carbanions are displaced from the surface by CO, leaving only polymeric species of butene along with CO-anions. Let us recall now the observed effect of a decrease in the intensity of the CO spectrum with increasing Ca concentration. This could be an effect of the polymeric butene residue decreasing the number of available sites by simple steric hindrance, the blockage being more serious the smaller the lattice parameter.

Conclusions

The postulated carbanionic species due to butene adsorption on CaO-SrO solid solutions do not interact chemically with CO at room temperature. It can be inferred that these carbanions are probably sufficiently stable to make them unreactive towards CO but they are not very strongly attached to the surface and are thus able to be displaced.

Residual butene probably in the form of polymeric species is postulated to be responsible for the shift in the position of the low-energy CO band and the change of intensity with Ca concentration. This residual butene hinders the sites where the ionic effect is important, probably by blocking the strongest basic sites surrounded by the strongest positive charge.

(e) Butene interaction with preadsorbed CO

There is very little that can be said about the results, since butene did not have any substantial effect on the spectrum of chemisorbed CO. This series of experiments can only be used to confirm the high stability of the anionic CO clusters. However, this affirmation can only be applied to the

polymeric clusters since it was the lower energy band whose features could be followed under the experimental conditions.

General Conclusions

The reflectance studies have brought out a great deal of information on the surface properties of the CaO-SrO solid solutions.

The basic character of the surface has been brought out by the formation of anionic species when neutral molecules were allowed into contact with the solid. The basic properties of the surface are governed by different factors. Besides the strength of the surface O^{2-} ions, factors such as the ionicity of the metal-oxygen bond, the cationic field strength, the surface area (taken as the proportion of lower coordinatively unsaturated surface O^{2-}), and the lattice dimensions (as a geometric factor introduced by the steric requirements of the adsorbate) also affect the overall basicity.

In these terms each solid solution behaves as a new, individual and different entity with surface properties which cannot be interpolated from the properties of the pure oxides. In particular, OS.60 presents special characteristics in the series indicative of especially strong basic properties suggesting that it should have the highest catalytic activity in base-catelyzed reactions.

Activity towards polymerization was found to exist at room temperature. CO can be polymerized and cyclized, and butene can be polymerized. The polymerization reaction can inhibit further reactions by the polymer blocking the basic sites.

4.2.4 E.S.R. Studies

(a) Nitrobenzene as adsorbate

The observed three-line spectrum can be interpreted as due to the anisotropic interaction with a nitrogen atom. Nitrogen with a nuclear spin I=1 is normally expected to give three lines (2I+1) of equal intensity; however, when any hyperfine anisotropy is present a different situation will arise. In solution where a molecule is tumbling rapidly the anisotropic interactions vanish. In the adsorbed state with movement restriction they will appear. The fact of having a three-line spectrum and the absence of proton hyperfine interactions suggests that we probably have a nitro-radical on the surface of CaO-SrO solid solutions. The axial g-tensor and the observed hyperfine splitting indicate that the electron is localized in the 2p orbital of the nitrogen atom. Such localization of the electron on the nitro-group would be expected for a strongly adsorbed species.

The adsorbed nitrobenzene anion radical has been widely studied by means of UV-Vis reflectance spectroscopy (21, 24, 183) and by ESR spectroscopy (183-185). The g-values have been determined for different solid surfaces, for instance on CaO (24) g_{av} = 2.0043, on MgO (183) g_{av} = 2.0037, in alumina (184) g_{av} = 2.0048 and on ZnO (185) g_1 = 2.0225, g_2 = 2.0055 and g_3 = 1.9840. A value of g_{av} = 2.0044 has been reported for the anion radical in the solid state (186). Our values (listed in Table 3.4.1) are in good agreement with those mentioned above. The observed three-line spectrum is therefore attributed to the anion radical of nitrobenzene.

The formation of these anion radicals involves an electron transfer from the surface ions to the neutral NB molecule. The participation of transition metal impurity ions can be excluded because firstly, the spectrum (e.g. Mn^{2+}) did not change after adsorption and secondly the intensity of the NB spectrum shows too high a spin concentration.

A possible mechanism for chemisorption involves a direct electron donation from a lattice O^{2-} ion on the surface to the adsorbed NB molecule, as follows :

$$O^{2-} \rightarrow O^{-} + e^{-}$$

$$NB + e^{-} \rightarrow NB^{-}$$

Because of the high electron-donor character of the O_s^{2-} and the high electron-affinity of the NB molecule this mechanism is very plausible. Another possibility is dissociative chemisorption of nitrobenzene, yielding H^{+} and $(C_6H_4NO_2)^{-}$, followed by electron transfer from this anion to another molecule of NB, producing the radical anion (180). The end result is the same. The surface concentration of radical species reveals that only approximately 0.02% of the surface O^{2-} are involved in the chemisorption process. If we consider the large area occupied by each NB anion of approximately 160 $\mathring{A}^2$ (183) which can block ~25 O_s^{2-} it implies that the low proportion of O_s^{2-} involved in chemisorption can be partially due to the inaccessibility of these O_s^{2-} ions. However, this cannot be the only reason because the proportion of O_s^{2-} ions impeded from chemisorbing NB is only ~0.2%.

The second postulated mechanism which involves the dissociative chemisorption of NB leads to the formation of many non-paramagnetic

species. Thus, the blockage of the surface for those non-paramagnetic species leaves only a fraction of sites available for the formation of the NB anion radicals.

However, we suggest that the formation of the anion radicals introduces further geometric and electronic requirements which can be fulfilled by only a fraction of surface sites. Next, we consider the experimental evidence of that.

Comparison of the tendencies shown in Figs. 3.4.9 and 4.2.2 reveals a very interesting feature. This comparison is made in Figure 4.2.5 where the curve from Figure 3.4.9 corresponds to the change of spin surface concentration with composition of the CaO-SrO solid solutions and the one from Figure 4.2.2 the change of band maxima position of chemisorbed CO with composition. It seems that the same geometric and electronic requirements are involved in both processes. We therefore postulate that chemisorption of NB takes place on the lower coordinatively unsaturated O_s^{2-} and the resulting NB anion radical is additionally stabilized by the cationic electrical field.

The presence of a singlet line at high coverage is due to dipole-dipole interactions. Spin-spin dipolar interactions exist because of the magnetic field associated with the electron magnetic moment. If another unpaired electron is at a distance r, the magnitude of this field at the electron can take any value between $\pm\mu_e/r^3$ depending on orientation. Electron spin exchange consists of a bimolecular reaction in which the unpaired electrons of two free radicals exchange their spin states. Finally, electron transfer between a radical and a diamagnetic species is another cause of line broadening arising from dipole-dipole interaction.

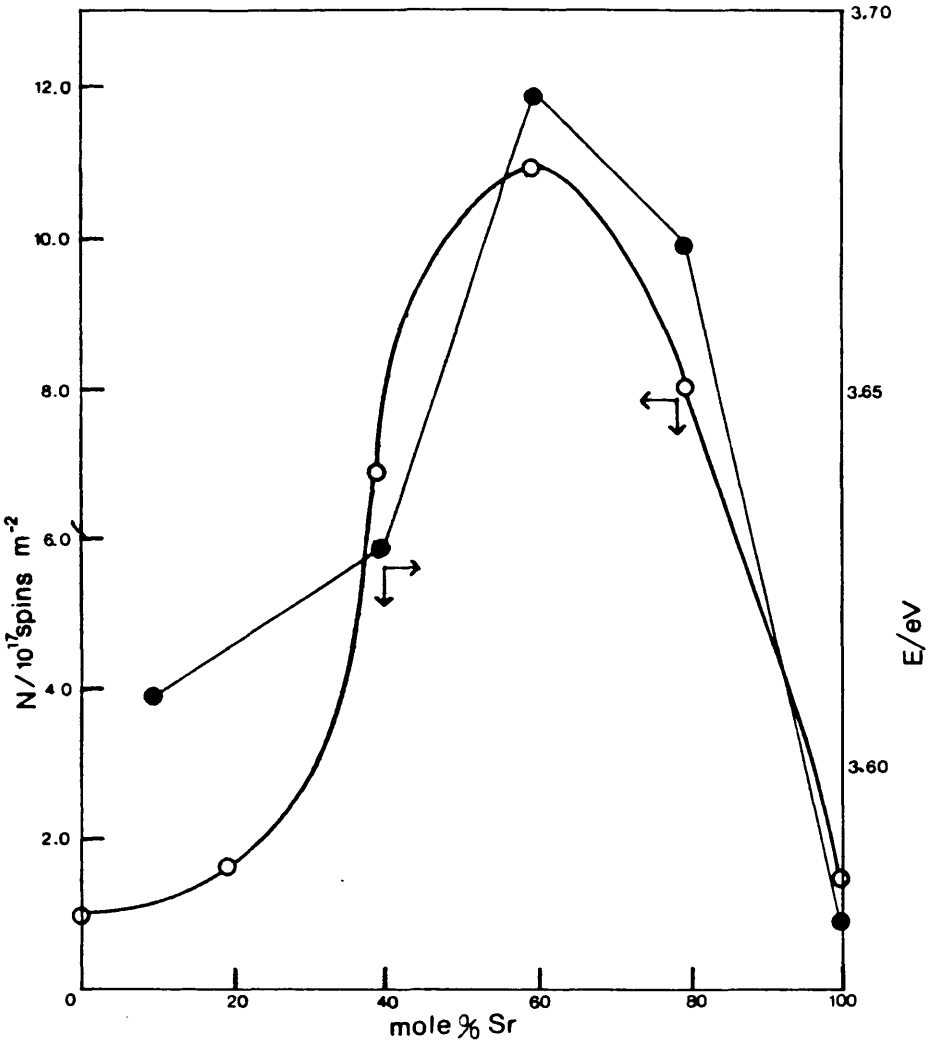

Figure 4.2.5

Surface Radical COncentration of Chemisorbed Nitrobenzene and Low Energy Absorption Band for Chemisorbed CO vs. COmposition of CaO - SrO Solid Solutions

An increase in the linewidth on increasing coverage has been observed when NB was adsorbed on CaO (24). Evacuation by heating decreased the linewidth. This indicated that decreasing the amount of adsorbed radical anions diminishes the interaction which causes line broadening. The analysis of the spectra at temperatures ranging from 77 to 373 K at the same adsorbed amount also indicated that no factors other than dipole-dipole interaction affect the linewidth. The magnitude of ΔHpp was ~18 gauss.

Therefore, our singlet line of g_{av}-value ranging between 2.0025 to 2.0049 (Table 3.4.2) and with ΔHpp of 15-20 gauss can still be attributed to the NB anion radicals. The lack of hyperfine splitting is only due to dipole-dipole interactions caused by the proximity of the anions.

Conclusions

The ESR spectrum observed when nitrobenzene is adsorbed on CaO-SrO solid solutions is due to nitrobenzene anion radicals. The chemisorption process involves an electron transfer from the low coordinatively unsaturated O_s^{2-} or from dissociatively chemisorbed NB and the stabilization of the formed anion radicals by the cationic electrical field.

The surface concentration of NB anion radicals is a measure of the activity of the surface towards anion formation in general. OS.60 which shows the highest spin concentration can be expected to have the highest catalytic activity among the solid solutions toward reactions involving anionic intermediates.

The lack of hyperfine splitting at high coverage is due to purely dipole-dipole interactions caused by the proximity of the adsorbed anion radicals.

(b) Oxygen as Adsorbate

Three different anion radicals have so far been identified by ESR specroscopy as arising from oxygen adsorption, namely O^-, O_2^- and O_3^-.

The O^- spectrum depends upon the energy level configuration and separation in the oxygen 2p orbitals. In a tetragonal symmetry an axial g-tensor is expected with

$$g_{zz} \sim g_e$$

and

$$g_{xx} = g_{yy} = g_e + 2\lambda/\Delta E$$

where λ is the spin-orbit coupling constant. For orthorhombic symmetry a three-component g-tensor should be observed. Tench et al. (187) have reported the spectrum of O^- on MgO which was characterized by $g_{xx} = 2.0016$, $g_{yy} = 2.0297$ and $g_{zz} = 2.0505$, the outermost components being the strongest. This radical is rather unstable even at 77 K (188) but it may be stabilized by forming complexes with other molecules (166).

The superoxide ion O_2^- has been widely studied on surfaces because of its ease of formation and stability. An extensive analysis of its spectrum has been given by Lunsford and Jayne (173). Cordischi, Indovina and Occhiuzzi (189) have reported the g-tensor components for O_2^- on MgO as follows : 4-component g_z ranging from 2.0623 to 2.0895, $g_y = 2.0074$ and $g_x = 2.0012$, the g_z being rather small and the high field component the strongest.

The ozonide ion O_3^- was formed by a fast reaction between O^- and O_2. Wong and Lunsford (190) have obtained O_3^- on MgO; a g-tensor with the following components was reported $g_1 = 2.0172$, $g_2 = 2.0100$ and $g_3 = 2.0014$. Tench (191) has demonstrated that the

O_3^- radical on MgO was somewhat unstable and slowly dissociated into O_2^-.

The spectra obtained in the present work when O_2 was adsorbed on the CaO-SrO solid solutions at 298 K are rather complicated. The shape of the signal does not resemble any of the signals described above. However, it looks as though there is overlapping of the O_2^- and the O_3^- signals. Furthermore, careful examination of the spectra reported in Figs. 3.4.10 to 3.4.15 shows a very broad and weak signal centered at approximately g = 2.05. With the exception of OS.0 (CaO) we assign the g_1 and g_3 values listed in Table 3.4.4 as due to O_3^-; the g_2-value arises from both O_2^- and O_3^-. Finally the broad band at g ~ 2.05 confirms the presence of O_2^- since it can be interpreted as the g_z-component of an O_2^- species. On OS.0, for which a better resolution was attained, the assignment is rather easier. g_1, g_2 and g_5 correspond to O_3^- and g_3, g_4 (and probably g_5) correspond to O_2^-. These results are in agreement with the observations of Cordischi, Indovina and Occiuzzi for O_2 adsorbed on CaO (26).

The broadening and new shape observed when the gas phase was not removed seems to indicate that the O_3^- concentration increases at the expense of the O_2^- species.

Table 3.4.6 lists the g-values for the signals recorded one month after adsorption. Although the intensity of the signals decreased, their shape inclines us to think that they are due to O_2^-, the lack of observation of the broad component (at g ~ 2.05) being explained by its having decreased to the noise level. Thus we postulate that the O_3^- species have decayed completely, but also the O_2^- species have decayed to some extent causing the overall intensity of

the signal to decrease.

Lowering the temperature of the sample during recording revealed a more intense spectrum which very closely resembles the O_2^- spectrum. The temperature effect on the intensity is a purely statistical effect. A more favourable Boltzman distribution of electron spins between the two allowed energy levels enhances the detection sensitivity and consequently increases the intensity of the signal. However, decreasing the temperature greatly affects the linewidth by its effect on the spin-lattice relaxation time. Thus the shifts observed in the g-values are an artefact of the error introduced by the line broadening effect (i.e. lack of resolution).

The observation that anionic species can be formed by the direct exposure of the clean surfaces to O_2 is rather relevant. It emphasizes the very strong electron-donor character of these solids. Apart from the work of Cordischi et al. (26) on CaO, most authors dealing with alkaline earth oxides had obtained the formation of O_2 anionic species either by induction using preadsorbed molecules or by activation of the surface using irradiation or neutron bombardment.

Conclusions

This short and introductory study of the oxygen adsorption on CaO-SrO solid solutions has revealed that there is no need for induction by preadsorption or activation by irradiation of the surface to form the anionic O_2^- and O_3^- species. They have been formed on the surface by a direct electron transfer from the lattice.

The small intensity of the signal compared to that obtained when nitrobenzene was adsorbed indicates that an even smaller fraction

of the surface sites are involved in the chemisorption of O_2. This very small fraction must be the really strong electron-donor site.

General Conclusions

The use of ESR spectroscopy has allowed the detection of paramagnetic species formed on the surface of CaO-SrO solid solutions when neutral molecules are adsorbed.

Nitrobenzene adsorption produces nitrobenzene anion radicals and oxygen adsorption yields superoxide ions and ozonide ions. The formation of these species involves an electron-transfer from the lattice to the adsorbed molecule. Accordingly the concentration of paramagnetic species can be used as a measure of the activity of the solid towards reduction reactions. On this basis, OS.60 is expected to be the most active catalyst in the series for this type of reaction.

The fact that nitrobenzene uses a fraction of the surface sites and oxygen uses an even smaller fraction indicates that by choosing the appropriate molecules a complete evaluation of the site distribution might be possible. Simple molecules with different electronic affinities whose anionic ESR spectrum is easy to interpret and evaluate will facilitate this task.

4.3.5 Catalytic Studies

The isomerization of trans-but-2-ene was chosen as a model reaction for the comparison of the catalytic activity of the CaO-SrO solid solutions.

The complete evaluation of the kinetic parameters of this unimolecular reacting system, as detailed by Pines and Haag and

described in Section 1.4, is very complicated. Many authors have attempted the solution, but none have yet succeeded. The treatment of Pines and Haag has been applied to the present results (see Appendix), but again complete evaluation has not proved possible. The different methods of non-linear multiparameter evaluation, namely steepest descent, neighbourhood search and the quasi-Newton algorithm (191) did not yield a good fit of the data. As with previous authors, this can be attributed to two factors, the limited amount of experimental data and the experimental error of the data. The triangular system, which is considered here, involves six rate constants inter-related by the equilibrium constants. When a heterogeneous catalytic reaction is to be considered even this complicated approach of Pines and Haag is only an approximation. No adsorption desorption steps have been considered, in other words the interaction with the catalyst has been ignored. Kallo (192) has very recently introduced the effect of the catalyst participation into the kinetic evaluation of parameters. He proposes the kinetic solution of different mechanistic schemes. However, the limited amount of data obtained in the present study prevents application of this treatment. We therefore were left with the option of applying the simplified treatment of a first order reversible reaction, as used by previous authors. Our results have been reported in Table 3.5.3. In spite of its simplified form, this treatment will allow us to make a comparison of the activities of the catalysts.

The activity of a catalyst is formally defined as the rate of the catalytic reaction at a given composition, pressure and temperature. However, it is often difficult to determine reaction

rates under the same conditions when comparing different catalysts. For example, examination of Table 3.5.2 shows that a comparison based on reaction rates under the same conditions cannot be performed in the present case because the range of conversion varies among the catalysts. Furthermore, using the micorcatalytic technique the partial pressures of the reactant and products are unknown.

Activity therefore has to be defined more elastically. In some cases, composition and pressure are kept identical and activity is defined in terms of the temperature at which the reaction rates are the same. This definition of activity carries the same difficulties as the first one when one is making use of the micro-catalytic technique. Conversions are sometimes used as a criterion of activity, but in our case it would be subject to error because of the high differences in surface area of the catalysts.

A better approach to compare activities can be achieved when both surface area and kinetic parameters are available. In these cases, specific activity is defined as the activity per unit surface area. Thus, specific rate constants constitute a measure of the activity. However, in view of the compensation effect this is not always valid. The experimentally measurable activation energy of a reaction is an average of the different activation energy values characteristic of the sites of varying activity. In other words (and considering the surface reaction as the rate controlling step) the heterogeneity of the surface implies the presence of different sites with different catalytic activity. Consequently, the activation energy and preexponential factor might compensate each other to give the same rate constants and a false interpretation of the activity. Thus the activation energy can be a better scale

of comparison; furthermore, it does not depend upon the units in which the rate is expressed.

We shall therefore base our activity comparison on the values of the activation energy listed in Table 3.5.3.

Little research has been done on the isomerization of trans-but-2-ene. Most of the reported data refer to but-1-ene and cis-but-2-ene. On transition metal oxides (110) activation energy values ranging from 25 to 130 kJ mol^{-1} have been reported for both the isomerization of but-1-ene and cis-but-2-ene. On the alkaline earth oxides, the activation energy has been evaluated only for MgO and only for but-1-ene isomerization, and a value of 18.4 kJ mol^{-1} has been reported (106). Activation energy values in the present work range between 14 and 33 kJ mol^{-1}. These are lower values than are found for isomerization of butenes on alumina and silica-alumina (Ea ~ 40-80 kJ mol^{-1} (101, 102)), and are consistent with the high activity of the present oxides in catalyzing isomerization at 30^{o}- 60^{o}C.

The variation of activation energy observed in the range of catalysts studied is shown in Figure 3.5.6. Two features can be distinguished, a maximum at OS.10 and a minimum at OS.60. This minimum on OS.60, corresponding to the highest activity in the series, agrees with the expectation derived from the analysis of the surface properties (Sections 4.2.3 and 4.2.4). This also indicates that the isomerization of butene on CaO, SrO and their solid solutions occurs via a carbanionic mechanism, as has been widely proposed and accepted for basic catalysts (104-106). The maximum value at OS.10 is not significantly greater than that for pure CaO.

Another important feature is the preferential formation of cis-but-2-ene from trans-but-2-ene. Selectivities calculated as the

ratio X_c/X_b decrease with increasing temperature, the values ranging between 4 and 7 approximately. The favoured formation of cis-but-2-ene from but-1-ene has been explained as due to the better stabilization of the anti conformation of the π-allyl carbanion by the cationic field (106). However, since the π-allyl carbanion from trans-but-2-ene corresponds to the syn conformation, further explanation is needed. Thus, the preferential formation of the cis-isomer in this work is even more relevant, especially if we consider the low values of the activation energy.

Considering the relative magnitudes of the rate constants in the triangular system (see Fig.1.1 in the Appendix), if k_3 and k_5 are high compared to the back reactions, if $k_1 \sim 0$ and if $k_5 >> k_3$, then the preferential formation of cis-but-2-ene involving a low average activation energy will be explained. This is because but-1-ene will be an intermediate for the trans-cis conversion and but-1-ene can without restrictions, yield either conformation of the π-allyl carbanions. However, the impossibility of determining the relative magnitudes of the individual rate constants prevents us from discussing this kinetic explanation in more detail.

A mechanistic explanation is that a common intermediate for the direct trans-cis conversion exists, and thus the anti-syn conversion is not precluded. This can only be achieved if a transformation from π-allyl to a σ-allyl carbanion is possible. In this way a σ-allyl carbanion, being less restricted in rotation, could mediate in the exchange between the anti and syn conformations. Furthermore, if this is the case here, it would imply that the anti-syn transformation is a fast process involving a low activation energy. Unfortunately, more data are required for a detailed discussion and descrimination

of these two possibilities, and so far we cannot propose which of them will be valid.

Conclusions

The isomerization of trans-but-2-ene takes place on the CaO-SrO solid solutions under very mild conditions. The catalysts have been found to be highly active towards this reaction, with activation energies of 14 to 33 kJ mol^{-1}. The low value of the total conversion (not greater than ~ 25%) is due to the thermodynamic limitations of using trans-but-2-ene (the most stable isomer) as reactant. A preferential formation of the cis isomer has been found and two possible explanations have been proposed. However, the limited amount of available data prevented the postulation of a unique explanation.

OS.60 has been found to be the most active catalyst and this has been attributed to its basic properties which also confirm that a carbanionic mechanism should be operating.

4.3 General Conclusions

The present research has been concerned with calcium oxide and strontium oxide and their solid solutions.

Double carbonates of calcium and strontium were found to be suitable as starting materials for the preparation of CaO-SrO solid solutions. However, phase characterization of the co-precipitated carbonates showed that they do not form a single phase solid solution through the full range of composition, but instead that there is a solid solution below 20% Sr content (solution of Sr in aragonite) and another back from 100% to ~40% (solution of Ca in strontianite) with a two-phase region between 20-40% which defines

the miscibility gap.

CaO-SrO was found to form a single phase solid solution in the full range of composition. The lattice parameter increases linearly with the mol % of Sr content.

Application of UV-Vis diffuse reflectance spectroscopy and of ESR spectroscopy have provided a great deal of information on the surface properties of the CaO-SrO solutions. The ease with which they transform a neutral molecule into anionic species indicates high basicity.

The factors which govern the surface properties of CaO-SrO may be summarized as follows :

1. Structural effects

(a) Lattice dimensions. Increasing Sr concentration increases the lattice parameter; accordingly the cation-cation distance increases and thus can counteract the stabilization of the anionic charge of the adsorbed species.

(b) Surface area. Increasing Sr concentration decreases the surface area which can be interpreted as a decrease in the proportion of higher index planes. Accordingly the proportion of O_s^{2-} with lower coordinative unsaturation will decrease and so the overall surface Madelung potential will increase.

2. Ionic and electronic effects

(a) Polarizing effect. The greater the polarizing effect the smaller the net charge on the cation and the smaller its electrical field. Ca^{2+} has a stronger polarizing effect than Sr^{2+}.

(b) Ionicity of the metal-oxygen bond. Increasing Sr^{2+} concentration increases the ionicity of the metal-oxygen bond; consequently the net charge on the O_s^{2-} increases and hence its electron

donor character.

A final effect which influences the properties is the preferential vaporization of SrO from the surface layer at high temperature, producing an enrichment in CaO. The effect is greater the greater the strontium content of the starting solution.

The above effects all act simultaneously and only a thorough analysis will explain the observed surface properties. Distinction into individual effects is often unjustified, the so-called structural effects have immediate ionic and electronic consequences and the effect of the surface area, for instance, has opposing consequences to those of the lattice dimensions. Furthermore, if one considers effects 1(b) and 2(b) it can be deduced that increasing Sr concentration decreases the proportion of the stronger electron-donor O_s^{2-} (lower coordinatively unsaturated surface O^{2-} ions) but increases their strength.

Regarding catalytic activity toward base-catalyzed reactions, the activity will be determined by two factors, the ease of forming a carbanion and of stabilizing it and the strength of the bonding of the adsorbed species to the surface. Considering the electronic effects by themselves, increasing Sr content increases the electron-donor character of O_s^{2-} and accordingly the charge on the anionic adsorbed species increases. On the other hand, considering the structural effects by themselves, increasing Sr content decreases the stabilization of the adsorbed species, as already stated. Therefore it is logical to predict that there should be an intermediate composition in the solid solution range where these two effects balance each other to provide the optimum surface properties for catalytic activity. Moreover, interpretation

of the surface exciton spectra led to the conclusion that the ionic and electronic effects are stronger at the Sr-rich end and the structural effect at the Ca-rich end.

Consequently, no predictions can be made beforehand about the surface properties of a particular solid solution, nor can they be interpolated from the properties of the end members. Each solid solution should be regarded as a new chemical entity.

Hitherto only a few physicists have been interested in CaO-SrO solid solutions, and this work constitutes the first investigation into their chemical properties. Much remains to be done and several suggestions can be given for the scope of future research.

Regarding surface chemistry, the first suggestion would be to make a surface analysis by electron spectroscopy (XPS, Auger spectroscopy) to determine the magnitude of SrO vaporization.

Secondly, the basic strength distribution through the whole range of composition would be a very useful scale for comparison and correlations with catalytic activity. This could be studied by titration with Lewis acids.

The nature of the surface sites could be studied by infra-red and UV-Vis spectroscopy in combination with adsorption experiments.

In the catalysis field, as mentioned before, the CaO-SrO solid solutions present high catalytic activity towards isomerization reactions (and also polymerization), and thus more reactions, including those involving selectivity, could be studied. A possible area of study would be hydrogenation and hydrogenolysis of hydrocarbons.

The solid solutions are highly reactive towards water and CO_2 and consequently they must be installed and used in systems free from these gases. This greatly reduces their practicability. Thus, a useful step would be to look for a suitable additive to incorporate in the solid which could inhibit this reactivity towards water vapor and CO_2. Once they are more stable, an attempt could be made to increase the specific surface area by varying the preparation conditions.

APPENDIX

APPENDIX

1.1 Haag and Pines Approach

The isomerization of butene is considered as a 3 component system interconnected by 3 first order reversible reactions as sketched in Figure 1.1.

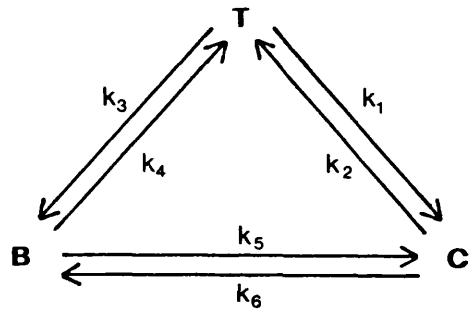

Figure 1.1

In this appendix a detailed solution of the kinetic problem is intended.

Let us assume t-2-butene (T) as reactant with initial concentration a; let b be the concentration of 1-butene (B) at any time t and c the concentration of c-2-butene, as referred in Figure 1.1.

The kinetic equation for the formation of B is given by :

$$\frac{db}{dt} = k_3 a + (k_6 - k_3)c - (k_3 + k_4 + k_5)b \qquad 1.1$$

and from here c is obtained as :

$$c = \frac{1}{k_6 - k_3} \frac{db}{dt} - k_3 A + (k_3 + k_4 + k_5)b \qquad 1.2$$

Similarly, the kinetic equation for the formation of C is :

$$\frac{dc}{dt} = k_1a + (k_5-k_1)b - (k_1+k_2+k_6)c \qquad 1.3$$

and from here b is obtained as :

$$b = \frac{1}{k_5-k_1}\frac{dc}{dt} - k_1a + (k_1+k_2+k_6)c \qquad 1.4$$

Differentiation of equations 1.1 and 1.3 produces equations 1.5 and 1.6 respectively :

$$\frac{d^2b}{dt^2} = (k_6-k_3)\frac{dc}{dt} - (k_3+k_4+k_5)\frac{db}{dt} \qquad 1.5$$

$$\frac{d^2c}{dt^2} = (k_5-k_1)\frac{db}{dt} - (k_1+k_2+k_6)\frac{dc}{dt} \qquad 1.6$$

Equation 1.5 has to be converted as g(b) = f(t) by substitution of 1.2 in 1.3 and the result in 1.5, and so 1.6 might be converted as g(c) = f(t) by substitution of 1.4 in 1.1 and the result in 1.6. Thus equations 1.7 and 1.8 are obtained as :

$$\frac{d^2b}{dt^2} + m\frac{db}{dt} + nb = P_1a \qquad 1.7$$

$$\frac{d^2c}{dt^2} + m\frac{dc}{dt} + nc = P_2a \qquad 1.8$$

where :

$$m = k_1+k_2+k_3+k_4+k_5+k_6 \qquad 1.9$$

$$n = k_1k_4 + k_1k_5 + k_1k_6 + k_2k_3 + k_2k_4 + k_3k_5 + k_3k_6 + k_4k_6 \qquad 1.10$$

$$P_1 = k_1k_4 + k_1k_5 + k_3k_5 \qquad 1.10$$

$$P_2 = k_1k_6 + k_2k_3 + k_3k_6 \qquad 1.12$$

The first solution of equations 1.7 and 1.8 is g(b) or g(c) equal to a constant which might be evaluated by substitution in the respective equation, say :

$$\left.\begin{array}{l} b = A \\ \dfrac{db}{dt} = 0 \\ \dfrac{d^2b}{dt^2} = 0 \end{array}\right\} \Rightarrow \quad nA = P_1 a$$

$$A = \frac{P_1 a}{n} \qquad 1.13$$

or

$$g_1(b) = \frac{P_1 a}{n} \qquad 1.14$$

$$g_1(c) = \frac{P_2 a}{n} \qquad 1.15$$

The dependence on time t_m can be calculated from the homogeneous quadratic equation :

$$y^2 + my + n = 0 \qquad 1.16$$

with roots given by :

$$y = \frac{-m \pm (m^2-4n)^{\frac{1}{2}}}{2} \qquad 1.17$$

and so,

$$g_2(b) = c_1 e^{y_1 t} \qquad 1.18$$

$$g_3(b) = c_2 e^{y_2 t} \qquad 1.19$$

$$g_2(c) = c_1 e^{y_1 t} \qquad 1.20$$

$$g_3(c) = c_2 e^{y_2 t} \qquad 1.21$$

becoming

$$g(b) = g_1(b) + g_2(b) + g_3(b)$$

$$g(c) = g_1(c) + g_2(c) + g_3(c)$$

or

$$b = c_1 e^{y_1 t} + c_2 e^{y_2 t} + \frac{p_1 a}{n} \qquad 1.22$$

$$c = c_1' e^{y_1 t} + c_2' e^{y_1 t} + \frac{p_2 a}{n} \qquad 1.23$$

The constants c_1, c_2, c_1', c_2' are evaluated using the boundary conditions at t = o

$$b = o \qquad\qquad c = o$$

$$\frac{db}{dt} = k_3 a \qquad\qquad \frac{dc}{dt} = k_1 a$$

or

$$c_1 + c_2 + \frac{p_1 a}{n} = 0 \qquad 1.24$$

$$c_1 y_1 + c_2 y_2 = 0 \qquad 1.25$$

$$c_1' + c_2' + \frac{p_2 a}{n} = 0 \qquad 1.26$$

$$c_1' y_1 + c_2' y = k_1 a \qquad 1.27$$

which yield :

$$c_1 = \frac{a}{(m^2 - 4n)^{\frac{1}{2}}} \left(k_3 + \frac{p_1}{n} y_2 \right) \qquad 1.28$$

$$c_2 = \frac{-a}{(m^2-4n)^{\frac{1}{2}}}\left(k_3 + \frac{p_1}{n}y_1\right) \qquad 1.29$$

$$c_1' = \frac{a}{(m^2-4n)^{\frac{1}{2}}}\left(k_1 + \frac{p_2}{n}y_2\right) \qquad 1.30$$

$$c_2' = \frac{-a}{(m^2-4n)^{\frac{1}{2}}}\left(k_1 + \frac{p_2}{n}y_1\right) \qquad 1.31$$

The following substitutions seem to be reasonable to simplify the final expressions for b and c :

$$q = (m^2 - 4n)^{\frac{1}{2}} \qquad 1.32$$

$$r_1 = \frac{-m + q}{2} \qquad 1.33$$

$$r_2 = \frac{-m - q}{2} \qquad 1.34$$

and so ,

$$b = \frac{a}{q}\left(k_3 + \frac{p_1}{n}r_2\right)\exp(r_1t) - \left(k_3 + \frac{p_1}{n}r_1\right)\exp(r_2t) + \frac{p_1a}{n} \qquad 1.35$$

$$c = \frac{a}{q}\left(k_1 + \frac{p_2}{n}r_2\right)\exp(r_1t) - \left(k_3 + \frac{p_2}{n}r_1\right)\exp(r_2t) + \frac{p_2a}{n} \qquad 1.36$$

Division of 1.35 and 1.36 by $\underline{a}$ leaves the expressions in terms of the molar fractions X_b and X_c as given in 1.37 and 1.38 respectively

$$X_b = \left(k_3 + \frac{p_1}{n}r_2\right)\exp(r_1t) - \left(k_3 + \frac{p_1}{n}r_1\right)\exp(r_2t)\ /q + \frac{p_1}{n} \qquad 1.37$$

$$X_c = \left(k_3 + \frac{p_2}{n}r_2\right)\exp(r_1t) - \left(k_3 + \frac{p_2}{n}r_1\right)\exp(r_2t)\ /q + \frac{p_2}{n} \qquad 1.38$$

1.2 Wei and Prater Approach

In this section a three-component monomolecular system will be considered. The general ideas will be pointed out and the complete method for determining the rate constants will be developed. Figure 1.2 sketches the terminology with which we are going to be concerned.

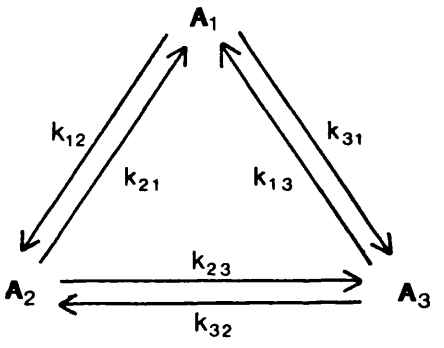

Figure 1.2

The rate of change of the amount of each species (a_i) is given by :

$$\frac{da_1}{dt} = -(k_{21} + k_{31})a_1 + k_{12}a_2 + k_{13}a_3$$

$$\frac{da_2}{dt} = k_{21}a_1 - (k_{12} + k_{32})a_2 + k_{23}a_2$$

$$\frac{da_3}{dt} = k_{31}a_1 + k_{32}a_1 - (k_{13} + k_{23})a_3 \qquad 1.39$$

The general solution to a set of linear first order equations such as 1.39 is well known to be :

$$a_1 = c_{10} + c_{11}e^{-\lambda_1 t} + c_{12}e^{-\lambda_2 t}$$

$$a_2 = c_{20} + c_{21}e^{-\lambda_1 t} + c_{22}e^{-\lambda_2 t}$$

$$a_3 = c_{30} + c_{31}e^{-\lambda_1 t} + c_{32}e^{-\lambda_2 t} \qquad 1.40$$

where c_{ij} and λ_i are constant parameters related to the rate constants.

The structural analysis of the set of equations 1.39 and 1.40 provides us with certain keys :

(i) There is a strong coupling between the variables, i.e. changes in the amount of A_i during the reaction affect the amount of species A_j.

(ii) There is a set of species B_i equivalent to a set of species A_i such that the variables b_i in the rate equations for the b species are completely uncoupled.

Let us begin by expressing set 1.39 in its matrix form

$$\frac{d\underline{\alpha}}{dt} = \underline{\underline{k}}\underline{\alpha} \qquad 1.41$$

where :

$$\underline{\alpha} = \begin{pmatrix} a_1 \\ a_2 \\ a_3 \end{pmatrix} \qquad 1.42$$

$$\underline{\underline{k}} = \begin{pmatrix} -(k_{21} + k_{31}) & k_{12} & k_{13} \\ k_{21} & -(k_{12} + k_{32}) & k_{23} \\ k_{31} & k_{32} & -(k_{13} + k_{23}) \end{pmatrix} \qquad 1.43$$

Two constraints have to be taken into account :

(1) the total mass of the reaction system is conserved

$$\sum_{1\ 1}^{3} a_i = 1 \qquad 1.44$$

(2) no negative amounts can arise $a_i > 0$ 1.45

The characteristic directions given by the eigenvectors ($\underline{\alpha}_j^+$) in equation 1.46 have the very desirable property that the rate of change of $\underline{\alpha}_j^+$ depends only on $\underline{\alpha}_j^+$ (it is completely uncoupled from vectors along other characteristic directions)

$$\underline{k}\ \underline{\alpha}_j^+ = -\lambda_j \underline{\alpha}_j^+ \qquad 1.46$$

which combines with 1.4.48 to give :

$$\frac{d\underline{\alpha}_j^+}{dt} = -\lambda_j \underline{\alpha}_j^+ \qquad 1.47$$

Then by choosing a unit vector in the jth characteristic direction ($\underline{x}_j$) we can express the amount of the new B species as :

$$\underline{\beta} = \begin{pmatrix} b_o \\ b_1 \\ b_2 \end{pmatrix} \qquad 1.48$$

which is another representation of the α vector but in different coordinate axes, and so :

$$\underline{\alpha}_j^+ = b_j \underline{x}_j \qquad 1.49$$

Substitution of 1.49 in 1.47 and knowing that x_j is constant :

$$\frac{db_j}{dt} = \lambda_j b_j \qquad 1.50$$

which is a set of equations similar to 1.39, but this time, formed by uncoupled differential equations

$$\frac{d\underline{\beta}}{dt} = \underline{\Delta}\,\underline{\beta} \qquad 1.51$$

$$\underline{\Delta} = -\begin{pmatrix} \lambda_o & 0 & 0 \\ 0 & \lambda_1 & 0 \\ 0 & 0 & \lambda_2 \end{pmatrix} \qquad 1.52$$

Therefore, the solutions to the set 1.51 are :

$$\begin{aligned} b &= b_o{}^o e^{-\lambda_o t} \\ b &= b_1{}^o e^{-\lambda_1 t} \\ b &= b_2{}^o e^{-\lambda_2 t} \end{aligned} \qquad 1.53$$

The relation of $\underline{\alpha}$ and $\underline{\beta}$ is given by equation 1.54

$$\underline{\alpha} = \underline{\underline{X}}\,\underline{\beta} \qquad 1.54$$

where

$$\underline{\underline{X}} = (\underline{x}_j) \qquad 1.55$$

The choice of the vectors $\underline{x}_j$ is as follows :

$$\underline{X}_o = \alpha^* \qquad 1.56$$

where α^* is the composition at equilibrium.

By choosing an initial composition (which can be 1, 0, 0) and following its path to the equilibrium, points near the equilibrium

behaving linearly can be extrapolated away towards the axes in order to determine a new initial composition ($\underline{\alpha x}_1$) which is then chosen for the next experiment; by carrying out the same procedure again another new initial composition ($\underline{\alpha x}_2$) can be determined, and so on

$$\underline{X}_1 = \underline{X}_o - \alpha_{x_1} \qquad 1.57$$

$$\underline{X}_2 = \underline{X}_o - \alpha_{x_2} \qquad 1.58$$

The set of equations for the B species can then be written as

$$\underline{k}\ \underline{x}_j = -\lambda_j \underline{x}_j \qquad 1.59$$

from where equation 1.60 is obtained :

$$\underline{k} = \underline{X}\ \underline{\Delta}\ \underline{X}^{-1} \qquad 1.60$$

which gives us the way of transforming the rate constant for the B species into the real rate constants.

Thus, the choice of $\underline{x}$ determines the necessary experimental conditions to carry out this method. The different compositions of the system through which an initial composition passes in its route to equilibrium form the data of an experiment. From one experiment the needed initial composition for the next one can be determined as well.

REFERENCES

1. Allred A.L.: J. Inorg. Nucl. Chem. 1961, 17, 215

2. Moore C.E.: Ionization Potentials from Optical Spectra, NSRDS-NBS 34, US Government, Printing Office, Washington DC, 1970

3. Shannon R.D. and Prewitt C.T.: Acta Cryst. 1969, 925

4. a) Swanson H.E. et al.: J.C. Fel. Reports, NBS 1950,
   b) Swanson H.E. et al.: NBS Circular 539, 1955, 5

5. Krylov O.V.: Catalysis by Non Metals, Academic Press, NY. 1970

6. a) Schofield K.: Chem. Rev. 1967, 67, 707;
   b) Huggins M.L. and Sakamoto Y.: J. Phys. Soc. Japan 1957, 12, 241;
   c) Handbook of Chem. and Phys. 52nd. Ed. 1971-72

7. Surplice N.A.: Br. J. Appl. Phys. 1966, 17, 175

8. Mitoff S.P.: J. Chem. Phys. 1962, 36, 1383

9. Copeland W.D. and Swalin R.A.: J. Phys. Chem. Solids 1968, 29, 313

10. Swalin R.A.: J. Phys. 1973, 34, 167

11. Henderson G. and Wertz J.E.: Adv. Phys. 1968, 17, 749

12. a) Whited R.C. and Walker W.C.: Phys. Rev. Lett. 1969, 22 (26), 1428;
   b) Saum G.A. and Hansley E.B.: Phys. Rev. 1959, 113, 1019;
   c) Kerney R.J., Cottini M., Grilli E. and Baldini G.: Phys. Status Solidi B, 1974, 64, 49

13. Tanabe K.: Solid Acids and Bases, their catalytic activity. Academic Press, New York 1970

14. Nelson R.L. and Hale W.J.: Disc. Faraday Soc. 1971, 52, 77

15. Zecchina A., Lofthouse M.G. and Stone F.S.: J.C.S. Faraday I, 1975, 71 1476

16. Zecchina A. and Stone F.S.: J.C.S. Faraday I, 1976, 72, 2364

17. Coluccia S., Deane A.M. and Tench A.J.: J.C.S. Faraday I, 1978, 74, 2913

18. Zeitlin H., Frei R. and Mc. Carter M.: J. Catalysis 1965, 4, 77

19. Zeitlin H., Frei R. and Fujie G.: Can. J. Chem. 1966, 44, 3051

20. Zecchina A. and Stone F.S.: J.C.S. Faraday I, 1978, 74, 2278

21. Trevethan M.: Ph.D. Thesis, University of Bath 1977

22. Coluccia S., Hemidy J.F. and Tench A.J.: J.C.S. Faraday I, 1978 74, 2763

23. Coluccia S., Chiorino A., Guglielminotti E. and Morterra C.: J.C.S. Faraday I, 1979, 75, 2177

24. Iizuka T., Hattori H., Ohno Y., Sohma J. and Tanabe K.: J. Catalysis 1971, 22, 130

25. Iizuka T., Hattori H., Endo Y. and Tanabe K.: Chem. Lett. 1976, 803

26. Cordischi D., Indovina V. and Occiuzzi M.: J.C.S. Faraday I, 1978, 74, 833

27. Che M., Coluccia S. and Zecchina A.: J.C.S. Faraday I, 1978 74, 1324

28. Ohno Y., Takagiwa H. and Fukuzumi S.: J.C.S. Faraday I, 1979 75, 1613

29. Take J., Kikuchi N. and Yoneda Y.: J. Catalysis 1971, 21, 164

30. Mochida I., Take J., Saito J. and Yoneda Y.: J. Org. Chem. 1967, 32, 3894

31. a) Hattori H., Tanabe K. and Tanaka V.: Chem. Lett. 1975, 7 659;

b) Okamoto V., Imanaka T., Teramischi S.: Bull. Chem. Soc. Japan, 1972, 45 (10), 3207;

c) Mc. Caffrey E.F., Micka T.A. and Ross R.A.: J. Phys. Chem. 1972, 76 (23), 3372;

d) Tanabe K. and Sayto K.: J. Catalysis 1974, 35, 247;

e) Tanabe K. and Fukuda Y.: Reac. Kinet. Catal. Lett. 1974, 1 (1), 21;

f) Misono M. and Yoneda Y.: J. Catalysis 1974, 33, 474;

g) Meubus P.: J. Electrochem. Soc. 1977, 124 (1), 49;

h) Krylov O.V. and Fokina E.A.: Doklady Akad. Nauk. SSSR., 1958, 120, 333

32. a) Katsuaki S., Hattori H. and Tanabe K.: J. Catalysis 1977, 48, 302;

b) Arata K., Akutawa S. and Tanabe K.: J. Catalysis 1976,41

c) Morishige K., Hattori H. and Tanabe K.: J.C.S. Chem. Commun. 1975, 14, 559

d) Ohmisshi R. and Tanabe K.: Chem. Lett. 1974, (3), 207

33. Megaw H.D.: Crystal Structures, W.B. Saunders and Co. Philadelphia 1973

34. Wyckoff R.W.G.: Crystal Structures V.2, Interscience Pub. 2nd. Ed., New York 1964

35. Evans G.C.: Crystal Chemistry, University Press, 2nd. Ed. Cambridge 1964

36. Swanson H.E. and Fuyat R.K.: NBS Circular 539, 1953, 2, 51

37. Bragg W.L.: Proc. Roy. Soc. A., 1924, 105, 16

38. Swanson H.E. and Fuyat R.K.: NBS Circular 539, 1953, 3

De Villiers J.P.R.: Am. Miner. 1971, 56, 758

39. Kamhi S.R.: Acta Cryst. 1963, 16, 770

40. Deer W.A., Howie R.A. and Zussman J.: Rock Forming Minerals V.5, Longmans, Great Britain 1962

41. Bischoff J.L. and Fife W.S.: Am. J. Science 1968, 266, 65

42. a) Garrews R.M. and Christ C.L.: Solutions, Minerals and Equilibria, Harger and Raw, New York 1965;

b) Bischoff J.L. and Fife W.S.: Special Pub. Econ. Paleontologists and Mineralogists 1965, 13, 3

43. Faust G.I.: Amer. Miner. 1950, 35, 207

44. Wray J.L. and Daniels F.: J. Am. Chem. Soc. 1957, 79, 2031

45. Remy H.: Lehbr 1931, 225

46. Dutoit W.: J. Chim. Phys. 1927, 24, 110

47. Cuthbert F.L. and Rowland R.A.: Amer. Miner. 1947, 32, 111

48. Grimm H.G.: Hanb. d. Phys. 1927, 24, 589;
Grimm H.G. and Wolff H.: Handb. d. Phys. 1933, 24(2), 1096

49. Guggenheim E.A.: Mixtures, Clarendon Press, Oxford 1952

50. Vegard L. and Schjelderup H: Phys. Z. 1917, 18, 93
Vegard L.: Z. Phys. 1921, 5, 17

51. Zen E,: Amer. Miner. 1956, 41, 523

52. Frevel L.K.: Anal. Chem. 1970, 42(13), 1583

53. Huber H. and Wagener S.: Z. Tech. Physik 1942, 23, 1

54. Guichard M. and Wyart J.: Compt. Rend. 1943, 216, 844

55. Terada J.: J. Phys. Soc. Japan; 1952, 7, 432

56. Ostapchenko E.P.: Bull. Acad. Sci. USSR Phys. Ser 1956, 20
a) 687 b) 997

57. Oxburg U.M., Segnit R.E. and Holland H.D.: Bull. Geol. Soc. Amer. 1959, 70, 1653

58. Holland H.D., Borcsik M. and Munoz J.: Geochim. Cosmochim. Acta 1963, 27, 957

59. Holland H.D., Holland H.J. and Munoz J.: Geochim. Cosmochim. Acta 1964, 28, 1287.

60. Evstigneeva M.M., Iofis N.A. and Bundel A.A.: Zh. Fiz. Khim. 1974, 48(6), 1360

61. Hall R.W.S. and Sharp J.H.: Proc. Europ. Symp. Therm. Anal. 1st. 1976, 261

62. Zentsova S.N., Prodan E.A. and Pavlyuchenko M.M.: Zh. Fiz. Khim. 1977, 51(6), 1406

63. Heinz K. and Muenchberg W.: Tonind. Ztg. Keram. Rundsch 1968, 92(6), 201

64. Grey L.E.: Nature 1951, 167, 522

65. Logatchov YU.A. and Moijes B.IA.: Surface Sci. 1969, 17, 504

66. King A.: J. Chem. Soc. 1937, 1489

67. Schwab G.M. and Kral H.: Proc. Intern. Congr. Catal. 3rd. Amsterdam 1964, I, N. 20

68. Kortum G.: Angew. Chem. 1958, 70, 651

69. Zaugg H.E. and Schaffer A.D.: J. Am. Chem. Soc. 1965, 87, 1857

70. Zeitlin H., Kondo N. and Jordan W.: J. Phys. Chem. Solids 1964, 25, 641

71. Terenin A.N.: Adv. Catal. 1964, 15, 227

72. Walverkar S.P. and Halgeri A.B.: Technology (Sindry, India) 1974, 11, 73

73. Malinowski S. and Szczepanska S.: J. Catal. 1963, 2, 310

74. Kijenski J., Hombek R. and Malinowski S.: J. Catal. 1977, 50, 186

75. Tanabe K. and Yamaguchi T.: J. Res. Inst. Catalysis Hokkaido Univ. 1964, 11, 179

76. Pines H. and Schaap L.A.: Adv. Catal. 1960, 12, 117

77. Pines H.: Acc. Chem. Rev. 1974, 7(5), 155

78. Pines H. and Stalick W.M.: Base-catalyzed Reactions of Hydrocarbons and Related Compounds, Academic Press, New York 1977

79. Schachter Y. and Pines H.: J. Catal. 1968, 11, 147

80. Shimazu K., Hattori H. and Tanabe K.: J. Catal. 1977, 48, 302

81. Zierzak A. and Pines H.: J. Org. Chem. 1962, 27, 4084

82. Pines H., Vesely J.A. and Ipatieff V.N.: J. Am. Chem. Soc. 1955, 77, 554

83. Hambling J.K.: Chem. Brit. 1969, 5, 354

84. Bush W.B., Holzman G. and Shaw A.W.: J. Org. Chem. 1965, 30, 3290

85. Eberhardt G.G. and Peterson H.J.: J. Org. Chem. 1965, 30, 82

86. Carter G.B., Dewing J. and Pumphrey N.W.J.: Proc. Inter. Congr. Catal. 5th Miami 1972, 2, 1445

87. Pines H. and Eschinazi H.E.: J. Am. Chem. Soc. 1955, 77, 6314

88. Arata K., Akutagawa S. and Tanabe K.: J. Catal. 1976, 41, 173

89. Tanabe K. and Fokuda Y.: React. Kinet. Catal. Lett. 1974, 1, 405

90. McCarthy W.W. and Turkevich J.: J. Chem. Phys. 1944, 12, 405

91. Haag W.O. and Pines H.: J. Am. Chem. Soc. 1960, 82, 387

92. Wey J. and Prater CH.D.: Adv. Catal. 1962, 13, 203

93. Hightower J. and Hall W.K.: Chem. Eng. Prog. Sym. Ser. 1967, 63, (73), 122

94. Turkevich J. and Smith R.K.: J. Chem. Phys. 1948, 16, 466

95. Brouwer D.M.: J. Catal. 1962, 1, 22

96. Medema J. and Houtman J.P.W.: J. Catal. 1966, 6, 322

97. Haag W.O. and Pines H.: J. Am. Chem. Soc. 1960, 82, 2488

98. Hightower J. and Hall W.K.: J. Phys. Chem. 1967, 71, 1014

99. Lucchesi N.J., Barder D.L. and Longwell J.P.: J. Am. Chem. Soc. 1959, 81, 3235

100. Leftin H.P. and Hermana E.: Proc. Inter. Congr. Catal. 3rd. Amsterdam 1964, 2, 1064

101. Gerberich H.R. and Hall W.K.: J. Catal. 1966, 5, 99

102. Hightower J., Gerberich H.R. and Hall W.K.: J. Catal. 1967 7, 57

103. Hightower J., Hall W.K.: J. Am. Chem. Soc. 1967, 89, 778

104. Wilke G., Bogdanovic B., Hardt P., Heinbach P., Kein W., Kroner M., Oberkirch W., and Tanaka K.: Angew. Chem. Int. Ed. Engl. 1966, 5, 151

105. Chang C.C., Conner W.C. and Kokes R.J.: J. Phys. Chem. 1973, 77, 1957

106. Baird M.J. and Lunsford J.H.: J. Catal. 1972, 26, 440

107. Chuvylkin N.D., Zhidomirov G.M. and Kasanski V.B.: J. Catal. 1976, 44, 76

108. Clark A and Finch J.N.: Proc. Inter. Congr. Catal. 4th,Moscow, 1968, 4, 1355

109. Kubokawa Y., Adachi T., Tomino T. and Ozawa T.: Proc. Inter. Congr. Catal. 4th, Moscow, 1968, 4, 692

110. Shannon I.R., Kemball C. and Leach H.F.: Chemisorption and Catalysis, P. Hepple Ed., London 1970, pp 46-57

111. Hattori H. and Satoh A.: J. Catal. 1976, 43, 32

112. Mohri M., Tanabe K. and Hattori H.: J. Catal. 1974, 32, 144

113. Hattori H., Yoshii N. and Tanabe K.: Proc. Intern. Congr. Catal. 5th, Miami, 1972, 1, 233

114. Klug H.P. and Alexander L.E.: X-Ray Diffraction Procedures, for polycrystalline and amorphous material, John Wiley & Sons, New York, 1974, 2nd. Ed.

115. Azaroff L.W. and Buerger M.J.: The Powder Method in X-Ray Crystallography. McGraw Hill Co., New York 1958

116. D'Eye R.W.M. and Wait E.: X-Ray Powder Photography in Inorganic Chemistry, Butterworth, London 1960

117. Wilson A.J.C.: Elements of X-Ray Crystallography. Addison-Wesley Publishing Co., New York 1970.

118. Bearden J.A.: Rev. Mod. Phys. 1967, 39, 78

119. Bradley A.J. and Jay A.H.: Proc. Phys. Soc. (London) 1932, 44, 563

120. Straumanis M.E.: J. Appl. Phys. 1949, 20, 726

121. Nelson J.B. and Riley D.P.: Proc. Phys. Soc. (London) 1945, 57 160

122. Brillouin L.: Wave Propogation in Periodic Structures. Dover, New York 1953

123. von Hippel A.: Z. Phys. 1936, 101, 680

124. Klemm W.: Z. Phys. 1933, 82, 529

125. De Boer J.H.: Electron and Emission Phenomena. Cambridge 1935

126. Frenkel J.: Phys. Rev. 1931, 37, 17; 276

127. Wannier G.H.: Phys. Rev. 1936, 52, 191

128. Rayleigh J.W.: Phil. Mag. 1881, 12, 81; 1899, 47, 375

129. Mie G.: Ann. Physik. 1908, 38, 448

130. Kubelka P.: J. Opt. Soc. Ann. 1948, 38, 448

131. Lambert J.H.: Photometria Augsburg 1760. Anding Liepzig 1982

132. Kubelka P. and Munk F.: Z. Tech. Physik 1931, 12, 593

133. a) Kortum G. and Schreyer G.: Angew. Chem. 1955, 67, 694

b) Kortum G. and Schreyer G.: Z. Naturforsch 1956, 11a, 1018

c) Kortum G. and Vogel J.: Z. Physik Chem. (Frankfurt) 1958, 18, 230

134. Kortum G., Braum W. and Herzog G.: Angew. Chem. 1963, 75, 635

135. Kortum G.: Reflectance Spectroscopy. Springer-Verlag, Berlin 1969

136. Wendlandt W.W. and Hecht H.G.: Reflectance Spectroscopy. Interscience Publishers, New York, 1966

137. Terenin A.: Adv. Catal. 1964, 15, 227

138. Klier K.: Catal. Rev. 1967, 1, 207

139. Ayscough P.B.: Electron SPin Resonance in Chemistry. Methuen & Co., London 1967

140. Blumenfeld L.A., Voevodski V.V. and Semenov A.G.: Electron Spin Resonance in Chemistry, translated by Assenheim H.M., Adan Hilger Ltd., London 1973

141. Wertz J.E. and Bolton J.R.: ESR, Elementary Theory and Applications. McGraw-Hill Book Co., United States 1972

142. Poole C.P.: ESR. A Comprehensive treatise on experimental techniques. Interscience Publishers, New York 1967

143. Swartz H.M., BOlton J.R. and Borg D.C.: Biological Applications of ESR. Wiley-Interscience, New York 1972

144. O'Reilly D.E.: Adv. Catal. 1960, 12, 31

145. Kokes R.J.: Experimental Methods in Catalytic Research (R.B. Anderson, Ed.) pp 436-473. Academic Press, New York 1968

146. Adrian F.J.: J. Colloid. Interface Sci. 1968, 26, 317

147. Kasanski V.B. and Pariiski G.B.: Proc. Intern. Congr. Catalysis, 3rd. Amsterdam 1964, 1, 367

148. Voevodski V.V.: Proc. Inter. Congr. Catalysis, 3rd. Amsterdam 1964, 1, 88

149. Lunsford J.H.: Adv. Catal. 1971, 22, 265

150. Gardner C.L. and Casey E.J.: Cat. Rev. 1974, 9(1), 1

151. Hyde J.S.: Varian Associates, Anal. Instr. Div., Palo Alto, California. 7th Annual NMR-ESR Workshop 1963

152. Andrew R.: Phys. Rev. 1953, 91, 425

153. Halbach K.: Phys. Rev. 1960, 119, 1230

154. Randolph M.L.: Rev. Sci. Instr. 1960, 31, 949

155. Wyard S.J.: J.Sci. Instr. 1965, 42 669

156. James A.T., Martin A.J.P. and Smith G.H.: Biochem. J. 1952, 52, 238

157. Kokes R.J., Tobin H.H. and Emmett P.H.: J. Am. Chem. Soc. 1955, 77, 5860

158. Langer S.H., Yurchak J.Y. and Patton J.E.: Ind. and Eng. Chem. 1969, 61 (4), 11

159. Murakami Y. and Hattori T.: J. Catal. 1968, 10, 114; 123

160. Arean C.O. and Stone F.S.: J.C.S. Faraday I, 1979, 75, 2285

161. Holden A.N., Kittel C., Merrit F.R. and Yager W.A.: Phys. Rev. 1950, 77, 147

162. Hutchinson C.A., Pastor R.C. and Kowalsky A.G.: J. Chem. Phys. 1952, 20, 534

163. Johnston J., Merwin H.E. and Williamson E.D.: Amer. J. Sci. 1916, 41, 473,

164. Glasson D.R.: J. Appl. Chem. 1958, 8, 793

165. Atkins P.W.: Molecular Quantum Mechanics(III) Clarendon Press,Oxf. 1978

166. Lunsford J.H.: Cat. Rev. 1973, 8 (1), 135

167. Levine J.D. and Mark P.: Phys. Rev. 1966, 144, 751

168. Nelson R.L., Hale J.W. and Harmsworth B.J.: J.C.S. Faraday I, 1971, 67, 1164

169. Solomon I.J., Hattori K., Kacmarek A.N., Platz G.M. and Klein M.J.: J. Am. Chem. Soc. 1962, 84, 34

170. Garrone E., Zecchina A. and Stone F.S.: Phil. Mag. (in press)

171. Ivey H.F.: Phys. Rev. 1947, 72, 341;
Hilsch R. and Pohl R.W.: Z. Physik 1930, 59, 812

172. Habersbergerova A., Janovsky I. and Kourim P.: Radiation Res. Rev. 1972, 4, 123;
Jaffe H.H. and Orchin M.: Theory and Application of Ultraviolet Spectroscopy, Wiley, New York 1962;
Muller A., Seidel H.and Ritter W.: Spectrochimica Acta A, 1967, 23, 1619;
Gradon D.P.: J. Inor. Nuclear Chem. 1956, 3, 308

173. Lunsford J.H. and Jayne J.P.: J. Chem. Phys. 1966, 44, 1487

174. Cordischi D., Indovina V. and Occhiuzzi M.: J.C.S. Faraday I 1980, 76, 1147

175. Guglielminotti E., Coluccia S., Garrone E., Cerruti L. and Zecchina A.: J.C.S. Faraday I 1979, 75, 96

176. Pauling L.: The Nature of the Chemical Bond, Cornell Univ. Press, Ithaca, New York 1939, p72

177. Phillips J.C.: Rev. mod. Phys. 1970, 42, 317

178. Goyal S.C. and Tripathi S.P.: J. Phys. Chem. Solids 1977, 38, 351

179. A.P.I. Research Project N. 44, 1953, pp 556-558

180. Garrone E., Zecchina A. and Stone F.S.: J. Catal. 1980, 62, 396

181. Rosenbaum J. and Symons M.C.R.: J. Chem. Soc. 1961, 1

182. Deno N.C., Groves P.J. and Saines G.: J. Am. Chem. Soc. 1959, 81, 5790

183. Tench A.J. and Nelson R.L.: J.C.S. Faraday I, 1967, 63, 2254

184. Flockhart B.D., Leigh I.R. and Pink R.C.: Chem. Comm. 1966, 855

185. Subba Rao V.V., Iyengar R.D. and Zettlemoyer K.: J. Catal. 1968, 12, 278

186. Fox W.M., Gross J.M. and Symons M.C.R: J.Chem. Soc. (A) 1966, 448

187. Tench A.J. and Lawson T.: Chem. Phys. Lett. 1970, 7, 459; Tench A.J., Lawson T. and Kibblewhite J.F.J.: Faraday I 1972, 68, 1169

188. Ben Taarit Y. and Lunsford J.H.: Proc. Inter. Congr. Catalysis, 5th (Miami), 1972, 2, 1401

189. Cordischi D., Indovina V. and Occiuzzi M.: J.C.S. Faraday I 1978, 74 456

190. Wong N.B. and Lunsford J.H.: J. Chem. Phys. 1972, 56, 2664

191. Bekey G.A. and Yamashiro S.: Adv. Biomedical Eng. 1976, 6, 1

192. Kallo D.: J. Catal. 1980, 66, 1